UC Davis
UC Davis Electronic Theses and Dissertations

Title

Layered and Low Dimensional Zintl Phases for Thermoelectric Applications

Permalink

https://escholarship.org/uc/item/2mt689wd

Author

Hauble, Ashlee

Publication Date

2023

Peer reviewed|Thesis/dissertation

eScholarship.org Powered by the California Digital Library
University of California

Layered and Low Dimensional Zintl Phases for Thermoelectric Applications.

By

ASHLEE KATHRYN HAUBLE

DISSERTATION

Submitted in partial satisfaction of the requirements for the degree of

DOCTOR OF PHILOSOPHY

in

Chemistry

in the

OFFICE OF GRADUATE STUDIES

of the

UNIVERSITY OF CALIFORNIA

DAVIS

Approved:

_____

Susan M. Kauzlarich, Chair

_____

Valentin Taufour

_____

Jesús M. Velázquez

Committee in Charge

2023

© Copyright by

Ashlee K. Hauble

2023

Dedicated to Mary Weltin Bible and Jocelyn Axelson Hauble

Layered and Low Dimensional Zintl Phases for Thermoelectric Applications.

Abstract

Thermoelectric generators (TEGs), which are fabricated from thermoelectric materials, convert heat into electricity with no moving parts, making them a robust and appealing renewable energy technology, given that approximately two thirds of the energy produced on earth is lost as waste heat. TEGs could be employed to scavenge heat from industrial plants and combustion engines to boost the efficiency of existing processes, or they could be used independently to generate usable electricity from geothermal sources and the sun. The efficiency of a TEG is dependent on the thermoelectric figure of merit, *zT*, of the materials used to create the device. *zT* is determined using a material's Seebeck coefficient (*S*), temperature (*T*), electrical resistivity (ρ), and thermal conductivity (κ), according to the relationship: $zT = \frac{S^2T}{\rho\kappa}$. To make TEGs attractive for large scale applications, thermoelectric materials with high *zT* need to be designed. This dissertation investigates the chemistry of several potential thermoelectric materials to gain deeper understanding of structure-property relationships that enable the design of highly efficient materials.

Layered Zintl phases are a class of materials that inherently exhibit low thermal conductivity due to their complex crystal structures and chemical tunability. They are composed of covalent networks with diverse bonding motifs separated by layers of cations, and the ionic

and covalent portions can be tuned separately to optimize thermal and electronic properties. The directional nature of the covalent bonding can also give rise to low dimensional electronic structures, which are beneficial for thermoelectric properties. The first project described in Chapter 2 of this dissertation is a study on defect chemistry in a solid solution of the layered Zintl phase $Yb_{2-x}Eu_xCdSb_2$. The goal of this research was to understand the unusually low thermal conductivity, high Seebeck coefficient and low electrical resistivity of this promising thermoelectric material by examining changes in defect chemistry as Eu is substituted for Yb using pair distribution function analysis. The local structures of $x = 0.2$ and 0.3 deviated substantially from the average structure due to large concentrations of Eu and Sb vacancies that give rise to structural distortions that alter electronic properties. Predictions suggest that $zT > 2$ at 550 K could be achieved for $x = 0.3$ if the carrier concentration can be tuned via doping. This work highlights the importance of understanding crystallographic disorder and defect structure in thermoelectric materials. This work was published in ACS Chemistry of Materials (2022, 34, 20, 9228–9239).

The next project presented in Chapter 3 focuses on $Ba_{2-x}Eu_xZnSb_2$, a Zintl phase that contains one-dimensional covalent chains and was predicted to exhibit $zT > 2$ at 900 K. Eu was substituted for Ba ($x = 0.2, 0.3, 0.4$) to reduce the air sensitivity of this compound, as well as reduce thermal conductivity through alloy scattering. Samples were prepared using binary precursors via ball milling and annealing and then consolidated by spark plasma sintering for thermoelectric property measurement. All compositions exhibited high Seebeck coefficients and low thermal conductivity, as well as high charge carrier mobility, an important quality for high efficiency thermoelectric materials, which is likely due to the one-dimensional chains.

Experimental results agreed well with theory and predictions suggest higher *zT* is achievable through doping.

$Eu_{11}Zn_4Sn_2As_{12}$ is another layered Zintl phase expected to exhibit a low-dimensional electronic structure due to high mobility hexagonal $[Zn_2As_3]^{5-}$ sheets in two crystallographic directions and ionic bonding in the third. This project presented in Chapter 4 brings theory and experiment together to understand a complex, disordered, modulated crystal structure, and develop a road map for further optimization of this promising thermoelectric material. Experimental results show high Seebeck coefficient and low thermal conductivity and electrical resistivity that decreases 5-fold with Na-doping. Denisty Functional Theory (DFT)computations show that, when doped, this material possesses a two-dimensional Fermi surface, and band structure calculations highlight the presence of multiple bands just below E_F, making $Eu_{11}Zn_4Sn_2As_{12}$ a promising candidate for further optimization.

Finally, theory and experiment are employed together again to characterize the electronic and structural transitions in $Yb_5Sb_3H_x$ as H content varies from $x = 0.25$ to 1. $Yb_5Sb_3H_x$ has been known to exist in two polymorphs, a hexagonal and an orthorhombic crystal structure, and previous work has suggested that H content drives the transition. In the study presented in Chapter 5, DFT calculations confirm that at lower H content ($x < 0.25$), the hexagonal crystal structure is energetically favored, while at $x > 0.25$, the orthorhombic cell is more stable and the synthesized polycrystalline samples for $x = 0.25$, 0.5, 0.75, and 1 support this finding. Previous theoretical work also suggests that $Yb_5Sb_3H_x$ is an electride with localized anionic electrons present in zero-dimensional cavities when $x < 1$ and a charge balanced semiconductor at $x = 1$. Thermoelectric properties were used to map this transition, and they show a shift from the low

charge carrier mobility associated with highly localized electride states (x = 0.25 and 0.5) to high mobility associated with free electrons in a semiconductor (x = 0.75 and 1). At x = 1, the compound exhibits high Seebeck coefficients and low thermal conductivity up at 775 K, in addition to excellent charge carrier mobility that make it a potential thermoelectric material if charge carrier concentration can be increased.

Acknowledgments

I would like to thank my advisor, Professor Susan M. Kauzlarich for her support and mentorship throughout my time in graduate school. She encouraged my ideas and helped me develop into a confident scientist. In my first year, I told her that I wanted to spend a quarter doing research in Germany, and she helped make that a reality, and with her support, I was able to present my work at conferences and educational programs around the country that helped inspire me to complete this dissertation. I would also like to thank my committee members, Professor Valentin Taufour and Professor Jesús Velázquez for their guidance and recommendations.

Drs. Kasey P. Devlin and Christopher Perez are brilliant scientists and wonderful people who took the time to mentor me and gave me the tools I needed to be successful as a solid-state chemist. They taught me the basics of synthesis, X-ray diffraction, thermoelectric measurements, and theory that I relied upon for the duration of my graduate studies. Beyond professional development, they welcomed me into the lab and helped me to feel at home in Davis and supported me through my qualifying exam. Their encouragement and willingness to help me and calm me down when things in the lab were broken was integral to my success. Dr. Allan He also

helped me with theory and pair distribution function analysis. I am grateful for my former labmates' mentorship, support, and friendship.

I would also like to thank Tanner Kimberly and Luis Garay for being amazing lab mates and friends. I wouldn't be where I am without them. They supported me through discussions of science, personal life, humor, and adventures, and I am forever grateful. I would also like to thank Benito Gonzalez for being the best undergraduate mentee I could have ever asked for.

Dr. Ali Abdel-Mageed inspired me to go to graduate school and to be a scientist—I have no doubt that I would not be here without his mentorship. Professor Bret Findley, my undergraduate advisor also played a major role in getting me to UC Davis and his kindness, humor, and calm guidance helped me become the person that I am. Professor David Heroux inspired me to pursue inorganic chemistry and helped me get into graduate school, and Professor Shane Lamos ignited my love of chemistry. Dr. Laura Bristow's mentorship and company also played a critical role in my scientific journey, as did Dr. Cory Padilla's.

I am grateful for the rest of the Kauzlarich group and their support, encouragement, humor, and conversation, as well. Dr. Elizabeth Kunz-Wille, Dr. Zheng Ju, Dr. Andrew Justl, and Professor Kathryn Newton were all great resources and brought humor to my graduate career. Nick Mrachek and Jennifer Liem, whose curiosity and questions helped sharpen my own knowledge were an important part of my scientific development as well, and discussions with Ivan Opara, Mohammad Islam, and Joel Shirey have also contributed.

I also want to thank my family for all that they've done to get me to where I am—I could not have made it through this program without them—and my friends Lindsey Rogers, Miriam Pritschet, Trisha Nguyen, Nathan Phipps, Subra Nagappan, Ashley O'Dell, Coyla Munson, and

Steven Gralinski for their support, encouragement, and all the stressed-out rants they've listened to over the past few years.

Thank you to Dean Cheikh at JPL for Seebeck and Hall measurements, and to Dr. Sabah Bux, Dr. Max Wood, and Dr. Giacomo Cerretti for useful discussion and scientific inspiration.

Table of Contents

Abstract iv

Acknowledgments vii

Table of Contents ix

List of Figures xii

List of Tables xx

List of Equations xxi

Chapter 1 : Introduction 1

1.1 Thermoelectric Generators 1

1.2 Layered Zintl Phases 6

1.3 Electrides 7

1.4 References 8

Chapter 2 : Deciphering Defects in $Yb_{2-x}Eu_xCdSb_2$ and their Impact on Thermoelectric Properties 12

2.1 Abstract 13

2.2 Introduction 13

2.3 Experimental 17

2.4 Results and Discussion 21

2.5 Conclusion 46

2.6 Acknowledgements 48

2.7 Appendix 48

2.8 References 61

Chapter 3 : Thermoelectric properties of $Ba_{2-x}Eu_xZnSb_2$, a Zintl phase with one-dimensional covalent chains 70

3.1 Abstract 71

3.2 Introduction 72

3.3 Methods 74

3.4 Results and Discussion 77

3.5 Conclusions 88

3.6 Acknowledgements 89

3.7 Appendix 90

3.8 References 98

Chapter 4 : Theory and experiment in concert to unravel the remarkable electronic properties of Na-doped $Eu_{11}Zn_4Sn_2As_{12}$: A layered Zintl phase 105

4.1 Abstract 106

4.2 Introduction 107

4.3 Experimental 110

4.4 Results and Discussion 114

4.5 Summary 127

4.6 Acknowledgements 128

4.7 Appendix 129

4.8 References 137

Chapter 5 : Electride or Semiconductor? Mapping the structural and electronic transitions in $Yb_5Sb_3H_x$ using theory and thermoelectric properties 148

5.1 Abstract 148

5.2 Introduction 149

5.3 Methods 153

5.4 Results and Discussion 157

5.5 Conclusions 173

5.6 Acknowledgements 174

5.7 Appendix 175

5.8 References 183

List of Figures

Figure 1-1: Schematic of a thermoelectric device. 2

Figure 2-1. (a) crystal structure of $Yb_{2-x}Eu_xCdSb_2$. Turquoise spheres represent Yb/Eu, gray spheres represent Cd, dark blue spheres represent Sb1 and black spheres represent Sb2; (b) anionic corner-shared $[CdSb_{4/2}]^{4-}$ tetrahedral chains. Sb1 sites shown in blue and Sb2 shown in black; (c) Yb1 interlayer and Yb2 intralayer coordination environments. 22

Figure 2-2. Occupancy of the Yb1 and Yb2 sites in $Yb_{2-x}Eu_xCdSb_2$ by Eu and Yb for single crystals of varying Eu content. Eu preferentially occupies the larger, interlayer octahedral site. 22

Figure 2-3. (a) Backscattered electron image of $Yb_{1.7}Eu_{0.3}CdSb_2$ shows Z contrast and homogeneity (b) Secondary electron image shows topography; (c) Elemental maps from EDS are shown for Yb, Eu, Cd, and Sb. Images confirm elements are well dispersed and the sample is homogenous. 26

Figure 2-4. PXRD patterns post SPS of $Yb_{2-x}Eu_xCdSb_2$ $x = 0$, 0.1, 0.2, 0.3, 0.5 samples compared with the calculated diffraction pattern for $x = 0$. The asterisk marks the largest diffraction peak for the $YbCd_2Sb_2$ impurity. 28

Figure 2-5. Lattice parameters from single experimental crystal (90 K), literature (ref. [30]) and powder x-ray diffraction (room temperature) are plotted as a function of Eu content. Lattice parameters increase with increasing Eu content. 29

Figure 2-6. Site occupancy as determined by short *r*-range PDF analysis for different Eu concentrations for (a) Yb1 cation site and (b) Sb2 site; (c) comparison of Yb1 site occupancy and Sb2 site occupancy. Cation site is in turquoise and Sb site is in black. The dotted lines mark site occupancy of 1 for reference. 31

Figure 2-7. Lattice parameters from Rietveld refinement (blue triangles), PDF from 2.5 to 5 Å (black squares) and PDF from 2.5 to 20 Å (red circles). 33

Figure 2-8. Bond angles for Yb1 octahedra determined by single crystal XRD (black triangles) performed on single crystal samples and short-range PDF analysis (red circles) performed on polycrystalline samples. a: Equatorial Sb2-Yb1-Sb2 bond angle; b: Axial Sb2-Yb1-Sb2 bond angle; c: Sb1-Yb1-Sb1 Bond Angle; d: Sb1-Yb1-Sb2 bond angle; e: Yb1-Sb2 bond distance; f: Yb1 octahedron from $x = 0.5$ for reference. The yellow highlights the compositions $x = 0.2$ and 0.3, which deviate from the trend. 33

Figure 2-9**.** (a) Cd-Sb2-Cd and (b) Yb1-Yb1 angles from single crystal XRD (black triangles) and short-range PDF analysis (red circles) of polycrystalline samples. The yellow box highlights compositions $x = 0.2$ and 0.3, which deviate from the trend. 36

Figure 2-10. (a) Seebeck coefficients (b) electrical resistivity and (c) weighted mobility for $Yb_{2-x}Eu_xCdSb_2$ at 525 K. Points are color-coded in a gradient according to weighted mobility. 39

Figure 2-11**.** Reduced chemical potential for $Yb_{2-x}Eu_xCdSb_2$ at 525 K. The yellow box highlights compositions $x = 0.2$ and $x = 0.3$, which have the lowest and highest chemical potential. 41

Figure 2-12. (a) Total thermal conductivity (b) electronic component of thermal conductivity (c) lattice component of thermal conductivity for $Yb_{2-x}Eu_xCdSb_2$. 44

Figure 2-13. Quality Factor (B) plotted as a function of reduced chemical potential (η) and zT. B values at 525 K for select $Yb_{2-x}Eu_xCdSb_2$ samples are shown color-coded as filled circles. Figure reprinted from reference [52] with the permission of AIP Publishing. 46

Figure 2-14. zT as a function of temperature for leading p-type Zintl phases, $Yb_{1.64}Eu_{0.36}CdSb_2$,[11] $Eu_2Zn_{0.98}Sb_2$,[9] $YbZn_2Sb_2$,[12] $Yb_{14}MgSb_{11}$,[53] and $Yb_{14}MnSb_{11}$[54]. $Yb_{1.6}Eu_{0.4}CdSb_2$ from this work (purple) gives a higher zT across the low temperature range (300-525 K) than any other material shown. 47

Figure 2-15. Depicts energy of characteristic X-rays from EDS used to determine the composition of $Yb_{1.7}Eu_{0.3}CdSb_2$. 48

Figure 2-16. Backscattered electron SEM micrographs (top left), secondary electron SEM micrographs (bottom left), and EDS elemental maps (green: Yb, red: Eu, blue: Cd, pink: Sb) for $Yb_{2-x}Eu_xCdSb_2$, x = 0, 0.1 and 0.2. 49

Figure 2-17. Backscattered electron SEM micrographs (top left), secondary electron SEM micrographs (bottom left), and EDS elemental maps (green: Yb, red: Eu, blue: Cd, pink: Sb) for $Yb_{2-x}Eu_xCdSb_2$, x = 0.3, 0.4 and 0.5. 50

Figure 2-18. Rietveld refinements for $Yb_{2-x}Eu_xCdSb_2$. Experimental data are in blue, calculated in red, and difference in gray. Tick marks give the expected peak positions for the Si standard (blue/top) $Yb_{2-x}Eu_xCdSb_2$ (black/middle) and $YbCd_2Sb_2$ (green/bottom). 53

Figure 2-19. PDFGui refinements for $Yb_{2-x}Eu_xCdSb_2$ from r = 2.5 to 5 Å. Experimental data are in blue, calculated in red, and difference in green. 57

Figure 2-20. PDFGui refinements for $Yb_{2-x}Eu_xCdSb_2$ from r = 2.5 to 20 Å. Experimental data are in blue, calculated in red, and difference in green. 60

Figure 3-1. Ba_2ZnSb_2 structure viewed along the *b*-axis (left) and c-axis (right). Ba, Zn, and Sb are indicated by purple, grey, and blue colored spheres, respectively. 78

Figure 3-2. PXRD patterns for $Ba_{2-x}Eu_xZnSb_2$ (x = 0.2, 0.3, 0.4) compared to the calculated pattern from the single crystal CIF[19] on bottom. 79

Figure 3-3. Lattice parameters determined via Rietveld refinement as a function of Eu content for $Ba_{2-x}Eu_xZnSb_2$ (x = 0, 0.2, 0.3, 0.4). 79

Figure 3-4. Secondary electron micrograph (top left), backscattered electron micrograph (top right), and elemental maps for $Ba_{2-x}Eu_xZnSb_2$ x = 0.4 pellet with Ba in turquoise, Eu in green, Zn in dark blue, Sb in red (bottom). 80

Figure 3-5. Temperature dependent magnetization for $Ba_{2-x}Eu_xZnSb_2$ (x = 0.2, 0.3, 0.4). 82

Figure 3-6. Polynomial fits of (a) Seebeck coefficients as a function of temperature; (b) electrical resistivities; (c) Hall mobilities for $Ba_{2-x}Eu_xZnSb_2$ (x = 0.2, 0.3, 0.4). 85

Figure 3-7. Polynomial fit of total thermal conductivity as a function of temperature for $Ba_{2-x}Eu_xZnSb_2$ (x = 0.2 (black filled squares), 0.3 (grey filled triangles), 0.4 (blue filled circles). 87

Figure 3-8. Temperature dependent zT's for $Ba_{2-x}Eu_xZnSb_2$ (x = 0.2 (black filled squares), 0.3 (grey filled triangles), 0.4 (blue filled circles). 88

Figure 3-9. Experimental electronic transport data from the first heating cycle. 90

Figure 3-10. Experimental thermal conductivity data. 91

Figure 3-11. Rietveld refinements of $Ba_{2-x}Eu_xZnSb_2$ (x = 0, 0.2, 0.3, 0.4). The observed data are shown in black, calculated pattern in red, and difference curve is in gray. The sloping background observed at low angle is due to scattering from the Kapton tape used to keep the

sample air free. The x marks an unidentified impurity peak. Bragg peaks are indicated by tick marks at the bottom. Blue indicates Ba_2ZnSb_2 and black indicates $BaZn_2Sb_2$. 93

Figure 3-12. SEM micrographs and EDS elemental maps for $Ba_{1.8}Eu_{0.2}ZnSb_2$ (top) and $Ba_{1.7}Eu_{0.3}ZnSb_2$ (bottom). 95

Figure 3-13. Typical EDS spectrum for $Ba_{2-x}Eu_xZnSb_2$ samples..... 96

Figure 3-14. Inverse magnetic susceptibility (red) and modified Curie-Weiss fit (black). 97

Figure 4-1. A view of the crystal structure of $Eu_{11}Zn_4Sn_2As_{12}$ (*C2/c* space group) showing the layered aspect of the structure. Eu atoms are indicated in green, Zn in turquoise, Sn in yellow and As in red. 108

Figure 4-2. PXRD patterns for $Eu_{11-x}Na_xZn_4Sn_2As_{12}$ (x = 0, 0.05, 0.075, 0.1) compared to the calculated *R*3*m* pattern (bottom) and *R*3 (second from bottom). 116

Figure 4-3. SEM micrographs from secondary electrons (top left) and backscattered electrons (top right), and EDS elemental maps (bottom) for a pressed pellet of $Eu_{11-x}Na_xZn_4Sn_2As_{12}$ with greatest Na content, x = 0.1..... 117

Figure 4-4. Temperature-dependent thermal conductivity from 300–675 K for $Eu_{11-x}Na_xZn_4Sn_2As_{12}$ (x = 0, 0.05, 0.075, 0.1). 118

Figure 4-5. Temperature-dependent (a) electrical resistivity and (b) Seebeck coefficients from 300- 675 K for $Eu_{11-x}Na_xZn_4Sn_2As_{12}$ (x = 0, 0.05, 0.075, 0.1). The legend is the same for both plots. 120

Figure 4-6. Temperature dependent (a) Weighted mobility and (b) Hall mobility for $Eu_{11-x}Na_xZn_4Sn_2As_{12}$ (x = 0, 0.05, 0.075, 0.1) from 300 – 675 K. 122

Figure 4-7. (a) Band structure of $Eu_{11}Zn_4Sn_2As_{12}$ calculated with spin-orbit coupling. An indirect band gap of E_g = 0.6 eV forms between the valence band maximum (VBM) at the Γ-point and the conduction band minimum at the X-point. A secondary valence band maximum exists 60 meV below the VBM. (b-e) Fermi surfaces at the listed Fermi levels inside the valence band, along with the corresponding carrier concentrations at 300 K. The ellipsoidal Fermi surfaces suggest anisotropic electrical transport. 123

Figure 4-8. (a) Predicted hole mobility in $Eu_{11}Zn_4Sn_2As_{12}$ at a hole concentration of 1×10^{18} cm^{-3}, where scattering by acoustic phonons (blue), ionized impurities (green), and polar optical phonons (cyan) are shown. The predicted temperature-dependent electrical resistivity (b) and Seebeck coefficient (c) are shown for different hole concentrations. The transport properties are averaged over the three Cartesian directions in (b-c), and the direction components are shown in (d) at a carrier concentration of 1×10^{18} cm^{-3}. Pisarenko relations at 300 K (e) and 500 K (f) are used to compute the hole effective mass, calculated using the formula in Ref. 60. 126

Figure 4-9. Experimental thermal conductivity data. 129

Figure 4-10. Experimental Seebeck coefficient data. 129

Figure 4-11. Experimental electrical resistivity data. 130

Figure 4-12. Experimental Hall mobility data. 130

Figure 4-13. A portion of typical Rietveld refinement for EuAs (ICSD- 26265, the Na_2O_2 structure type).[29] Observed data are shown in black, calculated pattern in red, and difference curve in gray. Tick marks indicate EuAs (blue) and Eu_3As_4 (black). 131

Figure 4-14. A portion of a typical Rietveld refinement for $Eu_{11}Zn_4Sn_2As_{12}$ (top) and $Eu_{10.95}Na_{0.05}Zn_4Sn_2As_{12}$ (bottom) prepared from EuAs. Observed data are shown in black, calculated pattern in red, and difference curve in gray..... 132

Figure 4-15. A portion of a typical Rietveld refinement for $Eu_{10.925}Na_{0.075}Zn_4Sn_2As_{12}$ (top) and $Eu_{10.9}Na_{0.1}Zn_4Sn_2As_{12}$ (bottom) made from EuAs. Observed data are shown in black, calculated pattern in red, and difference curve in gray..... 133

Figure 4-16. A portion of a typical Rietveld refinement for a pressed pellet of $Eu_{11-x}Na_xZn_4Sn_2As_{12}$ made from EuAs. Observed data are shown in black, calculated pattern in red, and difference curve in gray. No preferred orientation is observed..... 134

Figure 4-17. Secondary electron SEM micrographs and EDS elemental maps of $Eu_{11-x}Na_xZn_4Sn_2As_{12}$ for x = 0 (top), 0.05 (middle) and 0.075 (bottom). Eu is in green, Zn in turquiose, Sn in red and As in blue..... 136

Figure 4-18. XPS spectra in the As 3d (left) and the Eu 3d (right) region. 137

Figure 5-1. The structure of the (a) orthorhombic β- and (b) hexagonal α-structure types of $Yb_5Sb_3H_x$. Yb and Sb atoms are indicated in blue and gray, respectively. The polyhedra show the interstitial 0D cavities that house either an anionic electron or an H^-. H atom is not shown. 152

Figure 5-2. Calculated formation energy, in eV/atom, for $Yb_5Sb_3H_x$ in both the orthorhombic and hexagonal structure types as a function of H content (x)..... 159

Figure 5-3. PXRD patterns of SPS'ed $Yb_5Sb_3H_x$ (x = 0.25, 0.5, 0.75, 1) samples compared to the calculated pattern (bottom). The asterisks in x = 0.25 indicate peaks corresponding to the hexagonal $Yb_5Sb_3H_x$ structure. 161

Figure 5-4.Lattice parameters of $Yb_5Sb_3H_x$ as a function of H content determined via Rietveld refinement of PXRD data..... 162

Figure 5-5. (a) Secondary electron SEM micrograph, (b) backscattered electron SEM micrograph, (c) Yb EDS elemental map, (d) Sb EDS elemental map for $Yb_5Sb_3H_x$, x = 0.75. The scale bar shown in panel (a) is the same for all panels. 163

Figure 5-6.^{1}H NMR spectra in the isotropic chemical shift region, with instrument background deduction and sample weight normalization for $Yb_5Sb_3H_x$. 164

Figure 5-7.^{1}H MAS NMR signal intensity vs amount of hydrogen content in $Yb_5Sb_3H_x$..... 165

Figure 5-8. Charge carrier concentration determined via Hall effect measurements from 300 to 775 K for $Yb_5Sb_3H_x$. 167

Figure 5-9.Charge carrier mobility from 300 to 775 K for $Yb_5Sb_3H_x$. 168

Figure 5-10.Temperature dependent (a) electrical resistivity and (b) Seebeck coefficient from 300 to 775 K for $Yb_5Sb_3H_x$. 170

Figure 5-11. Total thermal conductivity (top); electronic component of thermal conductivity (middle) and lattice thermal conductivity (bottom) of $Yb_5Sb_3H_x$. 171

Figure 5-12. Thermoelectric figure of merit as a function of temperature for $Yb_5Sb_3H_x$..... 173

Figure 5-13. Experimental Hall effect measurement data. (a) carrier concentration; (b) mobility; (c) mobility scaled for x = 0.25 and 0.5 175

Figure 5-14. Experimental electronic transport data. (a) electrical resistivity; (b) electrical resistivity scaled for x = 0.25 and 0.5mobility; (c) Seebeck coefficients. 176

Figure 5-15. Experimental thermal conductivity data. 177

Figure 5-16. Portion of typical Rietveld refinements of $Yb_5Sb_3H_x$ (x = 0.25, 0.5, 0.75, 1). The observed data are shown in black, calculated pattern in red, and difference curve is in gray. ... 179
Figure 5-17. Portion of a typical Rietveld refinement of Yb_4Sb_3 precursor ... 180
Figure 5-18. (a) Secondary electron SEM micrograph, (b) backscattered electron SEM micrograph, (c) Yb EDS elemental map, (d) Sb EDS elemental map for x = 0.25 (top), x = 0.5 (middle), and x = 1 (bottom). The scale bar shown in panel a is the same for all panels. ... 182
Figure 5-19. ^{1}H MAS NMR spectra of $Yb_5Sb_3H_x$ with x = 0.25, 0.50, 0.75 and 1.00. Instrument ^{1}H background is also displayed for comparison. ... 183

List of Tables

Table 2-1. Data Collection Details and Selected Single Crystal Parameters from $Yb_{2-x}Eu_xCdSb_2$ ... 23
Table 2-2. Eu Content Determined by EDS for Polycrystalline Pelletized Samples ... 25
Table 2-3. Thermoelectric Quality factor (B) for $Yb_{2-x}Eu_xCdSb_2$ at 525K. ... 46
Table 2-4. Statistics from Rietveld refinements ... 54
Table 3-1. Eu Composition Determined by EDS and Magnetic Data for $Ba_{2-x}Eu_xZnSb_2$ ... 81
Table 3-2. Hall Carrier Concentration at 300 K for $Ba_{2-x}Eu_xZnSb_2$ ... 83
Table 3-3 Selected Rietveld Refinement Statistics ... 94
Table 4-1. Hall Carrier Concentration and Mobility of $Eu_{11-x}Na_xZn_4Sn_2As_{12}$ at 300 K ... 119
Table 4-2. Selected Rietveld Refinement Statistics for a Typical Powder X-ray Diffraction Pattern of EuAs (ICSD- 26265, the Na_2O_2 structure type) ... 131

Table 4-3. Selected Rietveld Refinement Statistics from $Eu_{11-x}Na_xZn_4Sn_2As_{12}$ (x = 0, 0.05, 0.075, 0.1) 134

Table 5-5-1.^{1}H MAS NMR Results for $Yb_5Sb_3H_x$ 165

Table 5-2. Selected Rietveld Refinement Statistics from $Yb_5Sb_3H_x$. 180

Table 5-3. Selected Rietveld Refinement Statistics from Yb_4Sb_3 precursor 181

List of Equations

Equation 1-1. The dimensionless thermoelectric figure of merit for a thermoelectric material..... 3

Equation 1-2. Seebeck coefficient relationship with carrier concentration according to single parabolic band model..... 3

Equation 1-3 Total thermal conductivity as a sum of electronic and lattice components 4

Equation 1-4. Relationship between the electronic portion of thermal conductivity and carrier concentration..... 4

Equation 1-5. Electrical resistivity relationship to carrier concentration 4

Equation 5-1. Formation energy calculation..... 158

Chapter 1: Introduction

1.1 Thermoelectric Generators

The combustion of fossil fuels and resulting environmental devastation due to climate change is a key global issue that is tied to growing social and political unrest.[1] Moving away from fossil fuels and implementing renewable energy sources is a critical challenge that needs to be addressed quickly. Thermoelectric generators (TEGs) are one potential solution to the energy crisis, as they convert heat directly to electricity and could be used to replace batteries, generate electricity from solar heat, and scavenge waste heat from industrial processes.[2] TEGs operate via the Seebeck effect, in which a temperature gradient applied to a material drives charge carriers from the higher energy hot side to the lower energy cool side, producing a voltage. When *n*- and *p*-type materials are connected electrically in series and thermally in parallel, the motion of the charge carriers can be harnessed as electricity, as shown in Figure 1-1. As solid-state devices, TEGs are robust and have no moving parts or emissions, resulting in low maintenance costs, and are easily scalable.[2] They can be built with high degrees of redundancy and can withstand pressure, temperature, shock and radiation.[3,4] These devices are currently employed in military, aerospace, transportation, and HVAC appliances, and could find more widespread use if efficiency can be improved.[2]

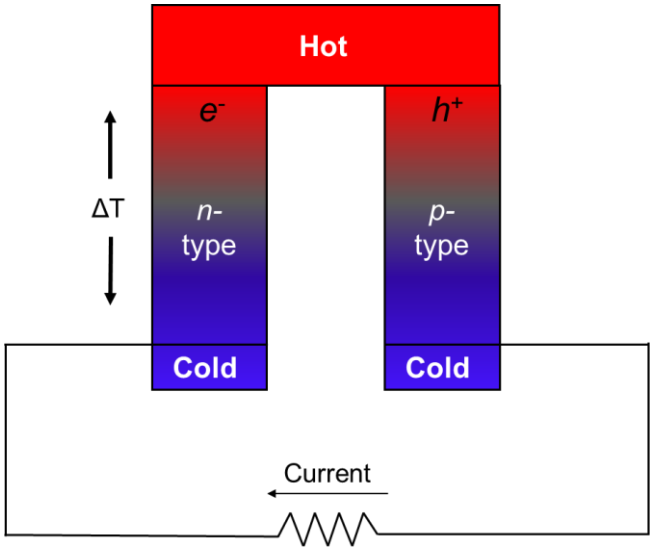


Figure 1-1: Schematic of a thermoelectric device.

TEGs are Carnot heat engines in which the charge carriers are the working fluid.[5] The conversion efficiency of a device is defined by the Carnot efficiency times the dimensionless thermoelectric material figure of merit (zT) averaged over the TEG's operational temperature.[6] The figure of merit is given in equation 1-1, where S is the Seebeck coefficient (V/K), T is the operating temperature (K), ρ is the electrical resistivity (Ω-m) and κ is the thermal conductivity (W/m-K). Most terrestrial heat sources are < 900K, meaning that highly efficient materials are needed from across the entire temperature range from 300 K to 900 K. Currently, commercial thermoelectric materials such as Bi_2Te_3, PbTe, Bi-Sb and Si-Ge alloys can achieve zT ~1, but higher zT's are needed to make TEGs competitive with combustion engines.[3]

Equation 1-1. The dimensionless thermoelectric figure of merit for a thermoelectric material

$$zT = \frac{S^2 T}{\rho \kappa}$$

Optimization of thermoelectric materials is difficult because the properties that define *zT* are interrelated via carrier concentration, n, according to the single parabolic band (SPB) model which assumes one approximately isotropic band dominates electronic transport in a material. *S* and κ are optimized at low *n* (equations 1-2, 1-3, and 1-4), while ρ is optimized at high *n* (equation 1-5), so tuning materials by adjusting *n* results in tradeoffs and is of limited usefulness. Most materials reach their peak *zT* between $n = 10^{19}$ and 10^{21} carriers/cm^3, when a balance is struck between *S*, κ, and ρ. Because the lattice component of the thermal conductivity (κ_L) (equation 1-3) is the only variable that is independent of *n*, much research has focused on designing materials that minimize κ_L by scattering phonons, implementing strategies such as large unit cells with heavy atoms, alloy scattering, nano-structuring, and composites. Many materials with thermal conductivities approaching the theoretical minimum have been discovered, and more recently, focus has shifted to finding creative ways to improve the electronic transport described by *S* and ρ, such as tuning defect structure, band engineering to achieve high valley degeneracy (N_v), taking advantage of anisotropic band structures, and designing low dimensional materials.

Equation 1-2. Seebeck coefficient relationship with carrier concentration according to single parabolic band model

$$S = \frac{8\pi^2 k_b^2}{3eh^2} m^* T \left(\frac{\pi}{3n}\right)^{\frac{2}{3}}$$

Equation 1-3 Total thermal conductivity as a sum of electronic and lattice components

$$\kappa = \kappa_{electronic\ (e)} + \kappa_{lattice\ (l)}$$

Equation 1-4. Relationship between the electronic portion of thermal conductivity and carrier concentration

$$\kappa_e = ne\mu LT$$

Equation 1-5. Electrical resistivity relationship to carrier concentration

$$\frac{1}{\rho} = ne\mu$$

Understanding and controlling defect chemistry is known to be an important part of optimizing thermoelectric materials. Studies on leading *p*-type Zintl phases Eu_2ZnSb_2,[7–10] Mg_3Sb_2,[11] and AZn_2Sb_2 (A = Eu, Yb, Sr, Ca)[12,13] highlight the role that defect structure plays in electronic transport and maximizing *zT* experimentally, and a theoretical studies on A_2CdP_2 (A = Ba, Sr)[14,15] showed how calculations taking defect formation into account can be used to identify compositions with optimal band structures and transport properties.

Increasing valley degeneracy improves *S* without significantly altering ρ, leading to an overall improvement to zT. As indicated in equations 1-2 and 1-5, *S* is directly proportional to the density of states effective mass, *m**, and ρ is inversely proportional to mobility, μ, which is low for individual bands with heavy effective mass (m_b*). An important distinction needs to be made here between the density of states effective mass, *m**, and the effective mass of a single band or valley, m_b*. The density of states effective mass is defined by $m^* = N_v^{2/3} m_b^*$, where N_v is the number of degenerate bands. According to this relationship, increasing N_v has the advantage of increasing *m**, and thus *S*, without changing m_b*, or μ, so there is no negative impact on ρ.[16,17]

Weighted mobility is one method of examining changes in valley degeneracy. It can be used to elucidate whether changes in electronic properties in a series of samples are due to simple doping, changes in band structure, or differing scattering mechanisms. Weighted mobility (μ_w) is a carrier concentration-independent indicator of the inherent quality of the electronic transport properties of a material and is defined as the charge carrier mobility weighted by the density of states effective mass according to the relationship $\mu_w \approx \mu \left(\frac{m^*}{m_e}\right)^{3/2}$ (where μ is mobility, m^* is effective mass and m_e is the electron mass).[16] When a single isotropic band dominates transport, μ_w is constant at a given temperature, regardless of doping level, making it a useful way to determine whether changes in properties are due to doping or if they are due to changes in band structure due to alloying. The temperature dependence of μ_w gives information about scattering mechanisms that dominate transport and can indicate changes in scattering due to disorder, grain boundaries, and other effects.[11,16]

Targeting materials with anisotropic and low dimensional electronic structures is another strategy to simultaneously improve *S* and ρ.. In materials where transport is highly anisotropic, *i.e.* m_b* is light in one crystallographic direction and heavy in another, ρ is dominated by the light mass in one direction, while *S* is governed by the average effective mass, resulting in high *S* and low ρ.[18–21] This operating principle is similar to that of low dimensional materials. Low dimensionality is typically achieved by nano-structuring materials to confine transport in at least one direction, but recent research suggests that 1 or 2D electronic structures can arise in 3D materials when bonding is highly directional, such as in layered materials.[19,20,22–24] Layered Zintl phases are a class of compounds that are particularly promising in this way because of their anisotropic bonding, varied structural motifs, and tunability.[24–27]

1.2 Layered Zintl Phases

Zintl phases are valence precise semiconductors that are composed of both covalent and ionic bonding. They are considered polar intermetallic compounds and contain metals with electronegativities that are different enough to assume complete charge transfer between them. The more electropositive elements, usually alkali, alkaline earth, or rare earth metals, donate their electrons to the more electronegative elements which use the extra electrons to make covalent bonds to fill their valence shells, often giving rise to diverse polyanions and complex crystal structures.[26] They are expected to be semiconducting, and their electrons can be counted using the octet rule. However, in reality the electron transfer is often not complete, giving rise to metallic behavior in some compounds.[25] The presence of covalent networks can lead to high charge carrier mobility and thus low electrical resistivity, while the

interspersed cations create disorder and scatter phonons, making Zintl phases interesting for a wide variety of applications, but especially thermoelectricity.

Layered Zintl phases are a subset of materials with highly directional bonding. They can be understood as alternating polyanionic and cationic layers stacked along a particular crystallographic axis.[24] A great variety of different bonding schemes are found in these compounds, including hexagonal nets, corner-shared tetrahedral chains, edge-shared tetrahedral sheets, polyanionic ribbons, and many other configurations.[25,26,28] As a result of the anisotropic bonding, electronic transport can also be directional, with high charge carrier mobility in the crystallographic direction(s) parallel to the covalent networks, and low mobility along the stacking (ionic) direction, potentially giving rise to low dimensional transport when taken to an extreme, a characteristic that can be advantageous for thermoelectric performance and a variety of other applications.[18,19,21,22,24,27,29] Several layered Zintl phases, including compounds with the $CaAl_2Si_2$ structure-type[28], Eu_2ZnSb_2,[7,9,10] and $Yb_{2-x}Eu_xCdSb_2$,[30] have been found to exhibit high zT, sparking further research on this class of materials. This dissertation focuses on characterizing and improving thermoelectric performance in three layered Zintl phases and one low dimensional Zintl phase.

1.3 Electrides

Materials that possess a localized anionic electron that is not associated with a particular atom are called electrides. The electron is trapped in a vacant crystallographic site and, when present in a high enough concentration, can interact with other anionic electrons and give rise to unusual electronic properties with potential applications in superconductivity, batteries, spintronics, catalysis, nonlinear optics and photonics.[31,32] Trapped electrons can exist in sites

with different dimensionalities, including 0D cavities, 1D chains, 2D sheets, and 3D structures and the properties of the electride are closely linked to its topology.[32] Such structural variation creates vast opportunity for discovery of new and exciting properties within this class of materials and research on electrides is expanding rapidly. The general requirement for discovery of an electride is the presence of an excess of electropositive cations to donate electrons, and the localization of the electride state becomes more pronounced when low dimensional sites are present in a structure.[33] In some situations, electronic properties can be tuned by introducing an acceptor atom to act as an electron sink by forming a bond with the anionic electron.[34] This dissertation investigates this type of transition in $Yb_5Sb_3H_x$ by varying H content probe the electronics as the compound changes from a low dimensional electride to a charge-balanced Zintl phase using thermoelectric property measurements.

1.4 References

(1) Schlosberg, D.; Collins, L. B. From Environmental to Climate Justice: Climate Change and the Discourse of Environmental Justice. *Wiley Interdiscip. Rev. Clim. Chang.* **2014**, *5* (3), 359–374. https://doi.org/10.1002/wcc.275.

(2) Pourkiaei, S. M.; Ahmadi, M. H.; Sadeghzadeh, M.; Moosavi, S.; Pourfayaz, F.; Chen, L.; Pour Yazdi, M. A.; Kumar, R. Thermoelectric Cooler and Thermoelectric Generator Devices: A Review of Present and Potential Applications, Modeling and Materials. *Energy* **2019**, *186*, 115849. https://doi.org/10.1016/j.energy.2019.07.179.

(3) Fleurial, J. P. Thermoelectric Power Generation Materials: Technology and Application Opportunities. *J. Miner. Met. Mater. Soc.* **2009**, *61* (4), 79–85. https://doi.org/10.1007/s11837-009-0057-z.

(4) Fleurial, J.-P.-. P.; Borshchevsky, A.; Caillat, T.; Ewell, R.; Ewe11, R. New Materials and Devices for Thermoelectric Applications. In *Proceedings of the Intersociety Energy Conversion Engineering Conference*; 1997; Vol. 2, pp 1080–1085. https://doi.org/10.1109/IECEC.1997.661920.

(5) Fleurial, J.-P.; Borshchevsky, A.; Caillat, T. New Thermoelectric Materials and Devices for Terrestrial Power Generators. In *Space technology and applications international forum (STAIF - 97)*; ASCE, 1997; pp 293–298. https://doi.org/10.1063/1.52005.

(6) Snyder, G. J.; Snyder, A. H. Figure of Merit ZT of a Thermoelectric Device Defined from Materials Properties. *Energy Environ. Sci.* **2017**, *10* (11), 2280–2283. https://doi.org/10.1039/c7ee02007d.

(7) Chanakian, S.; Uhl, D.; Neff, D.; Drymiotis, F.; Park, J.; Petkov, V.; Zevalkink, A.; Bux, S. Exceptionally High Electronic Mobility in Defect-Rich $Eu_2ZnSb_{2-x}Bi_x$ Alloys. *J. Mater. Chem. A* **2020**, *8* (12), 6004–6012. https://doi.org/10.1039/c9ta14170g.

(8) Yao, H.; Chen, C.; Xue, W.; Bai, F.; Cao, F.; Lan, Y.; Liu, X.; Wang, Y.; Singh, D. J.; Lin, X.; Zhang, Q. Vacancy Ordering Induced Topological Electronic Transition in Bulk Eu_2ZnSb_2. *Sci. Adv.* **2021**, *7* (6), 1–7. https://doi.org/10.1126/sciadv.abd6162.

(9) Chen, C.; Xue, W.; Li, S.; Zhang, Z.; Li, X.; Wang, X.; Liu, Y.; Sui, J.; Liu, X.; Cao, F.; Ren, Z.; Chu, C.-W.; Wang, Y.; Zhang, Q. Zintl-Phase Eu_2ZnSb_2: A Promising Thermoelectric Material with Ultralow Thermal Conductivity. *Proc. Natl. Acad. Sci.* **2019**, *116* (8), 2831–2836. https://doi.org/10.1073/PNAS.1819157116.

(10) Chen, C.; Li, X.; Xue, W.; Bai, F.; Huang, Y.; Yao, H.; Li, S.; Zhang, Z.; Wang, X.; Sui, J.; Liu, X.; Cao, F.; Wang, Y.; Zhang, Q. Manipulating the Intrinsic Vacancies for Enhanced Thermoelectric Performance in Eu_2ZnSb_2 Zintl Phase. *Nano Energy* **2020**, *73* (104771), 1–8. https://doi.org/10.1016/j.nanoen.2020.104771.

(11) Wood, M.; Kuo, J. J.; Imasato, K.; Snyder, G. J. Improvement of Low-Temperature ZT in a Mg_3Sb_2–Mg_3Bi_2 Solid Solution via Mg-Vapor Annealing. *Adv. Mater.* **2019**, *31* (35), 1–5. https://doi.org/10.1002/adma.201902337.

(12) Pomrehn, G. S.; Zevalkink, A.; Zeier, W. G.; Van De Walle, A.; Snyder, G. J. Defect-Controlled Electronic Properties in AZn_2Sb_2 Zintl Phases. *Angew. Chemie - Int. Ed.* **2014**, *53* (13), 3422–3426. https://doi.org/10.1002/anie.201311125.

(13) Zevalkink, A.; Zeier, W. G.; Cheng, E.; Snyder, J.; Fleurial, J. P.; Bux, S. Nonstoichiometry in the Zintl Phase $Yb_{1-\delta}Zn_2Sb_2$ as a Route to Thermoelectric Optimization. *Chem. Mater.* **2014**, *26* (19), 5710–5717. https://doi.org/10.1021/cm502588r.

(14) Balvanz, A.; Qu, J.; Baranets, S.; Ertekin, E.; Gorai, P.; Bobev, S. New N-Type Zintl Phases for Thermoelectrics: Discovery, Structural Characterization, and Band Engineering of the Compounds A_2CdP_2 (A = Sr, Ba, Eu). *Chem. Mater* **2020**, *32*, 10697–10707. https://doi.org/10.1021/acs.chemmater.0c03960.

(15) Qu, J.; Balvanz, A.; Baranets, S.; Bobev, S.; Gorai, P. Computational Design of Thermoelectric Alloys through Optimization of Transport and Dopability. *Mater. Horizons* **2022**, *9* (2), 720–730. https://doi.org/10.1039/d1mh01539g.

(16) Snyder, G. J.; Snyder, A. H.; Wood, M.; Gurunathan, R.; Snyder, B. H.; Niu, C. Weighted Mobility. *Adv. Mater.* **2020**, *32* (2001537), 1–5. https://doi.org/10.1002/adma.202001537.

(17) Pei, Y.; Shi, X.; Lalonde, A.; Wang, H.; Chen, L.; Snyder, G. J.; Snyder, & G. J. Convergence of Electronic Bands for High Performance Bulk Thermoelectrics. *Nature* **2011**, *473* (7345), 66–69.

https://doi.org/10.1038/nature09996.

(18) Sun, J.; Singh, D. J. Thermoelectric Properties of AMg_2X_2, AZn_2Sb_2 (A = Ca, Sr, Ba; X = Sb, Bi), and Ba_2ZnX_2 (X = Sb, Bi) Zintl Compounds. *J. Mater. Chem. A* **2017**, *5* (18), 8499–8509. https://doi.org/10.1039/c6ta11234j.

(19) Parker, D.; Chen, X.; Singh, D. J. High Three-Dimensional Thermoelectric Performance from Low-Dimensional Bands. *Phys. Rev. Lett.* **2013**, *110* (14), 1–5. https://doi.org/10.1103/PhysRevLett.110.146601.

(20) Dylla, M. T.; Kang, S. D.; Snyder, G. J. Effect of Two-Dimensional Crystal Orbitals on Fermi Surfaces and Electron Transport in Three-Dimensional Perovskite Oxides. *Angew. Chemie - Int. Ed.* **2019**, *58* (17), 5503–5512. https://doi.org/10.1002/anie.201812230.

(21) Dresselhaus, M. S.; Chen, G.; Tang, M. Y.; Yang, R.; Lee, H.; Wang, D.; Ren, Z.; Fleurial, J.-P.; Gogna, P. New Directions for Low-Dimensional Thermoelectric Materials. *Adv. Mater.* **2007**, *19*, 1043–1053. https://doi.org/10.1002/adma.200600527.

(22) Bilc, D. I.; Hautier, G.; Waroquiers, D.; Rignanese, G. M.; Ghosez, P. Low-Dimensional Transport and Large Thermoelectric Power Factors in Bulk Semiconductors by Band Engineering of Highly Directional Electronic States. *Phys. Rev. Lett.* **2015**, *114* (13), 1–5. https://doi.org/10.1103/PhysRevLett.114.136601.

(23) Brod, M. K.; Snyder, G. J. Orbital Chemistry of High Valence Band Convergence and Low-Dimensional Topology in PbTe. *J. Mater. Chem. A* **2021**, *9* (20), 12119–12139. https://doi.org/10.1039/d1ta01273h.

(24) Guechi, N.; Bouhemadou, A.; Medkour, Y.; Al-Douri, Y.; Khenata, R.; Bin-Omran, S. Electronic and Thermoelectric Properties of the Layered Zintl Phase $CaIn_2P_2$: First-Principles Calculations. *Philos. Mag.* **2020**, *100* (23), 3023–3039. https://doi.org/10.1080/14786435.2020.1799101.

(25) Ovchinnikov, A.; Bobev, S. Zintl Phases with Group 15 Elements and the Transition Metals: A Brief Overview of Pnictides with Diverse and Complex Structures. *J. Solid State Chem.* **2019**, *270*, 346–359. https://doi.org/10.1016/j.jssc.2018.11.029.

(26) Liu, K. F.; Xia, S. Q. Recent Progresses on Thermoelectric Zintl Phases: Structures, Materials and Optimization. *J. Solid State Chem.* **2019**, *270* (November 2018), 252–264. https://doi.org/10.1016/j.jssc.2018.11.030.

(27) Zhang, J.; Song, L.; Sist, M.; Tolborg, K.; Iversen, B. B. Chemical Bonding Origin of the Unexpected Isotropic Physical Properties in Thermoelectric Mg_3Sb_2 and Related Materials. *Nat. Commun.* **2018**, *9* (1), 4716. https://doi.org/10.1038/s41467-018-06980-x.

(28) Shuai, J.; Mao, J.; Song, S.; Zhang, Q.; Chen, G.; Ren, Z. Recent Progress and Future Challenges on Thermoelectric Zintl Materials. *Mater. Today Phys.* **2017**, *1*, 74–95. https://doi.org/10.1016/J.MTPHYS.2017.06.003.

(29) Song, J.; Song, H. Y.; Wang, Z.; Lee, S.; Hwang, J. Y.; Lee, S. Y.; Lee, J.; Kim, D.; Lee, K. H.; Kim, Y.; Oh, S. H.; Kim, S. W. Creation of Two-Dimensional Layered Zintl Phase by Dimensional Manipulation of Crystal Structure. *Sci. Adv.* **2019**, *5* (6), 1–9. https://doi.org/10.1126/sciadv.aax0390.

(30) Cooley, J. A.; Promkhan, P.; Gangopadhyay, S.; Donadio, D.; Pickett, W. E.; Ortiz, B. R.;

Toberer, E. S.; Kauzlarich, S. M. High Seebeck Coefficient and Unusually Low Thermal Conductivity Near Ambient Temperatures in Layered Compound $Yb_{2-x}Eu_xCdSb_2$. *Chem. Mater.* **2018**, *30* (2), 484–493. https://doi.org/10.1021/acs.chemmater.7b04517.

(31) Zhang, X.; Yang, G. Recent Advances and Applications of Inorganic Electrides. *J. Phys. Chem. Lett.* **2020**, *11* (10), 3841–3852. https://doi.org/10.1021/acs.jpclett.0c00671.

(32) Hosono, H.; Kitano, M. Advances in Materials and Applications of Inorganic Electrides. *Chem. Rev.* **2021**, *121* (5), 3121–3185. https://doi.org/10.1021/acs.chemrev.0c01071.

(33) Novoselov, D. Y.; Anisimov, V. I.; Oganov, A. R. Strong Electronic Correlations in Interstitial Magnetic Centers of Zero-Dimensional Electride β-Yb_5Sb_3. *Phys. Rev. B* **2021**, *103* (23), 1–6. https://doi.org/10.1103/PhysRevB.103.235126.

(34) Lu, Y.; Wang, J.; Li, J.; Wu, J.; Kanno, S.; Tada, T.; Hosono, H. Realization of Mott-Insulating Electrides in Dimorphic Yb_5Sb_3. *Phys. Rev. B* **2018**, *98* (12), 1–12. https://doi.org/10.1103/PhysRevB.98.125128.

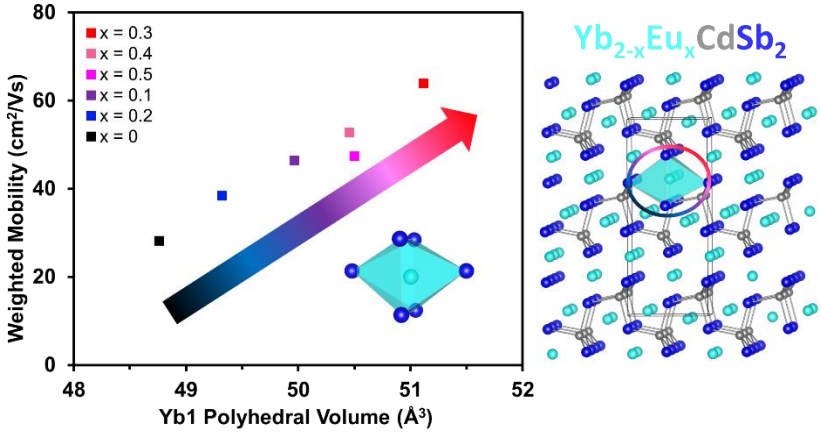
Chapter 2: Deciphering Defects in $Yb_{2-x}Eu_xCdSb_2$ and their Impact on Thermoelectric Properties

Ashlee K. Hauble,[1] Caitlin M. Crawford,[2] Jesse M. Adamczyk,[2] Maxwell Wood,[3] James C. Fettinger,[2] Eric S. Toberer,[2] and Susan M. Kauzlarich*[1]

[1]Chemistry Department, University of California, One Shields Ave, Davis, CA 95616, United States

[2]Department of Physics, Colorado School of Mines, 1500 Illinois St, Golden, CO 80401, United States

[3]Thermal Energy Conversion Research and Advancement Group, Jet Propulsion Laboratory, California Institute of Technology, 4800 Oak Grove Drive, Pasadena, California 91109-8099, United States



This chapter was adapted with permission from:

Hauble, A. K.; Crawford, C. M.; Adamczyk, J. M.; Wood, M.; Fettinger, J. C.; Toberer, E. S.; Kauzlarich, S. M. Deciphering Defects in $Yb_{2-x}Eu_xCdSb_2$ and Their Impact on Thermoelectric Properties. *Chem. Mater.* **2022**, *34* (20), 9228–9239. https://doi.org/10.1021/acs.chemmater.2c02402. © Copyright 2022 American Chemical Society

2.1 Abstract

Layered Zintl phases with A_2MPn_2 stoichiometry are an underexplored class of potential thermoelectric materials with complex and diverse chemistry. The solid solution $Yb_{2-x}Eu_xCdSb_2$ is an example of the promise these compounds hold, as one composition, $Yb_{1.64}Eu_{0.36}CdSb_2$, has reported one of the highest *zT*s of any Zintl phase material at 525 K. The present study examines changes in structure and bonding of this solid solution that impacts thermoelectric performance. Pair Distribution Function analysis are combined with electronic structure modeling to take a chemical bonding-based approach to deconvolute the impact of defects on thermal and electronic properties in $Yb_{2-x}Eu_xCdSb_2$. $Yb_{2-x}Eu_xCdSb_2$ (x = 0, 0.1, 0.2, 0.3, 0.4, 0.5) samples were synthesized and thermoelectric properties and defect chemistry investigated. Samples from the middle of the series, x = 0.2 and 0.3 were found to be the most highly defected, exhibiting Yb and Sb vacancies, as well as distortions in the Yb-Sb coordination spheres that correlate with thermoelectric properties. The highest efficiency is reported for x = 0.4 ($zT \approx 0.9$ at 525 K), and thermoelectric quality factor predicts that x = 0.3 could achieve $zT > 2$ by synthetically tuning the defect structure and thereby carrier concentration. The strategy of investigating local structure outlined in this study can be applied to a variety of other thermoelectric materials to provide insight into the hidden role of defect chemistry in understanding the structure-property relationships in extended solids.

2.2 Introduction

The world's rising demand for energy is driving research for renewable electricity solutions, as well as ways to make current technologies more efficient. Thermoelectric generators (TEGs) are one option that could help slow climate change by providing a power source that is not

dependent on the combustion of fossil fuels. TEGs convert waste heat directly to electricity via the Seebeck effect, where charge carriers are driven from the hot side of a thermal gradient to the cold side to relieve thermal energy. This is an important technology, given that only about one-third of the energy currently consumed in the world is effectively used, with most being lost as heat.[1] One area where TEGs could shine is industrial waste heat scavenging. If harnessed, waste heat from industrial processes in the United States could provide more than 10 gigawatts of electricity; enough to power 10 million homes and save industries more than $3 billion a year.[2] TEGs could also be used to generate electricity from natural heat sources, such as the sun.[3] For these applications and many others, discovery and optimization of thermoelectric materials that exhibit high heat to electricity conversion efficiency in the 100 - 500 ˚C range is an active area of research.[2]

The conversion efficiency of a thermoelectric material is defined by the unitless figure of merit, $zT = (S^2T)/\kappa\rho$ where S is the Seebeck coefficient, T is the operating temperature, κ is thermal conductivity, and ρ is electrical resistivity. The primary challenge in designing thermoelectric materials is decoupling these interrelated properties, a task that layered Zintl phase semiconductors are well suited for given that their structures include both ionic and covalent bonding.[3–7] A_2MPn_2 (A = alkaline earth, Yb, Eu; M = transition metal, Pn = group 14 element) Zintl phases in particular comprise a promising and underexplored family of potential thermoelectric materials. More than 20 compounds and three major structure types have been discovered, most of which are narrow band gap semiconductors.[4] Several A_2MPn_2 compounds have also been predicted to be good p-type thermoelectric materials at low temperatures.[4,7] However, thermoelectric properties have only been reported for a handful of compounds, leaving plenty of room for further investigation. The most promising compounds that have been measured, Eu_2ZnSb_2[8–10] and $Yb_{2-x}Eu_xCdSb_2$,[11] exhibit

*zT*s comparable to $YbZn_2Sb_2$,[12] Zn_4Sb_3,[13–15] and TAGS[16] at temperatures relevant for energy applications on earth and serve as indications of the great thermoelectric potential that could be uncovered in this class of layered Zintl phases.[1,2,9–11,16] While Eu_2ZnSb_2 and $Yb_{2-x}Eu_xCdSb_2$ are both layered structures with similar composition, their structures differ, with $[ZnSb_2]^{4-}$ having a defect honeycomb structure and $[CdSb_2]^{4-}$ having an undulating layered structure.

This diverse bonding, if well understood, gives researchers a great deal of control in tuning properties. In a simple picture, the covalent networks in these layered structures are largely responsible for electrical transport[17] and the interspersed cations create disorder that helps scatter phonons and reduce thermal conductivity. However, in some structure types, cations play a key role in controlling carriers, and the chemistry of each compound must be investigated carefully to enable optimization of *zT*. Compounds with AM_2Pn_2 and A_2MPn_2 stoichiometry illustrate an example of the benefits and drawbacks of this generalized understanding of layered structures.[17] Recent works have emphasized the importance of cation bonding, identity, disorder, and defects in $Yb_{2-x}Ca_xCdSb_2$, $Ca_{2-x}Eu_xCdSb_2$, $Yb_{2-x}Eu_xCdSb_2$, $Ca_{2-x}Lu_xCdSb_2$, A_2CdP_2 (A = Ba, Sr) and AZn_2Sb_2 (A = Ca, Sr, Yb, Eu) in determining electronic properties and structure type.[12,18–23] In addition, studies on Mg_3Sb_2 have revealed that the Zintl formalism does not adequately describe interactions between cations and $[Mg_2Sb_2]^{2-}$ slabs in AMg_2Pn_2 compounds, which cannot be considered layered structures due to isotropic bonding networks, even though they adopt the $CaAl_2Si_2$ structure type.[24,25] These examples highlight the need for better understanding of chemical bonding, defects, and local structure in each system to enable optimization of thermoelectric properties.

In some materials, cation substitution can also be used to tune defect structure and vary carrier concentration while simultaneously reducing lattice thermal conductivity.[21,26–28] In materials where the valence band edge is sensitive to cation identity, such as $Yb_{2-x}Eu_xCdSb_2$ and $Ba_{2-x}Sr_xCdP_2$, solid solutions are useful tools for band engineering.[18,19,22] This is especially true when paired with electronic structure calculations that show which molecular orbitals are located near the Fermi level. Using density of states (DOS) calculations as a guide, chemical intuition can be applied to tune the relevant orbital interactions and improve properties while gaining a deeper understanding of the structure. Crystal orbital Hamilton population (COHP) curves can also be used to assist in understanding the influence of defects and disorder on bonding when paired with a local structure analysis technique such as Pair Distribution Function (PDF) analysis.

This investigation was motivated by the exciting properties reported for one composition in the $Yb_{2-x}Eu_xCdSb_2$ system, $x = 0.36$,[6] and the possibility that compositions on either side of $x = 0.36$ might show even better thermoelectric properties. Given recent studies that have highlighted the sensitivity of this material to cation substitution, showing that subtle shifts in bonding drive a transition to a different structure type, obtaining a more complete picture of how the structure changes with cation substitution is critical.[18,19,29] Additionally, understanding the chemical origins of these excellent properties provide an improved framework for designing more efficient thermoelectric materials with this structure type. The analysis of the impact of local defect structure on chemical bonding and electronic transport also provide a framework for understanding defects from a structure-property perspective that can be broadly applied to Zintl phases. The present work offers an examination of the $Yb_{2-x}Eu_xCdSb_2$ composition ($x = 0$, 0.1, 0.2, 0.3, 0.4, and 0.5) to provide insight to the thermoelectric properties. An improved synthetic method

employing EuH_2 as a reactive precursor to facilitate mixing is presented. This reagent eliminated a $Yb_{11-x}Eu_xSb_{10}$ impurity that was present when elemental Eu was used as a precursor. The structure is investigated with single crystal and powder x-ray diffraction with pair distribution function (PDF) analyses and thermoelectric properties from 323 - 523 K measured.

2.3 Experimental

Synthesis

Single crystals of $Yb_{2-x}Eu_xCdSb_2$were synthesized according to the literature procedure.[30] The elements (Yb (Edge Tech, 99.95%), Eu (Stanford Materials, 99.99%), Cd (shot, Alfa Aesar, 99.95%), and Sb (shot, 5NPlus, 99.999%)) were combined in in a 2-*x*:*x*:1:2 molar ratio along with 10 molar equivalents of Pb flux (Pb needles, Alfa Aesar, 99.99%) in a 5 mL alumina crucible set[31] for a total mass of ~3 g. Samples were made for Eu concentrations of x = 0, 0.1, 0. 2, 0.3, 0.4. The crucibles were sealed into silica tubes evacuated to < 50 mTorr, placed upright in a box furnace, and heated at 120 °C/h to 960 °C where they dwelled for 20 h and were cooled to 500 °C at 5 °C/hr. The flux was removed by hot centrifugation and the tube was opened in an argon-filled glove box, where crystals were selected for X-ray diffraction.

Polycrystalline $Yb_{2-x}Eu_xCdSb_2$ samples were synthesized: in an Ar-filled glove box, Sb shot was loaded into a 5 mL tungsten carbide ball mill with two 8 mm tungsten carbide balls and sealed with tungsten carbide end caps fitted with Viton O-rings. The canister was hermetically sealed in two Uline 4 mil polyethylene bags and milled in a SPEX 8000 M mixer mill for 15 minutes, then transferred to a glove box. After scraping with a metal spatula, Yb filings, EuH_2 (American Elements), and cut Cd pieces in a stoichiometric ratio of 2-*x*:*x*:1, were added to the Sb

powder for a total reaction mass of ~3 g. All four substituents were milled together for 30 more minutes, and the container was again transferred to the glove box to be scraped before milling for an additional 20 minutes to ensure the elements were intimately mixed before the resulting powder was loaded into a Nb tube. The Nb tube was sealed in an Ar-filled arc welder and placed inside a fused silica tube, evacuated to <50 mTorr and sealed. The jacketed Nb tube was put into a box furnace to be annealed. For Eu-containing $Yb_{2-x}Eu_xCdSb_2$ samples, the temperature was increased at a rate of 120 °C/hr to 800°C and annealed at that temperature for 96 hours. Phase pure Yb_2CdSb_2 was not able to be synthesized at the same temperature, and the heating profile had to be adjusted to anneal at 600 °C.

All thermoelectric and PDF data were collected on the same set of polycrystalline samples. Three independent batches of samples were made and measured to confirm reproducible results.

Spark Plasma Sintering

The annealed black powder was then ground, sieved (100 mesh) and loaded into a graphite die with a diameter of 12.7 mm which was hermetically sealed with graphite foils. The powder was consolidated using a Dr. Sinter Junior Spark Plasma Sintering system (Fuji Electronic Industrial Co., LTD) under ~385 torr of Ar. The sample heated to 550°C, where it was left to dwell for 15 minutes. The force was slowly increased from 6 to 10.5 kN, beginning at 350°C. The geometric densities of the resulting pellets were determined to be >95% of the theoretical value.

Single Crystal X-ray Diffraction

Silver needle-like crystals were selected in Paratone oil in air and mounted on the goniometer of a Bruker APEX DUO CCD X-ray diffractometer with Mo Kα radiation ((λ = 0.71073 Å) at 90 K

with crystal detector distance 5 cm. The unit cell was indexed using three sets of 0.5 ° wide ω-scans, 10 seconds per frame and 30 frames per set. Additional data collection included four ω-scan data frame series with 0.3 ° wide scans, 20 seconds per frame and 606 frames per series with at 32.0 °, and with φ = 0 °, 90 °, 180 °, and 270 ˚. The programs, SAINT was used to correct for Lorentz and Polarization effects, and SADABS was utilized to correct for absorption and merge the data. SHELXTL software was used to determine a space group.[15] The structure was then determined using XT and further refined with XL. All structure solutions (CSD 2194398-2194400) agreed well with those previously described.[13,16,17]

Powder X-ray Diffraction

Polycrystalline sample purity was assessed using powder X-ray diffraction. Pellets of the polycrystalline samples were cut with a diamond saw and a piece was ground into a fine powder with an agate mortar. Data were collected by a Bruker D8 Advance diffractometer with Cu Kα radiation operated at 40 kV and 25 mA at room temperature with 2θ range 20-75 ° with a 0.015 ° interval and a scan rate of 1 s per step. $Yb_{2-x}Eu_xCdSb_2$ was confirmed to be the majority phase via Rietveld refinement, which was carried out using TOPAS5 software.[32]

Pair Distribution Function (PDF) Analysis

Total scattering data on all polycrystalline pressed pellets were collected at beamline 11-ID-B at the Advanced Photon Source via the mail-in program. The sintered, polycrystalline samples were ground with a mortar and pestle and loaded into 0.8 mm inner diameter Kapton capillary tubes prior to data collection. X-ray wavelength was 0.2115 Å and intensities were measured with a 2D area detector with distance 180 mm with maximum wave vector q = 24 $Å^{-1}$.

The 2D images were integrated using GSAS-II and converted to G(r) using pdfgetx3. Refinements were carried out using the small box method in PDFgui starting with a crystallographic information file (CIF).[33,34]

Elemental Analysis and SEM Imaging

Pelletized, polycrystalline samples were mounted in epoxy discs and polished using sandpaper and a polishing wheel (1 μm colloidal diamond suspension) prior to analysis. Stoichiometry was determined via energy dispersive spectroscopy (EDS) using a FEI Scios DualBeam FIB/SEM with an Oxford Instruments X-Max50 50 mm^2 Si drift detector and 15 kV accelerating voltage. An Everhart-Thornley detector was used to collect secondary electron images with 20 kV accelerating voltage.

Thermoelectric Properties

Thermal diffusivity was measured on the sintered, polycrystalline pellets using a Netzsch Laser Flash Analysis (LFA) instrument and thermal conductivity was calculated from diffusivity using the equation $\kappa = \lambda\rho Cp$, where κ is thermal conductivity, Cp is heat capacity (calculated using the Dulong-Petit equation, which was reported to be consistent with measured heat capacity),[11] λ is diffusivity, and is ρ is sample density.

High-temperature measurement of the Seebeck coefficient was performed from 323 K to 523 K in steps of 10 K using a custom-built apparatus previously described.[35] An atmosphere of low pressure nitrogen (5 torr) was using during the Seebeck measurements to ensure good thermal contact between the sample, heater blocks, and measurement thermocouples. Graphite foil spacers placed between the measurement thermocouples and the sample protect the thermocouple junction

from contamination and ensure high quality measurements. All samples underwent a minimum of 2 heating and cooling cycles during measurement to ensure that samples were not undergoing evolution during measurement. High temperature resistivity and Hall effect measurements were performed on a custom built apparatus with a Van der Pauw geometry from 323 K to 523 K under vacuum.[36,37] Test current values of 0.1 A and a magnetic field value of 1 T were used for the measurements. Confirmation of ohmic contacts was determined before each measurement by generating a current-voltage curve across all combinations of contacts.

2.4 Results and Discussion

Structure and Composition

Figure 2-1a illustrates the crystal structure of $Yb_{2-x}Eu_xCdSb_2$ (orthorhombic space group $Cmc2_1$), as determined by single crystal X-ray diffraction. It is a layered Zintl phase composed of anionic corner-shared $[CdSb_{4/2}]^{4-}$ tetrahedra connected to form an undulating layered structure that are separated by layers of Yb^{2+} and Eu^{2+} cations. The two unique Sb sites are shown in Figure 2-1b. Sb1 (blue) links the chains in the *c*-direction while Sb2 (black) connects the layers in the *a*-direction. There are two unique cation sites and the polyhedra are highlighted in Figure 2-1c: a Yb1 interlayer site and a Yb2 intralayer site. Eu preferentially occupies the larger interlayer Yb1 site (Figure 2-2), consistent with previous reports.[11,18,19,38] In the case of the highest Eu concentration of the crystals investigated herein, $x = 0.42$, the preference is for the interlayer site (Yb1), although there is a small amount on the intralayer Yb2 site. Table 2-1 outlines relevant single crystal data, including lattice parameters, which increase with increasing Eu concentration, as expected due to the larger ionic radius of Eu compared to Yb.

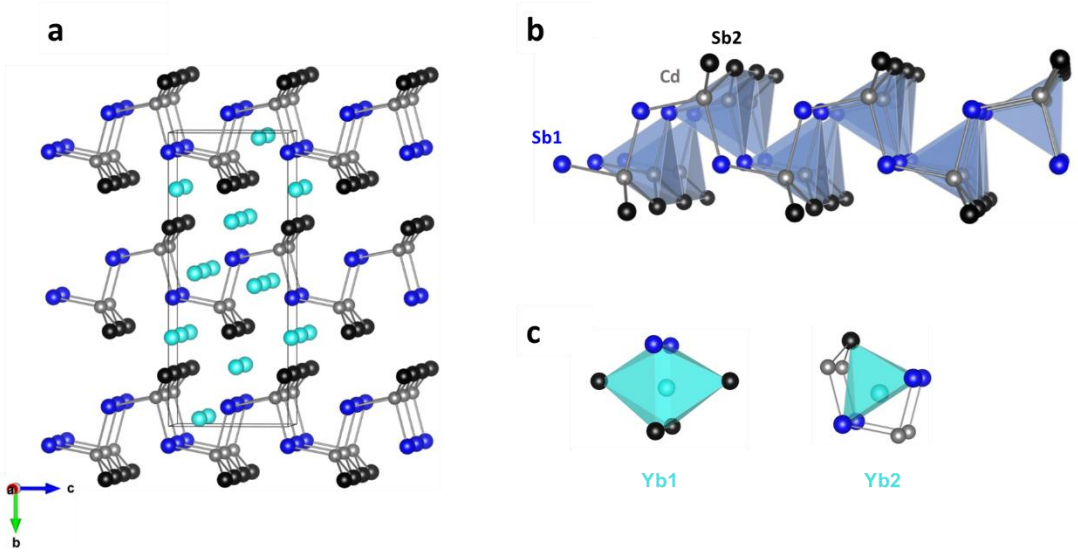


Figure 2-1. (a) crystal structure of $Yb_{2-x}Eu_xCdSb_2$. Turquoise spheres represent Yb/Eu, gray spheres represent Cd, dark blue spheres represent Sb1 and black spheres represent Sb2; (b) anionic corner-shared $[CdSb_{4/2}]^{4-}$tetrahedral chains. Sb1 sites shown in blue and Sb2 shown in black; (c) Yb1 interlayer and Yb2 intralayer coordination environments.

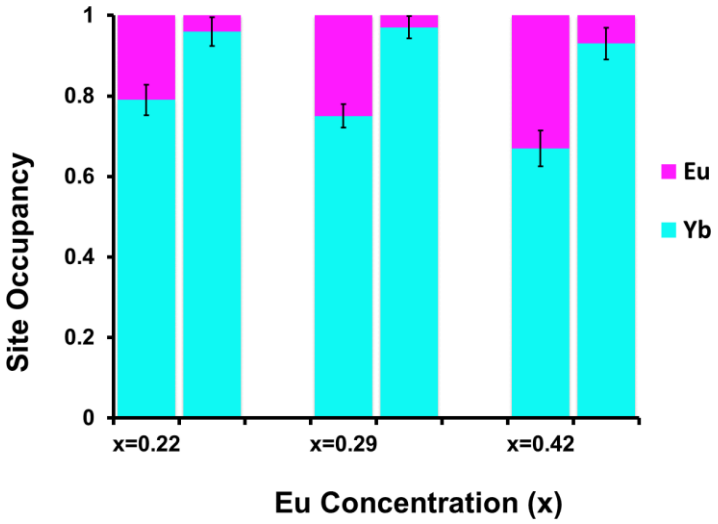


Figure 2-2. Occupancy of the Yb1 and Yb2 sites in $Yb_{2-x}Eu_xCdSb_2$ by Eu and Yb for single crystals of varying Eu content. Eu preferentially occupies the larger, interlayer octahedral site.

Table 2-1. Data Collection Details and Selected Single Crystal Parameters from $Yb_{2-x}Eu_xCdSb_2$

Empirical Formula	$Yb_{1.78(2)}Eu_{0.22}CdSb_2$	$Yb_{1.71(3)}Eu_{0.29}CdSb_2$	$Yb_{1.58(3)}Eu_{0.42}CdSb_2$
Crystal System	Orthorhombic		
Space Group, Z	C*mc2₁* (no. 36), 4		
T (K)	90 K		
a (Å)	4.6317(7)	4.6367(13)	4.6393(15)
b (Å)	17.518(3)	17.566(5)	17.607(6)
c (Å)	7.1942(11)	7.204(2)	7.205(2)
Volume ($Å^3$)	583.71(15)	586.8(3)	588.5(3)

Density (calculated, g/cm^3)	7.94	7.88	7.82
Absorption coefficient (cm^{-1})	43.1	42.5	41.7
Reflections collected	3386	3779	4624
Independent reflections	990	758	1005
Flack parameter	0.403	0.379	0.040
R_1, wR_2 (I>2σ(I))	0.0181, 0.0381	0.0129, 0.0316	0.0177, 0.0400
Goodness of fit	1.11	1.239	1.064
Largest diff. peak/hole (e$^-$/Å^3)	1.142/-1.324	1.253/-1.762	1.544/-2.342
Deposited CIFs (CSD) reference numbers	2194398	219399	2194400

Here, we focused on synthesizing a series of x values close to the best thermoelectric composition reported: $x = 0.36$.[11] We employed EuH_2, a salt-like precursor that aids in mixing the elements and provides a clean by-product of hydrogen gas during the reaction. The polycrystalline samples are from milled powders of the constitutional elements that were annealed in silica jacketed niobium tubes prior to spark plasma sintering densification into pellets. Stoichiometry of

polycrystalline pellets was confirmed by EDS (Table 2-2) and elemental maps are given in Figure 2-3a. Eu content was in good agreement with the preparative amount and the elemental maps show that it was dispersed evenly throughout the sample, highlighting the advantage of using a EuH_2 precursor.

Table 2-2. Eu Content Determined by EDS for Polycrystalline Pelletized Samples

Preparative Eu content (*x*)	**Experimental Eu Content (*x*)**
0	0.00
0.1	0.11(6)
0.2	0.17(1)
0.3	0.27(3)
0.4	0.35(1)
0.5	0.51(2)

Because of the good agreement between nominal and experimental compositions, nominal compositions will be employed to describe the samples. Secondary electron micrographs (Figure 2-3b) confirm the high density of the pellets (<95 % of theoretical value) and backscattered electron micrographs confirm homogeneity via Z contrast imaging (Figure 2-3c).

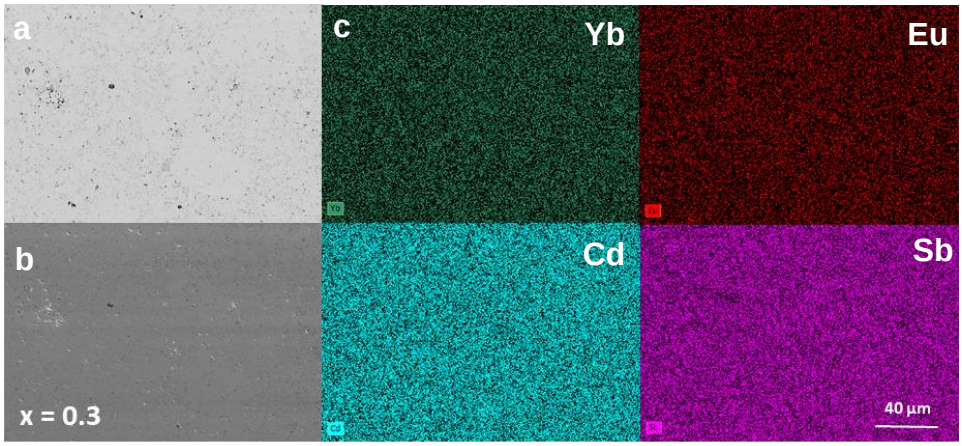


Figure 2-3. (a) Backscattered electron image of $Yb_{1.7}Eu_{0.3}CdSb_2$ shows Z contrast and homogeneity (b) Secondary electron image shows topography; (c) Elemental maps from EDS are shown for Yb, Eu, Cd, and Sb. Images confirm elements are well dispersed and the sample is homogenous.

Figure 2-4 shows the powder x-ray diffraction (PXRD) patterns for polycrystalline $Yb_{2-x}Eu_xCdSb_2$ pressed pellet samples. All samples show a small impurity (<4% by weight for all samples) that is attributed to $YbCd_2Sb_2$. Because the amount is small and consistent throughout the series, the thermoelectric measurements provided here should be representative of the systematic change in properties of the majority phase, $Yb_{2-x}Eu_xCdSb_2$.[19] The observed diffraction peaks shift left with increasing Eu concentration, indicating that the unit cell volume increases, consistent with single crystal data and Figure 2-5.[16] The *b* lattice parameter, which is in the stacking direction of the layers, exhibits the greatest increase with Eu concentration and is consistent with Eu preferentially occupying the interlayer site. The *c* lattice parameter from PXRD data is notably larger than those observed for the single crystal samples. This suggests a distortion of the tetrahedrally coordinated $[CdSb_{4/2}]^{4-}$ that extend along the *c*-axis. The large *c*-axis is likely due to structural disorder, which was investigated using pair distribution function (PDF) analysis.

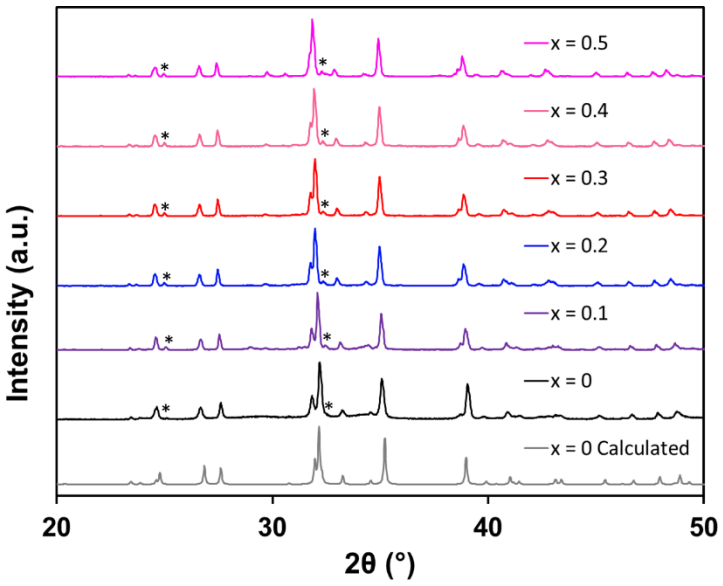


Figure 2-4. PXRD patterns post SPS of $Yb_{2-x}Eu_xCdSb_2$ x = 0, 0.1, 0.2, 0.3, 0.5 samples compared with the calculated diffraction pattern for x = 0. The asterisk marks the largest diffraction peak for the $YbCd_2Sb_2$ impurity.

Pair Distribution Function (PDF) Analysis

PDF analysis was employed to identify local deviations from the nominal structure and short-range structural disorder. Refinement of short *r*-range (2.5-5 Å) atomic site occupancies revealed significant cation deficiencies on the interlayer Yb1 site for x = 0.2-0.5, while the intralayer Yb2 site was fully occupied with the mixed cations Yb/Eu for all samples. Figure 2-6a shows that x = 0.3 has the lowest Yb1 occupancy. The variation in cation occupancy could be due to changing defect energy with Eu, as seen in related Zintl phase AZn_2Sb_2 (A = Yb, Eu, Sr, Ca). In the AZn_2Sb_2 system, cation vacancies are the dominant native defect, and equilibrium defect concentration has been shown to vary with electronegativity of the cation.[21]

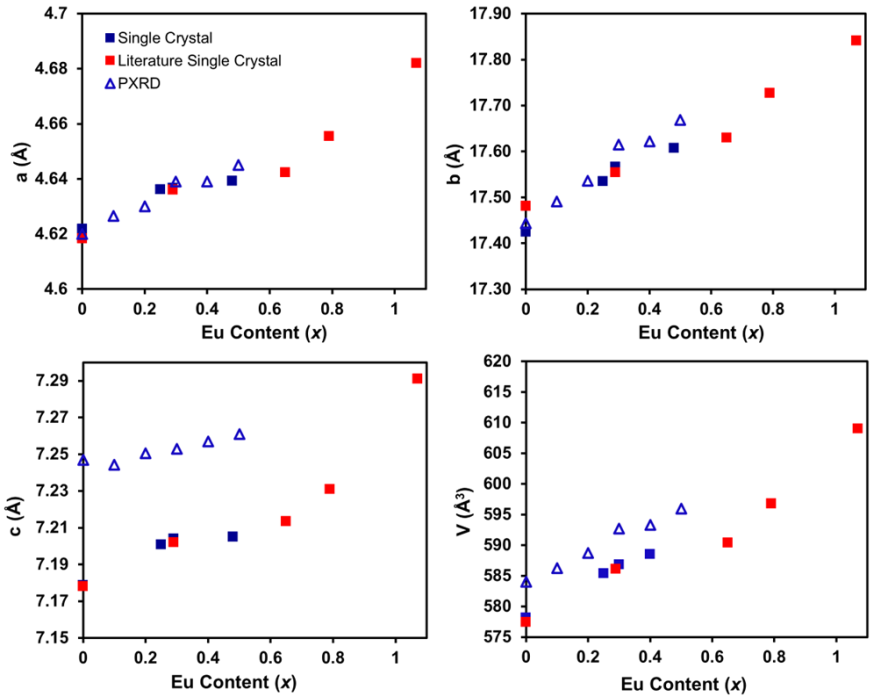


Figure 2-5. Lattice parameters from single experimental crystal (90 K), literature (ref. [30]) and powder x-ray diffraction (room temperature) are plotted as a function of Eu content. Lattice parameters increase with increasing Eu content.

Based on this reasoning, cation vacancies are expected to be the primary donor defect in this *p*-type semiconductor. However, the number of vacancies does not trend systematically with Eu amount, suggesting that factors other than cation substitution control defect energies. With these cation defects, Figure 6b shows that there are also Sb defects. Similar to the two cation sites, deficiencies were only present on the Sb2 sites and all Sb1 sites were fully occupied. Sb vacancies are expected to be "killer" acceptor defects that limit the number of free carriers that can be introduced through cation vacancies, similar to the $Ca_{11-x}RE_xSb_{10-y}$ system, which can contain up to 20 % Sb deficiencies to prevent population of antibonding orbitals and stabilize the structure.[39] Defect diagrams calculated for $Ca_5Al_2Sb_6$ and A_2CdP_2 (A = Sr, Ba, with the same structure type

as Yb_2CdSb_2) have also shown that pnictide vacancies are expected to be the lowest energy defects in these Zintl phases.[40,41] COHP curves calculated by Kim et al. for the related compound, $Yb_{1.5}Ca_{0.5}CdSb_2$, which is in this structure type reveal A1-A1 bonding states (A1 as a more generalized notation for the Yb/Eu/Ca1 mixed site) 0-0.25 eV below the E_F and Cd-Sb antibonding states from ~0.25-0.5 eV below E_F.[19] The Cd-Sb antibonding states may limit the *p*-type dopability window, resulting in charge compensating Sb defects to stabilize the compound by filling the bonding A1-A1 states. Figure 2-6c compares Yb1 and Sb2 site occupancies and shows the largest amounts of site defects are for compositions x = 0.2, 0.3. Interestingly, x = 0.2, 0.3 are the most cation deficient (Yb1 site occupancies 0.94 and 0.93, respectively), but their Sb content varies. For these compositions x = 0.2 is more Sb deficient, whereas x = 0.3 is more cation deficient. The lack of a systematic trend here could be explained by changes in the Yb1-Yb1 site bonding as different amounts of Eu are incorporated that alter the dopability window, possibly including additional Eu-Sb interactions as seen in the coinage-metal-stuffed Zintl phase $Eu_9Cd_4Sb_9$.[11,42] The variation in cation and Sb content between samples is expected to affect electronic properties.

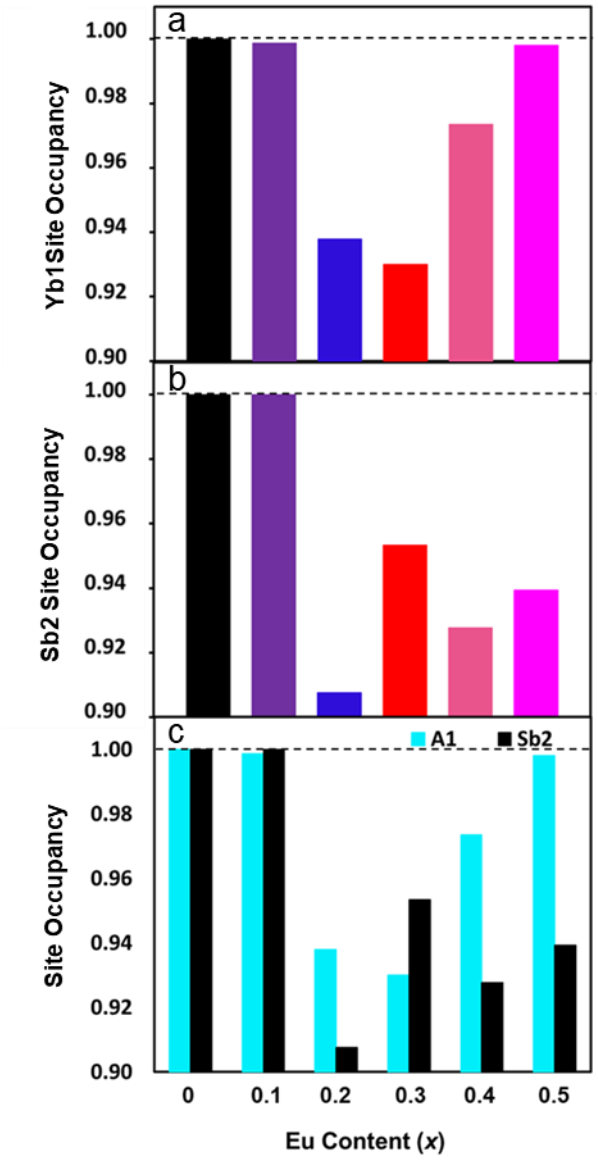


Figure 2-6. Site occupancy as determined by short *r*-range PDF analysis for different Eu concentrations for (a) Yb1 cation site and (b) Sb2 site; (c) comparison of Yb1 site occupancy and Sb2 site occupancy. Cation site is in turquoise and Sb site is in black. The dotted lines mark site occupancy of 1 for reference.

Short *r*-range PDF analysis indicates that the local structure differs from the average structure, observable from differences in lattice parameters (Figure 7). Lattice parameters determined by PDF from *r*-range 2.5 to 5 Å deviate from those determined by Rietveld refinement of PXRD data and long *r*-range PDF for all compositions. The *a* and *b* axes are larger than the average structure, while the *c* axis is smaller, indicating stretching of the stacking axis and compression of the $[CdSb_{4/2}]^{4-}$ chains. Additionally, lattice parameters for $x = 0.2$ and 0.3 deviate substantially from the expected trend with $x = 0.2$ having the smallest unit cell volume while $x = 0.3$ has the largest. Close examination of bond lengths and angles from PDF analysis and single crystal data shows that distortions in Yb1-Sb octahedra are responsible for the variation in lattice parameters.

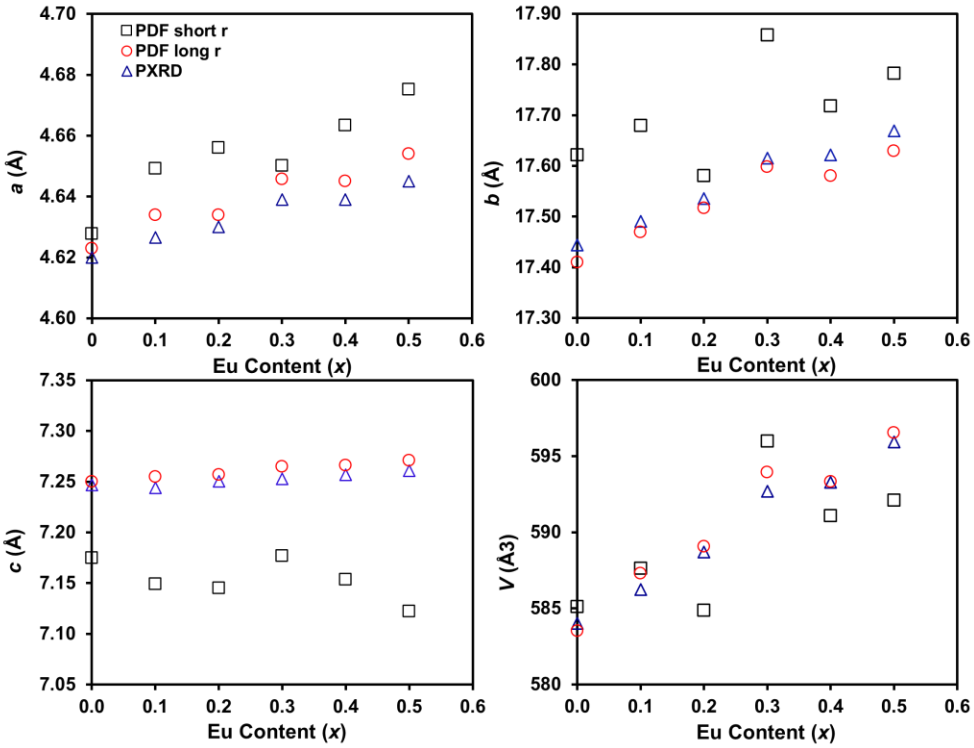


Figure 2-7. Lattice parameters from Rietveld refinement (blue triangles), PDF from 2.5 to 5 Å (black squares) and PDF from 2.5 to 20 Å (red circles).

Analysis of single crystal refinements show linear changes in all four bond angles in Yb1-Sb octahedra as Eu substitutes (Figure 2-8). The Sb1-Yb1-Sb2 bond angle increases to make room for the neighboring Eu atom, which is larger than Yb, in the *a*-direction. Equatorial Sb2-Yb1-Sb2 and Sb1-Yb1-Sb1 angles decreased with Eu substitution, which can be explained by steric and electronic effects of replacing

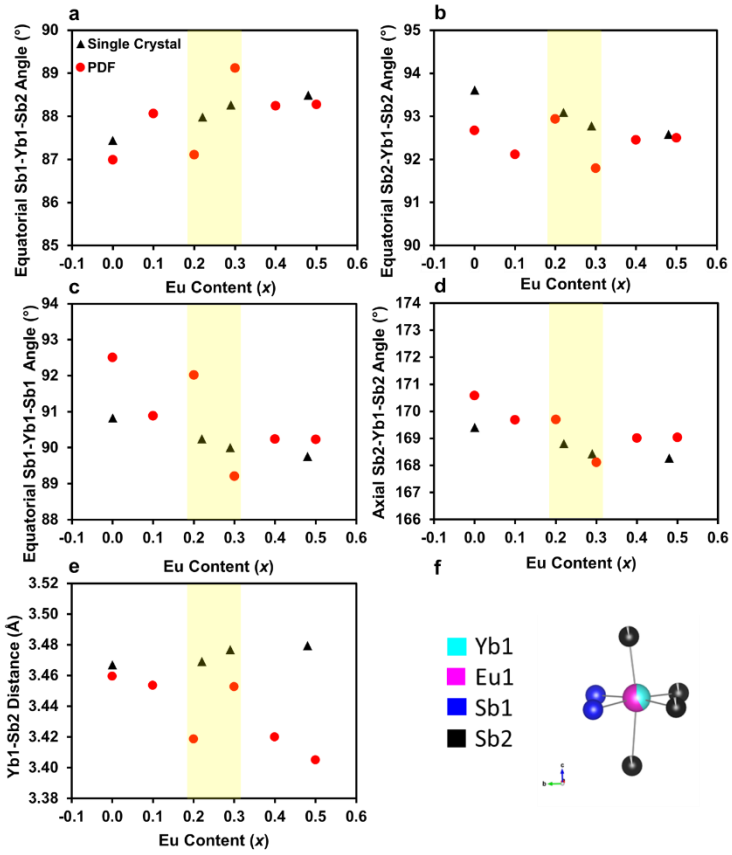


Figure 2-8. Bond angles for Yb1 octahedra determined by single crystal XRD (black triangles) performed on single crystal samples and short-range PDF analysis (red circles) performed on polycrystalline samples. a: Equatorial Sb2-Yb1-Sb2 bond angle; b: Axial Sb2-Yb1-Sb2 bond angle; c: Sb1-Yb1-Sb1 Bond Angle; d: Sb1-Yb1-Sb2 bond angle; e: Yb1-Sb2 bond distance; f:

Yb1 octahedron from $x = 0.5$ for reference. The yellow highlights the compositions $x = 0.2$ and 0.3, which deviate from the trend.

the smaller, more electronegative central Yb atom with larger, less electronegative Eu. Bond angles obtained from PDF analysis of polycrystalline samples do not show the same linear trend, which indicates that the local structure deviates from the average structure given by the single crystal refinement. These distortions may be a result of the large number of cation and Sb defects. Given the differences between local and average structure, predictions based on single crystal structures may not fully explain experimental properties observed in sintered polycrystalline samples. as vacancy ordering can alter band structure, as shown in Eu_2ZnSb_2.[8]

The most notable differences between single crystal and PDF bond angles are for $x = 0.2$ and 0.3. While $x = 0.2$ exhibits unexpectedly large equatorial Sb2-Yb1-Sb2 and Sb1-Yb1-Sb1 bond angles, $x = 0.3$ exhibits unexpectedly small angles for the same bonds. This results in a small equatorial Sb1-Yb1-Sb2 angle for $x = 0.2$ and small Sb1-Yb1-Sb1 for $x = 0.3$. In addition, the axial Yb1-Sb2 bond length is shorter than expected for $x = 0.2$ and longer for x = 0.3 (Figure 2-8e). The fluctuations in these angles and lengths result in distortions in the coordination environment of Yb1 for $x = 0.2$ and 0.3, as well as elongation of the *a*-axis and compression of the *b*-axis for $x = 0.2$ and compression of the *a*-axis with elongation of the *b*-axis for $x = 0.3$.

The observed distortions in Yb1 coordination environment can be understood by considering the electronics of Sb2-Cd bonding and Yb1-Yb1 bonding. An electron localization

function (ELF) analysis done on $Yb_{2-x}Ca_xCdSb_2$ in this structure type showed greater distribution of lone pairs on the Sb2 site compared to Sb1, which leads to a smaller Cd-Sb2-Sb angle due to the repulsive interaction of the excess electron density and the Cd-Sb2 bonding pairs.[19] The large number of vacancies on the Sb2 site in $x = 0.2$ allow the Cd-Sb2-Cd bond angle to relax (Figure 2-9a), distorting the *a*-direction of the covalent chains. This opening of the Cd-Sb2-Cd bond angle results in a larger equatorial Sb2-Yb1-Sb2 angle and thus a smaller Sb1-Yb1-Sb2 angle. Integrated COHP curves of Yb_2CdSb_2 and Ca_2CdSb_2, polytypes with identical layers but differing stacking sequences that lead to crystallization in *Cmc2₁* and *Pnma* space groups, respectively, indicated that stronger (Yb/Ca)1-Sb bonding in the *Cmc2₁* structure plays a key role in directing the structure transition of the solid solution.[18] This finding suggests that the Yb1-Sb coordination sphere is an important factor the stability and electronic properties of Yb_2CdSb_2.

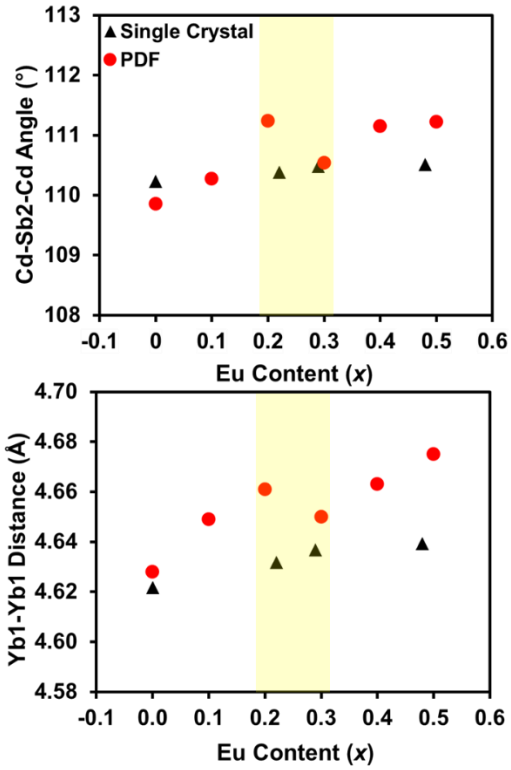


Figure 2-9. (a) Cd-Sb2-Cd and (b) Yb1-Yb1 angles from single crystal XRD (black triangles) and short-range PDF analysis (red circles) of polycrystalline samples. The yellow box highlights compositions x = 0.2 and 0.3, which deviate from the trend.

Yb1-Yb1 distances, plotted in Figure 2-9b, are also of interest in this compound. For short range PDF analysis, atomic distances in the *a*-direction show two distinct trends: increasing linearly from x = 0 to x = 0.2 before dropping at x = 0.3, and then increasing linearly to x = 0.5. Single crystal bond distances increase systematically as Eu is added. The variation in atomic distances could be explained by optimized Yb1-Yb1 bonding for each Eu composition given the distorted coordination environments in polycrystalline samples. In another theoretical study of the two polytypes of A_2CdSb_2 (A = Ca, Yb) by Kim et al., electronic interactions were analyzed for

both structure types in order to determine the important driving forces leading to increased stability in one structure type over the other.[19] Their calculations showed that the crystal structure is sensitive enough to A1-A1 bonding interactions that optimization of A1-A1 distances drives the transition from the related Ca_2CdSb_2-type *Pnma* structure to the Yb_2CdSb_2-type *Cmc*2_1 structure as more Yb is incorporated. The *Pnma* structure of Ca_2CdSb_2 has two unique A1-A1 bond distances, one long and one short, while the *Cmc*2_1 structure of Yb_2CdSb_2 has only one distance with an intermediate length that alleviates a repulsive A1-A1 interaction from the shorter bond in the *Pnma* structure for Yb-rich compositions, replacing an antibonding A1-A1 interaction with a slightly bonding one just below the Fermi level. The more energetically favorable A1-A1 bonding stabilizes Yb_2CdSb_2 in the *Cmc*2_1 space group. Given the sensitivity of this system to the A1-Sb and A1-A1 interactions discussed above, such distortions in Yb1 octahedra would be expected to impact the electronic properties.[18,19]

Electronic Properties

Seebeck coefficients (S) and electrical resistivity (ρ) values (Figures 2-10a and 2-10b) do not trend systematically with Eu, suggesting factors beyond cation substitution play an important role in the electronic structure of this compound. Notably, x = 0.3 has the smallest Seebeck coefficient and lowest resistivity while x = 0.2 has the largest Seebeck coefficient and highest resistivity. This can be explained by examining changes in weighted mobility (μ_w) with distortions in the Yb1 octahedra discussed above. μ_w is defined as charge carrier mobility weighted by the density of electron states according to the relationship $\mu_w \approx \mu\left(\frac{m^*}{m_e}\right)^{3/2}$ (where μ is mobility, m^* is effective mass and m_e is the electron mass) and is a carrier concentration independent indicator

of the inherent quality of electronic transport properties of a material.[43] When a single isotropic parabolic band dominates charge transport, μ_w is constant at a given temperature, regardless of doping level. This makes it a useful way to detect changes in band structure due to alloying—if changes in electronic properties are due to carrier concentration alone, μ_w will have the same value for all samples in a series.[43] At 525 K, μ_w in this system increases with Yb1 polyhedral volume (Figure 2-10c), indicating that the band structure changes as the Yb1-Sb octahedron is distorted. This agrees well with previous studies discussed above that have shown this structure to be highly sensitive to Yb1 bonding and small changes in interatomic distances dramatically affect bonding and antibonding states just below the Fermi level.[19,44] The published projected density of states (PDOS) suggests that the valence band is composed of Yb/Eu 5d, Sb 5p, and Cd 5p states,[11] so changes in Yb1-Yb1, Y1b-Sb and Cd-Sb bonding are likely to affect the electronic structure of the valence band.

Weighted mobility, μ_w, is lowest for the parent compound, which shows that Eu incorporation improves the intrinsic thermoelectric quality of the material. The next lowest μ_w is observed for x = 0.2, which has the smallest Yb1 octahedral volume of all Eu-containing samples. The shorter bond lengths indicate better

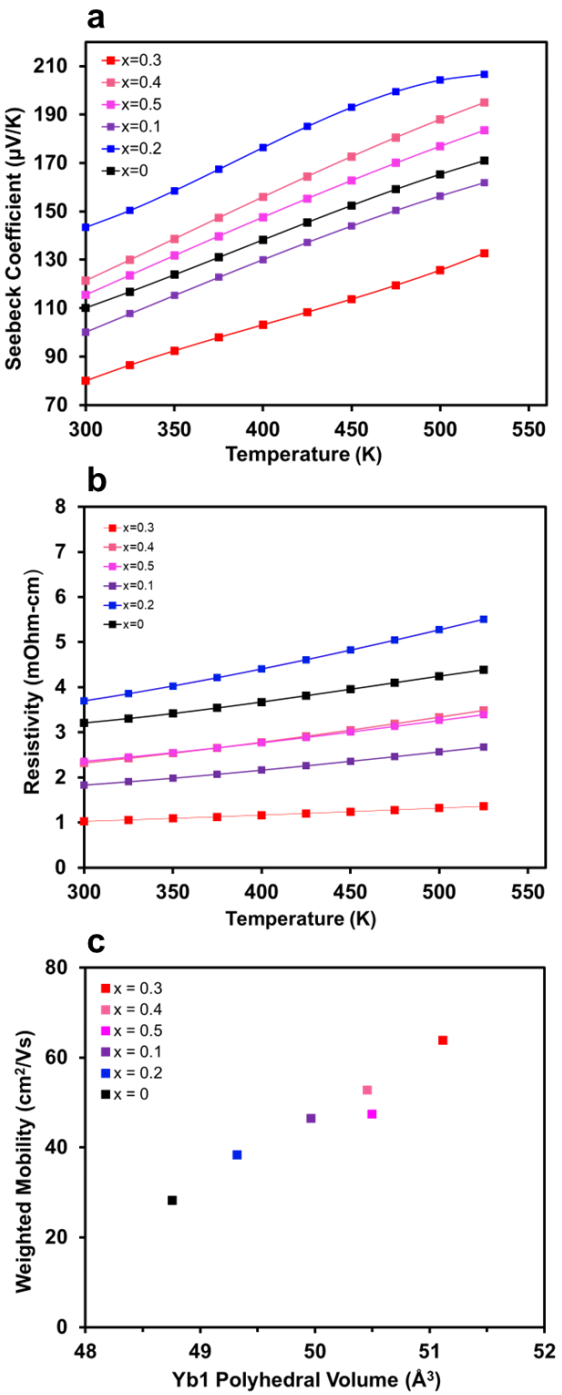


Figure 2-10. (a) Seebeck coefficients (b) electrical resistivity and (c) weighted mobility for $Yb_{2-x}Eu_xCdSb_2$ at 525 K. Points are color-coded in a gradient according to weighted mobility.

orbital overlap and stronger interactions, which leads to broader band dispersion, lower density of states, and a smaller effective mass of charge carriers. Weighted mobility is weighted by the effective mass of charge carriers in a sample, so it's not surprising that the polyhedral volume and weighted mobility are related. However, this change in bonding could be impacting transport in the materials studied here in several different ways. For example, distortions in the Yb1 coordination sphere that lead to less dispersion in the valence band maximum could lead to these deeper bands moving up in energy to create a convergence type event, which would improve the material's μ_w. Band structures previously calculated for $YbEuCdSb_2$ indicate the presence of three bands within ~0.25 eV of the Fermi level.[11] This idea is supported the increase in density of states near 400 K experienced by $x = 0.1$, 0.2, 0.4, and 0.5 when the fermi Dirac distribution is broader.[45] Calculations of the disordered structures would be necessary to confirm band convergence. The highest μ_w is observed for $x = 0.3$, which suggests bonding is optimized in this composition. Interestingly, the same composition exhibits a drop in Yb1-Yb1 distances discussed above, which are thought to play an important role in the stability of this compound.[19]

Given the high weighted mobility and expected band convergence in $x = 0.3$, it is surprising that the lowest Seebeck coefficient is reported for this sample. Further insight into this trend can be gained from examination of changes in the reduced Fermi level (η), an indicator of doping level calculated from Seebeck coefficients,[43] across the series. From Figure 2-11, it is apparent $x = 0.3$ is the most heavily doped at 525 K, which results in the lowest Seebeck coefficients and resistivity, despite having the highest weighted mobility. The reverse is true for $x = 0.2$, which has the lowest carrier concentration and highest Seebeck coefficients despite having the lowest μ_w. The

fluctuations in carrier concentration across the series makes direct comparison of changes in thermoelectric properties difficult and highlight the

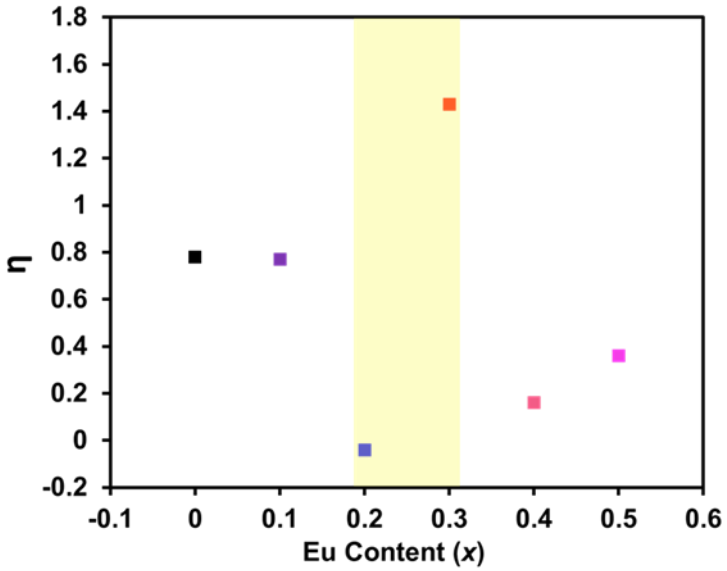


Figure 2-11. Reduced chemical potential for $Yb_{2-x}Eu_xCdSb_2$ at 525 K. The yellow box highlights compositions $x = 0.2$ and $x = 0.3$, which have the lowest and highest chemical potential.

usefulness of a carrier concentration independent factor such as μ_w to help separate contributions from carrier concentration and changes in band structure. The changing carrier concentration also underscores the importance of understanding and controlling native defects to optimize thermoelectric performance.

The origin of the difference in carrier concentration can be understood by returning to cation and Sb vacancies. As described above, cation vacancies are expected to be the dominant defect in this system, so the sample with the largest number of cation vacancies is expected to have the highest carrier concentration, while the sample with the lowest carrier concentration would be expected to have nearly fully occupied cation sites. Figure 2-6c shows that the lowest Yb1 occupancy is observed for $x = 0.3$ at 0.93, which is consistent with the highest carrier concentration.

However, x = 0.2 exhibits the second-lowest Yb1 occupancy at 0.94 but has the lowest carrier concentration. The discrepancy between cation deficiency and carrier concentration can be explained by the presence of a large amount of killer Sb defects in x = 0.2 compared to x = 0.3, with Sb2 site occupancies of 0.91 and 0.95, respectively (Figure 2-6c). One possible explanation for this difference is a change in orbital overlap that leads to differing COHP curves between samples. Previously calculated COHP curves show that the top of the valence band is composed of Yb1-Yb1 bonding states that stabilize the structure, along with Cd-Sb antibonding states just below the Yb1-Yb1 states.[19] The shorter Yb1-Yb1 distance in x = 0.3 increases the orbital overlap, increasing the Yb1-Yb1 bonding interaction just below the Fermi level, while the longer Yb1-Yb1 distance in x = 0.2 reduces orbital overlap and decreases the Yb1-Yb1 bonding interaction, pinning the Fermi level to a higher energy to avoid destabilizing the structure by emptying the Yb1-Yb1 bonding states and leaving the Cd-Sb antibonding states fully populated. For x = 0.3, stronger Yb1-Yb1 bonding character allows the Fermi level to be pushed deeper into the valence band before Sb defects begin compensating. COHP calculations for both compositions are necessary to confirm this explanation.

Thermal Properties

Total thermal conductivity (κ_{tot}), shown in Figure 2-12a, is very low for such a simple structure and is higher for Eu-containing samples than the parent compound, consistent with previous reports.[11] Calculations on this system have confirmed the presence of low frequency optical phonon branches that can couple to acoustic branches and result in a large number of 3-phonon scattering channels which lower lattice thermal conductivity.[11] $Yb_{2-x}Eu_xCdSb_2$ has also been compared to SnSe for its anomalously low thermal conductivity, which for SnSe has been

attributed to strong anharmonicity arising from soft, anisotropic bonding in its zig-zag structure[46–49] and more recently, an unstable electronic structure and electron-phonon coupling resulting in polaron formation.[48,50] These factors could play a role in this system, as well, given the similar morphology of the zig-zag layers, distorted bonding, and presence of localized Sb $5s^2$ lone pairs. Recent work on structures with zig-zag layers, such as Cu_3SbSe_3, SnSe, and $Cu_{12}Sb_3Se_{13}$, has shown that the repulsion between the Sb/Sn lone pair and bonding pairs in the covalent chains contribute to anharmonicity and soften phonon modes.[49] Lattice thermal conductivity for $Yb_{2-x}Eu_xCdSb_2$ is lower for compositions that have higher Sb2 site occupancy (x = 0, 0.1, and 0.3), suggesting that the lone pair localized on the Sb2 site plays a role in phonon scattering.

The electronic portion of the thermal conductivity (κ_e), shown in Figure 2-12b, was calculated using the Wiedemann-Franz relation ($\kappa_e = LT/\rho$), where L is the Lorenz number and was estimated using the Seebeck coefficient.[51] κ_e trends as expected based on electrical resistivity, with the least resistive x = 0.3 composition exhibiting the largest κ_e. The lattice contribution to thermal conductivity, κ_L, estimated by subtracting κ_e from κ_{tot}, is lowest for x = 0.3 and highest for x = 0.2 at 525 K (Figure 2-12c). The extremely low κ_L for x = 0.3 is likely due to local disorder in this highly defected composition discussed above, as well as the large unit cell volume.

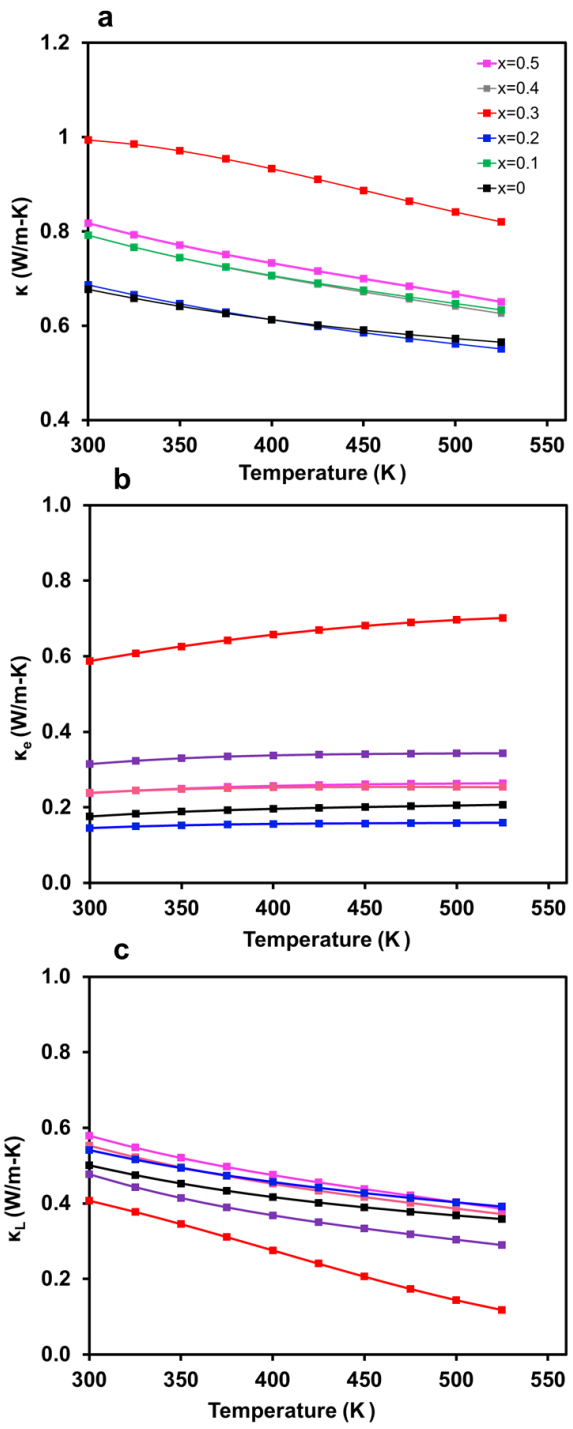


Figure 2-12. (a) Total thermal conductivity (b) electronic component of thermal conductivity (c) lattice component of thermal conductivity for $Yb_{2-x}Eu_xCdSb_2$.

Thermoelectric Quality Factor (B)

The high weighted mobility, μ_w, and low lattice thermal conductivity in the highly defected $x = 0.3$ composition of $Yb_{2-x}Eu_xCdSb_2$ make it a promising candidate for further optimization. To assess its potential, the thermoelectric quality factor (B) was employed. B uses μ_w and κ_L to predict the highest possible zT for a given material at a given temperature if carrier concentration is optimized.[52] The highest value was observed at 525 K for $x = 0.3$, $B \approx 1.5$ (Table 2-3, Figure 2-13), which predicts a maximum $zT > 2$ if carrier concentration is sufficiently reduced. Thermoelectric efficiency predictions based on B assume isotropic bands in which effective mass does not change when the Fermi level moves. $Yb_{2-x}Eu_xCdSb_2$ is a layered phase with anisotropic bonding so B predictions may not be attainable, as reducing the carrier concentration in $Yb_{2-x}Eu_xCdSb_2$ may also alter the transport properties. However, given the exceedingly high B value of the heavily defected $Yb_{1.7}Eu_{0.3}CdSb_2$, further optimization of this composition is of interest. Lu^{3+} would be a good candidate to reduce carrier concentration and would most likely occupy the Yb2 site; given its smaller size and higher electronegativity,[19] it is not expected to alter the valence band edge.

Table 2-3. Thermoelectric Quality factor (B) for $Yb_{2-x}Eu_xCdSb_2$ at 525K.

x	B
0	0.22
0.1	0.42
0.2	0.27
0.3	1.45
0.4	0.39
0.5	0.31

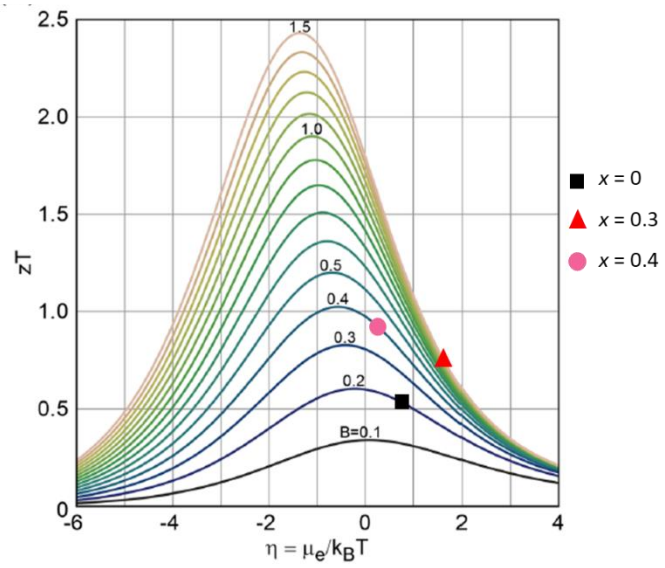


Figure 2-13. Quality Factor (B) plotted as a function of reduced chemical potential (η) and zT. B values at 525 K for select $Yb_{2-x}Eu_xCdSb_2$ samples are shown color-coded as filled circles. Figure reprinted from reference [52] with the permission of AIP Publishing.

2.5 Conclusion

Thermoelectric properties in the $Yb_{2-x}Eu_xCdSb_2$ solid solution are heavily impacted by disorder and defects, and defect structure needs to be considered alongside composition to optimize

efficiency. The best performing composition was found to be x = 0.4, with $zT \approx 0.9$ at 525 K, making this compound the highest efficiency p-type Zintl phase at low temperatures (Figure 2-14).[5] If defects can be controlled through the synthetic method and carrier concentration can be reduced, thermoelectric quality factor predicts $Yb_{2-x}Eu_xCdSb_2$ could achieve a zT of ~2.5 at 525 K. This work highlights the importance of understanding defects from a structure and bonding point of view to optimize thermoelectric properties. Employing COHP curves together with PDF analysis of local structure enables thermoelectric properties to be tuned using chemical intuition via substitution on relevant crystallographic sites while providing a detailed understanding of defect chemistry. These concepts can be applied to other promising thermoelectric materials to help understand and control electronic properties.

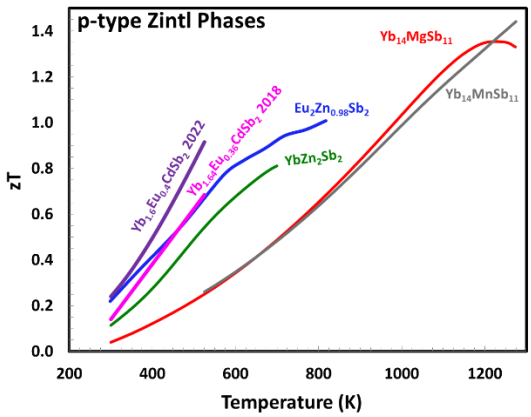


Figure 2-14. zT as a function of temperature for leading p-type Zintl phases, $Yb_{1.64}Eu_{0.36}CdSb_2$,[11] $Eu_2Zn_{0.98}Sb_2$,[9] $YbZn_2Sb_2$,[12] $Yb_{14}MgSb_{11}$,[53] and $Yb_{14}MnSb_{11}$[54]. $Yb_{1.6}Eu_{0.4}CdSb_2$ from this work (purple) gives a higher zT across the low temperature range (300-525 K) than any other material shown.

2.6 Acknowledgements

This work was supported by NSF DMR-2001156 and NSF DMR-1555340. This research used resources of the Advanced Photon Source; a U.S. Department of Energy (DOE) Office of Science User Facility operated for the DOE Office of Science by Argonne National Laboratory under Contract No. DE-AC02-06CH11357. The mail-in program at Beamline 11-ID-B (and/or 17-BM, 11-BM) contributed to the data. We thank the National Science Foundation (Grant CHE-1531193 and CHE-0840444) for the Dual Source X-ray diffractometers. Funding for this work was also received from the University of California, Davis Dean's Distinguished Graduate Student Fellowship. This research used the Advanced Materials Characterization and Testing laboratory (AMCaT) for SEM/EDS data. We thank Dr. Kasey P. Devlin for useful discussion and Jennifer Liem for preliminary experimental work.

2.7 Appendix

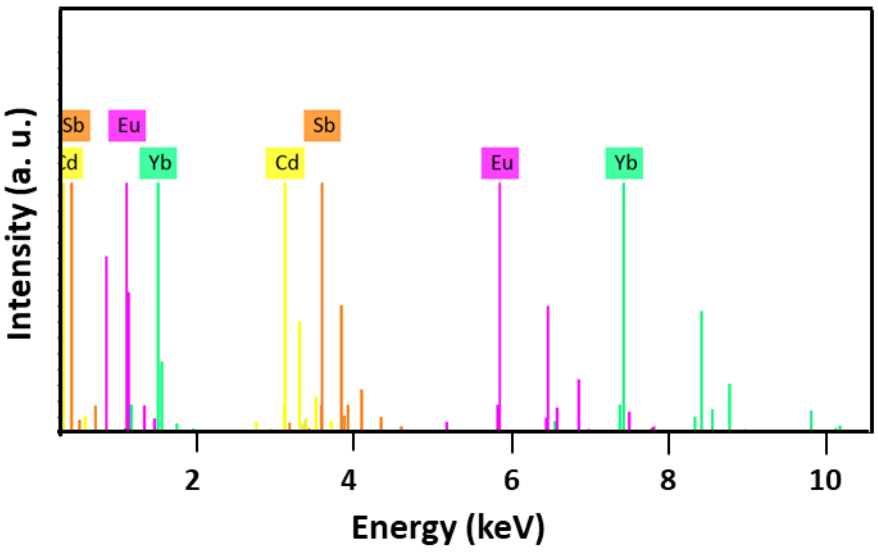


Figure 2-15. Depicts energy of characteristic X-rays from EDS used to determine the composition of $Yb_{1.7}Eu_{0.3}CdSb_2$.

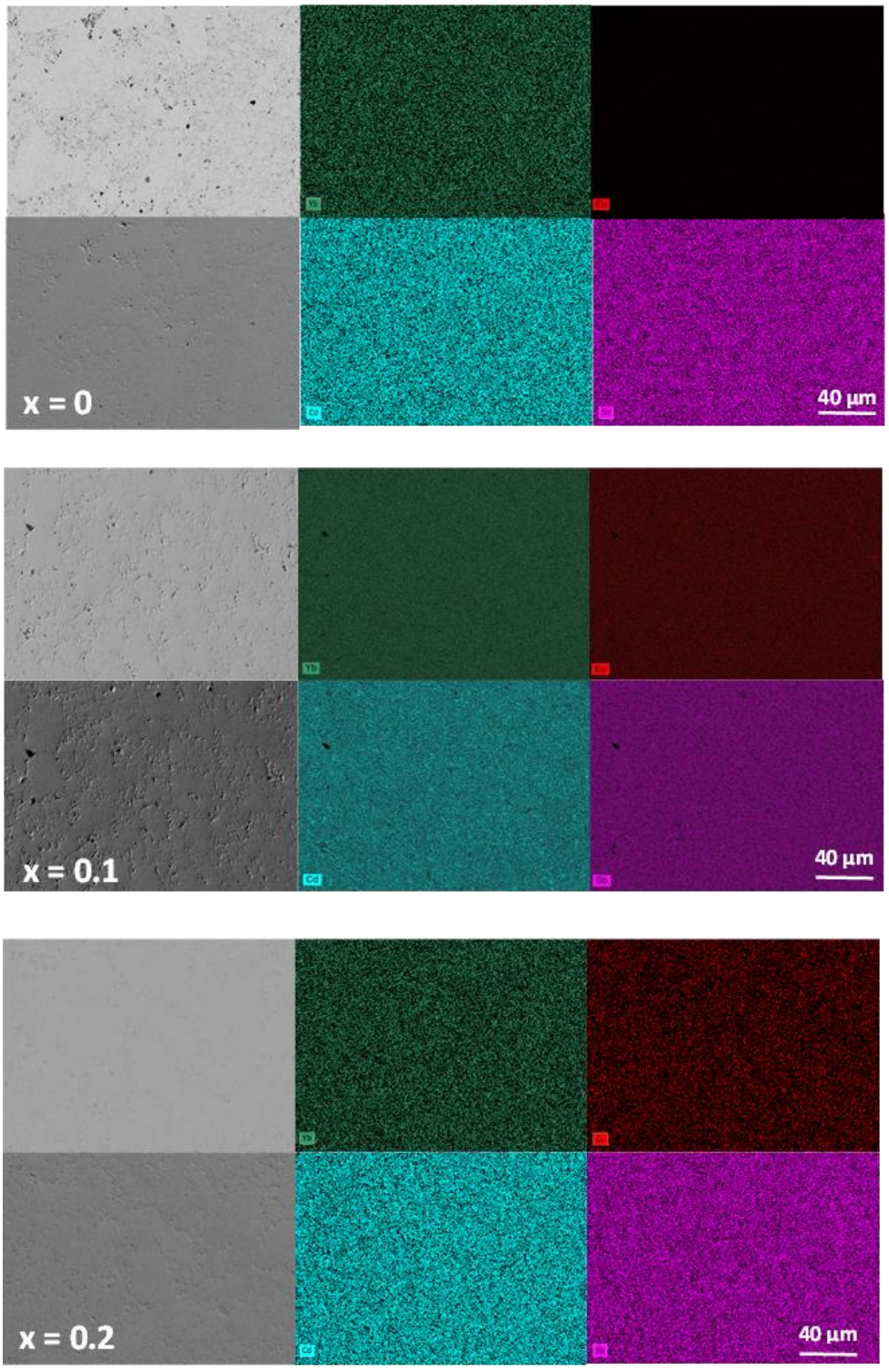


Figure 2-16. Backscattered electron SEM micrographs (top left), secondary electron SEM micrographs (bottom left), and EDS elemental maps (green: Yb, red: Eu, blue: Cd, pink: Sb) for $Yb_{2-x}Eu_xCdSb_2$, x = 0, 0.1 and 0.2.

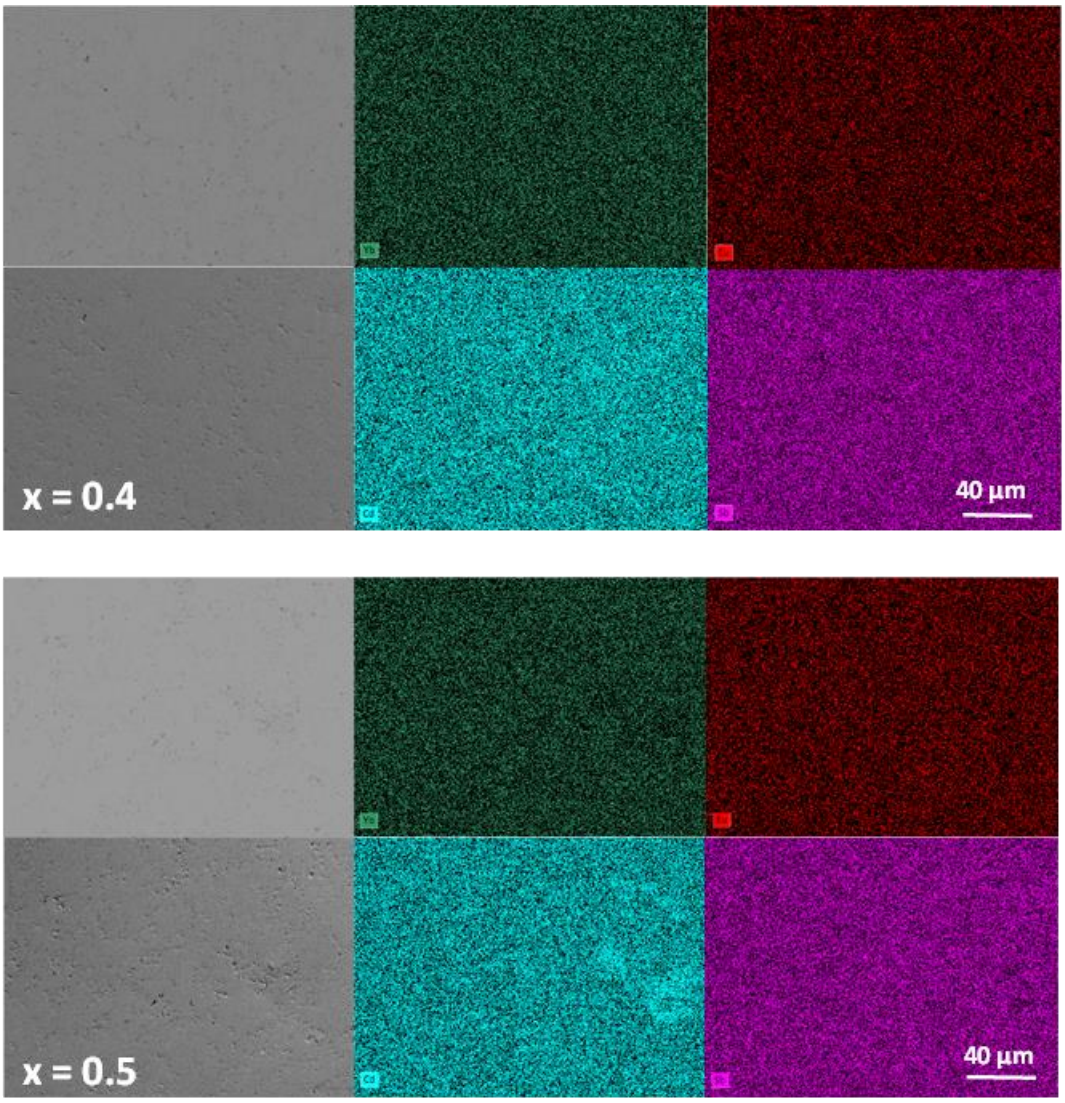
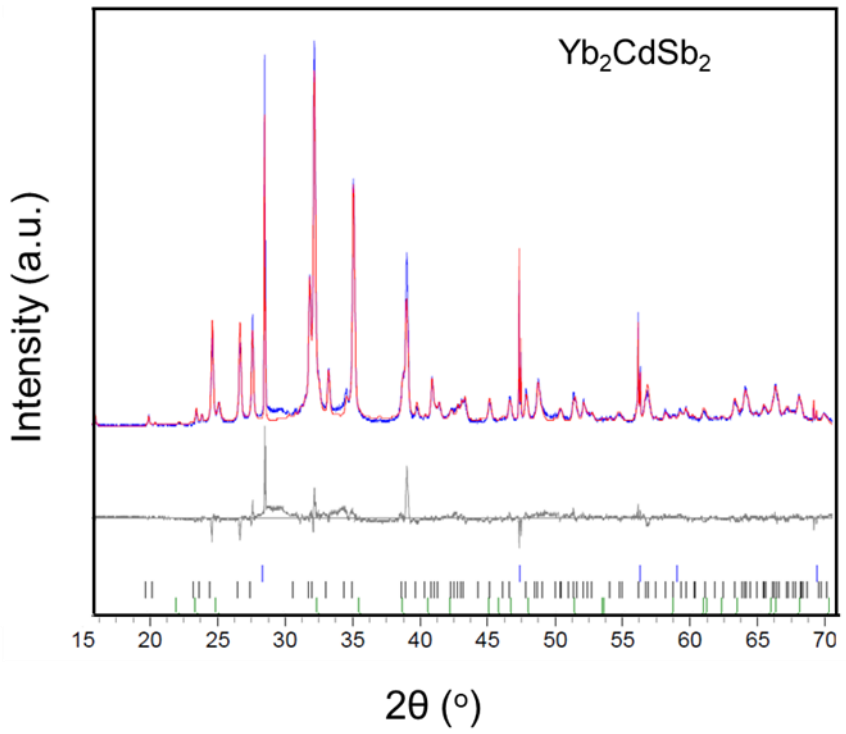
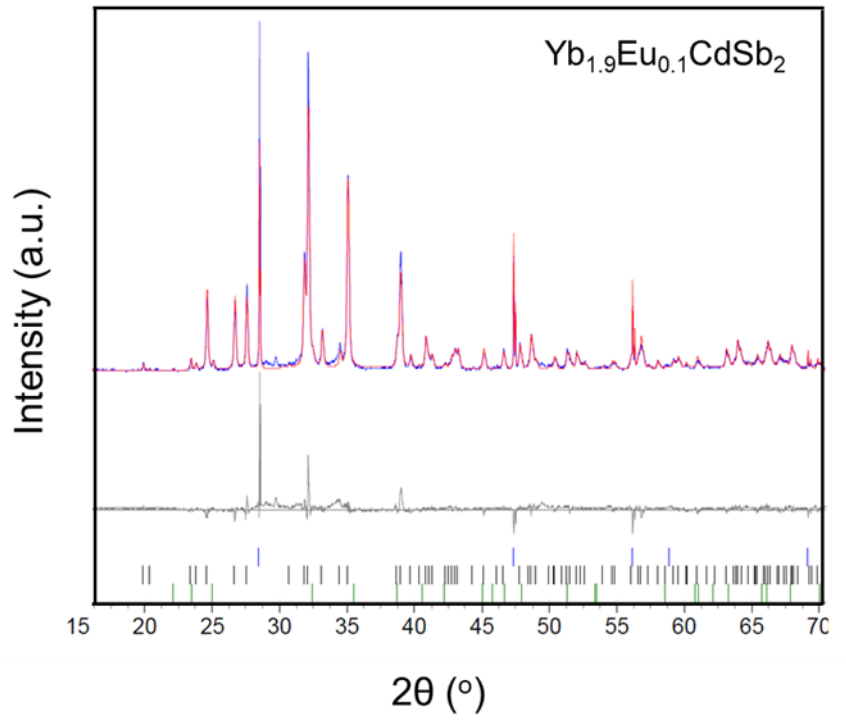
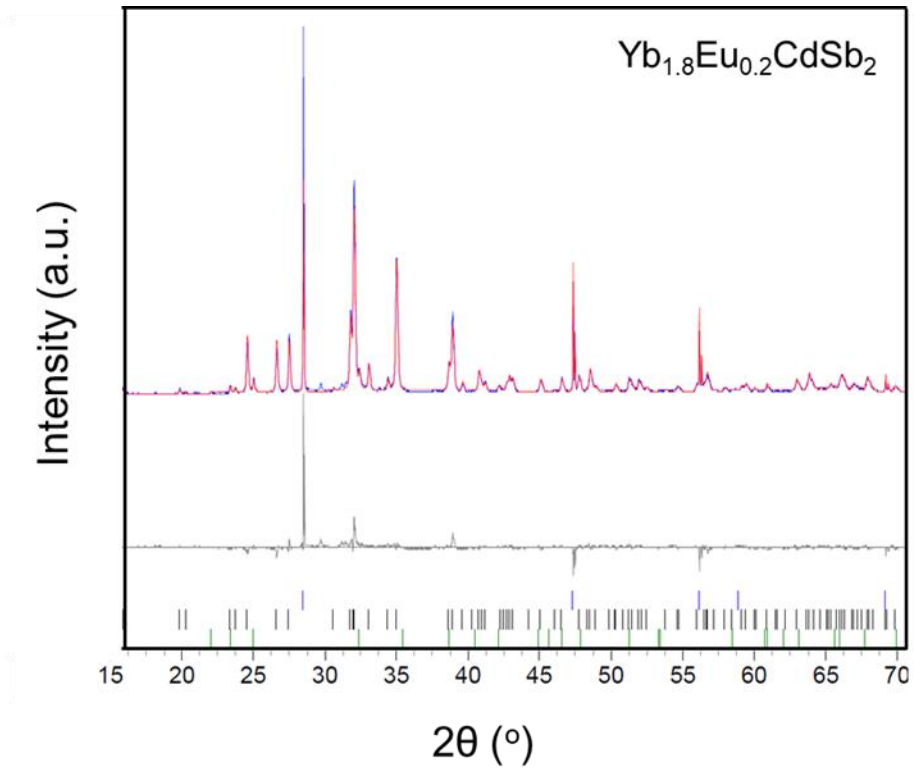
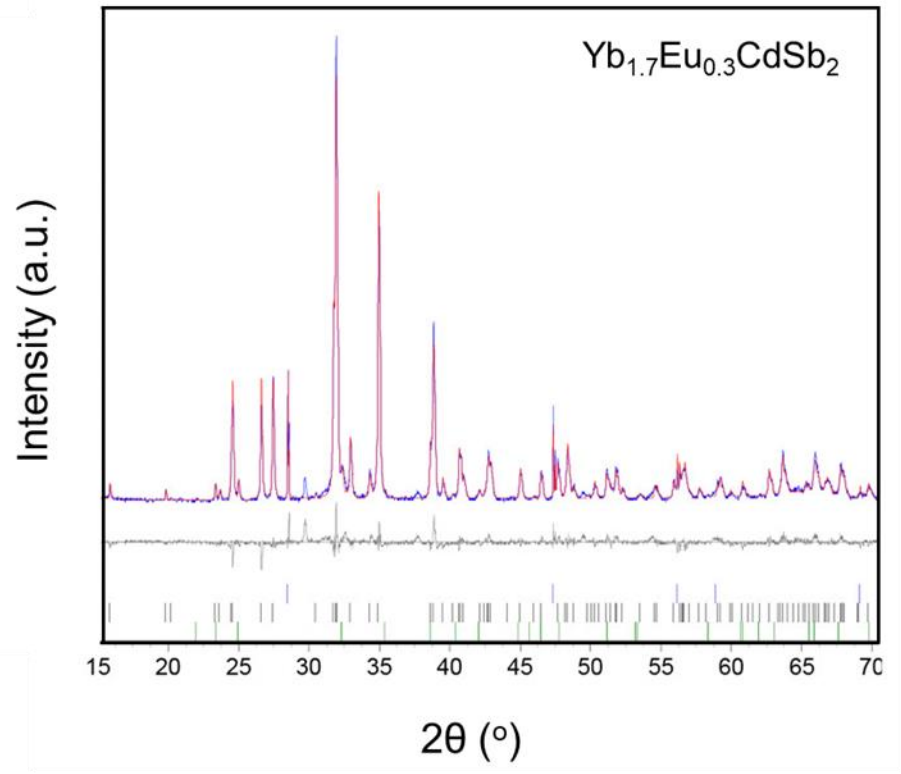


Figure 2-17. Backscattered electron SEM micrographs (top left), secondary electron SEM micrographs (bottom left), and EDS elemental maps (green: Yb, red: Eu, blue: Cd, pink: Sb) for $Yb_{2-x}Eu_xCdSb_2$, x = 0.3, 0.4 and 0.5.


Yb2CdSb2
Intensity (a.u.)
15 20 25 30 35 40 45 50 55 60 65 70
2θ (°)


Yb1.9Eu0.1CdSb2
Intensity (a.u.)
15 20 25 30 35 40 45 50 55 60 65 70
2θ (°)


$Yb_{1.8}Eu_{0.2}CdSb_2$
Intensity (a.u.)
15 20 25 30 35 40 45 50 55 60 65 70
2θ (°)


$Yb_{1.7}Eu_{0.3}CdSb_2$
Intensity (a.u.)
15 20 25 30 35 40 45 50 55 60 65 70
2θ (°)

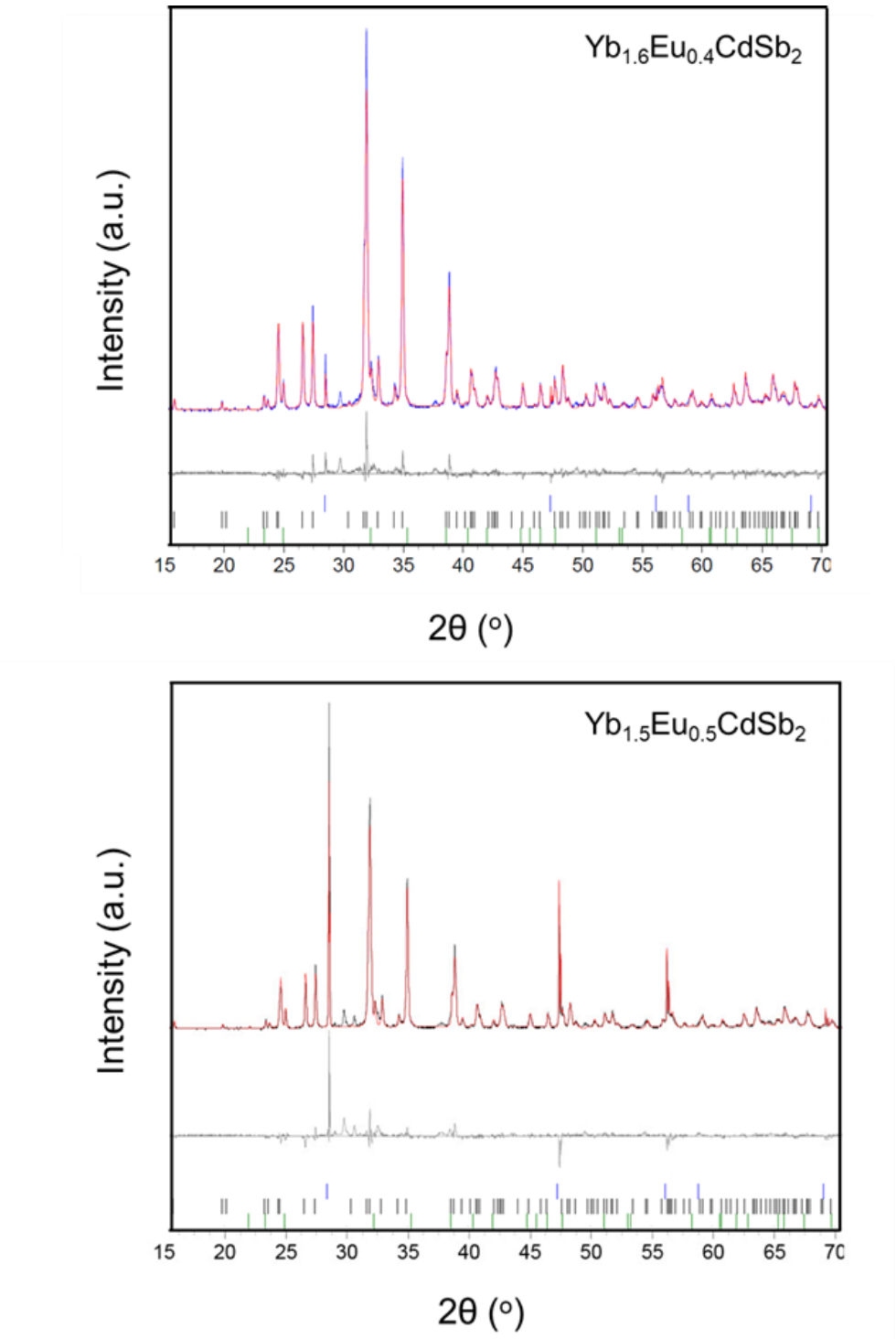
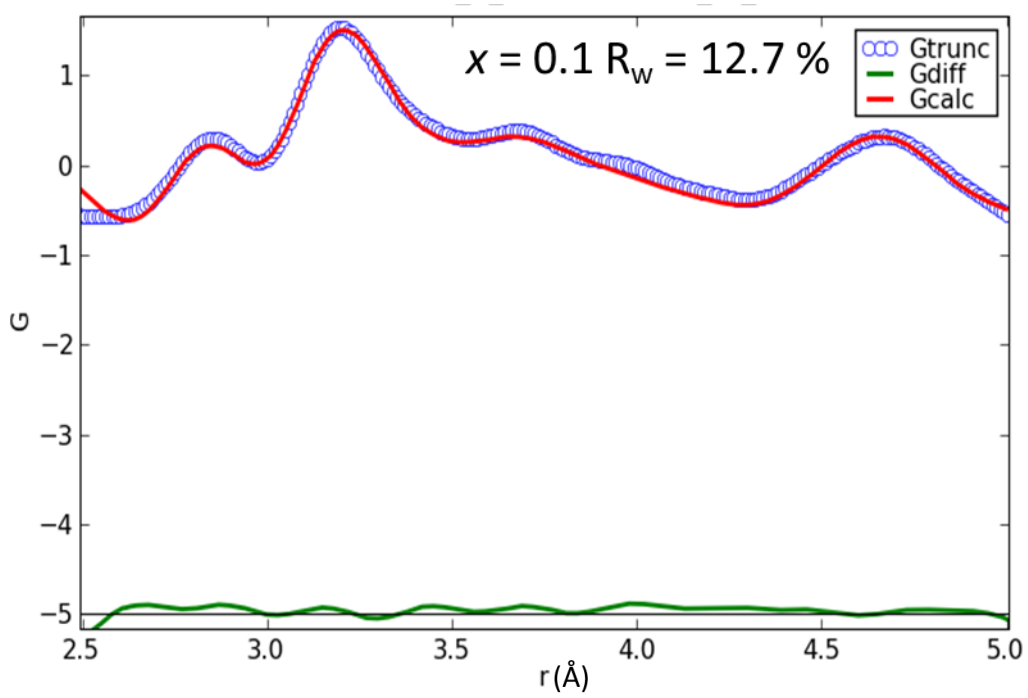
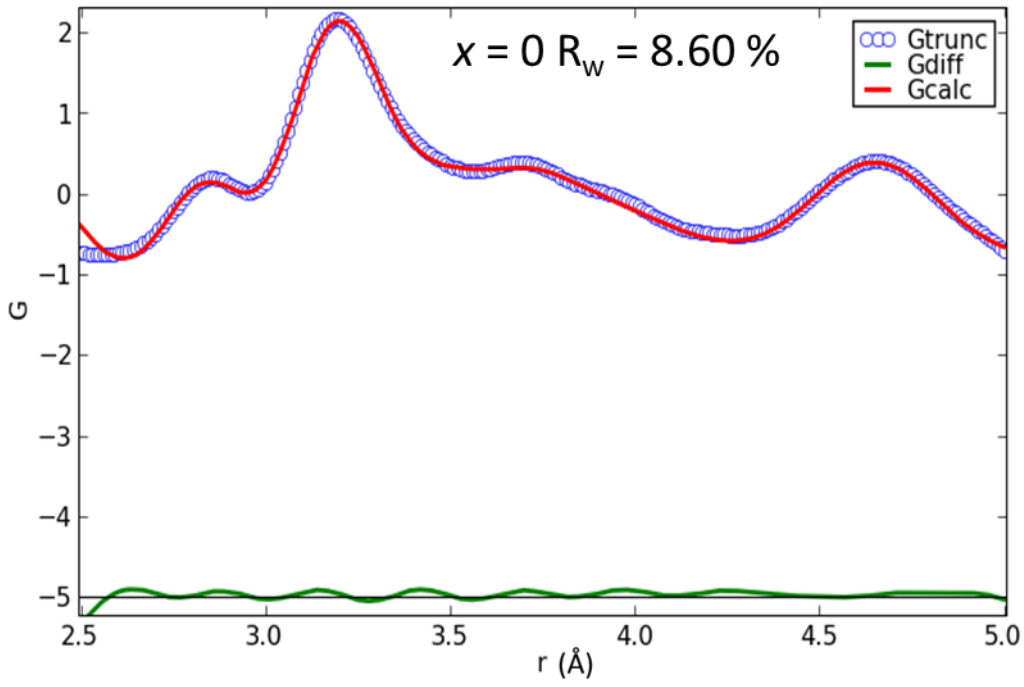


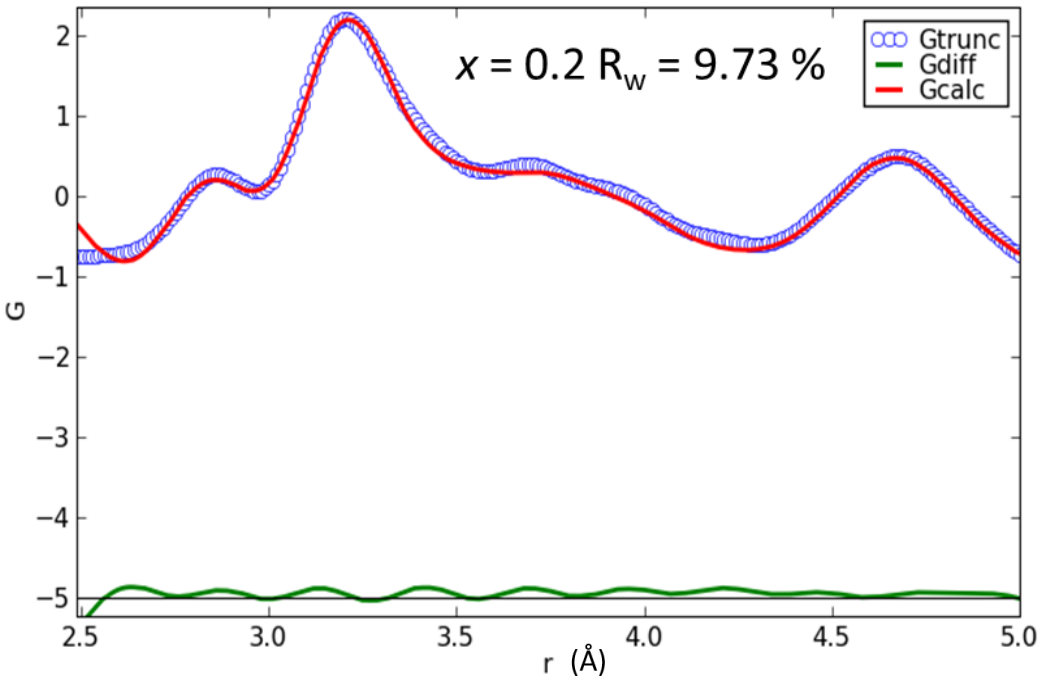
Figure 2-18. Rietveld refinements for $Yb_{2-x}Eu_xCdSb_2$. Experimental data are in blue, calculated in red, and difference in gray. Tick marks give the expected peak positions for the Si standard (blue/top) $Yb_{2-x}Eu_xCdSb_2$ (black/middle) and $YbCd_2Sb_2$ (green/bottom).

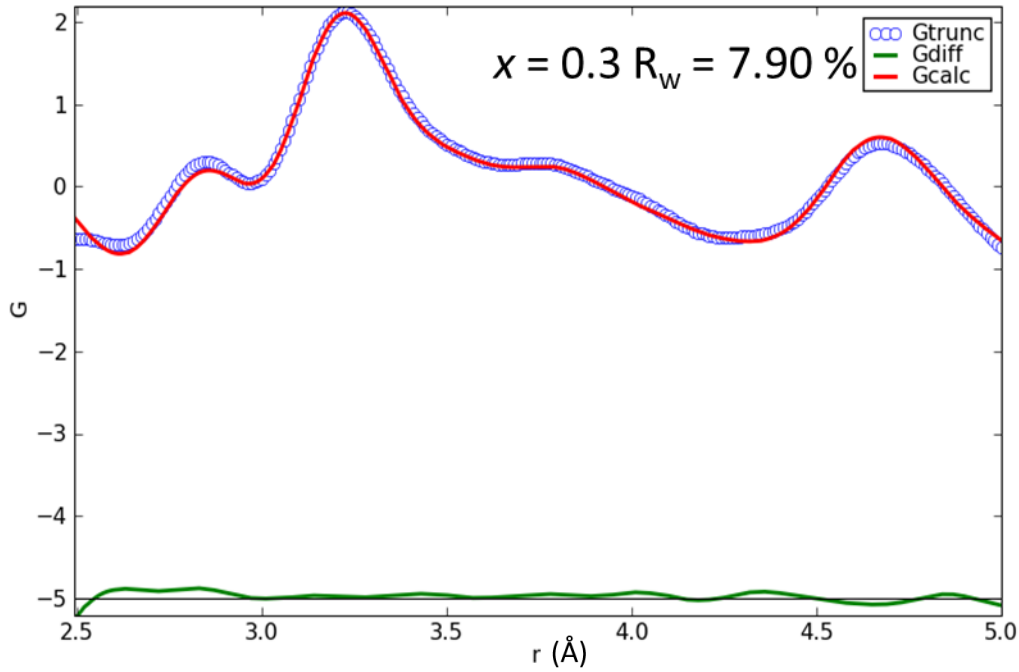
Table 2-4. Statistics from Rietveld refinements

x		Yb_2CdSb_2	$Yb_{1.9}Eu_{0.1}CdSb_2$	$Yb_{1.8}Eu_{0.2}CdSb_2$	$Yb_{1.7}Eu_{0.3}CdSb_2$	$Yb_{1.6}Eu_{0.4}CdSb_2$	$Yb_{1.5}Eu_{0.5}CdSb_2$
Unit Cell Parameters	*a*	4.6199(2)	4.6264(2)	4.6304(2)	4.6392(1)	4.6393(1)	4.6451(2)
	b	17.4439(9)	17.4903(7)	17.5353(7)	17.6147(5)	17.6217(5)	17.6676(7)
	c	7.2466(3)	7.2443(3)	7.2508(3)	7.2531(2)	7.2574(2)	7.2620(3)
	V	583.99(5)	586.18(4)	588.73(4)	592.72(3)	593.31(3)	595.98(4)
Rp (%), Rwp (%)		11.98, 16.32	11.58, 15.75	11.44, 15.65	10.08, 13.69	9.51, 12.95	11.24, 16.14
$Yb_{2-x}Eu_xCdSb_2$ (wt %)		66.73	66.37	56.26	79.05	87.77	54.89
$YbCd_2Sb_2$ (wt %)		4.91	1.83	3.96	3.79	6.7	3.2
Si (wt %)		28.36	31.81	39.78	17.17	5.53	41.91


x = 0.1 Rw = 12.7 %
Gtrunc
Gdiff
Gcalc
G
r (Å)


x = 0 Rw = 8.60 %
Gtrunc
Gdiff
Gcalc
G
r (Å)


x = 0.2 Rw = 9.73 %
Gtrunc
Gdiff
Gcalc
G
r (Å)


x = 0.3 Rw = 7.90 %
Gtrunc
Gdiff
Gcalc
G
r (Å)

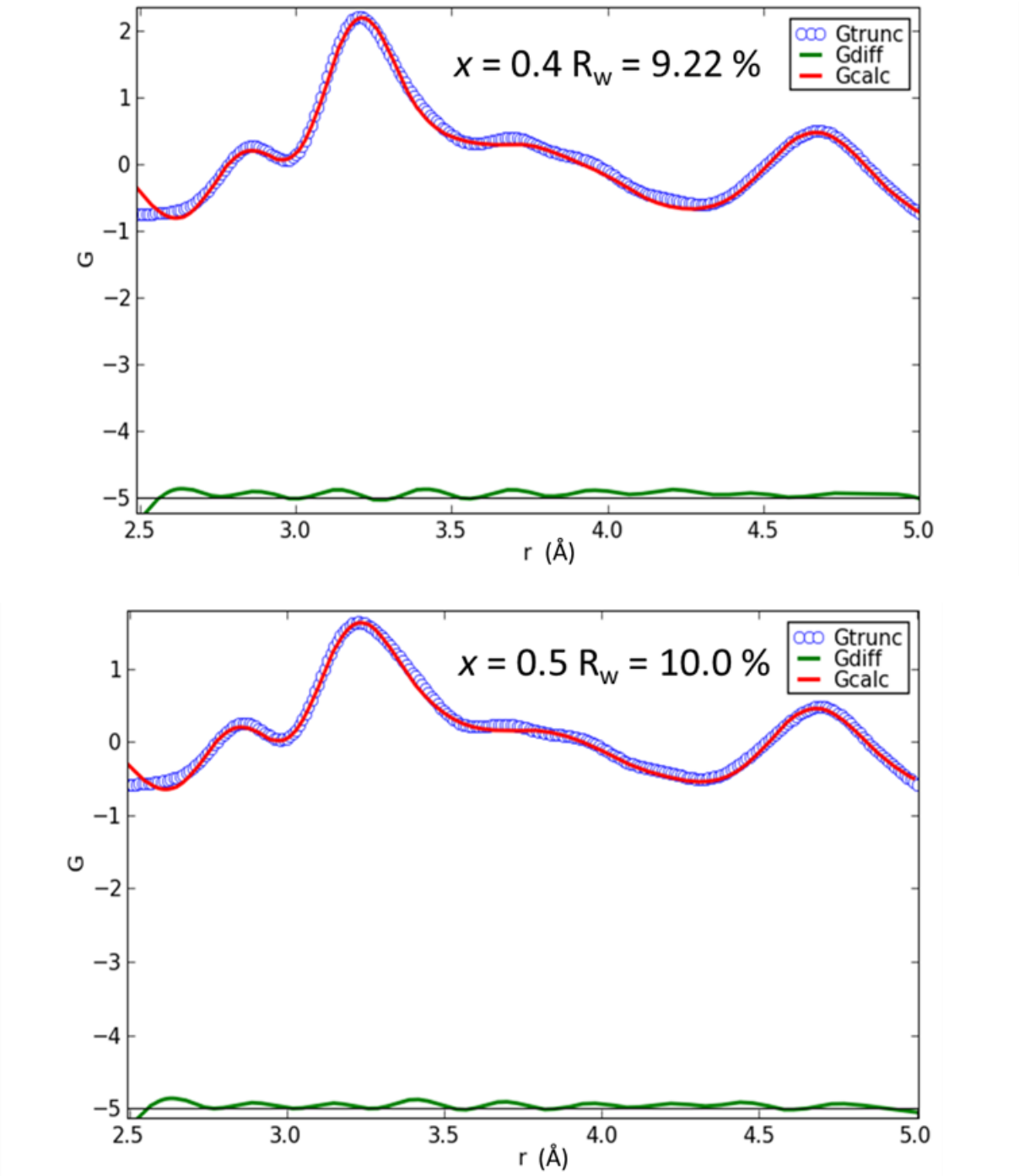
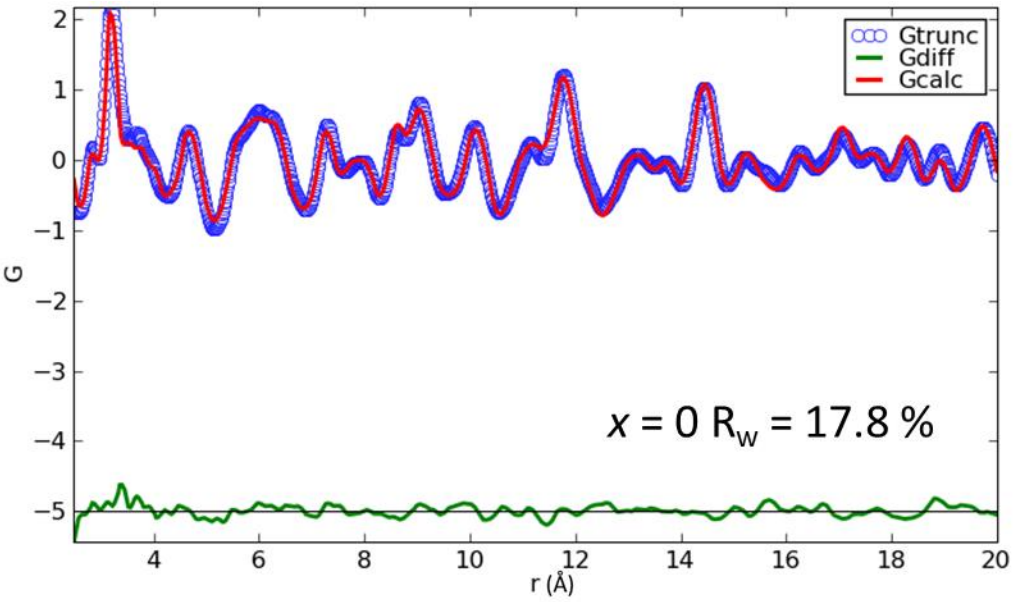
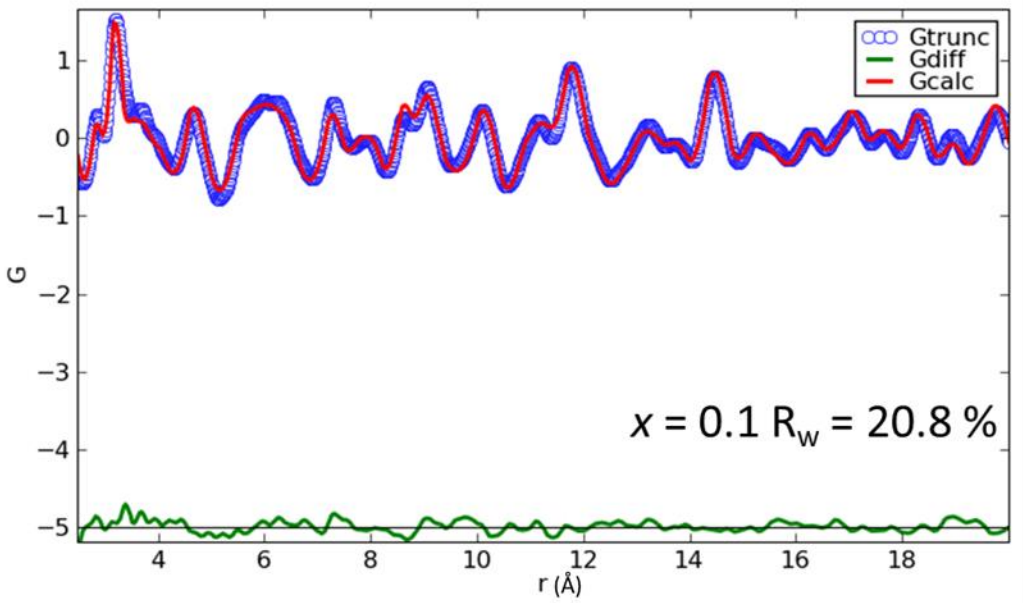
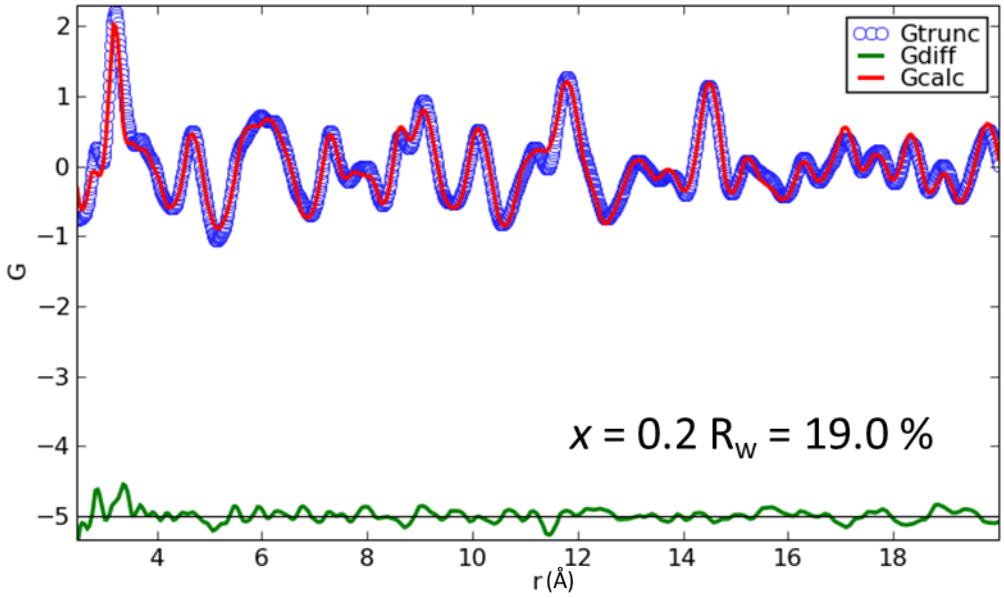
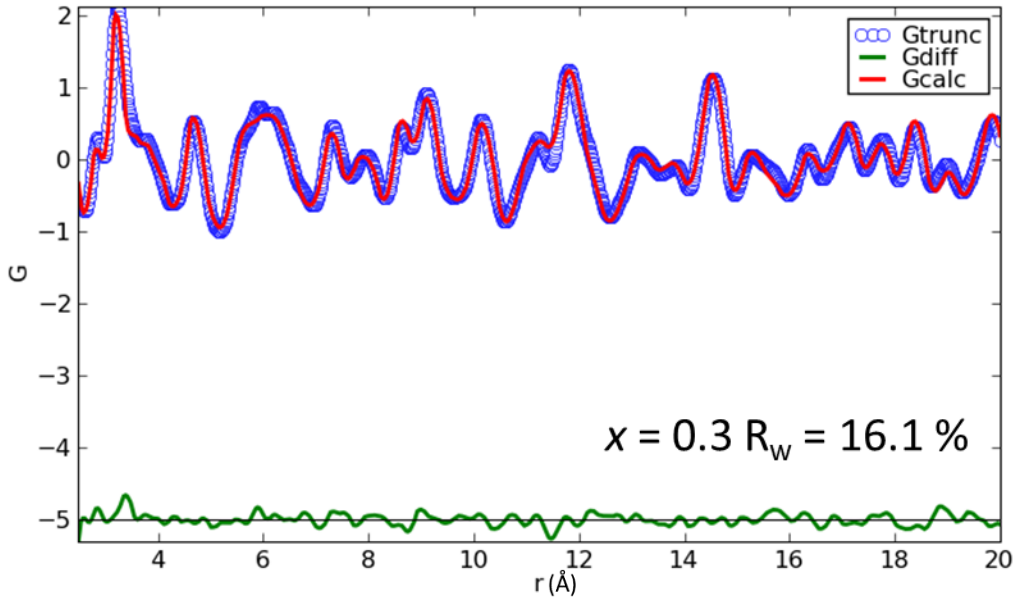


Figure 2-19. PDFGui refinements for $Yb_{2-x}Eu_xCdSb_2$ from r = 2.5 to 5 Å. Experimental data are in blue, calculated in red, and difference in green.


Gtrunc
Gdiff
Gcalc
G
r (Å)
x = 0 Rw = 17.8 %


Gtrunc
Gdiff
Gcalc
G
r (Å)
x = 0.1 Rw = 20.8 %


Gtrunc
Gdiff
Gcalc
G
r (Å)
x = 0.2 Rw = 19.0 %


Gtrunc
Gdiff
Gcalc
G
r (Å)
x = 0.3 Rw = 16.1 %

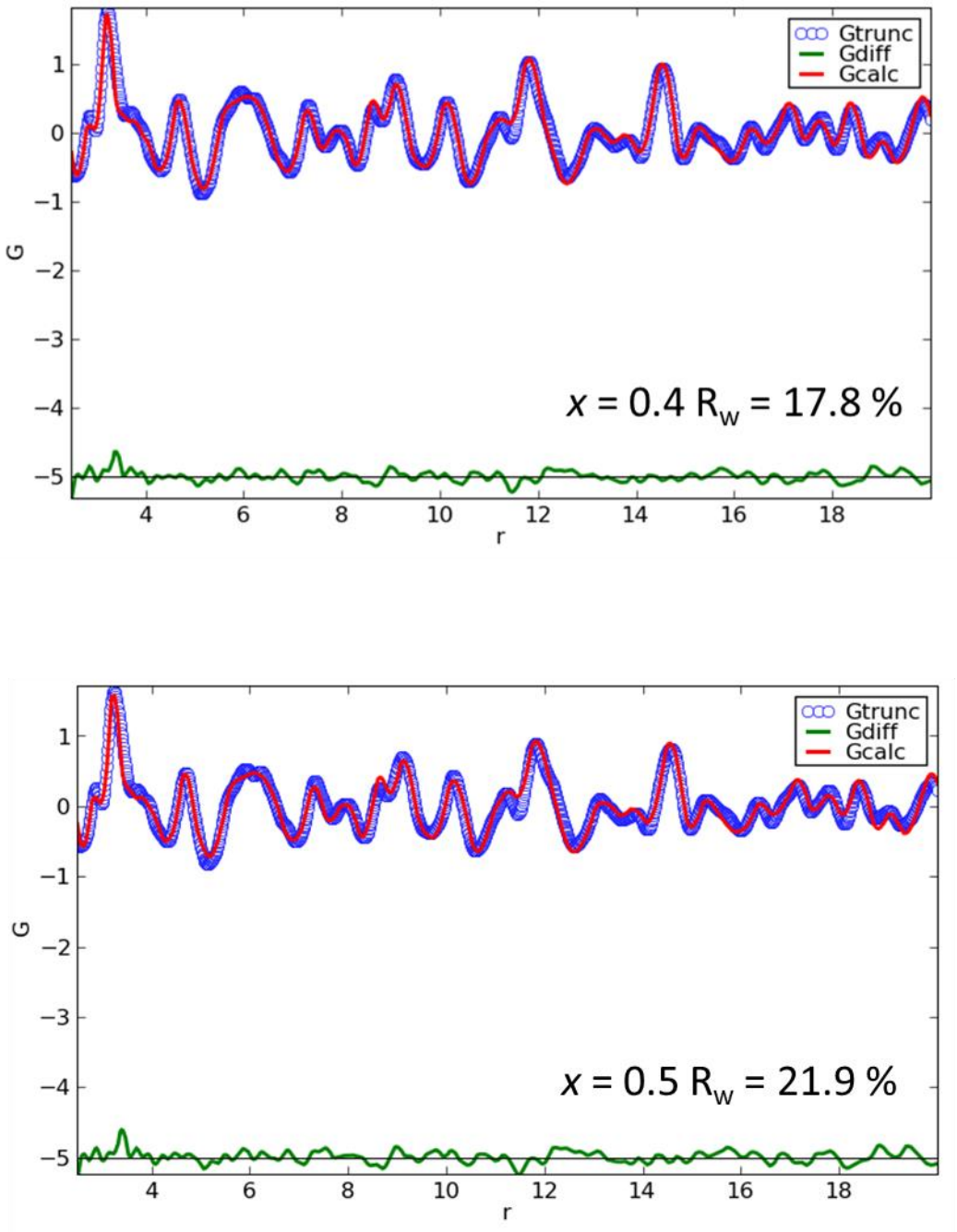


Figure 2-20. PDFGui refinements for $Yb_{2-x}Eu_xCdSb_2$ from r = 2.5 to 20 Å. Experimental data are in blue, calculated in red, and difference in green.

2.8 References

(1) Fleurial, J. P. Thermoelectric Power Generation Materials: Technology and Application Opportunities. *J. Miner. Met. Mater. Soc.* **2009**, *61* (4), 79–85. https://doi.org/10.1007/s11837-009-0057-z.

(2) Fleurial, J.-P.; Borshchevsky, A.; Caillat, T.; Ewe11, R. New Materials and Devices for Thermoelectric Applications. In *Proceedings of the Intersociety Energy Conversion Engineering Conference*; 1997; pp 1080–1085.

(3) Liu, K. F.; Xia, S. Q. Recent Progresses on Thermoelectric Zintl Phases: Structures, Materials and Optimization. *J. Solid State Chem.* **2019**, *270* (November 2018), 252–264. https://doi.org/10.1016/j.jssc.2018.11.030.

(4) Lee, K. H.; Kim, J. Y.; Choi, S. M. Recent Progress in Bi-Te-Based Thermoelectric Materials. *J. Korean Ceram. Soc.* **2015**, *52* (1), 1–8. https://doi.org/10.4191/kcers.2015.52.1.1.

(5) Shuai, J.; Mao, J.; Song, S.; Zhang, Q.; Chen, G.; Ren, Z. Recent Progress and Future Challenges on Thermoelectric Zintl Materials. *Mater. Today Phys.* **2017**, *1*, 74–95. https://doi.org/10.1016/J.MTPHYS.2017.06.003.

(6) Snyder, G. J.; Toberer, E. S. Complex Thermoelectric Materials. *Mater. Sustain. Energy A Collect. Peer-Reviewed Res. Rev. Artic. from Nat. Publ. Gr.* **2010**, *7* (February), 101–110. https://doi.org/10.1142/9789814317665_0016.

(7) Perez, C. J.; Wood, M.; Ricci, F.; Yu, G.; Vo, T.; Bux, S. K.; Hautier, G.; Rignanese, G.-M.;

Snyder, G. J.; Kauzlarich, S. M. Discovery of Multivalley Fermi Surface Responsible for the High Thermoelectric Performance in $Yb_{14}MnSb_{11}$ and $Yb_{14}MgSb_{11}$. *Sci. Adv.* **2021**, *7* (4). https://doi.org/10.1126/sciadv.abe9439.

(8) Yao, H.; Chen, C.; Xue, W.; Bai, F.; Cao, F.; Lan, Y.; Liu, X.; Wang, Y.; Singh, D. J.; Lin, X.; Zhang, Q. Vacancy Ordering Induced Topological Electronic Transition in Bulk Eu_2ZnSb_2. *Sci. Adv.* **2021**, *7* (6), 1–7. https://doi.org/10.1126/sciadv.abd6162.

(9) Chen, C.; Xue, W.; Li, S.; Zhang, Z.; Li, X.; Wang, X.; Liu, Y.; Sui, J.; Liu, X.; Cao, F.; Ren, Z.; Chu, C.-W.; Wang, Y.; Zhang, Q. Zintl-Phase Eu_2ZnSb_2: A Promising Thermoelectric Material with Ultralow Thermal Conductivity. *Proc. Natl. Acad. Sci.* **2019**, *116* (8), 2831–2836. https://doi.org/10.1073/PNAS.1819157116.

(10) Chanakian, S.; Uhl, D.; Neff, D.; Drymiotis, F.; Park, J.; Petkov, V.; Zevalkink, A.; Bux, S. Exceptionally High Electronic Mobility in Defect-Rich $Eu_2ZnSb_{2-x}Bi_x$ Alloys. *J. Mater. Chem. A* **2020**, *8* (12), 6004–6012. https://doi.org/10.1039/c9ta14170g.

(11) Cooley, J. A.; Promkhan, P.; Gangopadhyay, S.; Donadio, D.; Pickett, W. E.; Ortiz, B. R.; Toberer, E. S.; Kauzlarich, S. M. High Seebeck Coefficient and Unusually Low Thermal Conductivity Near Ambient Temperatures in Layered Compound $Yb_{2-x}Eu_xCdSb_2$. *Chem. Mater.* **2018**, *30* (2), 484–493. https://doi.org/10.1021/acs.chemmater.7b04517.

(12) Zevalkink, A.; Zeier, W. G.; Cheng, E.; Snyder, J.; Fleurial, J. P.; Bux, S. Nonstoichiometry in the Zintl Phase $Yb_{1-\delta}Zn_2Sb_2$ as a Route to Thermoelectric Optimization. *Chem. Mater.* **2014**, *26* (19), 5710–5717. https://doi.org/10.1021/cm502588r.

(13) Lin, J.; Li, X.; Qiao, G.; Wang, Z.; Carrete, J.; Ren, Y.; Ma, L.; Fei, Y.; Yang, B.; Lei, L.; Li, J. Unexpected High-Temperature Stability of β-Zn_4Sb_3 Opens the Door to Enhanced Thermoelectric Performance. *J. Am. Chem. Soc.* **2014**, *136* (4), 1497–1504. https://doi.org/10.1021/ja410605f.

(14) Caillat, T.; Fleurial, J. P.; Borshchevsky, A. Preparation and Thermoelectric Properties of Semiconducting Zn_4Sb_3. *J. Phys. Chem. Solids* **1997**, *58* (7), 1119–1125. https://doi.org/10.1016/S0022-3697(96)00228-4.

(15) Toberer, E. S.; Rauwel, P.; Gariel, S.; Taftø, J.; Snyder, G. J. Composition and the Thermoelectric Performance of β-Zn_4Sb_3. *J. Mater. Chem* **2010**, *20*, 9877–9885. https://doi.org/10.1039/c0jm02011g.

(16) Perumal, S.; Roychowdhury, S.; Biswas, K. High Performance Thermoelectric Materials and Devices Based on GeTe. *J. Mater. Chem. C* **2016**, *4*, 7520. https://doi.org/10.1039/c6tc02501c.

(17) Ovchinnikov, A.; Bobev, S. Zintl Phases with Group 15 Elements and the Transition Metals: A Brief Overview of Pnictides with Diverse and Complex Structures. *J. Solid State Chem.* **2019**, *270*, 346–359. https://doi.org/10.1016/j.jssc.2018.11.029.

(18) Xia, S. Q.; Bobev, S. Cation-Anion Interactions as Structure Directing Factors: Structure and Bonding of Ca_2CdSb_2 and Yb_2CdSb_2. *J. Am. Chem. Soc.* **2007**, *129* (13), 4049–4057. https://doi.org/10.1021/ja069261k.

(19) Kim, K.; Lee, J.; Shin, S.; Jo, H.; Moon, D.; Ok, K. M.; You, T.-S. Chemical Driving Force for Phase-Transition in the $Ca_{2-x}RE_xCdSb_2$ (RE = Yb, Eu; 0.11(1) ≤ x ≤ 1.36(2)) System. *Cryst. Growth Des.* **2020**, *20* (2), 746–754. https://doi.org/10.1021/acs.cgd.9b01154.s001.

(20) P. Devlin, K.; Chen, S.; Donadio, D.; M. Kauzlarich, S. Solid Solution $Yb_{2-x}Ca_xCdSb_2$: Structure, Thermoelectric Properties, and Quality Factor. *Inorg. Chem.* **2021**, *60* (17), 13596–13606. https://doi.org/10.1021/acs.inorgchem.1c01906.

(21) Pomrehn, G. S.; Zevalkink, A.; Zeier, W. G.; Van De Walle, A.; Snyder, G. J. Defect-Controlled Electronic Properties in AZn_2Sb_2 Zintl Phases. *Angew. Chemie - Int. Ed.* **2014**, *53* (13), 3422–3426. https://doi.org/10.1002/anie.201311125.

(22) Qu, J.; Balvanz, A.; Baranets, S.; Bobev, S.; Gorai, P. Computational Design of Thermoelectric Alloys through Optimization of Transport and Dopability. *Mater. Horizons* **2022**, *9* (2), 720–730. https://doi.org/10.1039/d1mh01539g.

(23) Ogunbunmi, M. O.; Baranets, S.; Bobev, S. Structural Complexity and Tuned Thermoelectric Properties of a Polymorph of the Zintl Phase Ca_2CdSb_2 with a Non-Centrosymmetric Monoclinic Structure. *Inorg. Chem.* **2022**, *61* (28), 10888–10897. https://doi.org/10.1021/ACS.INORGCHEM.2C01354.

(24) Zhang, J.; Song, L.; Iversen, B. B. Insights into the Design of Thermoelectric Mg_3Sb_2 and Its Analogs by Combining Theory and Experiment. *Npj Comput. Mater.* **2019**, *5* (76), 1–15. https://doi.org/10.1038/s41524-019-0215-y.

(25) Zhang, J.; Song, L.; Sist, M.; Tolborg, K.; Iversen, B. B. Chemical Bonding Origin of the Unexpected Isotropic Physical Properties in Thermoelectric Mg3Sb2 and Related Materials. *Nat. Commun.* **2018**, *9* (1), 4716. https://doi.org/10.1038/s41467-018-06980-x.

(26) Cao, Q.-G.; Zhang, H.; Tang, M.-B. Zintl Phase with Tunable Thermoelectric Properties Induced by Cation Substitution. *J. Appl. Phys* **2010**, *107*, 53714. https://doi.org/10.1063/1.3327443.

(27) Alemneh Wubieneh, T.; Wei, P.; Yeh, C.; Chen, S.; Chen, Y. Thermoelectric Properties of Zintl Phase Compounds of $Ca_{1-x}Eu_xZn_2Sb_2$ ($0 \le x \le 1$). *J. Electron. Mater.* **2016**, *45*, 1942–1946. https://doi.org/10.1007/s11664-015-4303-6.

(28) Zhang, H.; Fang, L.; Tang, M.-B.; Man, Z. Y.; Chen, H. H.; Yang, X. X.; Baitinger, M.; Grin, Y.; Zhao, J.-T. Thermoelectric Properties of $Yb_xEu_{1-x}Cd_2Sb_2$. *J. Chem. Phys.* **2010**, *133* (19), 194701. https://doi.org/10.1063/1.3501370.

(29) Devlin, K. P.; Chen, S.; Donadio, D.; Kauzlarich, S. M. Solid Solution $Yb_2Ca_xCdSb_2$: Structure, Thermoelectric Properties, and Quality Factor. *Inorg. Chem.* **2021**, *60* (17), 13596–13606. https://doi.org/10.1021/acs.inorgchem.1c01906.

(30) Saparov, B.; Saito, M.; Bobev, S. Syntheses, and Crystal and Electronic Structures of the New Zintl Phases Na_2ACdSb_2 and K_2ACdSb_2 (A=Ca, Sr, Ba, Eu, Yb): Structural Relationship with Yb_2 $CdSb_2$ and the Solid Solutions Sr<sub. *J. Solid State Chem.* **2011**, *184* (2), 432–440. https://doi.org/10.1016/j.jssc.2010.12.015.

(31) Canfield, P. C.; Kong, T.; Kaluarachchi, U. S.; Jo, N. H. Use of Frit-Disc Crucibles for Routine and Exploratory Solution Growth of Single Crystalline Samples. *Philos. Mag.* **2016**, *96* (1), 84–92. https://doi.org/10.1080/14786435.2015.1122248.

(32) Bruker AXS. TOPAS Version 5, 2014.

(33) Toby, B. H.; Von Dreele, R. B. GSAS-II: The Genesis of a Modern Open-Source All Purpose Crystallography Software Package. *J. Appl. Crystallogr.* **2013**, *46* (2), 544–549. https://doi.org/10.1107/S0021889813003531.

(34) Zhou, X.-J.; Tao, J.-Z.; Guo, H.; Lin, H. Atomic Pair Distribution Function Method Development at the Shanghai Synchrotron Radiation Facility Temperature Dependent Total Scattering Structural Study of CaCu3Ti4O12. *Chinese Phys. B* **2017**, *26* (7), 076101. https://doi.org/10.1088/0953-8984/19/33/335219.

(35) Iwanaga, S.; Toberer, E. S.; Lalonde, A.; Snyder, G. J. A High Temperature Apparatus for Measurement of the Seebeck Coefficient. *Rev. Sci. Instrum.* **2011**, *82* (6). https://doi.org/10.1063/1.3601358.

(36) Borup, K. A.; Toberer, E. S.; Zoltan, L. D.; Nakatsukasa, G.; Errico, M.; Fleurial, J.-P.; Iversen, B. B. Measurement of the Electrical Resistivity and Hall Coefficient at High Temperatures. *Rev. Sci. Instrum* **2012**, *83* (123902), 123902. https://doi.org/10.1063/1.4770124.

(37) Borup, K. A.; de Boor, J.; Wang, H.; Drymiotis, F.; Gascoin, F.; Shi, X.; Chen, L.; Fedorov, M.

I.; Eckhard, M.; Bo Iversen, B.; Jeffrey Snyder, G. Measuring Thermoelectric Transport Properties of Materials Energy & Environmental Science REVIEW. *423 Energy Environ. Sci* **2015**, *8*, 423–435. https://doi.org/10.1039/c4ee01320d.

(38) Ovchinnikov, A.; Darone, G. M.; Saparov, B.; Bobev, S. Exploratory Work in the Quaternary System of Ca-Eu-Cd-Sb: Synthesis, Crystal, and Electronic Structures of New Zintl Solid Solutions. *Materials (Basel).* **2018**, *11* (11), 1–13. https://doi.org/10.3390/ma11112146.

(39) Lee, J.; Ahn, K.; Kim, K.; Jo, H.; Yoon, J. S.; Moon, D.; Weon, ⊥; Shin, H.; Kang, ‖; Ok, M.; You, T.-S. Effect of Rare-Earth Metals Substitution for Ca on the Crystal Structure and Thermoelectric Properties of the $Ca_{10-x}RE_xSb_{10-y}$ System. *Growth Des* **2019**, *19*, 3498–3508. https://doi.org/10.1021/acs.cgd.9b00368.

(40) Gorai, P.; Goyal, A.; Toberer, E. S.; Stevanović, V. A Simple Chemical Guide for Finding Novel N-Type Dopable Zintl Pnictide Thermoelectric Materials. *J. Mater. Chem. A* **2019**, *7* (33), 19385–19395. https://doi.org/10.1039/c9ta03786a.

(41) Balvanz, A.; Qu, J.; Baranets, S.; Ertekin, E.; Gorai, P.; Bobev, S. New N-Type Zintl Phases for Thermoelectrics: Discovery, Structural Characterization, and Band Engineering of the Compounds A_2CdP_2 (A = Sr, Ba, Eu). *Cite This Chem. Mater* **2020**, *32*, 10697–10707. https://doi.org/10.1021/acs.chemmater.0c03960.

(42) Kazem, N.; Zaikina, J. V; Ohno, S.; Snyder, G. J.; Kauzlarich, S. M. Coinage-Metal-Stuffed Eu9Cd4Sb9 : Metallic Compounds with Anomalous Low Thermal Conductivities. *Chem.*

Mater **2015**, *27* (21), 7508–7519. https://doi.org/10.1021/acs.chemmater.5b03808.

(43) Snyder, G. J.; Snyder, A. H.; Wood, M.; Gurunathan, R.; Snyder, B. H.; Niu, C. Weighted Mobility. *Adv. Mater.* **2020**, *32* (2001537), 1–5. https://doi.org/10.1002/adma.202001537.

(44) Xia, S.; Bobev, S. Cation−Anion Interactions as Structure Directing Factors: Structure and Bonding of Ca_2CdSb_2 and Yb_2CdSb_2. *J. Am. Chem. Soc.* **2007**, *129* (13), 4049–4057. https://doi.org/10.1021/ja069261k.

(45) May, A. F.; Snyder, G. J. Introduction to Modeling Thermoelectric Transport at High Temperatures. In *Materials, Preparation, and Characterization in Thermoelectrics*; CRC Press, 2017; p 11.

(46) Liu, G.; Zhou, J.; Wang, H. Anisotropic Thermal Expansion of SnSe from First-Principles Calculations Based on Grü Neisen's Theory. *Phys. Chem. Chem. Phys* **2017**, *19*, 15187. https://doi.org/10.1039/c7cp00815e.

(47) Liu, F.; Parajuli, P.; Rao, R.; Wei, P. C.; Karunarathne, A.; Bhattacharya, S.; Podila, R.; He, J.; Maruyama, B.; Priyadarshan, G.; Gladden, J. R.; Chen, Y. Y.; Rao, A. M. Phonon Anharmonicity in Single-Crystalline SnSe. *Phys. Rev. B* **2018**, *98* (22), 224309. https://doi.org/10.1103/PhysRevB.98.224309.

(48) Li, C. W.; Hong, J.; May, A. F.; Bansal, D.; Chi, S.; Hong, T.; Ehlers, G.; Delaire, O. Orbitally Driven Giant Phonon Anharmonicity in SnSe. *Nat. Phys.* **2015**, *11* (12), 1063–1069.

https://doi.org/10.1038/nphys3492.

(49) Zhang, Y. First-Principles Debye–Callaway Approach to Lattice Thermal Conductivity. *J. Mater.* **2016**, *2* (3), 237–247. https://doi.org/10.1016/j.jmat.2016.06.004.

(50) René De Cotret, L. P.; Otto, M. R.; Pöhls, J.-H.; Luo, Z.; Kanatzidis, M. G.; Siwick, B. J. Direct Visualization of Polaron Formation in the Thermoelectric SnSe. *Proc. Natl. Acad. Sci.* **2022**, *119* (2). https://doi.org/10.1073/pnas.2113967119/-/DCSupplemental.

(51) Kim, H. S.; Gibbs, Z. M.; Tang, Y.; Wang, H.; Snyder, G. J. Characterization of Lorenz Number with Seebeck Coefficient Measurement. *APL Mater.* **2015**, *3* (4), 1–6. https://doi.org/10.1063/1.4908244.

(52) Zevalkink, A.; Smiadak, D. M.; Blackburn, J. L.; Ferguson, A. J.; Chabinyc, M. L.; Delaire, O.; Wang, J.; Kovnir, K.; Martin, J.; Schelhas, L. T.; Sparks, T. D.; Kang, S. D.; Dylla, M. T.; Snyder, G. J.; Ortiz, B. R.; Toberer, E. S. A Practical Field Guide to Thermoelectrics: Fundamentals, Synthesis, and Characterization. *Appl. Phys. Rev.* **2018**, *5* (2), 021303. https://doi.org/10.1063/1.5021094.

(53) Perez, C. J.; Chen, Z.; Beeson, W. B.; Chanakian, S.; Liu, K.; Bux, S. K.; Kauzlarich, S. M. Chemical Route to Yb14MgSb11 Composites with Nanosized Iron Inclusions for the Reduction of Thermal Conductivity. *ACS Appl. Energy Mater.* **2021**, *4* (4), 3748–3756. https://doi.org/https://doi.org/10.1021/ACSAEM.1C00163.

(54) Li, B.; Firdosy, S.; Paik, J. A.; Huang, C. K.; Cheng, B.; Gogna, P.; Nakatsukasa, G.; Caillat,

T.; Fleurial, J. P.; Ravi, V.; Nesmith, B.; Ewell, R.; Brandon, E. J. Development of New High Temperature Power Generating Couples for the Advanced Thermoelectric Converter (ATEC). *8th Annu. Int. Energy Convers. Eng. Conf.* **2010**, No. July 2010, 1–7. https://doi.org/10.2514/6.2010-7004.

Chapter 3: Thermoelectric properties of $Ba_{2-x}Eu_xZnSb_2$, a Zintl phase with one-dimensional covalent chains

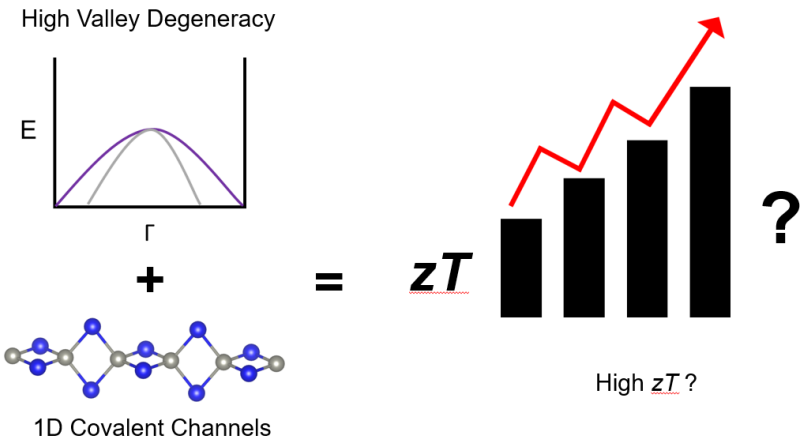
Ashlee K. Hauble, [1] Kamil Ciesielski,[2] Valentin Taufour, [3] Eric S. Toberer,[2] and Susan M. Kauzlarich[1]

Affiliations

[1]Department of Chemistry, University of California, One Shields Ave, Davis, California 95616, United States

[2]Department of Physics, Colorado School of Mines, 1500 Illinois St, Golden, CO 80401, United States

[3]Department of Physics and Astronomy, University of California, One Shields Avenue, Davis, California 95616, United States



3.1 Abstract

Thermoelectric generators could drastically reduce greenhouse gas emissions by converting waste heat to electricity. To realize this ideal, higher efficiency thermoelectric materials need to be designed—a challenging problem due to the interrelated nature of the key electronic properties, Seebeck coefficient and electrical resistivity. One method of simultaneously improving the Seebeck coefficient and electrical resistivity is to take advantage of highly anisotropic, low-dimensional bonding schemes in which one crystallographic direction has light effective mass and another direction has heavy effective mass. An example of this type of material is Ba_2ZnSb_2 a Zintl phase that possesses one-dimensional covalent chains and high valley degeneracy at the valence band maximum. Theoretical studies on *p*-type Ba_2ZnSb_2 have predicted $zT > 2$ at 900 K. Using theory to guide the experimental work, polycrystalline $Ba_{2-x}Eu_xZnSb_2$ (x = 0.2, 0.3, 0.4) samples were synthesized from binary precursors and

thermoelectric properties were measured. Samples showed low thermal conductivity and high Seebeck coefficient and predictions suggest that higher *zT* can be attained if carrier concentration can be increased via doping.

3.2 Introduction

Thermoelectric generators have the potential to alter the world's energy landscape by converting heat to usable electricity, which could reduce greenhouse gas emissions and dependence on fossil fuels. To make this possible, materials with high thermoelectric figure of merit, $zT = (S^2T)/\kappa\rho$ (where S is the Seebeck coefficient, T is the operating temperature, κ is thermal conductivity, and ρ is electrical resistivity), need to be designed. Zintl phases are a class of intermetallic compounds that is well suited to this application, given the rich structural chemistry that can result from the combination of ionic and covalent bonding found in these materials.[1] The primary challenge in designing a thermoelectric material is to simultaneously improve these three properties, a task that is difficult due to the interrelated nature of S, ρ, and the electronic component of κ. [2–4]

One method of optimizing both the Seebeck coefficient (S), and resistivity (ρ) simultaneously is to look for materials containing anisotropic bonding schemes that provide a favorable a Seebeck coefficient in one crystallographic direction and resistivity in another. Some anisotropic layered and low-dimensional materials have been shown to be promising candidates for thermoelectric applications because they decouple the Seebeck and electrical resistivity effective masses, with the electrical resistivity being governed by the light mass in one

crystallographic direction, while the Seebeck coefficient is controlled by the average mass.[5–8] Examples of this strategy include layered materials with A_2MPn_2 stoichiometry and materials containing 1D tetrahedral chains, such as the A_3MPn_3 and $A_5M_2Pn_6$ families of compounds have demonstrated competitive *zT*s due to their high charge carrier mobilities and Seebeck coefficients.[9–17]

Ba_2ZnSb_2 is a Zintl phase with infinite chains of 1D edge-shared $[ZnSb_{4/2}]^{4-}$ tetrahedra that are structurally similar to the corner-shared infinite tetrahedral chains in $Ca_5Al_2Sb_6$ compounds, the discrete corner-shared chains in Ca_3AlSb_3, and the isolated edge-shared chains in Sr_3AlSb_3.[3,18,19] These covalent chains can form channels that transport charge and result in high mobility, which is good for thermoelectric performance. Motivated by these structural motifs, theoretical investigations of the thermoelectric properties and electronic structure of p-type Ba_2ZnSb_2 revealed an anisotropic Fermi surface with high valley degeneracy ($N_v = 4$), low lattice thermal conductivity, and predicted an average $zT > 1$, with $zT > 2$ in the *z*-direction at 900 K.[5,18,20] The two bands at the edge of the valence band are flat and heavy, which give rise to a high Seebeck coefficient, while two that are just below are lighter bands that are expected to result in high charge carrier mobility and low electrical resistivity.[5,18]

The synthesis, characterization, and experimental thermoelectric properties for $Ba_{2-x}Eu_xZnSb_2$ ($x = 0.2, 0.3, 0.4$) is reported. Small amounts of Eu were substituted for Ba to reduce air-sensitivity enough to make measurements feasible while retaining the orthorhombic structure type of Ba_2ZnSb_2 and avoiding a phase transition to the hexagonal Eu_2ZnSb_2 structure type.

3.3 Methods

Synthesis

Samples were synthesized by ball milling elements with binary precursors and annealing the resultant powder. $Ba_{11}Sb_{10}$ and $Eu_{11}Sb_{10}$ were used as the cation sources to eliminate difficulties associated with milling highly malleable and reactive alkaline-earth and rare earth metals.[21] Due to the air-sensitivity of $Ba_{2-x}Eu_xZnSb_2$, all manipulations were carried out in an Ar-filled glovebox. The synthesized $A_{11}Sb_{10}$ (A = Ba, Eu) precursors were combined with elemental Zn flakes (Alfa, 99.98%) and a small amount of Sb shot (5NPlus, 99.999%) in a 65 mL stainless steel ball mill vial with two 12.7 mm diameter stainless steel balls, hermetically sealed in a metallized 4 mil polyethylene bag and milled in a SPEX 8000 M mill for 30 minutes, then scraped with a stainless-steel spatula, resealed, and milled for an additional 30 minutes. The homogenized powder was then scraped from the container and approximately 3 g was packed into a 7 cm long, 1 cm diameter Nb tube that was welded shut in an argon arc welder and flame sealed in an evacuated quartz jacket (<50 mTorr) to be annealed in a box furnace. The reaction was heated at a rate of 200 °C/hour to 800 °C to dwell for 96 hours. Samples of $Ba_{2-x}Eu_xZnSb_2$ with Eu content x = 0, 0.2, 0.3, 0.4 were successfully synthesized as determined by powder X-ray diffraction. Property measurements were not carried out for x = 0 due to air sensitivity. Attempts were made to increase Eu content, but products of x = 0.5 and 0.75 provided a combination of the orthorhombic Ba_2ZnSb_2 structure type and the hexagonal Eu_2ZnSb_2 structure type, while x = 1 gave only the Eu_2ZnSb_2 structure type. As this study is focused on the Ba_2ZnSb_2 structure type, characterization and properties are presented only for x = 0.2, 0.3, 0.4.

$A_{11}Sb_{10}$ precursors were also synthesized via high-energy ball milling and annealing. In an Ar-filled glovebox, pea-sized pieces were clipped off a Ba rod (Sigma Aldrich, 99.999%) and Eu pieces (Stanford materials, 99.99%) pieces were cut to a similar size and each was combined with Sb shot (5NPlus, 99.999%) that had been ground into a fine powder using an agate mortar and pestle. Both reactions were sealed in a ball mill vial as described above and milled. After 30 minutes, both reactions were brought into the glovebox to be scraped, resealed, and then milled for an additional 30 minutes. The milled powders were sealed into tubes (Nb for Ba, Ta for Eu) and jacketed in evacuated quartz to be annealed (200 °C/hour to 800 °C, dwell for 12 hours).

Spark Plasma Sintering

In a glovebox, the annealed powders of $Ba_{2-x}Eu_xCdSb_2$ x = 0.2, 0.3, 0.4 were ground with an agate mortar and pestle, sieved (100 mesh), and packed into a graphite die (12.7 mm inner diameter) that had been lined with graphite foil. The die was loaded into the chamber of a Dr. Sinter Jr. instrument (Fuji Electronic Industrial Co., LTD), which was evacuated below 15 Pa, refilled to 50,000 Pa of Ar and sintered according to the following profile: heated to 600 °C in 15 minutes and then to 650 °C in 1 minute (to prevent temperature overshoot) and dwelled at 650 °C for 20 minutes. At 400 ^{o}C, the pressure was slowly increased from 47 MPa to 83 MPa. Geometric densities of the consolidated pellets were > 95% of the theoretical values. Samples were polished with dried sandpaper inside an argon-filled glovebox to prevent oxidation.

Air-free Powder X-ray Diffraction (PXRD)

Portions of the pressed pellets were prepared for air-free PXRD characterization by grinding with an agate mortar and pestle and sieving the powder onto a zero background PXRD

plate covered with double-sided polyimide tape and covering with polyimide film in an Ar-filled glovebox. A Bruker D8 Advance Eco diffractometer with Cu Kα radiation operating at 40 kV and 25 mA was used to collected diffraction data from 2θ range 15-60^{o}. The step size was 0.015 and the scan rate was 1 s per step. TOPAS5 software was used for Rietveld refinement of the data.

Scanning Electron Microscopy (SEM) and Energy Dispersive X-ray Spectroscopy (EDS)

Slices of the consolidated pellets were mounted in epoxy pucks and polished using dried sandpaper (up to 1200 grit) inside a glovebox and loaded into a Thermo Fisher Quattro ESEM. An Everhart-Thornley detector was used to collect secondary electron micrographs with 20 kV accelerating voltage and an annular backscattered detector was used for Z-contrast micrographs. A Bruker Quantax EDX detector was used to determine stoichiometry and collect elemental maps.

Magnetism

Magnetization measurements were performed in a Quantum Design magnetic properties measurement system (MPMS). A polycrystalline sample (typical mass 50 mg) was placed in between two plastic straws, which was then attached to the sample holder rod and field-cooled (FC) from room temperature to 2 K. A magnetic field of 0.1T was applied and data collected from 2 to 300 K (ZFC) and from 300 to 2 K (FC). A modified Curie Weiss fit was used to determine the Eu^{2+} content, assuming the theoretical value of the effective moment for Eu^{2+} ions.

Thermoelectric Properties

A custom-built instrument was used for Seebeck Coefficient measurements from 300-600 K in a low pressure (300 torr) N_2 atmosphere.[22] Graphite foil was used between the sample and thermocouples to ensure good electrical contact. The upper temperature of measurements was determined based on sample behavior with repeated heating and cooling cycles. Above 550 K the materials seem to react with minuscule amount of impurities present in the atmosphere of the device. Resistivity and Hall effect measurements were carried out on a home-built system with Van der Pauw geometry.[23] A magnetic field of 1 T and current of 0.1 A were used for measurement. A voltage-current curve was generated before measurement to confirm ohmic contacts. Thermal diffusivity was measured using a Netzsch Laser Flash Analysis (LFA) 475 Microflash instrument and thermal conductivity was calculated according using the equation $\kappa = \lambda\rho Cp$, where κ is thermal conductivity, Cp is the Dulong-Petit heat capacity, λ is thermal diffusivity, and ρ is sample density. Plots show third order polynomial fits to thermoelectric data and raw data are shown in appendix 3.7.

3.4 Results and Discussion

Sample Purity and Composition

Figure 3-1 depicts the crystal structure of Ba_2ZnSb_2. It is a Zintl phase with three crystallographically unique sites corresponding to each atom: Ba, Zn, Sb. Ba cations are separated by isolated infinite chains of edge-shared 1D $^1_\infty[ZnSb_{4/2}]^{4-}$ tetrahedra.[18,19] These chains run along the *c* direction and are stacked in the *b* direction. The Zintl formalism can be used to rationalize charge balance as $(Ba^{2+})_2(Zn^{2+})(Sb^{3-})_2$. Ba_2ZnSb_2 adopts the *Ibam* space group and has the K_2SiP_2 structure type.

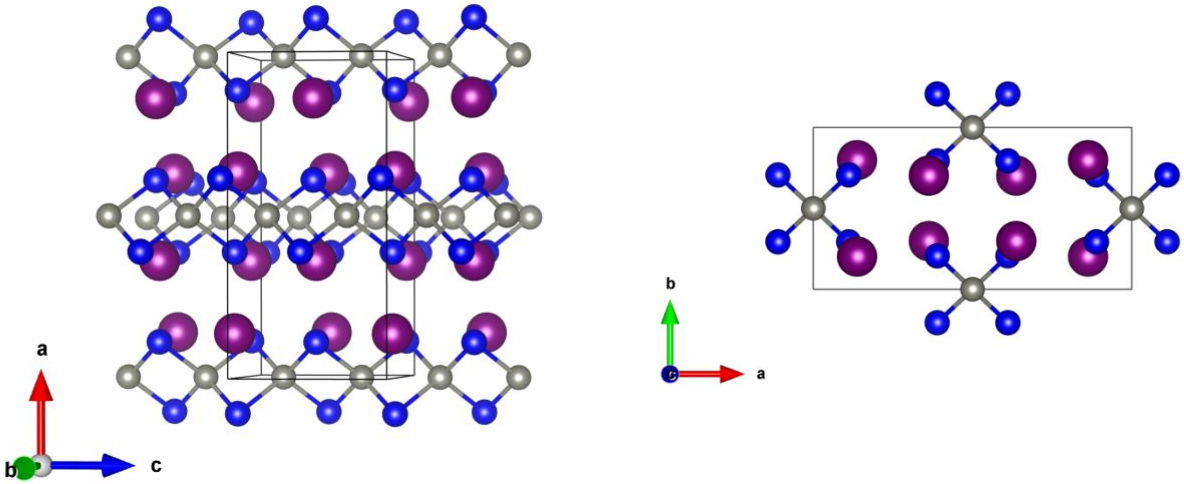


Figure 3-1. Ba_2ZnSb_2 structure viewed along the *b*-axis (left) and c-axis (right). Ba, Zn, and Sb are indicated by purple, grey, and blue colored spheres, respectively.

In the case of the solid solution of $Ba_{2-x}Eu_xZnSb_2$, Eu^{2+} is expected to substitute on the Ba^{2+} site and because it is less electropositive than Ba^{2+}, reduce the air-sensitivity of the compound. PXRD patterns for $Ba_{2-x}Eu_xZnSb_2$ (x = 0.2, 0.3, 0.4) are shown in Figure 3-2 compared to the calculated pattern[19] (bottom). Samples with x = 0.2 and 0.3 were confirmed phase pure via Rietveld refinements using the Ba_2ZnSb_2 cif.[19] Rietveld refinements yielded R_{wp} statistics < 10% and x = 0.4 had < 4% of a $BaZn_2Sb_2$ impurity, marked by asterisks. Lattice parameters (Figure 3-3) decrease with x, as expected due to the smaller size of Eu compared to Ba.

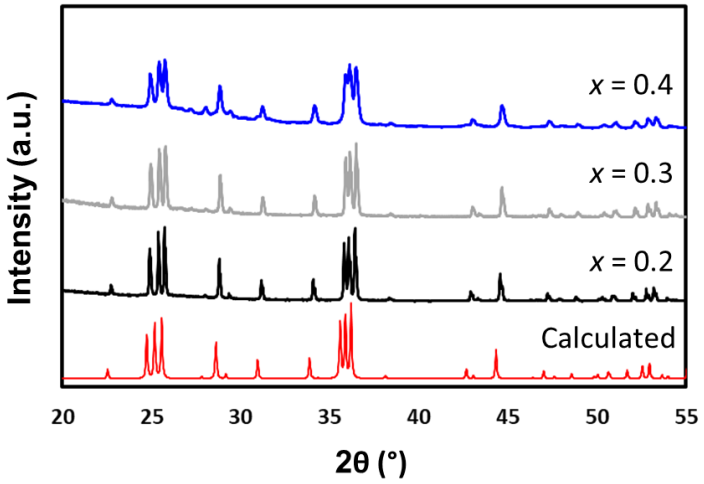


Figure 3-2. PXRD patterns for $Ba_{2-x}Eu_xZnSb_2$ (x = 0.2, 0.3, 0.4) compared to the calculated pattern from the single crystal CIF[19] on bottom.

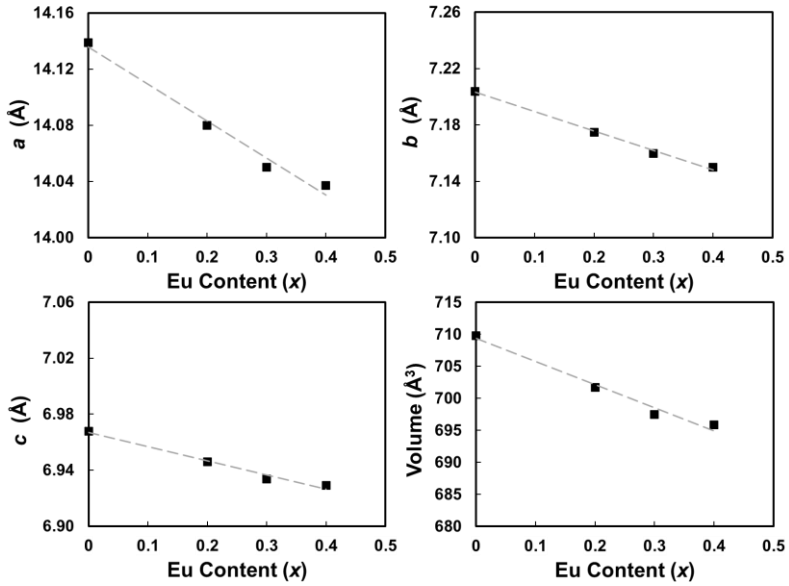


Figure 3-3. Lattice parameters determined via Rietveld refinement as a function of Eu content for $Ba_{2-x}Eu_xZnSb_2$ (x = 0, 0.2, 0.3, 0.4).

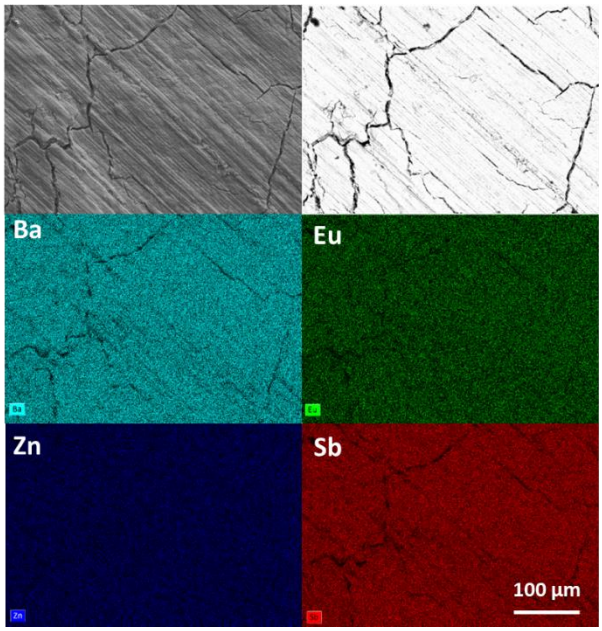


Figure 3-4. Secondary electron micrograph (top left), backscattered electron micrograph (top right), and elemental maps for $Ba_{2-x}Eu_xZnSb_2$ x = 0.4 pellet with Ba in turquoise, Eu in green, Zn in dark blue, Sb in red (bottom).

Elemental maps and backscattered electron micrograph of a pressed pellet of $Ba_{2-x}Eu_xZnSb_2$ x = 0.4 is shown in Figure 3-4. Elemental maps confirm uniform distribution of all elements and backscattered electron micrographs show that samples are single-phase. Cracks shown in the sample topography are due to surface oxidation that occurred during sample preparation. EDS characterization (Table 3-1) confirms Eu incorporation consistent with the nominal value for x = 0.2 and 0.3, and x = 0.4 . There are many examples of Eu substituting for an alkaline earth containing Zintl phases.[24–26] Typically, Eu substitutes into alkaline earth containing compounds as Eu^{2+}.[27–29] Therefore, temperature dependent magnetic susceptibility (Figure 3-5) was employed to further confirm the Eu content. The magnetization as a function of temperature of the samples follow a modified Curie-Weiss behavior with a small Weiss constant

and no notable magnetic ordering down to 2 K. It is expected that Eu should be Eu^{2+} and if we assume that is the case, then the *x* values are 0.177(1), 0.277(1), and 0.385(2), consistent with the amounts of Eu employed in the reaction. Attempts made to incorporate more Eu (*x* = 0.5, 0.75, 1) resulted in a mixture of the Ba_2ZnSb_2 and Eu_2ZnSb_2 structure types,[19,24] where lattice parameters for the Ba_2ZnSb_2 phase matched those determined for the *x* = 0.4 sample. This combined with the small a $BaZn_2Sb_2$ impurity and slightly larger lattice parameters than expected suggest that just less than *x* = 0.4 is the upper limit of Eu solubility in this system.

Table 3-1. Eu Composition Determined by EDS and Magnetic Data for $Ba_{2-x}Eu_xZnSb_2$

Loaded composition (x)	**Experimental *x* (EDS)**	**Experimental *x* (Magnetism)**	**μ*(μ_B)**	**θ_{CW} (K)**	**χ_0 e.m.u./g**
0.2	0.20(2)	0.177(1)	7.94	-0.9(2)	4.76(5) x 10^{-6}
0.3	0.29(2)	0.277(1)	7.94	-1.0(2)	1.17 (1) x 10^{-5}
0.4	0.37(4)	0.385(1)	7.94	-1.8(2)	4.21(1) x 10^{-6}

*****moment for Eu^{2+} employed to calculate *x*.

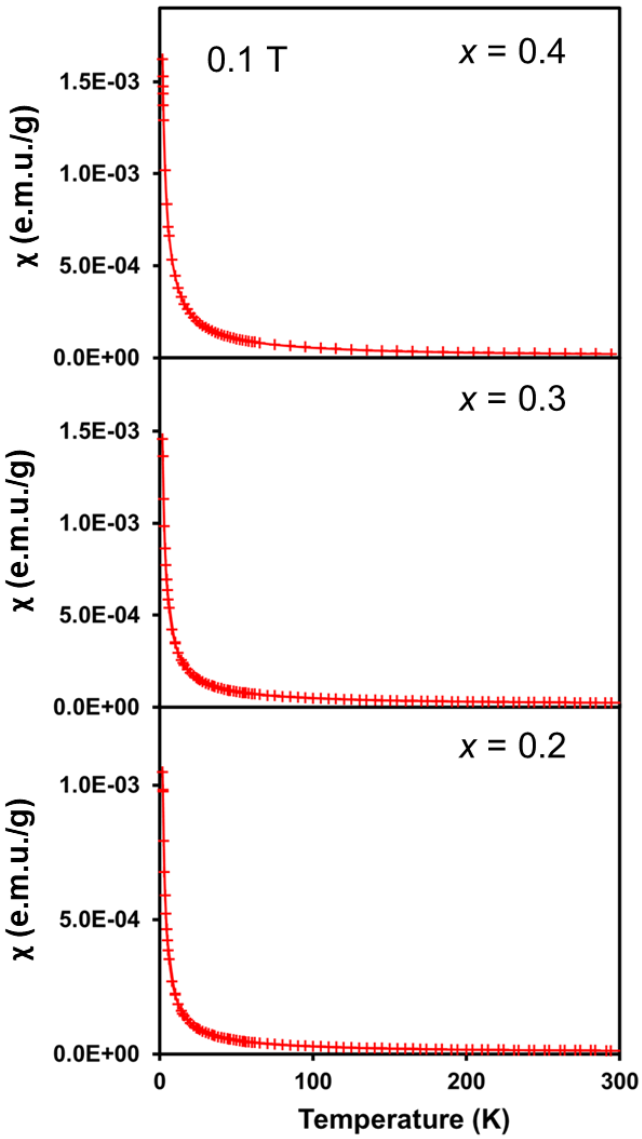


Figure 3-5. Temperature dependent magnetization for $Ba_{2-x}Eu_xZnSb_2$ (x = 0.2, 0.3, 0.4).

Electronic Transport

Figure 3-6 displays a polynomial fit to the data from the heating cycle. Carrier concentrations of the samples are quite low, on the order of 10^{17} - 10^{18} carriers/cm^{-3} (Table 3-2) and decrease with increasing Eu content. Given that Eu is confirmed to be in the 2+ oxidation state via magnetism, the reduction in charge carriers may be due to the changing defect energies of Eu compared to Ba, as has been shown in AZn_2Sb_2 (A = Yb, Eu, Sr, Ca), or to the higher electronegativity of Eu compared to Ba that could lead to incomplete electron donation.[30,31] Seebeck coefficients (Figure 3-6a) are high (> 300 μV/K) across the entire temperature range and increase with temperature, reaching a maximum value of ~550 μV/K for x = 0.4 at 500 K. In their theoretical study on the electronic structure and thermoelectric properties of Ba_2ZnSb_2, Zhang et al.[18] predicted values > 350 μV/K for < 10^{19} carriers/cm^{-3} at 600 K and experimental values range from 350-450 μV/K at 500 K. The experimental Seebeck coefficients reported here agree reasonably well with those predicted from theory, although direct comparison is not possible for all compositions due to the low carrier concentrations in the synthesized samples and lower measurement temperatures.

Table 3-2. Hall Carrier Concentration at 300 K for $Ba_{2-x}Eu_xZnSb_2$

x	**Carrier concentration (cm^{-3}), 300 K**
0.2	1.41E+18
0.3	1.02E+18
0.4	6.5E+17

Figure 3-6b shows electrical resistivities that decrease with temperature as expected for a lightly doped semiconductor.[18] Figure 3-6c gives Hall mobilities, which are high for a Zintl phase (up to 36 cm^2/Vs) and consistent with expectations from the infinite tetrahedral chains.[2,3] Electrical resistivity increases as more Eu is incorporated, consistent with the increase in Seebeck coefficient and decrease in carrier concentration. However, Hall mobility, which is expected to increase given lower carrier concentration in a single parabolic band (SPB) model where $1/\rho = ne\mu$, also decreases with increasing Eu content. The deviation from SPB behavior is expected given that band structures calculated for Ba_2ZnSb_2 are anisotropic with four degenerate bands present near the valence band edge. Experimentally determined effective masses also vary with carrier concentration ($m^* = 0.68, 1.07, 1.19\ m_e$ at 300 K for $x = 0.2, 0.3, 0.4$, respectively) which can be an indication of anisotropy or multivalley transport.[32,33] The valence band edge is composed of strongly hybridized Sb-Zn states with minimal contribution from Ba cations, while the conduction band has substantial Ba character.[5,18] This suggests that substitution on the Ba site is unlikely to significantly alter bonding near the VBM and changing mobility effective masses are likely a result of band anisotropy and the presence of additional light bands just below the Fermi level rather than Eu substitution. As Eu content decreases, the Fermi level moves towards the valence band and the two light bands are accessed while dispersion in the anisotropic heavier bands increases, resulting in lighter effective mass with greater mobility.[5,18]

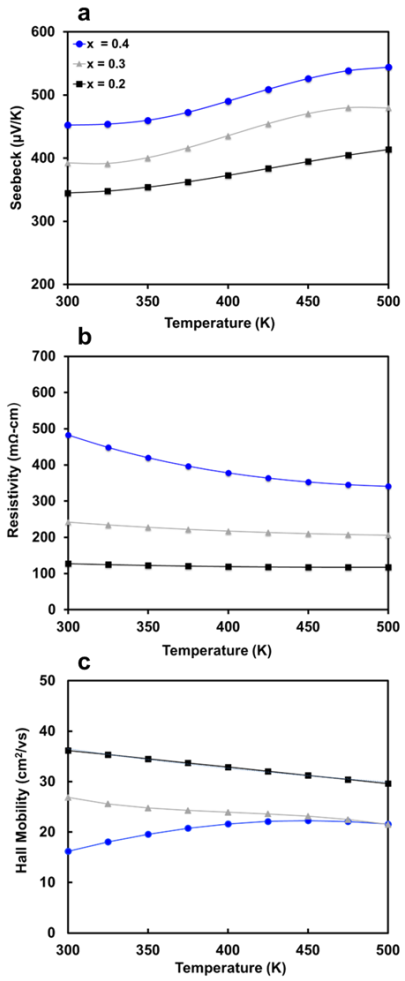


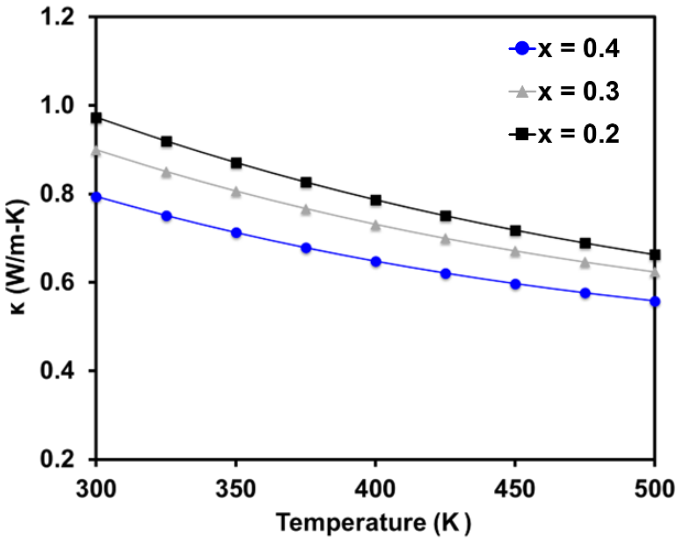
Figure 3-6. Polynomial fits of (a) Seebeck coefficients as a function of temperature; (b) electrical resistivities; (c) Hall mobilities for $Ba_{2-x}Eu_xZnSb_2$ (x = 0.2, 0.3, 0.4).

High charge carrier mobility that improves with doping makes this system promising for further optimization and high zT is predicted for Ba_2ZnSb_2 if carrier concentration can be increased to ~10^{20} h^+/cm^3. For x = 0.2 and 0.3, mobility exhibits negative temperature dependence, indicating that acoustic phonon scattering is the dominant mechanism, while x = 0.4 shows positive temperature dependence at low temperatures (< 425 K). This suggests activated mobility, which may be caused by grain boundary resistance and could be an indication that the solubility limit of Eu has been reached for x = 0.4, leaving a small amount of unreacted Eu

present at the grain boundaries.[9–11,34] This drop in low temperature mobility explains the higher electrical resistivity for x = 0.4 compared to x = 0.2 and 0.3, as well as the sharper decrease from 300-425 K.

Thermal Transport

Thermal conductivity calculated from thermal diffusivity and heat capacity (Dulong-Petit law) is shown in Figure 3-7. The Lorenz number was calculated from the Seebeck coefficient and electronic component of the thermal conductivity determined via the Wiedemann-Franz relationship was negligible (< 0.007 W/mK) due to the high electrical resistivity and low carrier concentration. Thus, the total thermal conductivity and the lattice component are virtually the same and only the total thermal conductivity is shown. Thermal conductivity (Figure 3-6) is low and comparable to the structurally similar Zintl phases $Ca_5M_2Sb_6$ (M = Al, Ga, In), Ca_3AlSb_3, and Sr_3GaSb_3, ranging from ~1 to 0.55 W/mK. The drop in thermal conductivity with Eu incorporation can be attributed to alloy scattering due to the size difference between Ba and Eu,



which has been shown to be an effective method of reducing lattice thermal conductivity in other Zintl phases.[2,35]

Figure 3-7. Polynomial fit of total thermal conductivity as a function of temperature for $Ba_{2-x}Eu_xZnSb_2$ (x = 0.2 (black filled squares), 0.3 (grey filled triangles), 0.4 (blue filled circles).

Thermoelectric Figure of Merit (zT)

Calculated zT's as a function of temperature for $Ba_{2-x}Eu_xZnSb_2$ (x = 0.2, 0.3, 0.4) are given in Figure 3-8. A maximum zT of 0.11 is obtained at 500 K for x = 0.2, the sample with the highest carrier concentration. This value is lower than the predicted maximum $zT \approx 0.8$ at 600 K with 10^{20} carriers/cm^3 for Ba_2ZnSb_2 because of the low carrier concentration in the synthesized samples, as well as the higher lattice thermal conductivity, 0.65 W/mK compared to the theoretically predicted values of κ_{min} = 0.41 and 0.11 W/mK .[18,20] It may be possible to obtain an experimental zT closer to the predicted value if carrier concentrations can be increased. This may be possible via K-doping on the Ba site. Incorporating less air sensitive elements may also improve zT by increasing the maximum operating temperature.

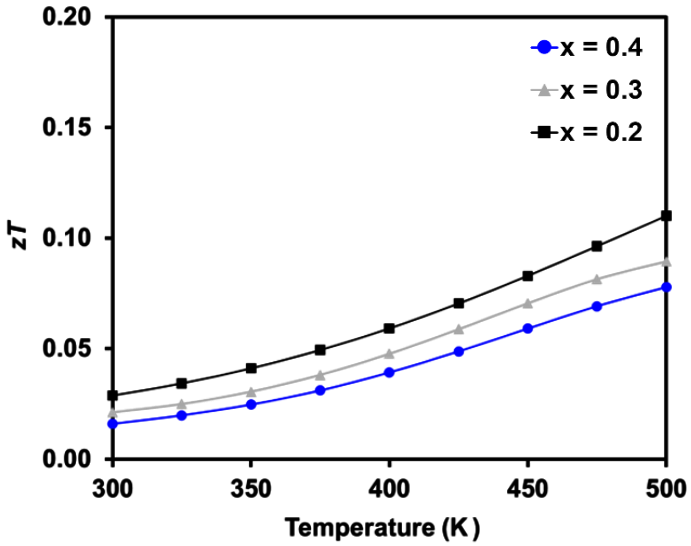


Figure 3-8. Temperature dependent *zT*'s for $Ba_{2-x}Eu_xZnSb_2$ (x = 0.2 (black filled squares), 0.3 (grey filled triangles), 0.4 (blue filled circles).

3.5 Conclusions

We have investigated thermoelectric properties for $Ba_{2-x}Eu_xZnSb_2$ (x = 0.2, 0.3, 0.4), a Zintl phase with isolated infinite 1D chains of edge-shared $[ZnSb_{4/2}]^{4-}$ tetrahedra that gives rise to anisotropic charge transport. High *zT* was predicted for Ba_2ZnSb_2 due to the presence of four degenerate bands (two heavy, two light) just below the Fermi level. Experimental data confirms high Seebeck coefficient and charge carrier mobility, as well as low lattice thermal conductivity. Predicted *zT*'s are higher than experimental values due to low carrier concentrations in synthesized samples but could likely be improved by aliovalent substitution as the carrier concentrations are quite low for these $Ba_{2-x}Eu_xZnSb_2$ compounds. The air sensitivity of the samples limited the measurement temperature range and further improvements to *zT* could likely be made by substituting with more air-stable elements to allow measurement to higher temperature. Since the solubility range of Eu is limited, another potential route for optimization is substituting Na^{1+} for some Eu^{2+} in this Ba/Eu solid solution or La^{3+} and K^{+} for Ba to

synthesize $LaKZnSb_2$, a hypothetical charge-balanced compound that may be expected to retain the same structure type due to the similar average size of La/K and Ba.

3.6 Acknowledgements

This work was supported by NSF DMR-2001156. SEM/EDS data were acquired from the Advanced Materials Characterization and Testing laboratory (AMCaT) supported by NSF DMR-1725618 at the University of California, Davis. Ashlee Hauble was supported by the University of California, Davis Dean's Distinguished Graduate Student Fellowship. E.S.T. and K.C. acknowledge DMR – 1555340 and DMR – 1729594 V.T. acknowledges support from the UC Lab Fees Research Program (LFR-20-653926) and support from the Physics Liquid Helium Laboratory fund.

3.7 Appendix

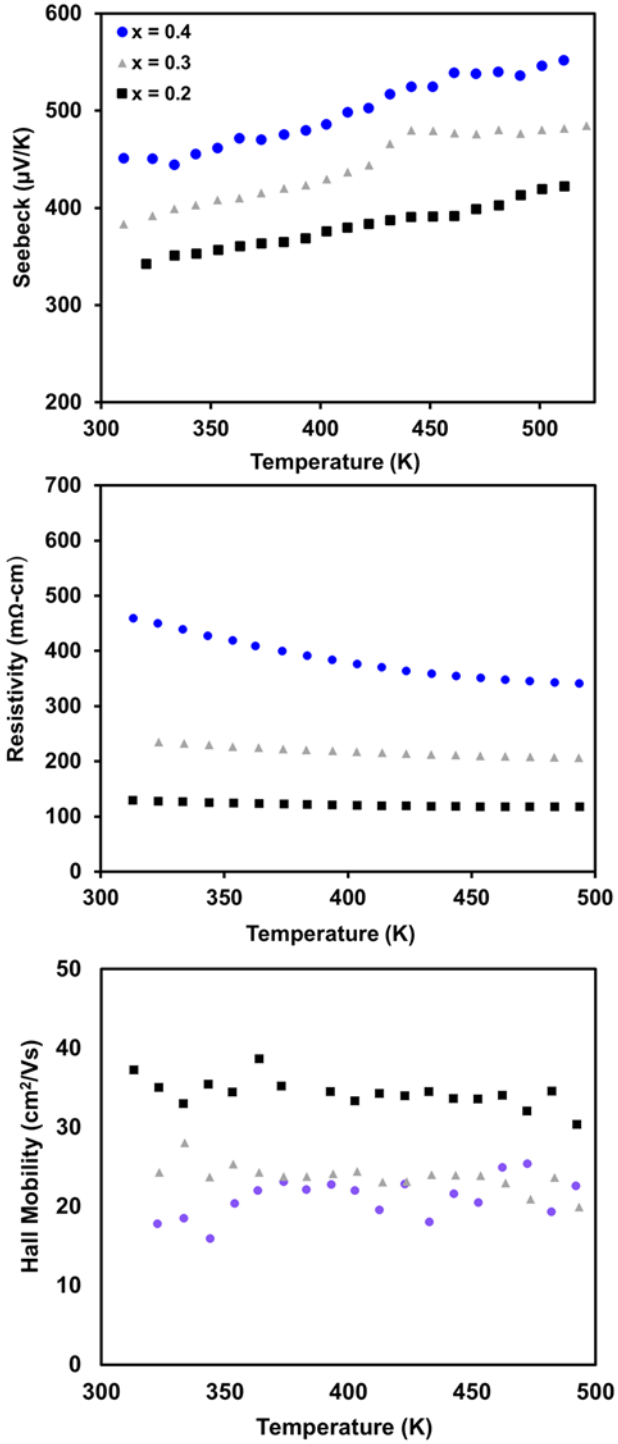


Figure 3-9. Experimental electronic transport data from the first heating cycle.

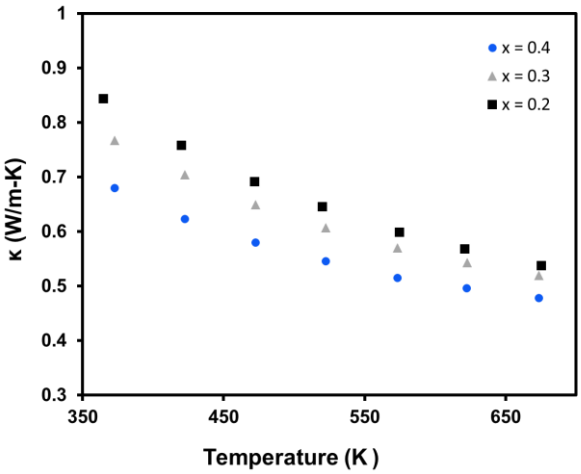
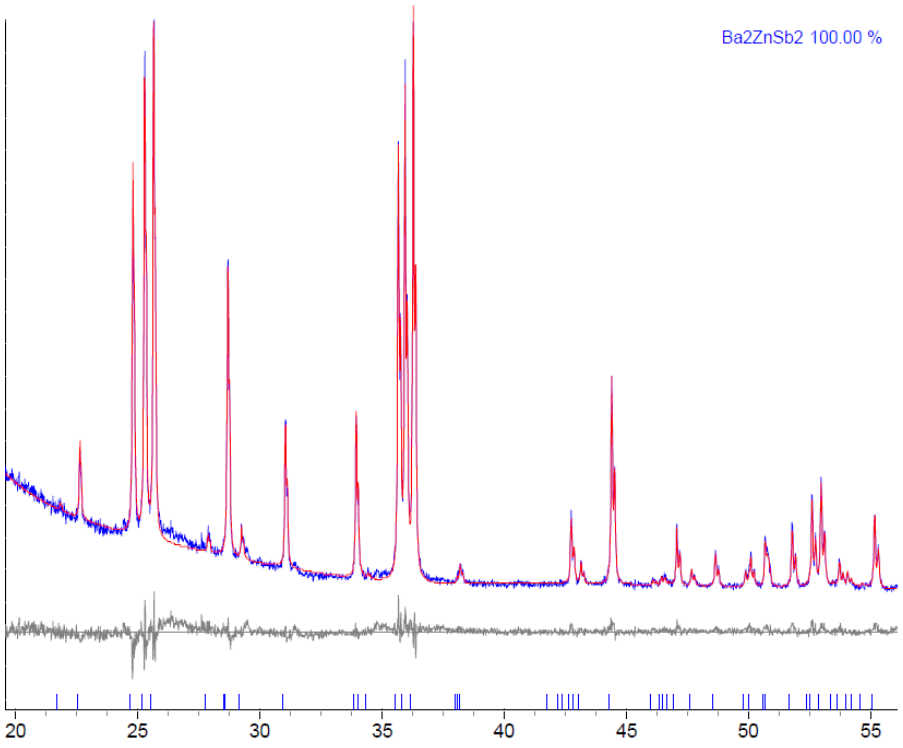
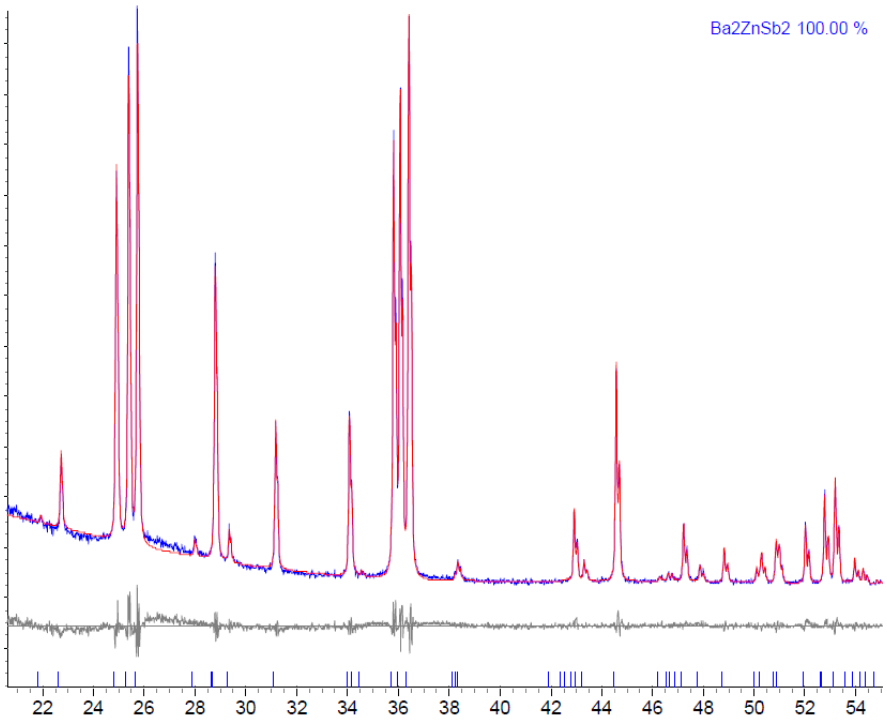


Figure 3-10. Experimental thermal conductivity data.


Ba2ZnSb2 100.00 %
20
25
30
35
40
45
50
55


Ba2ZnSb2 100.00 %
22
24
26
28
30
32
34
36
38
40
42
44
46
48
50
52
54

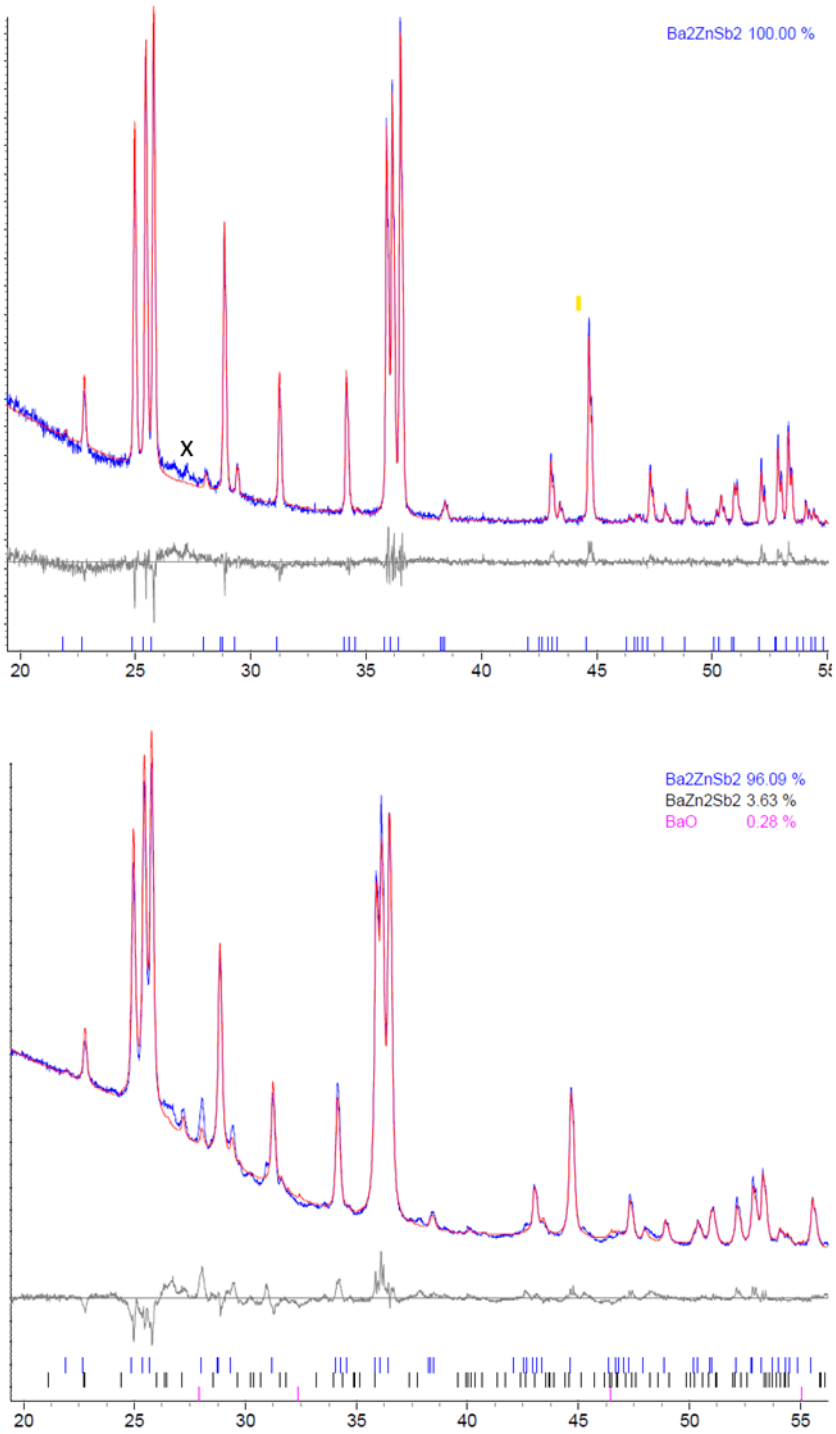


Figure 3-11. Rietveld refinements of $Ba_{2-x}Eu_xZnSb_2$ (x = 0, 0.2, 0.3, 0.4). The observed data are shown in black, calculated pattern in red, and difference curve is in gray. The sloping background observed at low angle is due to scattering from the Kapton tape used to keep the

sample air free. The x marks an unidentified impurity peak. Bragg peaks are indicated by tick marks at the bottom. Blue indicates Ba_2ZnSb_2 and black indicates $BaZn_2Sb_2$.

Table 3-3 Selected Rietveld Refinement Statistics

x		**0**	**0.2**	**0.3**	**0.4**
Unit Cell Parameters	*a* (Å)	14.1400(2)	14.0805(3)	14.0490(4)	14.0374(3)
	b (Å)	7.2041(1)	7.175(1)	7.1599(2)	7.1541(2)
	c (Å)	6.9681(1)	6.946(1)	6.9339(2)	6.9291(2)
	V (Å^3)	709.81(2)	701.76(2)	697.48(3)	695.86(3)
Rp (%), Rwp (%)		7.20, 9.19	5.38, 6.96	5.95, 7.58	4.00, 5.18
$Ba_{2-x}Eu_xZnSb_2$ (wt %)		100	100	100	96.37
$BaZn_2Sb_2$ (wt %)		0	0	0	3.63

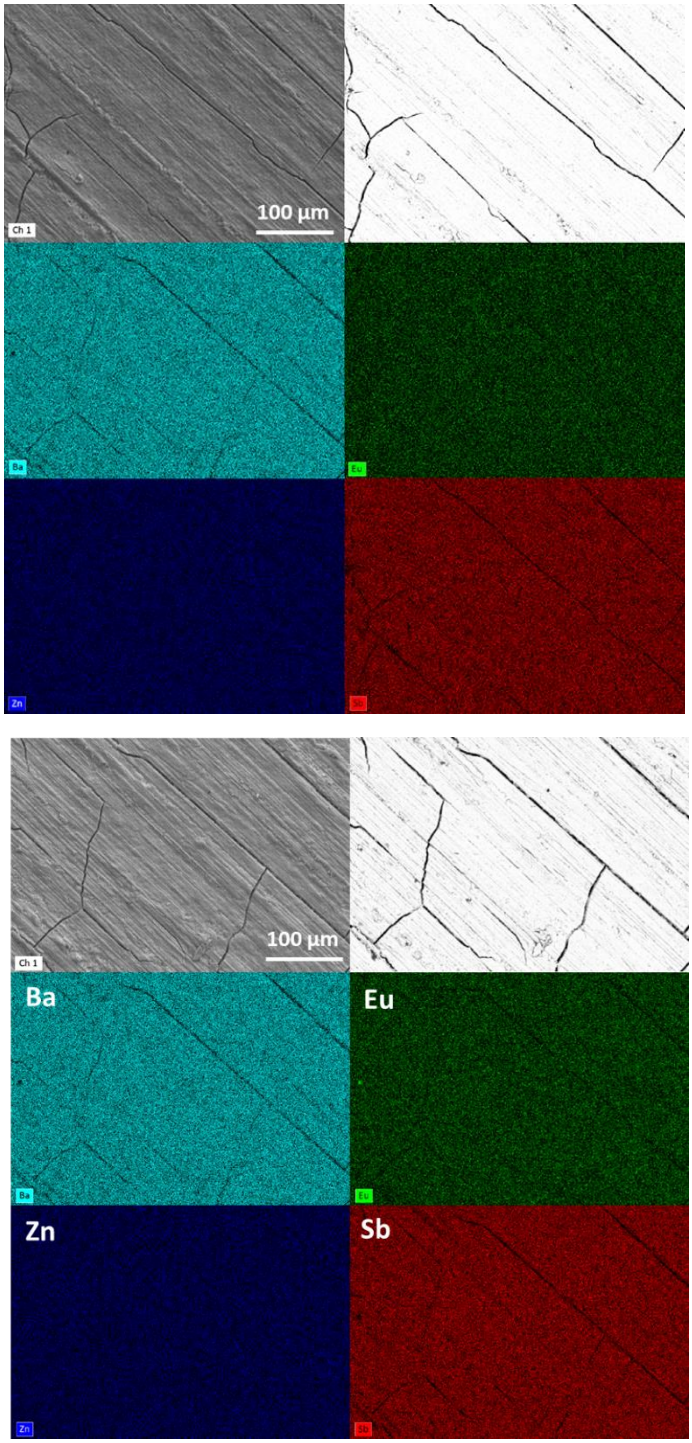


Figure 3-12. SEM micrographs and EDS elemental maps for $Ba_{1.8}Eu_{0.2}ZnSb_2$ (top) and $Ba_{1.7}Eu_{0.3}ZnSb_2$ (bottom).

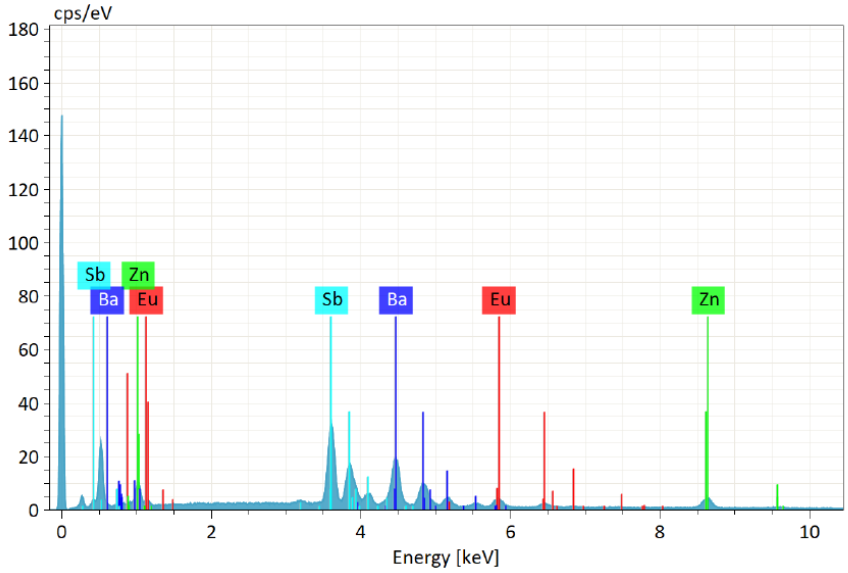


Figure 3-13. Typical EDS spectrum for $Ba_{2-x}Eu_xZnSb_2$ samples

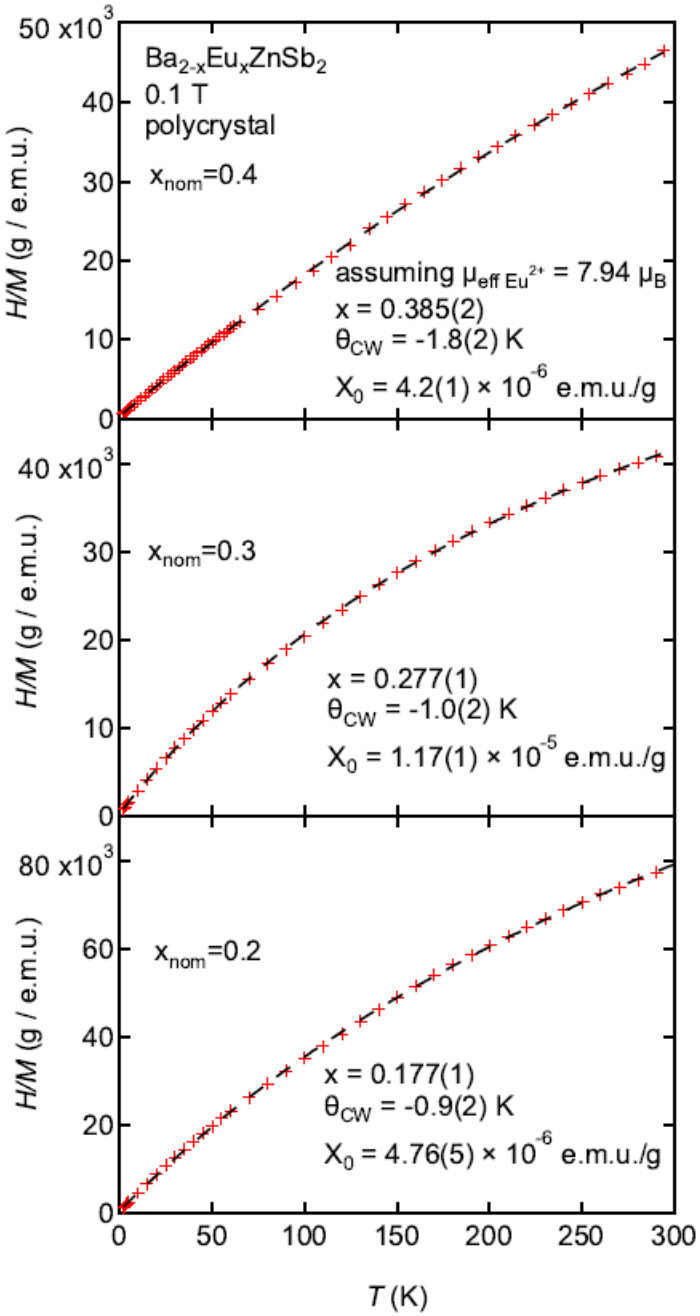


Figure 3-14. Inverse magnetic susceptibility (red) and modified Curie-Weiss fit (black).

3.8 References

(1) Ovchinnikov, A.; Bobev, S. Zintl Phases with Group 15 Elements and the Transition Metals: A Brief Overview of Pnictides with Diverse and Complex Structures. *J. Solid State Chem.* **2019**, *270*, 346–359. https://doi.org/10.1016/j.jssc.2018.11.029.

(2) Snyder, G. J.; Toberer, E. S. Complex Thermoelectric Materials. *Nat. Mater.* **2010**, *7* (February), 101–110. https://doi.org/10.1142/9789814317665_0016.

(3) Shuai, J.; Mao, J.; Song, S.; Zhang, Q.; Chen, G.; Ren, Z. Recent Progress and Future Challenges on Thermoelectric Zintl Materials. *Mater. Today Phys.* **2017**, *1*, 74–95. https://doi.org/10.1016/J.MTPHYS.2017.06.003.

(4) Zevalkink, A.; Smiadak, D. M.; Blackburn, J. L.; Ferguson, A. J.; Chabinyc, M. L.; Delaire, O.; Wang, J.; Kovnir, K.; Martin, J.; Schelhas, L. T.; Sparks, T. D.; Kang, S. D.; Dylla, M. T.; Snyder, G. J.; Ortiz, B. R.; Toberer, E. S. A Practical Field Guide to Thermoelectrics: Fundamentals, Synthesis, and Characterization. *Appl. Phys. Rev.* **2018**, *5* (2), 021303. https://doi.org/10.1063/1.5021094.

(5) Sun, J.; Singh, D. J. Thermoelectric Properties of AMg_2X_2, AZn_2Sb_2 (A = Ca, Sr, Ba; X = Sb, Bi), and Ba_2ZnX_2 (X = Sb, Bi) Zintl Compounds. *J. Mater. Chem. A* **2017**, *5* (18), 8499–8509. https://doi.org/10.1039/c6ta11234j.

(6) Parker, D.; Chen, X.; Singh, D. J. High Three-Dimensional Thermoelectric Performance from Low-Dimensional Bands. *Phys. Rev. Lett.* **2013**, *110* (14), 1–5. https://doi.org/10.1103/PhysRevLett.110.146601.

(7) Dylla, M. T.; Kang, S. D.; Snyder, G. J. Effect of Two-Dimensional Crystal Orbitals on Fermi Surfaces and Electron Transport in Three-Dimensional Perovskite Oxides. *Angew. Chemie - Int. Ed.* **2019**, *58* (17), 5503–5512. https://doi.org/10.1002/anie.201812230.

(8) Dresselhaus, M. S.; Chen, G.; Tang, M. Y.; Yang, R.; Lee, H.; Wang, D.; Ren, Z.; Fleurial, J.-P.; Gogna, P. New Directions for Low-Dimensional Thermoelectric Materials. *Adv. Mater.* **2007**, *19*, 1043–1053. https://doi.org/10.1002/adma.200600527.

(9) Zevalkink, A.; Toberer, E. S.; Zeier, W. G.; Flage-Larsen, E.; Snyder, G. J. Ca_3AlSb_3: An Inexpensive, Non-Toxic Thermoelectric Material for Waste Heat Recovery. *Energy Environ. Sci* **2011**, *5* (2), 510–518. https://doi.org/10.1039/c0ee00517g.

(10) Zevalkink, A.; Zeier, W. G.; Pomrehn, G.; Schechtel, E.; Tremel, W.; Snyder, G. J. Thermoelectric Properties of Sr_3GaSb_3-a Chain-Forming Zintl Compound. *Energy Environ. Sci* **2012**, *5* (10), 9121–9128. https://doi.org/10.1039/c2ee22378c.

(11) Zevalkink, A.; Pomrehn, G. S.; Johnson, S.; Swallow, J.; Gibbs, Z. M.; Snyder, G. J. Influence of the Triel Elements (M = Al, Ga, In) on the Transport Properties of $Ca_5M_2Sb_6$ Zintl Compounds. *Chem. Mater.* **2012**, *24* (11), 2091–2098. https://doi.org/10.1021/cm300520w.

(12) Chanakian, S.; Uhl, D.; Neff, D.; Drymiotis, F.; Park, J.; Petkov, V.; Zevalkink, A.; Bux, S. Exceptionally High Electronic Mobility in Defect-Rich $Eu_2ZnSb_{2-x}Bi_x$ Alloys. *J. Mater. Chem. A* **2020**, *8* (12), 6004–6012. https://doi.org/10.1039/c9ta14170g.

(13) Cooley, J. A.; Promkhan, P.; Gangopadhyay, S.; Donadio, D.; Pickett, W. E.; Ortiz, B. R.; Toberer, E. S.; Kauzlarich, S. M. High Seebeck Coefficient and Unusually Low Thermal Conductivity Near Ambient Temperatures in Layered Compound $Yb_{2-x}Eu_xCdSb_2$. *Chem. Mater.* **2018**, *30* (2), 484–493. https://doi.org/10.1021/acs.chemmater.7b04517.

(14) Devlin, K. P.; Chen, S.; Donadio, D.; Kauzlarich, S. M. Solid Solution $Yb_{2-x}Ca_xCdSb_2$: Structure, Thermoelectric Properties, and Quality Factor. *Inorg. Chem.* **2021**, *60* (17), 13596–13606. https://doi.org/10.1021/acs.inorgchem.1c01906.

(15) Chen, C.; Xue, W.; Li, S.; Zhang, Z.; Li, X.; Wang, X.; Liu, Y.; Sui, J.; Liu, X.; Cao, F.; Ren, Z.; Chu, C.-W.; Wang, Y.; Zhang, Q. Zintl-Phase Eu_2ZnSb_2: A Promising Thermoelectric Material with Ultralow Thermal Conductivity. *Proc. Natl. Acad. Sci.* **2019**, *116* (8), 2831–2836. https://doi.org/10.1073/PNAS.1819157116.

(16) Chen, C.; Li, X.; Xue, W.; Bai, F.; Huang, Y.; Yao, H.; Li, S.; Zhang, Z.; Wang, X.; Sui, J.; Liu, X.; Cao, F.; Wang, Y.; Zhang, Q. Manipulating the Intrinsic Vacancies for Enhanced Thermoelectric Performance in Eu_2ZnSb_2 Zintl Phase. *Nano Energy* **2020**, *73* (March), 1047711–1074418. https://doi.org/10.1016/j.nanoen.2020.104771.

(17) Shi, Q.; Feng, Z.; Yan, Y.; Wang, Y. X. Electronic Structure and Thermoelectric Properties of Zintl Compounds A_3AlSb_3 (A ¼ Ca and Sr): First-Principles Study. *RSC Adv.* **2015**, *5* (80), 65133–65138. https://doi.org/10.1039/c5ra09804a.

(18) Zhang, X.; Wang, C.; Wang, Y. X. Influence of the Elements (Pn = As, Sb, Bi) on the Transport Properties of p-Type Zintl Compounds Ba_2ZnPn_2. *Comput. Mater. Sci.* **2017**,

127, 8–14. https://doi.org/10.1016/j.commatsci.2016.10.022.

(19) Saparov, B.; Bobev, S. Isolated $^{1}_{\infty}[ZnPn_2]^{4-}$ Chains in the Zintl Phases Ba_2ZnPn_2 (Pn = As, Sb, Bi)--Synthesis, Structure, and Bonding. *Inorg. Chem.* **2010**, *49* (11), 5173–5179. https://doi.org/10.1021/ic100296x.

(20) Zhai, W.; Li, L.; Zhao, M.; Hu, Q.; Li, J.; Yang, G.; Yan, Y.; Zhang, C.; Liu, P. F. Phonon Transport in Zintl Ba2ZnAs2 and Ba2ZnSb2: A First-Principles Study. *Mater. Sci. Semicond. Process.* **2022**, *141* (July 2021), 1–6. https://doi.org/10.1016/j.mssp.2021.106446.

(21) Justl, A. P.; Cerretti, G.; Bux, S. K.; Kauzlarich, S. M. 2 + 2 = 3: Making Ternary Phases through a Binary Approach. *Chem. Mater.* **2022**, *34* (3), 1342–1355. https://doi.org/10.1021/acs.chemmater.1c04031.

(22) Iwanaga, S.; Toberer, E. S.; Lalonde, A.; Snyder, G. J. A High Temperature Apparatus for Measurement of the Seebeck Coefficient. *Rev. Sci. Instrum.* **2011**, *82* (6), 0639051–0639056. https://doi.org/10.1063/1.3601358.

(23) Borup, K. A.; Toberer, E. S.; Zoltan, L. D.; Nakatsukasa, G.; Errico, M.; Fleurial, J.-P.; Iversen, B. B. Measurement of the Electrical Resistivity and Hall Coefficient at High Temperatures. *Rev. Sci. Instrum* **2012**, *83* (123902), 123902. https://doi.org/10.1063/1.4770124.

(24) Wilson, D. K.; Saparov, B.; Bobev, S. Synthesis, Crystal Structures and Properties of the Zintl Phases Sr_2ZnP_2, Sr_2ZnAs_2, A_2ZnSb_2 and A_2ZnBi_2 (A = Sr and Eu). *Zeitschrift fur Anorg.*

und Allg. Chemie **2011**, *637* (13), 2018–2025. https://doi.org/10.1002/zaac.201100177.

(25) Ovchinnikov, A.; Darone, G. M.; Saparov, B.; Bobev, S. Exploratory Work in the Quaternary System of Ca-Eu-Cd-Sb: Synthesis, Crystal, and Electronic Structures of New Zintl Solid Solutions. *Materials (Basel).* **2018**, *11* (11), 1–13. https://doi.org/10.3390/ma11112146.

(26) Saparov, B.; Saito, M.; Bobev, S. Syntheses, and Crystal and Electronic Structures of the New Zintl Phases Na_2ACdSb_2 and K_2ACdSb_2 (A=Ca, Sr, Ba, Eu, Yb): Structural Relationship with Yb_2CdSb_2 and the Solid Solutions Sr<sub>. *J. Solid State Chem.* **2011**, *184* (2), 432–440. https://doi.org/10.1016/j.jssc.2010.12.015.

(27) Radzieowski, M.; Stegemann, F.; Klenner, S.; Zhang, Y.; Fokwa, B. P. T.; Janka, O. On the Divalent Character of the Eu Atoms in the Ternary Zintl Phases $Eu_5In_2Pn_6$ and Eu_3MAs_3 (Pn = As-Bi; M = Al, Ga). *Mater. Chem. Front.* **2020**, *4* (4), 1231–1248. https://doi.org/10.1039/c9qm00703b.

(28) Radzieowski, M.; Block, T.; Fickenscher, T.; Zhang, Y.; Fokwa, B. P. T.; Janka, O. Synthesis, Crystal and Electronic Structures, Physical Properties and ^{121}Sb and ^{151}Eu Mössbauer Spectroscopy of the Alumo-Antimonide Zintl-Phase $Eu_5Al_2Sb_6$. *Mater. Chem. Front.* **2017**, *1* (8), 1563–1572. https://doi.org/10.1039/c7qm00057j.

(29) Radzieowski, M.; Block, T.; Klenner, S.; Zhang, Y.; Fokwa, B. P. T.; Janka, O. Synthesis, Crystal and Electronic Structure, Physical Properties and ^{121}Sb and ^{151}Eu Mössbauer Spectroscopy of the $Eu_{14}AlPn_{11}$ Series (Pn = As, Sb). *Inorg. Chem. Front.* **2019**, *6* (1), 137–

147. https://doi.org/10.1039/c8qi01099d.

(30) Pomrehn, G. S.; Zevalkink, A.; Zeier, W. G.; Van De Walle, A.; Snyder, G. J. Defect-Controlled Electronic Properties in AZn_2Sb_2 Zintl Phases. *Angew. Chemie - Int. Ed.* **2014**, *53* (13), 3422–3426. https://doi.org/10.1002/anie.201311125.

(31) Shuai, J.; Wang, Y.; Liu, Z.; Kim, H. S.; Mao, J.; Sui, J.; Ren, Z. Enhancement of Thermoelectric Performance of Phase Pure Zintl Compounds $Ca_{1-x}Yb_xZn_2Sb_2$, $Ca_{1-x}Eu_xZn_2Sb_2$, and $Eu_{1-x}Yb_xZn_2Sb_2$. *Nano Energy* **2016**, *25*, 136–144. https://doi.org/10.1016/J.NANOEN.2016.04.023.

(32) Perez, C. J.; Wood, M.; Ricci, F.; Yu, G.; Vo, T.; Bux, S. K.; Hautier, G.; Rignanese, G.-M.; Snyder, G. J.; Kauzlarich, S. M. Discovery of Multivalley Fermi Surface Responsible for the High Thermoelectric Performance in $Yb_{14}MnSb_{11}$ and $Yb_{14}MgSb_{11}$. *Sci. Adv.* **2021**, *7* (4). https://doi.org/10.1126/sciadv.abe9439.

(33) Kang, S. D.; Snyder, G. J. Transport Property Analysis Method for Thermoelectric Materials: Material Quality Factor and the Effective Mass Model. In *Advances in Thermoelectricity: Foundational Issues, Materials and Nanotechnology*; 2017; pp 27–36.

(34) Jiahong Kuo, J.; Dongmin Kang, S.; Kazuki Imasato, A.; Tamaki, H.; Ohno, S.; Tsutomu Kanno, A.; Jeffrey Snyder, G. Grain Boundary Dominated Charge Transport in Mg_3Sb_2-Based Compounds. *Energy Environ. Sci* **2018**, *11*, 429. https://doi.org/10.1039/c7ee03326e.

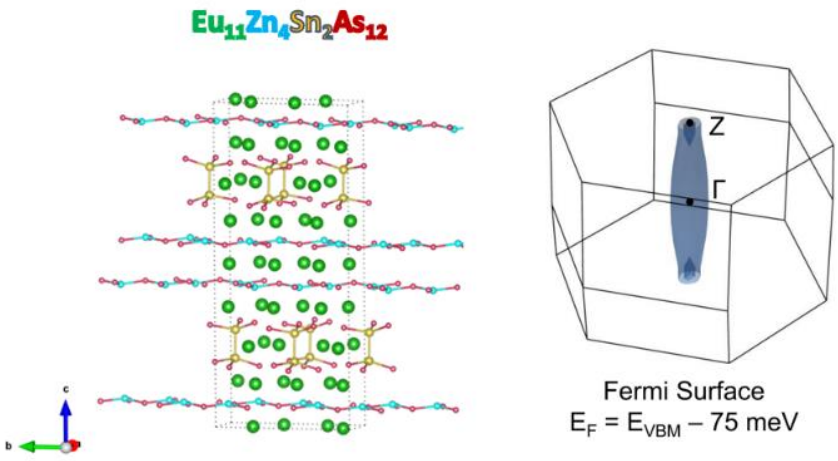
(35) Liu, K. F.; Xia, S. Q. Recent Progresses on Thermoelectric Zintl Phases: Structures, Materials and Optimization. *J. Solid State Chem.* **2019**, *270* (November 2018), 252–264. https://doi.org/10.1016/j.jssc.2018.11.030.

Chapter 4: Theory and experiment in concert to unravel the remarkable electronic properties of Na-doped $Eu_{11}Zn_4Sn_2As_{12}$: A layered Zintl phase

Ashlee K. Hauble[1], Michael Toriyama[2], G. Jeffrey Snyder[2*], and Susan M. Kauzlarich[1*]

Affiliations

[1]Department of Chemistry, One Shields Ave, University of California, Davis, California 95616, United
States
[2]Department of Materials Science and Engineering, Northwestern University, Evanston, IL 60208, United States



4.1 Abstract

Low-dimensional materials have unique optical, electronic, mechanical, and chemical properties that make them desirable for a wide range of applications. Nano-scaling materials to confine transport in at least one direction is a common method of designing materials with low-dimensional electronic structures, but bulk materials give rise to low-dimensional electronic structures when bonding is highly anisotropic. Layered Zintl phases are excellent candidates for investigation due to their directional bonding, structural variety, and tunability. However, the complexity of structure and composition of many layered Zintl phases poses a challenge for producing phase pure bulk samples to characterize. In this example, a binary EuAs phase was employed as a precursor, along with NaH to prepare phase pure $Eu_{11-x}Na_xZn_4Sn_2As_{12}$ to enable measurement of thermoelectric properties. Experimental measurements reveal low thermal conductivity and high Seebeck coefficient with an unusual trend, while electronic structure calculations reveal a transition from a 3D to 2D electronic structure with increasing carrier concentration. Simulated thermoelectric properties also indicate anisotropic transport and thermoelectric property measurements confirm nonparabolicity of the relevant bands near the Fermi energy. Thermoelectric efficiency is known to improve as dimensionality of electronic structure is decreased, making this a promising material for further optimization, and opening the door to further exploitation of layered Zintl phases with low-dimensional electronic structures for thermoelectric applications.

4.2 Introduction

Layered materials with low-dimensional electronic structures are of interest for a wide variety of applications including catalysis, optoelectronics, and energy harvesting.[1–5] While low-dimensional electronic structures are generally achieved by nano-scaling materials to confine electronic transport in one or two directions, 3D structures can give rise to 1 or 2D electronic structures in bulk samples when bonding is highly directional.[6–9] Layered materials are well-suited for this given their anisotropic bonding. Much of the current research on layered materials is focused on 2D graphene and transition metal chalcogenides. However, Zintl phases with layered structures are a vast and underexplored class of materials with directional bonding and great structural variety, making them excellent candidates for the quest to uncover low-dimensional electronic structures in bulk semiconductors.[3,4,10,11] The combination of ionic and covalent bonding in Zintl compounds gives rise to diverse bonding motifs that can be tuned to adjust the electronic structures, providing more opportunity to engineer low-dimensional transport. Several layered Zintl phases, including $Yb_{2-x}Eu_xCdSb_2$, Eu_2ZnSb_2, and $YbZn_2Sb_2$, have already been shown to be promising thermoelectric materials and may find other applications if their electronic structures can be better understood.[12–17] $Eu_{11}Zn_4Sn_2As_{12}$ is an example of a layered Zintl phase with complex, directional bonding (Figure 4-1), a commensurately modulated structure with crystallographic disorder that has potential for a wide variety of uses.[18,19]

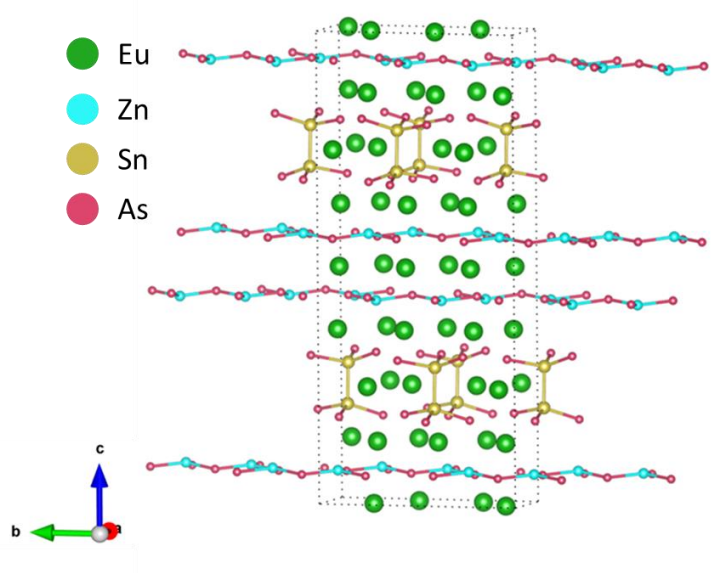


Figure 4-1. A view of the crystal structure of $Eu_{11}Zn_4Sn_2As_{12}$ (*C2/c* space group) showing the layered aspect of the structure. Eu atoms are indicated in green, Zn in turquoise, Sn in yellow and As in red.

The crystal structure of $Eu_{11}Zn_4Sn_2As_{12}$ is shown in Figure 4-1. It is composed of layers of Eu cations, $[Zn_2As_3]^{5-}$ defect honeycomb sheets, and pillars of ethane-like $[Sn_2As_6]^{12-}$ units with interspersed Eu atoms.[18] The delocalized bonding in the hexagonal $[Zn_2As_3]^{5-}$ sheets, similar to the $ZnSb_2$ layers found in the high-performing thermoelectric material Eu_2ZnSb_2, is expected to give rise to high charge carrier mobility in the *a*- and *b*-directions, while the ionic bonding along the *c*-direction is expected to contribute to high effective mass and low carrier mobility. In addition, the ethane-like $[Sn_2As_6]^{12-}$ units should provide weak dispersion of the wave functions associated with their respective layer, further enhancing the 2D-like nature of this compound. These features result in a highly anisotropic and potentially 2D Fermi surface. In addition to high charge carrier mobility, delocalized bonding in the hexagonal nets can also give rise to topologically nontrivial electronic structures.[20] A study on Eu_2ZnSb_2 revealed topological

electronic structure changes based on vacancy ordering at the Zn site that are driven by the same physics as topological edge states in honeycomb-like nanoribbons.[21–24] Complex, nonparabolic band structures, such as those present in topological materials, are often associated with high thermoelectric performance[25] and are useful for many other purposes, such as spintronics, quantum information science, and catalysis.[6,8,20,26–28] The known magnetic ordering and colossal magnetoresistance of $Eu_{11}Zn_4Sn_2As_{12}$ combined with the potential for topological behavior make this material an exciting candidate for a wide variety of applications.[18,19] The crystal structure and magnetic properties of a related phase, $Eu_{3-\delta}Zn_xSn_yAs_3$, were recently reported as a tunable structure for the study of topological and magnetic properties.[29]

Given the vast potential for $Eu_{11}Zn_4Sn_2As_{12}$ and related phases, characterization of its electronic properties is necessary. However, as with many Eu-based compounds and complex structures, overcoming synthetic challenges to prepare phase pure powders are a major consideration. Eu is malleable, reactive, and has high vapor pressure (3-4 times higher than that of other rare earth metals, not including Yb), making traditional solid state synthesis routes difficult, particularly for Zintl phases where many different compounds exist with the same elements and similar stoichiometry (e.g. 2-1-2, 9-4-9, 11-6-12, 5-2-6, etc.).[10,30] This work utilizes a binary synthesis route that was shown to provide excellent stoichiometric control in $Yb_{14}MSb_{11}$ (M = Mn, Mg, Zn, Al).[31] High quality polycrystalline powders of $Eu_{11}Zn_4Sn_2As_{12}$ are obtained by employing a EuAs precursor that eliminates side phases that arise from Eu loss and insufficient mixing during synthesis. Using Eu binary compounds as synthetic precursors could unlock a multitude of compounds with novel properties, as Eu-based compounds are known to exhibit ferromagnetism, superconductivity, Kondo behavior, zero thermal expansion,

high thermoelectric efficiency and more, but exploration of their properties has been limited by synthetic challenges.[10,13,14,18,19,30]

Here, we present the synthesis of phase pure $Eu_{11}Zn_4Sn_2As_{12}$ and dope the compound with Na to control carrier concentration. We measure thermoelectric properties and employ DFT calculations to probe the low-dimensional electronic structure of Na-doped $Eu_{11}Zn_4Sn_2As_{12}$.

4.3 Experimental

Synthesis

Synthesis of polycrystalline samples of $Eu_{11-x}Na_xZn_4Sn_2As_{12}$ from stoichiometric amounts of the elements or the elements plus EuH_2 lead to mixed phases with unidentified impurities. Therefore, polycrystalline $Eu_{11-x}Na_xZn_4Sn_2As_{12}$ (x = 0, 0.05, 0.075, 0.1) samples were synthesized via a balanced reaction using EuAs (ICSD- 26265, the Na_2O_2 structure type)[32] as a reactive precursor (synthesis described below) with NaH and the elements mixed via high-energy ball milling followed by annealing. In an Ar-filled glovebox, EuAs was combined with NaH powder (Aldrich, 90%), Zn flakes (Alfa, 99.98%), Sn shot (Alpha Aesar, 99.99%), and As lump (Johnson Matthey, Chemicals, 99.9999%) in a 65 mL stainless steel ball mill vial with two 12.7 mm diameter stainless steel balls. The vial was sealed in a mylar bag and placed in a SPEX 8000 M mill for 30 minutes, transferred to a glovebox to be scraped with a stainless-steel spatula and then milled for an additional 30 minutes to ensure homogenization. The vial was scraped, and the powder was loaded into a 7 cm Ta tube that was sealed in an Ar-filled arc welder. The Ta tube was placed inside a fused silica tube, evacuated to < 50 mTorr, flame sealed and placed in a box

furnace to be annealed at 800 ^{o}C for 96 hours. The heating rate was 200 ^{o}C/hour. The product was confirmed to be phase pure by powder X-ray diffraction and Rietveld refinement.

The EuAs precursor (ICSD- 26265, the Na_2O_2 structure type)[32] was synthesized from stoichiometric amounts of the elements via high-energy ball milling and annealing. In an Ar-filled glovebox, Eu metal (Stanford materials, 99.99%) was cut into pea-sized pieces and combined with As lumps in a stainless-steel ball mill, hermetically sealed in a mylar bag and milled for 30 minutes. Then the vial was rotated 180 degrees and milled for an additional 30 minutes before transferring to a glovebox to be scraped and loaded into a 7 cm Ta tube that was arc-welded and further sealed in an evacuated silica tube. The powder was heated to 800 ^{o}C at a rate of 200 ^{o}C/hour and annealed for 12 hours. The product was confirmed to be phase pure by powder X-ray diffraction and Rietveld refinement.

Spark Plasma Sintering

The phase pure powder of $Eu_{11-x}Na_xZn_4Sn_2As_{12}$ (x = 0, 0.05, 0.075, 0.1), confirmed via PXRD, was ground with an agate mortar and pestle and sieved (100 mesh) and placed in a 12.7 mm inner diameter graphite die in a glovebox. The die was placed in a Spark Plasma Sintering instrument (Dr. Sinter Jr., Fuji Electronic Industrial Co., LTD) to be consolidated. After evacuating to below 15 Pa, the chamber was refilled with Ar to ~50,000 Pa. The die was heated to 645 ^{o}C in 8 minutes and dwelled for 10 minutes. At 400 ^{o}C , the pressure was slowly increased from 47 MPa to 83 MPa. The geometric and Archimedes densities of the sintered pellets were > 95% of the theoretical density. Samples were sliced with a diamond saw (Buehler Isomet) and polished into thin, flat disks (<1.3 mm thick) for thermoelectric measurements.

Powder X-ray Diffraction (PXRD)

Pieces of the sintered pellets obtained from SPS were ground into fine powders using an agate mortar and pestle for additional PXRD analysis. One pellet was also measured to check for the possibility of preferred orientation. A Bruker D8 Advance Eco diffractometer with Cu Kα radiation was used to collect PXRD data. The diffractometer operated at 40 kV and 25 mA from 2θ range 20-80 ° with step size 0.015 ° and a scan rate of 1 s per step. Samples were determined to be single-phase $Eu_{11-x}Na_xZn_4Sn_2As_{12}$ via Rietveld refinement from the TOPAS5 software.[33]

Scanning Electron Microscopy (SEM) and Energy Dispersive X-ray Spectroscopy (EDS)

Pieces of sintered pellets were mounted in epoxy pucks and polished using sandpaper and a polishing wheel (1 μm colloidal diamond suspension) for SEM/EDS analysis with a Thermo Fisher Quattro ESEM equipped with a Bruker Quantax EDX detector. An Everhart-Thornley detector was used to collect secondary electron images with 20 kV accelerating voltage and an annular backscatter detector was used for Z-contrast to analyze composition.

Electronic Structure

First-principles density functional theory (DFT) calculations were performed using the Vienna *ab initio* simulation package (VASP)[34,35] under the projector augmented wave (PAW) formalism.[36,37] The Perdew-Burke-Ernzerhof (PBE) functional was used to describe the exchange-correlation interaction.[38] An energy cutoff of 340 eV and the experimentally-resolved crystal structure of $Eu_{11}Zn_4Sn_2As_{12}$ at 90 K[18] were used in all calculations. The Eu-*f* electrons were treated as core electrons. Spin-orbit coupling (SOC) was included in all calculations.

The transport properties, namely the electrical resistivity and Seebeck coefficient, were calculated from Onsager transport coefficients using the *Ab initio* Scattering and Transport (AMSET) software.[39] We found that the transport properties are well-converged when the 6×6×2 k-point mesh is interpolated by a factor of 15.[40] All required material parameters were calculated using DFT, namely the finite difference method to obtain the stiffness tensor and density functional perturbation theory to obtain the dielectric tensor.

Thermoelectric Properties

A Netzsch Laser Flash Analysis (LFA) 475 Microflash instrument was used to measure thermal diffusivity on sintered pellets under a flow of Ar (60 mL/min) from 300-675 K and back to down 350 K. Diffusivity was used to calculate thermal conductivity from the relationship $\kappa = \lambda\rho Cp$, where κ is thermal conductivity, Cp is the Dulong-Petit heat capacity, λ is thermal diffusivity, and ρ is sample density. Hall effect and resistivity measurements were done at the Jet Propulsion Laboratory via the Van der Pauw method with a 100 mA current and a 1.0 T magnet. Instrumental set up is described elsewhere.[41] Seebeck coefficients were measured at the Jet Propulsion Laboratory with a custom light pipe instrument via the two-probe method with tungsten-niobium thermocouples under high vacuum.[42] *zT* estimates are obtained from polynomial fits of transport data. Data shown are third order polynomial fits and raw data are given in appendix 4.7.

4.4 Results and Discussion

Sample Purity and Composition

The synthesis of phase-pure $Eu_{11-x}Na_xZn_4Sn_2As_{12}$ (x = 0, 0.05, 0.075, 0.1) via the elements or the elements and some amount of EuH_2 were unsuccessful. We found that by replacing Eu metal or metal hydride with EuAs (ICSD- 26265, the Na_2O_2 structure type)[32] as a reactive precursor produced phase-pure $Eu_{11-x}Na_xZn_4Sn_2As_{12}$ (x = 0, 0.05, 0.075, 0.1). Initially, samples were prepared for x = 0.05, 0.1, 0.2, 0.3, but the samples with higher Na content (x = 0.2, 0.3) sublimed Na vapor when heated, suggesting x = 0.1 is the maximum amount of Na that could be incorporated into the structure. This reactive precursor may be applied to other Eu-based compounds to enable high-quality synthesis of complex phases.

Zintl-Klemm electron counting rules can be used to rationalize $Eu_{11}Zn_4Sn_2As_{11}$ as a charge-balanced semiconductor by considering the $[Sn_2As_6]^{12-}$ units as Sn^0 (four bonds) and As^{2-} (one bonds), the $[Zn_2As_3]^{5-}$ sheets as As^- (two bonds) and Zn^- (three bonds) and the cations as isolated Eu^{2+}.[18] The compound was initially described as a monoclinic structure in the space group *C2/c* with site disorder and a stacking perturbation.[18] However, reinvestigation of the $Eu_{11}Zn_4Sn_2As_{11}$ structure showed that it is better described as a commensurately modulated structure in the $R\bar{3}m$ space group with a wave vector (Q) of 2/3, 2/3, 0.[19] Upon substitution of Eu with Sr, the symmetry is reduced and the structure is also described as a commensurately modulated structure in the $R\bar{3}$ space group but with a modified wave vector of 1/3, 1/3, 1/2. The $C2/c$ space group provides an average structure with disorder (shown in Figure 1 for simplicity and to emphasize the layered nature of the compound), but the rhombohedral space groups more accurately describe the modulation and partial site occupancy. In both rhombohedral space

groups, the Zn and Sn sites have vacancies, and their site occupancies are 2/3 and 1/3, respectively. For the $[Zn_2As_3]^{5-}$ sheets, the vacancies give rise to substitutional disorder and in the isolated Sn_2As_6 ethane-like units, there is a Eu site that is situated along the Sn–Sn bond such that the Sn site is occupied 1/3 of the time and the Eu site is occupied 2/3 of the time and can be described as a substitutional disorder. The more ionic and slightly larger Sr cation (ionic radii 1.18 Å) substitutes on the Eu sites between the $[Zn_2As_3]^{5-}$ sheets and those within the $[Sn_2As_6]^{12-}$ units and in a slightly shifted position relative to the Eu site that is found between the $[Zn_2As_3]^{5-}$ sheets and the $[Sn_2As_6]^{12-}$ units.[19] The Na ion is smaller (ionic radii 1.02 Å) and more electropositive than Eu (ionic radii, 2+, 1.17 Å) and could also exhibit site preference.

PXRD patterns of ground pellets of $Eu_{11-x}Na_xZn_4Sn_2As_{12}$ (x = 0, 0.05, 0.075, 0.1) are compared to the calculated $R\bar{3}m$ (bottom) and $R\bar{3}$ (second from bottom) patterns in Figure 4-2. The diffraction patterns for both space groups are nearly identical. The best refinement for the undoped sample was obtained using the $R\bar{3}m$ CIF and the best refinement for the Na-doped samples were obtained using the $R\bar{3}$ CIF. This suggests that Na-doping alters the symmetry and wave vector in a similar manner to Sr substitution. The small amount of Na dopant prevented further analysis of any possible site preference. A slight decrease in lattice parameters with Na was observed due to the smaller size of Na compared to Eu. Because of the layered nature of the structure, we also checked for preferred orientation of the pressed pellet and none was observed in the powder diffraction.

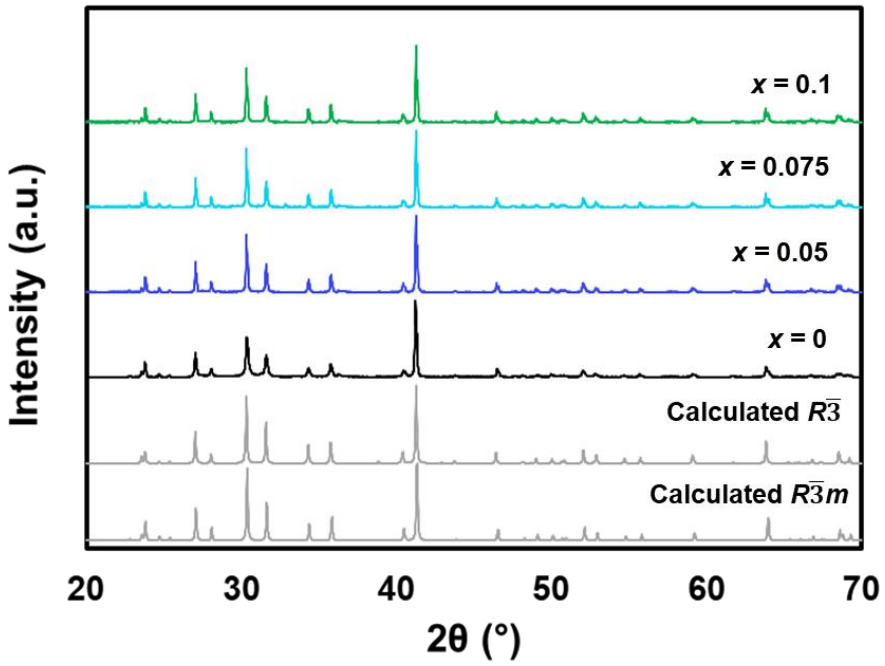


Figure 4-2. PXRD patterns for $Eu_{11-x}Na_xZn_4Sn_2As_{12}$ (x = 0, 0.05, 0.075, 0.1) compared to the calculated $R\bar{3}m$ pattern (bottom) and $R\bar{3}$ (second from bottom).

Figure 4-3 shows the SEM micrographs and EDS elemental maps for the sample with the largest amount of Na (x = 0.1). The backscattered electron image shows that the sample is uniform and there are no obvious pockets of a secondary phase. The elemental maps show spatial distribution of the element of interest and indicate a homogenous sample. The samples show similarly homogeneous distribution of elements with no obvious secondary phases. Na was not quantified as it was below the detection limit (<0.3 atomic %).

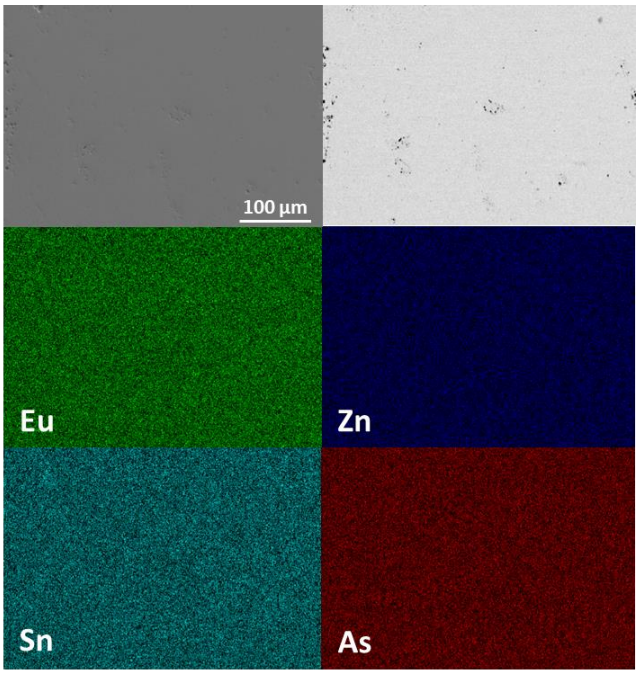


Figure 4-3. SEM micrographs from secondary electrons (top left) and backscattered electrons (top right), and EDS elemental maps (bottom) for a pressed pellet of $Eu_{11-x}Na_xZn_4Sn_2As_{12}$ with greatest Na content, $x = 0.1$.

Thermal Transport Properties

Total thermal conductivity for $Eu_{11-x}Na_xZn_4Sn_2As_{12}$ ($x = 0$, 0.05, 0.075, 0.1) is low as expected given the complex structure and crystallographic disorder (Figure 4-4).[2,43,44] As Na content increases, total thermal conductivity increases slightly, consistent with greater electronic contribution expected for doped samples, but remains lower than 0.8 W/m-K at 300 K for all compositions and falls to ~0.5 W/m-K at 675 K. These values are lower than those reported for the related $A_{11}Cd_6Pn_{12}$ systems and comparable to or lower than those reported for leading thermoelectric materials such as the Zintl phases $Yb_{14}MnSb_{11}$, Eu_2ZnSb_2, A_2CdSb_2, $Yb_{21}Mn_4Sb_{18}$, and $YbZn_2Sb_2$ as well as PbTe and $La_{3-x}Te_4$.[12–15,44–48] The lattice and electronic components of the thermal conductivity were not calculated because of difficulty in accurately

determining the Lorenz number due to the complex electronic transport in this lightly doped semiconductor.[49,50]

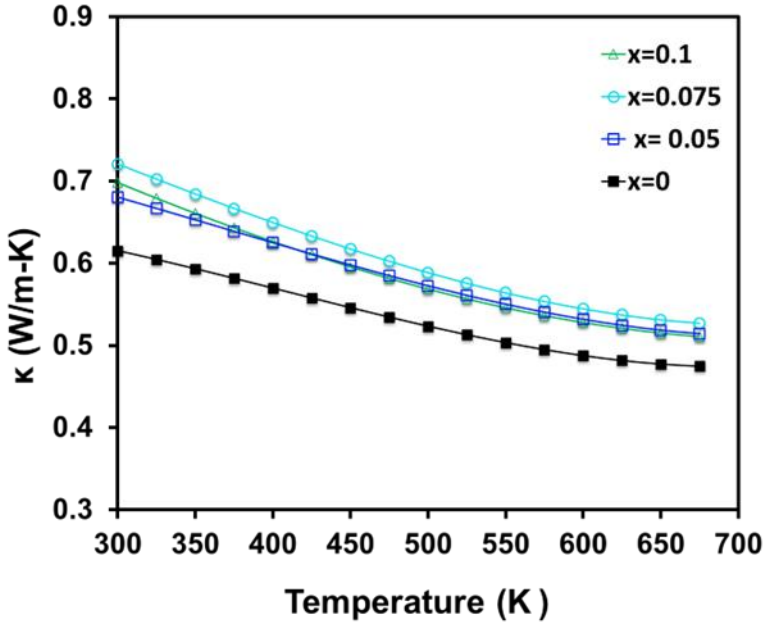


Figure 4-4. Temperature-dependent thermal conductivity from 300–675 K for $Eu_{11-x}Na_xZn_4Sn_2As_{12}$ (x = 0, 0.05, 0.075, 0.1).

Electronic Transport Properties

Experimental hole concentrations determined via the Hall effect for $Eu_{11-x}Na_xZn_4Sn_2As_{12}$ for x = 0.075, 0.1 are provided in Table 4-1. The carrier concentrations increase with Na, consistent with expectation for replacing Eu^{2+} with Na^+ in this p-type semiconductor. The relatively low starting carrier concentration suggests few intrinsic defects and is attributed to the precise stoichiometric control offered by the binary synthesis method.[31] Peak *zTs* typically occur at carrier concentrations between 10^{19} and 10^{20} carriers per cm^3, depending on the system;

however, attempts to further increase the number of carriers via Na-doping were unsuccessful and the solubility limit of Na was found to be $x \approx 0.1$.

Table 4-1. Hall Carrier Concentration and Mobility of $Eu_{11-x}Na_xZn_4Sn_2As_{12}$ at 300 K

x	**Carrier Concentration (cm^{-3})**	**Hall Mobility (cm^2/Vs)**
0.075	1.0×10^{18}	10
0.1	1.1×10^{18}	15

The observed increase in carrier concentration is accompanied by an increase in Hall mobility (Table 4-1), an anomalous result that could be due to changes in microstructure and leads to a nearly five-fold reduction in room temperature electrical resistivity with Na-doping, from ~1900 mΩcm for the undoped sample to ~400 mΩcm for $x = 0.1$ at 300 K (Figure 4-5a). Resistivity measurements show that $Eu_{11}Zn_4Sn_2As_{12}$ is a highly resistive semiconductor, as expected from Zintl-Klemm electron counting rules.

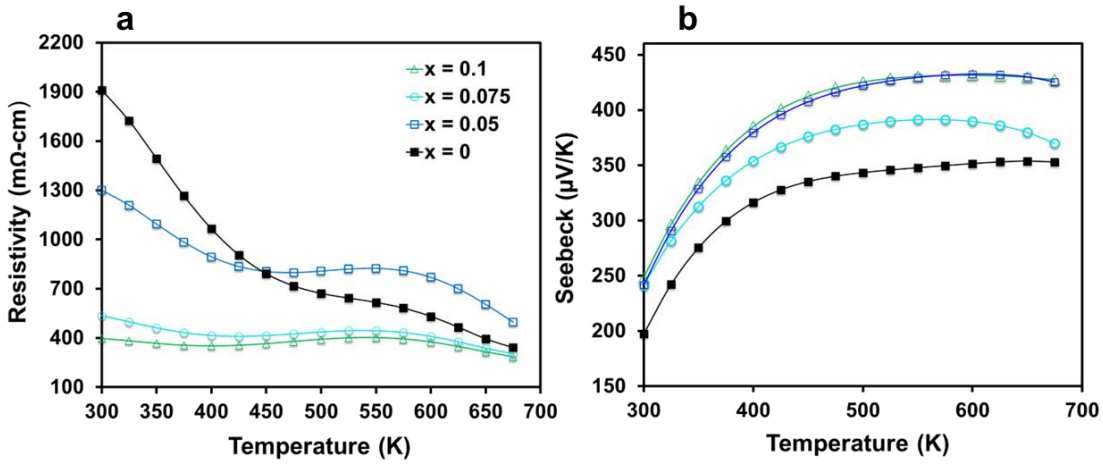


Figure 4-5. Temperature-dependent (a) electrical resistivity and (b) Seebeck coefficients from 300- 675 K for $Eu_{11-x}Na_xZn_4Sn_2As_{12}$ (x = 0, 0.05, 0.075, 0.1). The legend is the same for both plots.

Seebeck coefficients (Figure 4-5b) are high and positive across the entire series (from ~200 to ~450 μV/K) and increase with temperature up to ~600 K, giving a Goldsmid-Sharp band gap of 0.51 eV for x = 0 that agrees reasonably well with the calculated value of 0.6 eV (see next section. The Seebeck coefficients increase as Na content increases, which is unexpected due to the inverse relationship between Seebeck coefficient and carrier concentration in systems with a single dominant band.[44] While this result could be due to microstructure effects, such as commensurate modulation, dislocations, grain boundaries, impurities, or Na site preference, which have been shown to dominate charge transport in a variety of materials,[51–53] it could also be attributed to a rapidly changing effective mass with doping, which can be an indication of a highly anisotropic Fermi surface.[6,8,44] In 2D electronic structures, the effective mass in the direction parallel to the length of the tube is infinite, limiting electronic transport to the two lighter directions.[6,7] This can decouple the Seebeck coefficient and electrical resistivity effective masses because resistivity is dominated by the lightest mass direction, while the Seebeck coefficient is governed by the average effective mass, making it possible to increase the Seebeck

coefficient without increasing electrical resistivity.[6] This effect has been predicted to yield high power factor in AZn_2Sb_2 Zintl phases (A = Ca, Sr, Ba),[54] $Ca_5In_2Sb_6$,[55] Heusler compounds Fe_2YZ (*Y* = Ti, Zr, Hf, and *Z* = Si, Ge, Sn),[7] and lead chalcogenides.[8,9]

Parker et al. explains the increase in thermopower with decreasing dimensionality in terms of increasing Fermi surface volume.[9] For a given E_F, the carrier concentration (or volume of the Fermi surface) is larger in a 2D cylinder as compared to a 3D sphere because it is proportional to the length of the cylinder, which gives a much larger value than the radius of the cylinder or sphere. According to the Mott equation for the Seebeck coefficient, thermopower is inversely proportional to E_F. For a given carrier concentration, E_F is smaller in 2D than in 3D, so the resulting thermopower is larger.[9] As $Eu_{11-x}Na_xZn_4Sn_2As_{12}$ is more heavily doped, the Fermi surface should become increasingly cylindrical and 2D-like, leading to a higher surface area and greater thermopower.

Weighted mobility and Hall mobility are shown in Figure 4-6. Weighted mobility is the charge carrier mobility weighted by the electronic density of states and is independent of charge carrier concentration. When charge transport is dominated by a single parabolic band and charge carrier concentration is changed via doping, weighted mobility values are expected to be the same for samples at different doping levels. Changing weighted mobility values can indicate nonparabolicity or multi-band transport.[56] Figure 4-6a shows weighted mobility that increases with Na content, suggesting that carrier concentration is not the only variable changing. The weighted mobility increases rapidly with temperature from 300 – 450 K, while the Hall mobility given in Figure 4-6b displays thermally activated transport at low temperatures, consistent with

grain boundary scattering. It is also important to note that the thermally activated Hall mobility is an indication that microstructure influences electronic transport in these samples.

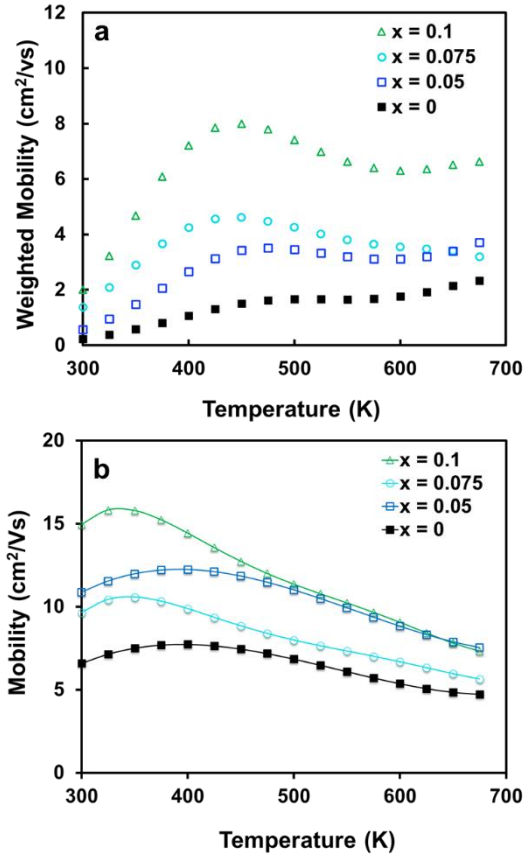


Figure 4-6. Temperature dependent (a) Weighted mobility and (b) Hall mobility for $Eu_{11-x}Na_xZn_4Sn_2As_{12}$ (x = 0, 0.05, 0.075, 0.1) from 300 – 675 K.

Calculated Electronic Structure and Transport Properties

The electronic band structure of $Eu_{11}Zn_4Sn_2As_{12}$ and the corresponding Fermi surfaces at different Fermi levels are shown in Figure 4-7. Note that the band structure in Figure 4-7 is equivalent to that of Devlin et al.,[18] except that a standard k-point path[57] is used and spin-orbit coupling (SOC) is included in the calculation. An indirect band gap of 0.6 eV is calculated for

$Eu_{11}Zn_4Sn_2As_{12}$, in good agreement with the Goldsmid-Sharp gap (~0.51 eV) calculated from the experimental data. The ellipsoidal geometry of the Fermi surfaces near the valence band maximum (VBM) suggests that the transport properties are anisotropic, as expected from the monoclinic space group (*C2/c*) and the layered structure. In addition to the valence band maximum (VBM) at the Γ-point, the band structure and Fermi surface show a secondary valence band at the Z-point which is 60 meV below the VBM, indicating that band convergence may be a route towards optimizing the thermoelectric performance of $Eu_{11}Zn_4Sn_2As_{12}$.

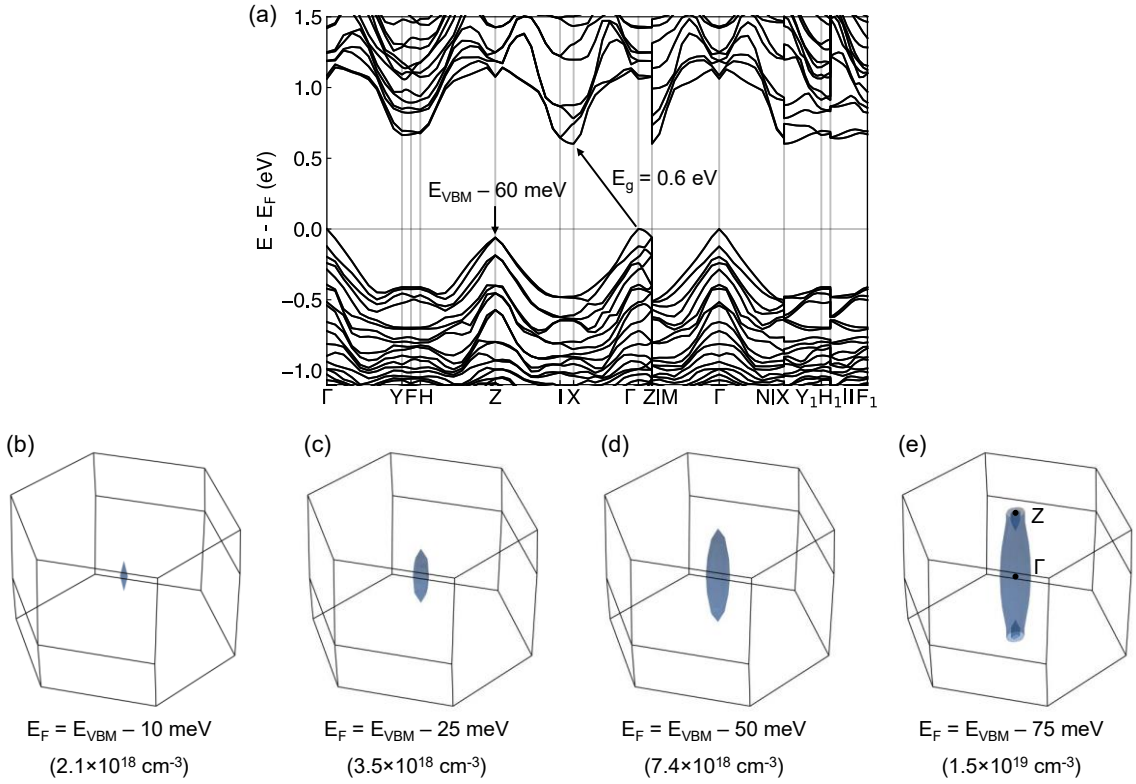


Figure 4-7. (a) Band structure of $Eu_{11}Zn_4Sn_2As_{12}$ calculated with spin-orbit coupling. An indirect band gap of E_g = 0.6 eV forms between the valence band maximum (VBM) at the Γ-point and the conduction band minimum at the X-point. A secondary valence band maximum exists 60 meV below the VBM. (b-e) Fermi surfaces at the listed Fermi levels inside the valence band,

along with the corresponding carrier concentrations at 300 K. The ellipsoidal Fermi surfaces suggest anisotropic electrical transport.

To understand the transport properties of pristine $Eu_{11}Zn_4Sn_2As_{12}$, detailed Boltzmann transport theory-based calculations were run. Since the $Eu_{11}Zn_4Sn_2As_{12}$ samples synthesized in the present study display p-type character, the properties of hole transport using DFT were investigated. The effects of deformation potential scattering by acoustic phonons, inelastic polar optical phonon scattering, and scattering by ionized impurities on charge carrier transport are addressed, as opposed to assuming a constant relaxation time.[58,59] The effects of the three scattering mechanisms on the hole mobility are shown in Figure 4-8a, indicating that hole transport in p-type $Eu_{11}Zn_4Sn_2As_{12}$ is limited by polar optical phonons. The predicted temperature-dependent electrical resistivity and Seebeck coefficient are shown in Figures 4-8b and 8c, along with experimentally-measured values for $x = 0.1$. The temperature dependency of the resistivity does not match between the DFT calculation where resistivity increases up to 700 K when the carrier concentration is 1×10^{18} cm^{-3}, and experiments where resistivity decreases with temperature. This is likely due to grain boundaries and other defects as discussed in more detail below. On the other hand, comparison of the Seebeck coefficient between DFT calculations and experiments suggest that the carrier concentration of the $x = 0.1$ is between 1×10^{18} cm^{-3} and 5×10^{18} cm^{-3}, in agreement with the Hall carrier concentration (Table 4-1). The anisotropy of hole transport is apparent from the direction-dependent resistivity and Seebeck coefficient (Figure 4-8d), as expected from the non-spherical Fermi surface (Figure 4-7). In particular, the electrical resistivity in the z-direction is higher than in the x- and y-directions due to the higher band effective mass in the z-direction, as evidenced by the elongation of the tubular Fermi surface geometry in that direction. Directional Seebeck coefficients and resistivities

highlight the fact that Seebeck coefficients depend on the DOS effective mass, which is not directional, while electrical resistivity depends on the band effective mass, which depends on direction. The effective mass from the Seebeck coefficient is calculated from the linear region of the predicted Pisarenko relation at 300 K (Figure 4-8e) and 500 K (Figure 4-8f), using the formula in Ref.60. We find that the effective mass increases from $0.47m_e$ at 300 K to $0.57m_e$ at 500 K. The calculated effective mass is slightly higher than the experimental value (determined using Seebeck coefficient and carrier concentration) of 0.24 +/- 0.1 m_e at 300 K $x = 0.075$ and 0.1.

Both calculated and experimental resistivities decrease with doping, but their temperature dependence differs (Figure 4-8b). It is important to note that effects on transport properties from grain boundaries, defects, site preference of Na, and commensurate structure modulation are not addressed in the simulated properties. Grain boundary scattering effects often result in a thermally activated decrease in resistivity with temperature, that would be observed especially at lower temperatures.[52] Since the calculated resistivity increases with temperature at low temperatures and the experimental resistivity decreases with temperature (Figure 4-8b), grain boundary scattering—as observed in the Hall mobility in Figure 4-6 discussed above—may cause discrepancies between the DFT predictions and experimental measurements. Grain boundary effects have also been shown to impact Seebeck coefficient in layered structures such as Mg_3Sb_2[51,52] and may explain why experimental Seebeck coefficients increase with doping while theoretical values decrease. Defect chemistry and cation site preference has also been shown to play a major role in electronic transport in layered Zintl phases[14,17,23] and is not considered in the calculations presented here.

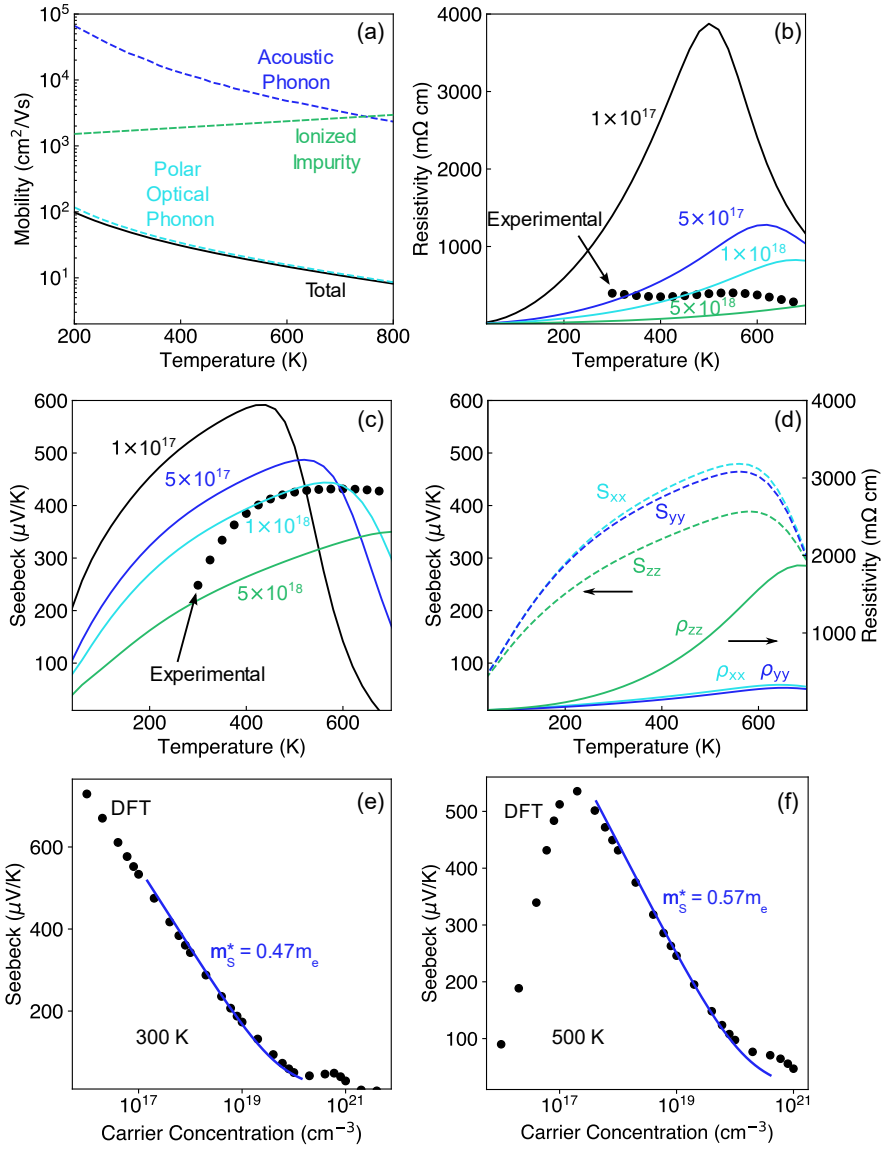


Figure 4-8. (a) Predicted hole mobility in $Eu_{11}Zn_4Sn_2As_{12}$ at a hole concentration of 1×10^{18} cm^{-3}, where scattering by acoustic phonons (blue), ionized impurities (green), and polar optical phonons (cyan) are shown. The predicted temperature-dependent electrical resistivity (b) and Seebeck coefficient (c) are shown for different hole concentrations. The transport properties are averaged over the three Cartesian directions in (b-c), and the direction components are shown in (d) at a carrier concentration of 1×10^{18} cm^{-3}. Pisarenko relations at 300 K (e) and 500 K (f) are used to compute the hole effective mass, calculated using the formula in Ref. 60.

4.5 Summary

Theory and experiment each provide partial understanding of $Eu_{11}Zn_4Sn_2As_{12}$, and when used in conjunction can provide deeper insight into this complex, modulated, layered material. Experimental samples are limited by defects, impurities, and microstructure effects, while theory is simplified, using a rigid band model that does not take Na site preference, defects, or the commensurate modulation of the structure into account. Employing both methods together, we get a fuller picture that helps untangle these effects to understand the intrinsic properties of this compound, as well as the way that defects and microstructure impact thermal and electronic transport. Experimental data reveal low lattice thermal conductivity, high Seebeck coefficient, and electrical resistivity that can be improved through doping, while theoretical results confirm anisotropic transport and a transition to 2D electronic structure when carrier concentration reaches 10^{19} cm^{-3}, and the electronic structure becomes more 2D-like with increasing Na content. Experimental results also reveal the complexity of this layered compound and the major influence that microstructure, site preference, and structural disorder have on electronic properties such as the Seebeck coefficient. Taken together, these results can be used as a roadmap to optimize this promising thermoelectric material by tuning the synthetic method to control microstructure and increasing the carrier concentration to push the Fermi level into the 2D regime.

The unique electronic structure and thermoelectric properties, as well as a new synthetic method to produce Na-doped $Eu_{11}Zn_4Sn_2As_{12}$ is presented. Employing a Eu binary precursor such as EuAs allows for high phase purity and reliable reproducibility of this complex structure. $Eu_{11}Zn_4Sn_2As_{12}$ is a 3D layered Zintl phase that exhibits a 2D electronic structure at carrier

concentrations greater than 1.5 x 10^{19} cm^{-3} due to anisotropic bonding between covalent nets and ionic layers. Experimental measurements are consistent with a complex, nonparabolic band structure. These results offer an initial understanding of a complicated system and guide further improvement of this material. Additional doping on the Zn, Sn, or As sites could take advantage of the 2D electronic transport, dramatically increasing *zT* and making this material promising for a variety of applications. This study also shows that directional bonding in layered Zintl phases with 3D crystal structures give rise to low-dimensional electronic structures, providing a new direction for research on these compounds.

4.6 Acknowledgements

This work was supported by NSF DMR-2001156 and performed in part at the Jet Propulsion Laboratory, California Institute of Technology by Dean Cheikh under contract with the NASA Science Missions Directorate's Radioisotope Power Systems Program. SEM/EDS data were acquired from the Advanced Materials Characterization and Testing laboratory (AMCaT) supported by NSF DMR-1725618 at the University of California, Davis. AKH was supported by the University of California, Davis Dean's Distinguished Graduate Student Fellowship. MYT is funded by the United States Department of Energy through the Computational Science Graduate Fellowship (DOE CSGF) under grant number DE-SC0020347. GJS acknowledges the support of award 70NANB19H005 from the U.S. Department of Commerce, National Institute of Standards and Technology as part of the Center for Hierarchical Materials Design (CHiMaD).This research was supported in part through the computational resources and staff contributions provided for the Quest high performance computing facility at Northwestern University, which is jointly

supported by the Office of the Provost, the Office for Research, and Northwestern University Information Technology.

4.7 Appendix

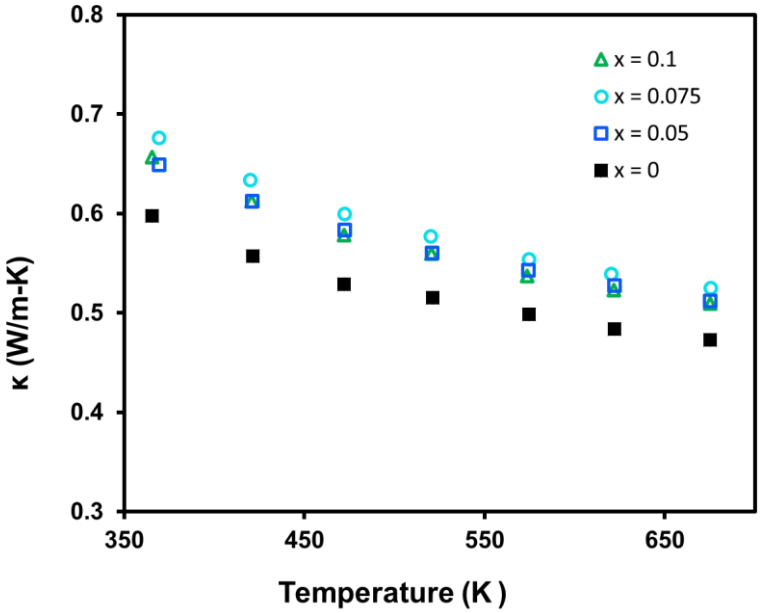


Figure 4-9. Experimental thermal conductivity data.

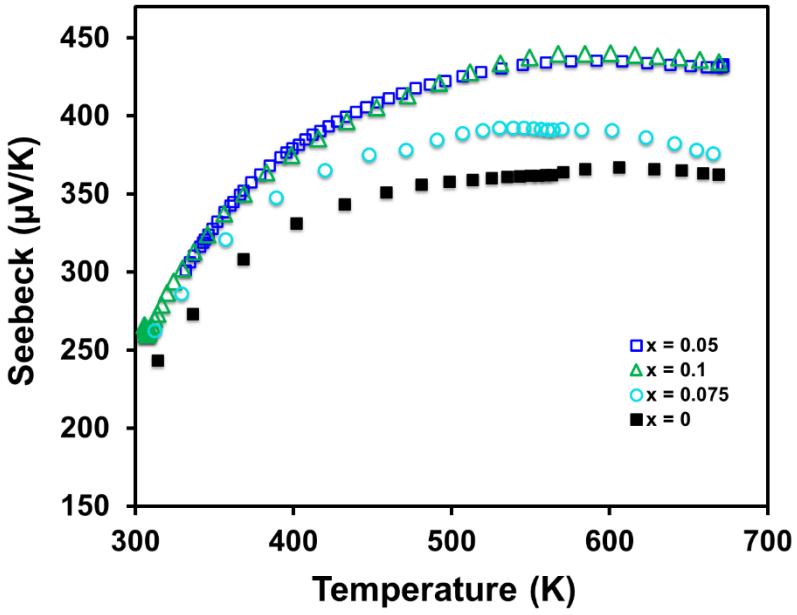


Figure 4-10. Experimental Seebeck coefficient data.

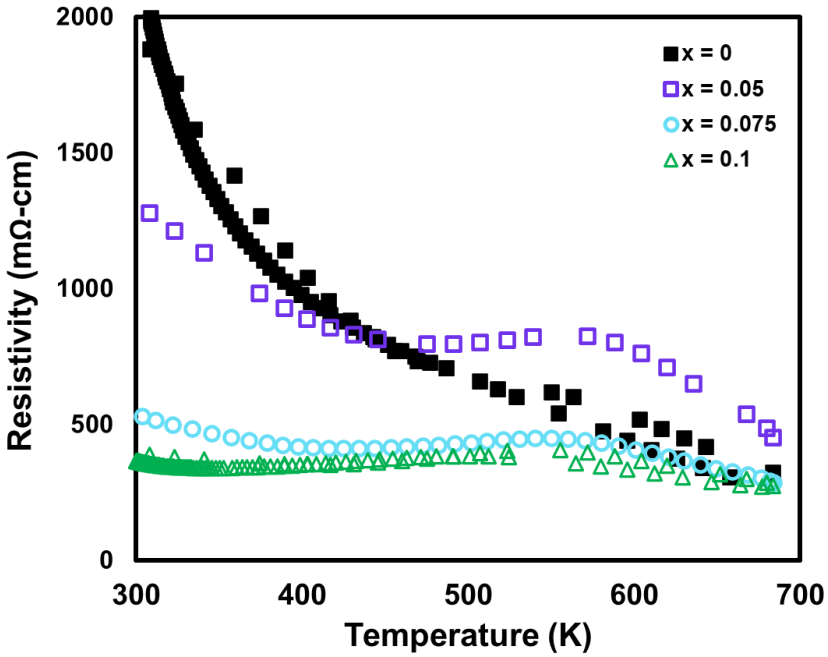


Figure 4-11. Experimental electrical resistivity data.

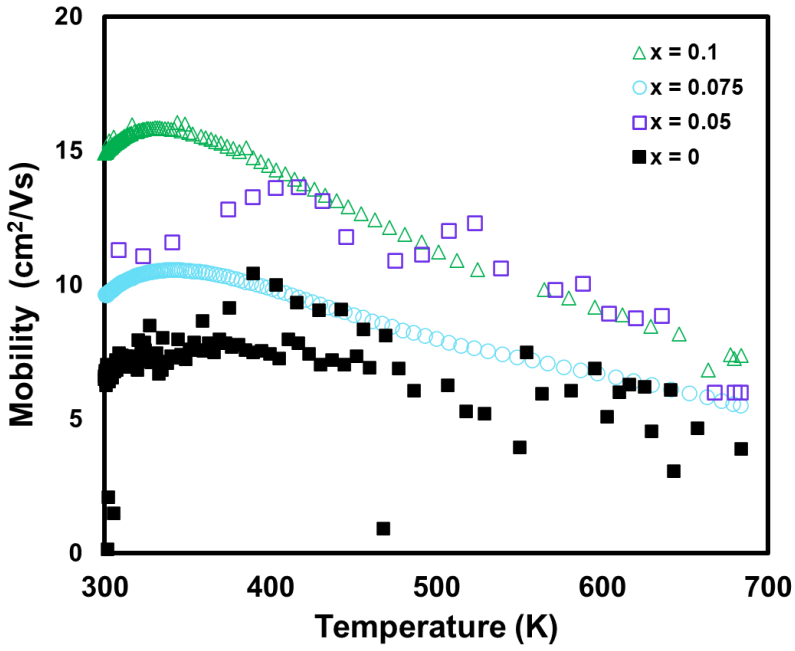


Figure 4-12. Experimental Hall mobility data.

Table 4-2. Selected Rietveld Refinement Statistics for a Typical Powder X-ray Diffraction Pattern of EuAs (ICSD- 26265, the Na_2O_2 structure type)

x		**EuAs**
Unit Cell Parameters	*a*	8.158(1)
	b	6.140(1)
	V	353.92(1)
Rp (%), Rwp (%)	11.01, 12.08	
EuAs (wt %)	97.02	
Eu_3As_4 (wt %)	2.98	

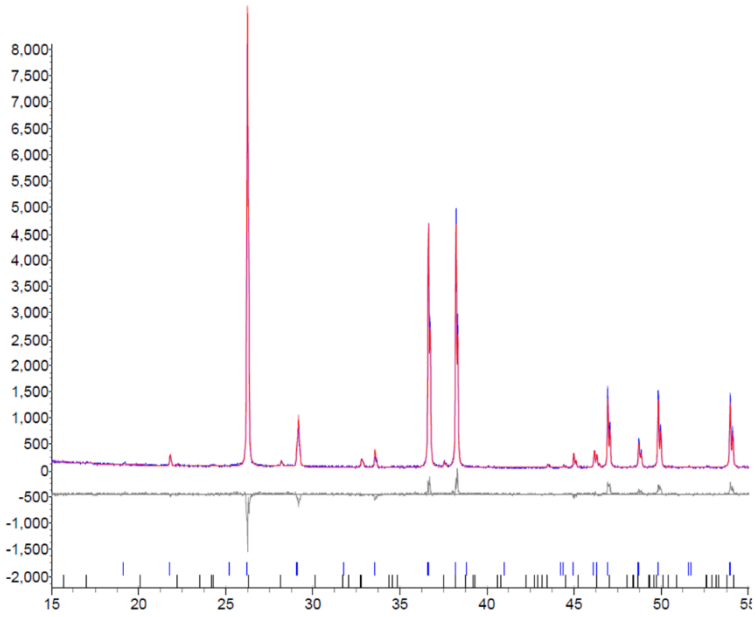


Figure 4-13. A portion of typical Rietveld refinement for EuAs (ICSD- 26265, the Na_2O_2 structure type).[29] Observed data are shown in black, calculated pattern in red, and difference curve in gray. Tick marks indicate EuAs (blue) and Eu_3As_4 (black).

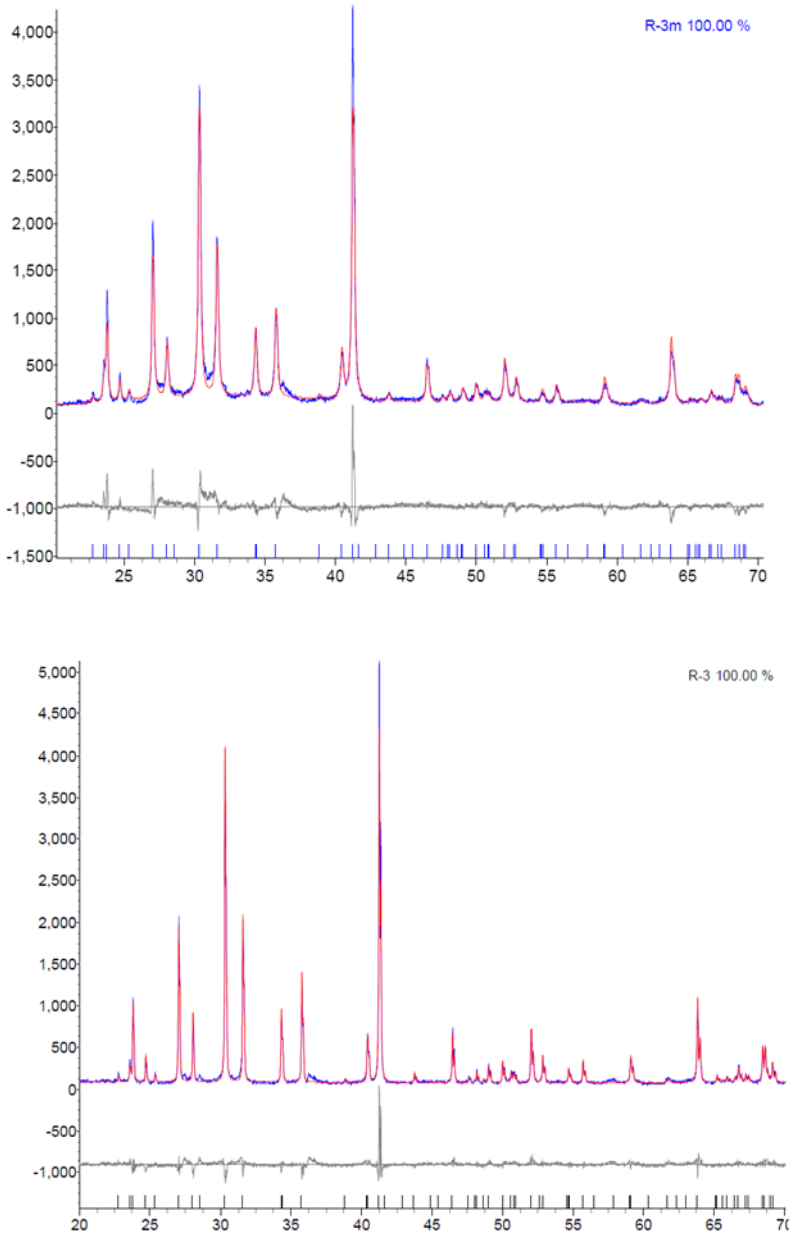


Figure 4-14. A portion of a typical Rietveld refinement for $Eu_{11}Zn_4Sn_2As_{12}$ (top) and $Eu_{10.95}Na_{0.05}Zn_4Sn_2As_{12}$ (bottom) prepared from EuAs. Observed data are shown in black, calculated pattern in red, and difference curve in gray.

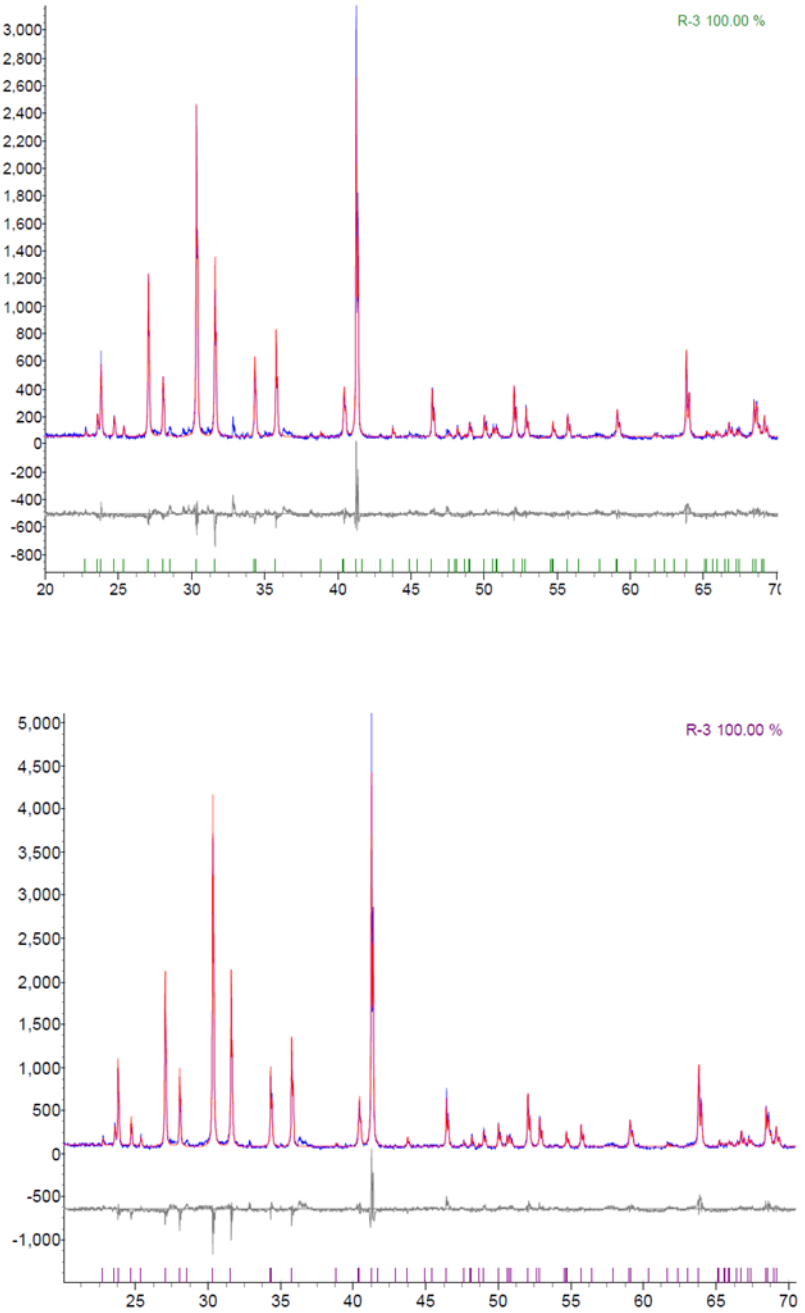


Figure 4-15. A portion of a typical Rietveld refinement for $Eu_{10.925}Na_{0.075}Zn_4Sn_2As_{12}$ (top) and $Eu_{10.9}Na_{0.1}Zn_4Sn_2As_{12}$ (bottom) made from EuAs. Observed data are shown in black, calculated pattern in red, and difference curve in gray.

Table 4-3. Selected Rietveld Refinement Statistics from $Eu_{11-x}Na_xZn_4Sn_2As_{12}$ (x = 0, 0.05, 0.075, 0.1)

X		**0**	**0.05**	**0.075**	**0.1**
Unit Cell Parameters	*a* (Å)	4.3794(2)	4.37661(9)	4.37658(9)	4.37544(7)
	c (Å)	46.865(3)	46.912(1)	46.910(1)	46.926(8)
	V (Å^3)	778.41(4)	778.20(4)	778.13(3)	778.02(3)
Rp (%), Rwp (%)		11.30, 13.96	11.34, 14.54	12.72, 16.63	11.50, 14.56
$Eu_{11}Zn_4Sn_2As_{12}$ (wt %)		100	100	100	100

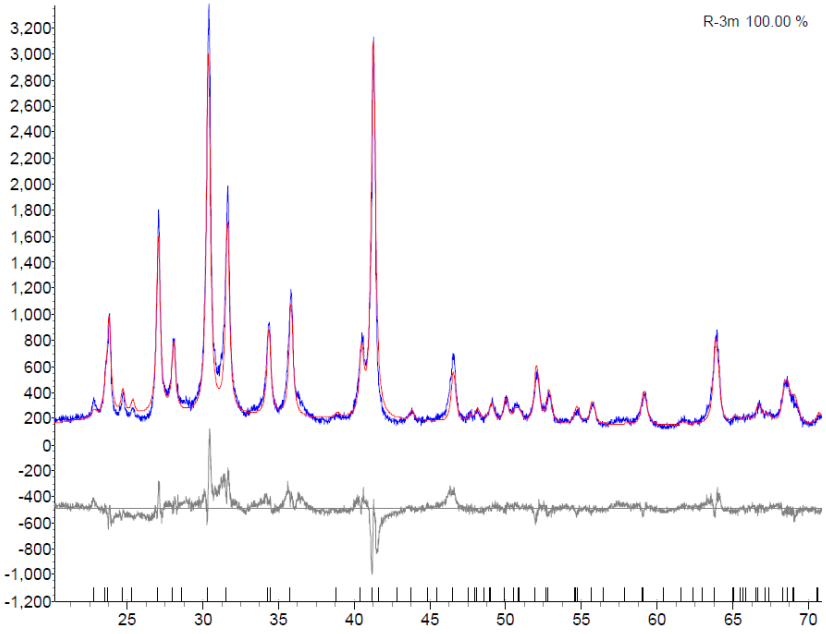
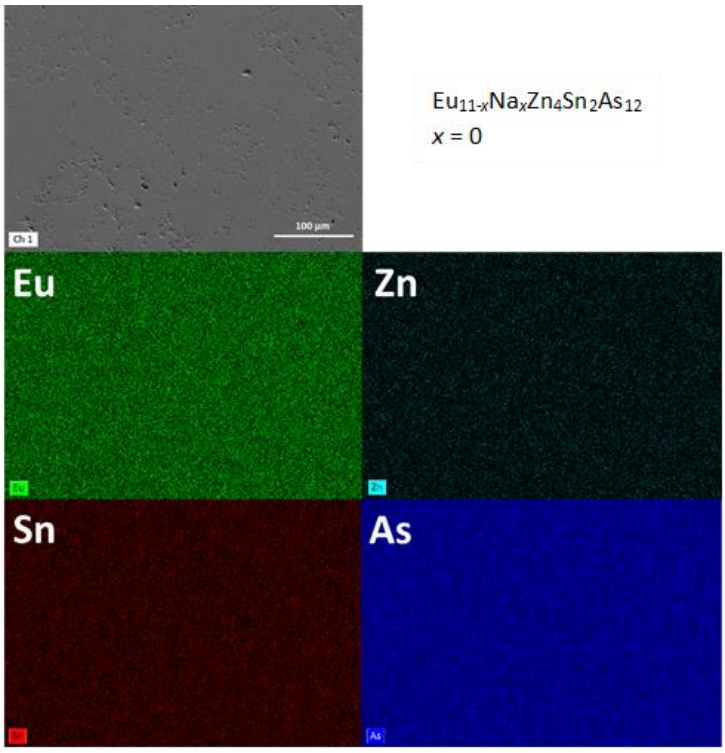
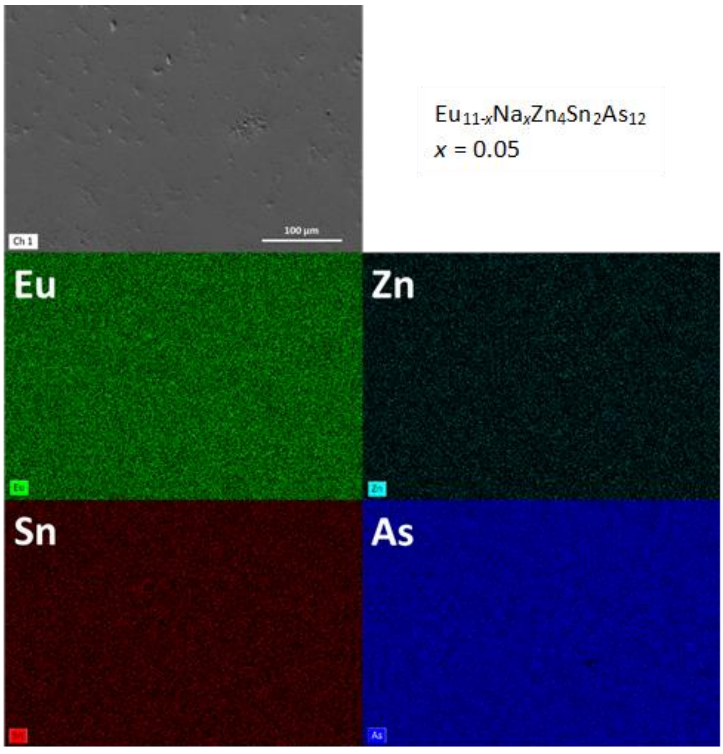


Figure 4-16. A portion of a typical Rietveld refinement for a pressed pellet of $Eu_{11-x}Na_xZn_4Sn_2As_{12}$ made from EuAs. Observed data are shown in black, calculated pattern in red, and difference curve in gray. No preferred orientation is observed.



$Eu_{11-x}Na_xZn_4Sn_2As_{12}$
$x = 0$



$Eu_{11-x}Na_xZn_4Sn_2As_{12}$
$x = 0.05$

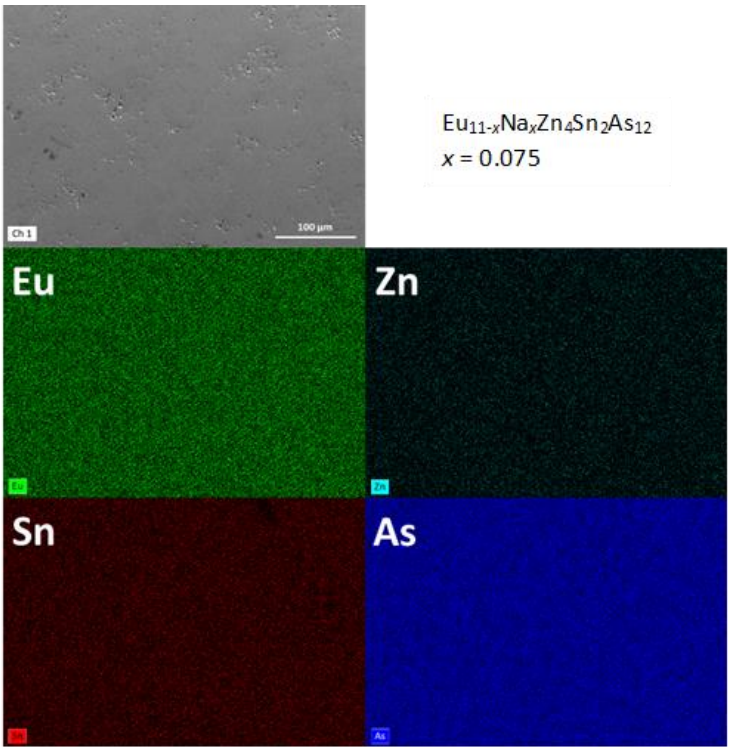


Figure 4-17. Secondary electron SEM micrographs and EDS elemental maps of $Eu_{11-x}Na_xZn_4Sn_2As_{12}$ for x = 0 (top), 0.05 (middle) and 0.075 (bottom). Eu is in green, Zn in turquiose, Sn in red and As in blue.

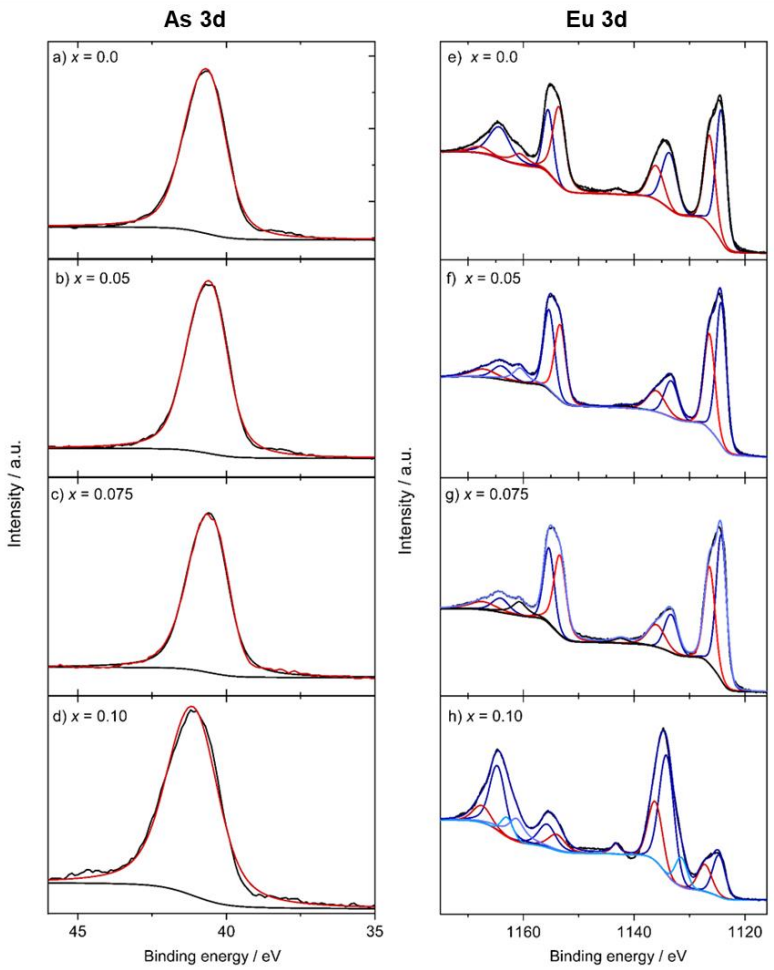


Figure 4-18. XPS spectra in the As 3d (left) and the Eu 3d (right) region.

4.8 References

(1) Du, L.; Hasan, T.; Castellanos-Gomez, A.; Liu, G.-B.; Yao, Y.; Ning Lau, C.; Sun, Z. Engineering Symmetry Breaking in 2D Layered Materials. *Nat. Rev. Phys.* **2021**, *3*, 193–205. https://doi.org/10.1038/s42254-020-00276-0.

(2) Zeier, W. G.; Zevalkink, A.; Gibbs, Z. M.; Hautier, G.; Kanatzidis, M. G.; Snyder, G. J. Thinking Like a Chemist: Intuition in Thermoelectric Materials. *Angew. Chemie - Int. Ed.*

2016, *55* (24), 6826–6841. https://doi.org/10.1002/anie.201508381.

(3) Shuai, J.; Mao, J.; Song, S.; Zhang, Q.; Chen, G.; Ren, Z. Recent Progress and Future Challenges on Thermoelectric Zintl Materials. *Mater. Today Phys.* **2017**, *1*, 74–95. https://doi.org/10.1016/J.MTPHYS.2017.06.003.

(4) Liu, K. F.; Xia, S. Q. Recent Progresses on Thermoelectric Zintl Phases: Structures, Materials and Optimization. *J. Solid State Chem.* **2019**, *270* (November 2018), 252–264. https://doi.org/10.1016/j.jssc.2018.11.030.

(5) Xia, F.; Wang, H.; Jia, Y. Rediscovering Black Phosphorus as an Anisotropic Layered Material for Optoelectronics and Electronics. *Nat. Commun.* **2014**, *5* (4458). https://doi.org/10.1038/ncomms5458.

(6) Dylla, M. T.; Kang, S. D.; Snyder, G. J. Effect of Two-Dimensional Crystal Orbitals on Fermi Surfaces and Electron Transport in Three-Dimensional Perovskite Oxides. *Angew. Chemie - Int. Ed.* **2019**, *58* (17), 5503–5512. https://doi.org/10.1002/anie.201812230.

(7) Bilc, D. I.; Hautier, G.; Waroquiers, D.; Rignanese, G. M.; Ghosez, P. Low-Dimensional Transport and Large Thermoelectric Power Factors in Bulk Semiconductors by Band Engineering of Highly Directional Electronic States. *Phys. Rev. Lett.* **2015**, *114* (13), 1–5. https://doi.org/10.1103/PhysRevLett.114.136601.

(8) Brod, M. K.; Snyder, G. J. Orbital Chemistry of High Valence Band Convergence and Low-Dimensional Topology in PbTe. *J. Mater. Chem. A* **2021**, *9* (20), 12119–12139.

https://doi.org/10.1039/d1ta01273h.

(9) Parker, D.; Chen, X.; Singh, D. J. High Three-Dimensional Thermoelectric Performance from Low-Dimensional Bands. *Phys. Rev. Lett.* **2013**, *110* (14), 1–5. https://doi.org/10.1103/PhysRevLett.110.146601.

(10) Ovchinnikov, A.; Bobev, S. Zintl Phases with Group 15 Elements and the Transition Metals: A Brief Overview of Pnictides with Diverse and Complex Structures. *J. Solid State Chem.* **2019**, *270*, 346–359. https://doi.org/10.1016/j.jssc.2018.11.029.

(11) Baranets, S.; Ovchinnikov, A.; Bobev, S. *Structural Diversity of the Zintl Pnictides with Rare-Earth Metals*, 1st ed.; Elsevier B.V., 2021; Vol. 60. https://doi.org/10.1016/bs.hpcre.2021.07.001.

(12) Cooley, J. A.; Promkhan, P.; Gangopadhyay, S.; Donadio, D.; Pickett, W. E.; Ortiz, B. R.; Toberer, E. S.; Kauzlarich, S. M. High Seebeck Coefficient and Unusually Low Thermal Conductivity Near Ambient Temperatures in Layered Compound $Yb_{2-x}Eu_xCdSb_2$. *Chem. Mater.* **2018**, *30* (2), 484–493. https://doi.org/10.1021/acs.chemmater.7b04517.

(13) Chen, C.; Xue, W.; Li, S.; Zhang, Z.; Li, X.; Wang, X.; Liu, Y.; Sui, J.; Liu, X.; Cao, F.; Ren, Z.; Chu, C.-W.; Wang, Y.; Zhang, Q. Zintl-Phase Eu_2ZnSb_2: A Promising Thermoelectric Material with Ultralow Thermal Conductivity. *Proc. Natl. Acad. Sci.* **2019**, *116* (8), 2831–2836. https://doi.org/10.1073/PNAS.1819157116.

(14) Chanakian, S.; Uhl, D.; Neff, D.; Drymiotis, F.; Park, J.; Petkov, V.; Zevalkink, A.; Bux, S.

Exceptionally High Electronic Mobility in Defect-Rich $Eu_2ZnSb_{2-x}Bi_x$ Alloys. *J. Mater. Chem. A* **2020**, *8* (12), 6004–6012. https://doi.org/10.1039/c9ta14170g.

(15) Zevalkink, A.; Zeier, W. G.; Cheng, E.; Snyder, J.; Fleurial, J. P.; Bux, S. Nonstoichiometry in the Zintl Phase $Yb_{1-\delta}Zn_2Sb_2$ as a Route to Thermoelectric Optimization. *Chem. Mater.* **2014**, *26* (19), 5710–5717. https://doi.org/10.1021/cm502588r.

(16) Pomrehn, G. S.; Zevalkink, A.; Zeier, W. G.; Van De Walle, A.; Snyder, G. J. Defect-Controlled Electronic Properties in AZn_2Sb_2 Zintl Phases. *Angew. Chemie - Int. Ed.* **2014**, *53* (13), 3422–3426. https://doi.org/10.1002/anie.201311125.

(17) Hauble, A. K.; Crawford, C. M.; Adamczyk, J. M.; Wood, M.; Fettinger, J. C.; Toberer, E. S.; Kauzlarich, S. M. Deciphering Defects in $Yb_{2-x}Eu_xCdSb_2$ and Their Impact on Thermoelectric Properties. *Chem. Mater.* **2022**, *34* (20), 9228–9239. https://doi.org/10.1021/acs.chemmater.2c02402.

(18) Devlin, K. P.; Kazem, N.; Zaikina, J. V; Cooley, J. A.; Badger, J. R.; Fettinger, J. C.; Taufour, V.; Kauzlarich, S. M. $Eu_{11}Zn_4Sn_2As_{12}$: A Ferromagnetic Zintl Semiconductor with a Layered Structure Featuring Extended Zn_4As_6 Sheets and Ethane-like Sn_2As_6 Units. *Chem. Mater.* **2018**, *30* (20), 7067–7076. https://doi.org/10.1021/acs.chemmater.8b02749.

(19) Devlin, K.; Zhang, J.; Fettinger, J.; Choi, E. S.; Hauble, A.; Taufour, V.; Hermann, R.; Kauzlarich, S. Deconvoluting the Magnetic Structure of the Commensurately Modulated Quinary Zintl Phase $Eu_{11-x}Sr_xZn_4Sn_2As_{12}$. *Inorg. Chem.* **2021**, *60* (8), 5711–5723. https://doi.org/10.1021/acs.inorgchem.0c03769.

(20) Khoury, J. F.; Schoop, L. M. Chemical Bonds in Topological Materials. *Trends Chem.* **2021**, *3* (9), 700–715. https://doi.org/10.1016/j.trechm.2021.04.011.

(21) Kong, D.; Randel, J. C.; Peng, H.; Cha, J. J.; Meister, S.; Lai, K.; Chen, Y.; Shen, Z.-X.; Manoharan, H. C.; Cui, Y. Topological Insulator Nanowires and Nanoribbons. **2010**, *10*, 329–333. https://doi.org/10.1021/nl903663a.

(22) Putz, M. V; Ori, O. Molecules Bondonic Effects in Group-IV Honeycomb Nanoribbons with Stone-Wales Topological Defects. *Molecules* **2014**, *19*, 4157–4188. https://doi.org/10.3390/molecules19044157.

(23) Yao, H.; Chen, C.; Xue, W.; Bai, F.; Cao, F.; Lan, Y.; Liu, X.; Wang, Y.; Singh, D. J.; Lin, X.; Zhang, Q. Vacancy Ordering Induced Topological Electronic Transition in Bulk Eu_2ZnSb_2. *Sci. Adv.* **2021**, *7* (6), 1–7. https://doi.org/10.1126/sciadv.abd6162.

(24) Schoop, L. M.; Pielnhofer, F.; Lotsch, B. V. Chemical Principles of Topological Semimetals. **2018**. https://doi.org/10.1021/acs.chemmater.7b05133.

(25) Toriyama, M. Y.; Brod, M. K.; Gomes, L. C.; Bipasha, F. A.; Assaf, B. A.; Ertekin, E.; Snyder, G. J. Tuning Valley Degeneracy with Band Inversion. *J. Mater. Chem. A* **2022**, *10* (3), 1588–1595. https://doi.org/10.1039/d1ta08379a.

(26) Shi, H.; Parker, D.; Du, M. H.; Singh, D. J. Connecting Thermoelectric Performance and Topological-Insulator Behavior: Bi_2Te_3 and Bi_2Te_2Se from First Principles. *Phys. Rev. Appl.* **2015**, *3* (1), 1–10. https://doi.org/10.1103/PhysRevApplied.3.014004.

(27) Chen, L.-C.; Chen, P.-Q.; Li, W.-J.; Zhang, Q.; Struzhkin, V. V; Goncharov, A. F.; Ren, Z.; Chen, X.-J. Enhancement of Thermoelectric Performance across the Topological Phase Transition in Dense Lead Selenide. *Nat. Mater. | 18*. https://doi.org/10.1038/s41563-019-0499-9.

(28) Fu, C.; Sun, Y.; Felser, C.; Affiliations,). Topological Thermoelectrics. *APL Mater.* **2020**, *8*, 40913. https://doi.org/10.1063/5.0005481.

(29) Yang, Y.; Cheng, G.; Blawat, J.; Moseley, D. H.; Wang, H.; Devlin, K. P.; Yu, Y.; Hermann, R. P.; Yao, N.; Jin, R.; Xie, W. Crystal Structure and Magnetic Properties in Semiconducting $Eu_{3-\delta}Zn_xSn_yAs_3$ with Eu-Eu Dimers. *J. Appl. Phys.* **2022**, *132* (4), 0439021–0439028. https://doi.org/10.1063/5.0094013.

(30) Ramarao, S. D.; Singh, A. K.; Subbarao, U.; Peter, S. C. An Overview on the Structural Diversity of Europium Based Ternary Intermetallics. *J. Solid State Chem.* **2020**, *281* (September 2019), 121048. https://doi.org/10.1016/j.jssc.2019.121048.

(31) Justl, A. P.; Cerretti, G.; Bux, S. K.; Kauzlarich, S. M. 2 + 2 = 3: Making Ternary Phases through a Binary Approach. *Chem. Mater.* **2022**, *34* (3), 1342–1355. https://doi.org/10.1021/acs.chemmater.1c04031.

(32) Iandelli, A.; Franceschi, E. On the Crystal Structure of the Compounds CaP, SrP, CaAs, SrAs and EuAs. *J. Less-Common Met.* **1973**, *30* (2), 211–216. https://doi.org/10.1016/0022-5088(73)90107-0.

(33) Bruker AXS. TOPAS Version 5, 2014.

(34) Kresse, G.; Furthmüller, J. Efficiency of Ab-Initio Total Energy Calculations for Metals and Semiconductors Using a Plane-Wave Basis Set. *Comput. Mater. Sci.* **1996**, *6* (1), 15–50. https://doi.org/10.1016/0927-0256(96)00008-0.

(35) Kresse, G.; Furthmüller, J. Efficient Iterative Schemes for Ab Initio Total-Energy Calculations Using a Plane-Wave Basis Set. *Phys. Rev. B - Condens. Matter Mater. Phys.* **1996**, *54* (16), 11169–11186. https://doi.org/10.1103/PhysRevB.54.11169.

(36) Blöchl, P. E. Projector Augmented-Wave Method. *Phys. Rev. B* **1994**, *50* (24), 17953–17979. https://doi.org/10.1103/PhysRevB.50.17953.

(37) Kresse, G.; Joubert, D. From Ultrasoft Pseudopotentials to the Projector Augmented-Wave Method. *Phys. Rev. B - Condens. Matter Mater. Phys.* **1999**, *59* (3), 1758–1775. https://doi.org/10.1103/PhysRevB.59.1758.

(38) Perdew, J. P.; Burke, K.; Ernzerhof, M. Generalized Gradient Approximation Made Simple. *Phys. Rev. Lett.* **1996**, *77* (18), 3865–3868. https://doi.org/10.1103/PhysRevLett.77.3865.

(39) Ganose, A. M.; Park, J.; Faghaninia, A.; Woods-Robinson, R.; Persson, K. A.; Jain, A. Efficient Calculation of Carrier Scattering Rates from First Principles. *Nat. Commun.* **2021**, *12* (1). https://doi.org/10.1038/s41467-021-22440-5.

(40) Pack, J. D.; Monkhorst, H. J. “special Points for Brillouin-Zone Integrations”-a Reply. *Phys. Rev. B* **1977**, *16* (4), 1748–1749. https://doi.org/10.1103/PhysRevB.16.1748.

(41) Borup, K. A.; Toberer, E. S.; Zoltan, L. D.; Nakatsukasa, G.; Errico, M.; Fleurial, J.-P.; Iversen, B. B. Measurement of the Electrical Resistivity and Hall Coefficient at High Temperatures. *Rev. Sci. Instrum* **2012**, *83* (123902), 123902. https://doi.org/10.1063/1.4770124.

(42) Wood, C.; Zoltan, D.; Stapfer, G. Measurement of Seebeck Coefficient Using a Light Pulse. *Rev. Sci. Instrum.* **1985**, *56* (5), 719–722. https://doi.org/10.1063/1.1138213.

(43) Zevalkink, A.; Smiadak, D. M.; Blackburn, J. L.; Ferguson, A. J.; Chabinyc, M. L.; Delaire, O.; Wang, J.; Kovnir, K.; Martin, J.; Schelhas, L. T.; Sparks, T. D.; Kang, S. D.; Dylla, M. T.; Snyder, G. J.; Ortiz, B. R.; Toberer, E. S. A Practical Field Guide to Thermoelectrics: Fundamentals, Synthesis, and Characterization. *Appl. Phys. Rev.* **2018**, *5* (2), 021303. https://doi.org/10.1063/1.5021094.

(44) Snyder, G. J.; Toberer, E. S. Complex Thermoelectric Materials. *Nat. Mater.* **2010**, *7* (February), 101–110. https://doi.org/10.1142/9789814317665_0016.

(45) Deng, P.-Y.; Wang, K.-K.; Du, J.-Y.; Wu, H.-J.; Deng, P.-Y. H.; Wu, -J; Wang, K.-K.; Du, J.-Y. From Dislocation to Nano-Precipitation: Evolution to Low Thermal Conductivity and High Thermoelectric Performance in n-Type PbTe. **2020**. https://doi.org/10.1002/adfm.202005479.

(46) He, A.; Bux, S. K.; Hu, Y.; Uhl, D.; Li, L.; Donadio, D.; Kauzlarich, S. M. Structural Complexity and High Thermoelectric Performance of the Zintl Phase: $Yb_{21}Mn_4Sb_{18}$. *Chem. Mater.* **2019**, *31* (19), 8076–8086. https://doi.org/10.1021/acs.chemmater.9b02671.

(47) Chen, C.; Li, X.; Xue, W.; Bai, F.; Huang, Y.; Yao, H.; Li, S.; Zhang, Z.; Wang, X.; Sui, J.; Liu, X.; Cao, F.; Wang, Y.; Zhang, Q. Manipulating the Intrinsic Vacancies for Enhanced Thermoelectric Performance in Eu_2ZnSb_2 Zintl Phase. *Nano Energy* **2020**, *73* (March), 1047711–1074418. https://doi.org/10.1016/j.nanoen.2020.104771.

(48) Devlin, K. P.; Chen, S.; Donadio, D.; Kauzlarich, S. M. Solid Solution $Yb_{2-x}Ca_xCdSb_2$: Structure, Thermoelectric Properties, and Quality Factor. *Inorg. Chem.* **2021**, *60* (17), 13596–13606. https://doi.org/10.1021/acs.inorgchem.1c01906.

(49) Kim, H. S.; Gibbs, Z. M.; Tang, Y.; Wang, H.; Snyder, G. J. Characterization of Lorenz Number with Seebeck Coefficient Measurement. *APL Mater.* **2015**, *3* (4), 1–6. https://doi.org/10.1063/1.4908244.

(50) Gibbs, Z. M.; Kim, H.-S.; Wang, H. Band Gap Estimation from Temperature Dependent Seebeck Measurement—Deviations from the 2e|S|maxTmax Relation. *Appl. Phys. Lett* **2015**, *106*, 22112. https://doi.org/10.1063/1.4905922.

(51) Jiahong Kuo, J.; Dongmin Kang, S.; Kazuki Imasato, A.; Tamaki, H.; Ohno, S.; Tsutomu Kanno, A.; Jeffrey Snyder, G. Grain Boundary Dominated Charge Transport in Mg_3Sb_2-Based Compounds. *Energy Environ. Sci* **2018**, *11*, 429. https://doi.org/10.1039/c7ee03326e.

(52) Wood, M.; Kuo, J. J.; Imasato, K.; Snyder, G. J. Improvement of Low-Temperature ZT in a Mg_3Sb_2–Mg_3Bi_2 Solid Solution via Mg-Vapor Annealing. *Adv. Mater.* **2019**, *31* (35), 1–5. https://doi.org/10.1002/adma.201902337.

(53) Tan, G.; Zhao, L. D.; Kanatzidis, M. G. Rationally Designing High-Performance Bulk Thermoelectric Materials. *Chem. Rev.* **2016**, *116* (19), 12123–12149. https://doi.org/10.1021/acs.chemrev.6b00255.

(54) Sun, J.; Singh, D. J. Thermoelectric Properties of AMg_2X_2, AZn_2Sb_2 (A = Ca, Sr, Ba; X = Sb, Bi), and Ba_2ZnX_2 (X = Sb, Bi) Zintl Compounds. *J. Mater. Chem. A* **2017**, *5* (18), 8499–8509. https://doi.org/10.1039/c6ta11234j.

(55) Smiadak, D. M.; Claes, R.; Perez, N.; Marshall, M.; Peng, W.; Chen, W.; Hautier, G.; Schierning, G.; Zevalkink, A. Quasi-1D Electronic Transport and Isotropic Phonon Transport in the Zintl $Ca_5In_2Sb_6$. *Mater. Today Phys.* **2022**, *22*, 100597. https://doi.org/10.1016/j.mtphys.2021.100597.

(56) Snyder, G. J.; Snyder, A. H.; Wood, M.; Gurunathan, R.; Snyder, B. H.; Niu, C. Weighted Mobility. *Adv. Mater.* **2020**, *32* (2001537), 1–5. https://doi.org/10.1002/adma.202001537.

(57) Setyawan, W.; Curtarolo, S. High-Throughput Electronic Band Structure Calculations: Challenges and Tools. *Comput. Mater. Sci.* **2010**, *49* (2), 299–312. https://doi.org/10.1016/j.commatsci.2010.05.010.

(58) Chen, W.; Pöhls, J. H.; Hautier, G.; Broberg, D.; Bajaj, S.; Aydemir, U.; Gibbs, Z. M.; Zhu, H.; Asta, M.; Snyder, G. J.; Meredig, B.; White, M. A.; Persson, K.; Jain, A. Understanding Thermoelectric Properties from High-Throughput Calculations: Trends, Insights, and Comparisons with Experiment. *J. Mater. Chem. C* **2016**, *4* (20), 4414–4426.

https://doi.org/10.1039/c5tc04339e.

(59) Katsura, Y.; Kumagai, M.; Kodani, T.; Kaneshige, M.; Ando, Y.; Gunji, S.; Imai, Y.; Ouchi, H.; Tobita, K.; Kimura, K.; Tsuda, K. Data-Driven Analysis of Electron Relaxation Times in PbTe-Type Thermoelectric Materials. *Sci. Technol. Adv. Mater.* **2019**, *20* (1), 511–520. https://doi.org/10.1080/14686996.2019.1603885.

(60) Snyder, G. J.; Pereyra, A.; Gurunathan, R. Effective Mass from Seebeck Coefficient. *Adv. Funct. Mater.* **2022**, *32* (20), 1–6. https://doi.org/10.1002/adfm.202112772.

Chapter 5: Electride or Semiconductor? Mapping the structural and electronic transitions in $Yb_5Sb_3H_x$ using theory and thermoelectric properties

Ashlee K. Hauble, [1] Tanner Q. Kimberly,[1] Kamil Ciesielski,[2] Maxwell G. Wright,[3] Valentin Taufour, [3] Ping Yu,[1] Eric S. Toberer,[2] and Susan M. Kauzlarich[1]

Affiliations

[1]Department of Chemistry, University of California, One Shields Ave, Davis, California 95616, United States

[2]Department of Physics, Colorado School of Mines, 1500 Illinois St, Golden, CO 80401, United States

[3]Department of Physics and Astronomy, University of California, One Shields Avenue, Davis, California 95616, United States

5.1 Abstract

Electrides are materials that house a localized anionic electron in an empty crystallographic site and have a wide range of applications, including superconductivity, batteries, photonics, and catalysis. Both polymorphs of Yb_5Sb_3 (the orthorhombic Ca_5Sb_3F structure-type and hexagonal Mn_5Si_3 structure-type) are known to be electrides with electrons localized in 0D tetrahedral cavities and 1D octahedral chains, respectively. However, the orthorhombic structure is also thought to be stabilized by an interstitial H that would partially occupy the 0D tetrahedral cavity, accepting the anionic electron that would otherwise occupy the site, making the orthorhombic

structure better described as $Yb_5Sb_3H_x$. This work employs theory and experiment to map the structural and electronic transitions that occur as H is varied in $Yb_5Sb_3H_x$. DFT computations show that the hexagonal structure is energetically favored when $x < 0.25$ and the orthorhombic structure is more stable when $x > 0.2$. Polycrystalline samples of orthorhombic $Yb_5Sb_3H_x$ (x = 0.25, 0.5, 0.75, 1) were synthesized via ball milling and annealing and thermoelectric properties were measured to characterize the electronic transition from electride to charge balanced semiconductor and MAS ^{1}H NMR and PXRD lattice parameters are used to characterize H composition. At lower H content (x = 0.25, 0.5) low charge carrier mobility consistent with localized electride states is observed while at high H content (x = 0.75, 1) high charge carrier mobility consistent with free electrons in a semiconductor is observed. High Seebeck coefficient and low thermal conductivity are also observed for x = 0, which, when paired with the excellent mobility, make it a potentially promising thermoelectric material if charge carrier concentration can be tuned. This work provides understanding into the structure and electronic properties of electride and semiconductor $Yb_5Sb_3H_x$ and opens the door to the use of interstitial impurities to tune thermoelectric properties.

5.2 Introduction

Electrides contain an anionic electron that is trapped in a vacant crystallographic site, independent of any atom in the lattice, and in many cases, interactions between the anionic electrons and the cationic host contribute to the structural stability of the compound.[1] Electrides were originally discovered in organic salts in the 1980s[2] and in the last twenty years, this class of materials has been expanded to include a variety of inorganic compounds with different dimensions of confined electron space (0D cavities, 1D chains, 2D sheets, and 3D structures).[3]

Given that functional properties of electrides are closely linked to the topology of the confined electrons, this structural diversity has generated great interest in electrides for applications such as superconductivity, catalysis, batteries, spintronics, metal-insulator transitions, nonlinear optics, and photonics.[1,3] However, the study of electrides is still in its infancy and as they are better understood, these materials are likely to find applications in a variety of other fields.[1]

Exploration of new electrides via computational screening is becoming increasingly common using a crystal structure prediction tool,[3] since all known electrides contain an excess of highly electropositive cations and the localization of electride states is more extreme when low dimensional cavities are also present.[4] The two "polymorphs" of Yb_5Sb_3 fit this description, as the orthorhombic (*Pnma*) β-Yb_5Sb_3 structure type, or Ca_5Sb_3F structure type contain 0D isolated cavities within Yb_4 tetrahedra and 1D chains of interstitial cavities surrounded by 6Yb cations in the hexagonal (*P6$_3$/mmc*) Mn_5Si_3 or α-Yb_5Sb_3 structure type[4,5]. With 5 Yb^{2+} ions and 3 Sb^{3-} ions, the composition can be written as $(Yb_5Sb_3^{+})(e^{-})$,[6–8] and recent theoretical studies have confirmed that they are electrides.[4,5]

Both structure types are known to host interstitial impurities that can accept the extra electron, making them highly tunable,[6,7] and it has been shown that the orthorhombic β-Yb_5Sb_3 is only stable when an interstitial H or F atom is present.[7] Given this information, the β-Yb_5Sb_3 phase is better described according to composition as $Yb_5Sb_3H_x$, and the structure type was reclassified as Ca_5Sb_3F, a finding that went unknown for many years due to the presence of H as an impurity in commercial alkaline and rare earth metals and the experimental difficulty in identifying H atoms.[8] In this orthorhombic structure type, there are four interstitial cavities in the unit cell that accommodate either a localized, anionic electron or H (or F) atom, and when the

interstitial site is fully occupied, electron counting suggests that Yb_5Sb_3H should be a charge-balanced semiconductor rather than an electride. It is unclear how much H is required to drive the transition from the Mn_5Si_3 structure type to the β-Yb_5Sb_3 type, or how the electronic properties change as H content is increased for $x = 0$ to 1.[5,7,8] A theoretical study on Yb_5Sb_3, Yb_5Sb_3H, and Yb_5Sb_3F showed the presence of four electride bands, one for each anionic electron in the unit cell, in the hypothetical orthorhombic Yb_5Sb_3 (the polyhedra shown in Figure 5-1) that are not present in the charge-balanced Yb_5Sb_3H or Yb_5Sb_3F, supporting the idea that H and F act as electron acceptors and occupy the cavities where the confined electrons would be located.[5] Varying F content in $Yb_5Sb_3F_x$ ($x = 0$, 0.25, 0.5, 0.75, 1) caused the electride bands to disappear one at a time, suggesting the electronic properties can be tuned from electride to semiconductor/insulator by varying F or H content, making this material interesting for a wide variety of applications.

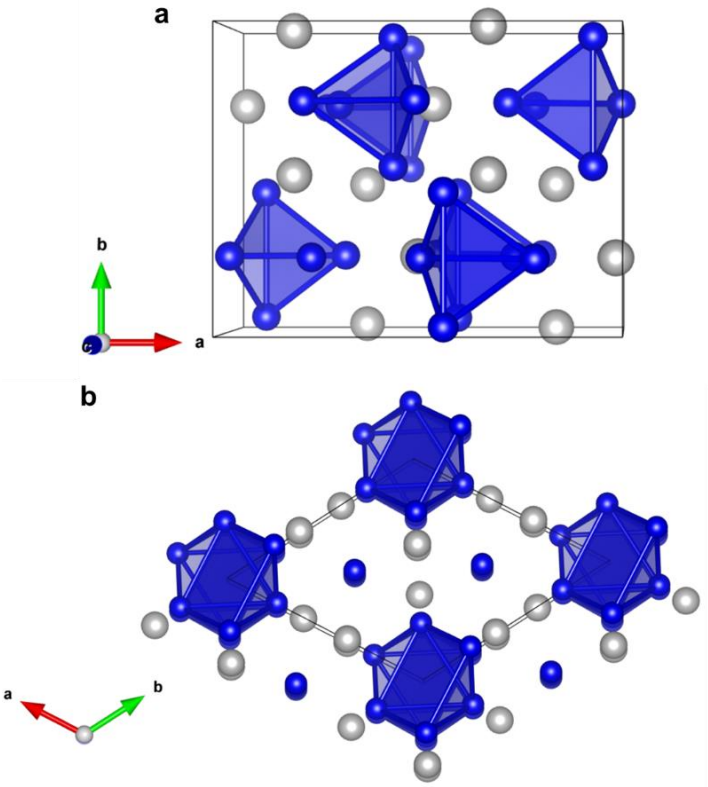


Figure 5-1. The structure of the (a) orthorhombic β- and (b) hexagonal α-structure types of $Yb_5Sb_3H_x$. Yb and Sb atoms are indicated in blue and gray, respectively. The polyhedra show the interstitial 0D cavities that house either an anionic electron or an H^-. H atom is not shown.

The anionic electrons present in electrides are free from onsite electron-nuclear interactions since they are not bound to a particular atom,[5] which can lead to unique properties like high charge carrier mobility,[9] anisotropic electronic properties,[1] low dimensional electronic structures and high electron concentration;[3,10,11] all qualities that are desirable for thermoelectric applications.[12–15] Many ytterbium antimonides have been studied for thermoelectric applications due to their high thermal stability and tunability,[16–20] but neither Yb_5Sb_3 and $Yb_5Sb_3H_x$ have been investigated, despite a high Seebeck coefficient reported for the orthorhombic phase, low electrical resistivity published for the hexagonal phase.[21–23] Additionally, research on Zintl

hydrides and other intermetallics shows that incorporation of small amounts of H can dramatically change the chemical structure and physical properties.[24–26] The rich structural chemistry of Yb_5Sb_3 and $Yb_5Sb_3H_x$ have been widely explored,[4–8,27–30] but the physical and electronic properties have not been well characterized. Here, we show that H content can be tuned to control the chemical and physical properties in orthorhombic $Yb_5Sb_3H_x$ and apply thermoelectric measurements to interrogate the electronic properties across the transition from electride to charge-balanced semiconductor.

5.3 Methods

Computational Methods

First-principles calculations were carried out in the framework of density functional theory (DFT) as implemented in the Quantum ESPRESSO code.[31,32] The exchange-correlation potential was described by the generalized gradient approximation (GGA) in the Perdew-Burke-Ernzerhof (PBE) functional.[33,34] The projector augmented wave (PAW) method was applied to electroncore interactions.[35] Plane waves with a kinetic energy cutoff of 680 eV were used as the basis set and a 4 x 4 x 4 k-point mesh was used for the first Brillouin zone sampling. Lattice structure relaxations were performed such that all residual forces on atoms were smaller than 0.009 eV/Å. Beginning with the experimental crystallographic coordinates of the orthorhombic and hexagonal structures,[21,22] the hydrogenated structures were computationally constructed by adding hydrogen atoms to the interstitial crystallographic sites. Structure relaxations were carried out for x = 0.0, 0.25, 0.5, 0.75, and 1.0 and x = 0.0, 0.5, and 1.0 for the $Yb_5Sb_3H_x$ orthorhombic and hexagonal phases, respectively. Structure relaxations were also done on the elements Yb and Sb, using experimental crystallographic coordinates.[36,37] The total energy of H was calculated by

using one isolated hydrogen with a vacuum space of 8 $Å^3$ to exclude interaction of neighboring images due to periodic boundary conditions. Formation energies were computed as described below.

Synthesis

Polycrystalline synthesis of $Yb_5Sb_3H_x$ (x = 0.25, 0.5, 0.75, 1) was carried out via ball milling the binary precursor Yb_4Sb_3 with stoichiometric amounts of Yb metal (Stanford Materials, 99.99%) and YbH_2 (American Elements, 99.999%) and annealing the milled powder. Yb_4Sb_3 was used instead of the elements as a way to control H content since rare earths are known to contain H impurities[38] and Yb_4Sb_3 is not known to take up H. The binary precursor, Yb metal and YbH_2 were combined in a 65 mL stainless steel ball mill vial with two 12.7 mm diameter stainless steel balls in an Ar-filled glove box. The vial was then sealed in a polyethylene bag and milled in a SPEX 8000 M ball mill for 30 minutes, transferred back into the glove box to be scraped with a stainless-steel spatula and then milled for an additional 30 minutes. The resulting powder was transferred into a Ta tube (7 cm length, 1 cm OD) which was crimped and welded using an arc welder in Ar atmosphere. The Ta tube was flame sealed in an evacuated (< 50 mTorr) quartz ampoule and annealed in a box furnace at 800 °C for 7 days (heating rate 200 °C/hour). Powder X-ray diffraction analysis confirmed that orthorhombic $Yb_5Sb_3H_x$ was synthesized.

The Yb_4Sb_3 precursor was synthesized from stoichiometric amounts of cut Yb pieces (Stanford Materials, 99.99%) and Sb (shot, 5NPlus, 99.999%) that were ground to a powder in an agate mortar and pestle and ball milled using the same milling scheme described above. The

powder was then sealed in a Nb tube and quartz jacket and annealed in a box furnace at 600 °C for 12 hours (heating rate 100 °C hour). The purity of the sample was confirmed by powder X-ray diffraction (PXRD) prior to use.

Spark Plasma Sintering

An agate mortar and pestle were used to grind annealed powders. The powder was sieved and packed into a 12.7 mm ID graphite die (lined with graphite foil) inside an Ar-filled glovebox and placed into the chamber of a Fuji Electronic Industrial Co., LTD Dr. Sinter Jr. for consolidation. The chamber was evacuated to 15 Pa and refilled with Ar(g) to 50,000 Pa to prevent H loss and the sample was cold-pressed to 83 MPa. The pressure was reduced to 23 MPa before increasing the temperature to 900 °C in 25 minutes and then to 950 °C in 1 minute, where it dwelled for 25 minutes. At 750 °C the pressure was again increased to 83 MPa. Densities of the resulting pellets were determined via the Archimedes method to be > 95 % of the theoretical value.

Powder X-ray diffraction

After sintering, the pellets were polished with sandpaper and isopropanol to remove any surface oxide and transferred into a glovebox to be ground in an agate mortar and pestle and sieved for PXRD. The samples were removed from the glovebox and loaded onto a zero background X-ray plate via solvent smear (ethanol) for data collection in a Bruker D8 Eco Advance diffractometer with Cu Kα radiation operating at 40 kV and 25 mA. Diffraction data were collected from 2θ range 15-70° with a 0.015 step size and 1 s scan rate per step. Rietveld refinement was carried out using Topas5 software.

NMR

Solid state ^{1}H MAS NMR experiments were performed on a Bruker AVANCE 500 widebore NMR spectrometer equipped with an 11.74 Tesla magnet and a 2.5-mm MAS probe. The powdered sample was loaded into a 2.5-mm Zirconia rotor with Vespel cap. The rotor weight was measured before and after sample loading so that known amount of powdered sample was directly associated with the ^{1}H NMR signal intensity. The 2.5-mm rotor was span at 26kHz. A direct polarization pulse sequence was used with a 30-degree tip angle and 5 seconds of recycle delay time. A total of 128 scans was acquired for signal averaging, and 100 Hz of line broadening was applied for data processing. The rotor background signal was also recorded at 26 kHz of MAS speed, and the rotor background was deducted from the spectrum of the sample for the data analysis. The source of ^{1}H signal could be from probe stator, and rotor cap.

Scanning Electron Microscopy (SEM) and Energy Dispersive X-ray Spectroscopy (EDS)

The sintered pellets were cut with a Buehler Isomet diamond saw and slices were mounted in epoxy pucks to be polished using sandpaper and a polishing wheel (1 μm colloidal diamond suspension) for SEM and EDS analysis. A Thermo Fisher Quattro ESEM equipped with a Bruker Quantax EDX detector, an Everhart-Thornley detector, and an annular backscattered detector with 15 kV accelerating voltage was used was used to collect elemental maps and electron micrographs.

Thermoelectric properties

Resistivity and Hall measurements were done using Van der Pauw geometry on a home-built system.[39] Measurements were performed using a current of 0.1 A and magnetic field of 1 T. Ohmic contacts were checked using a voltage-current cure before measurement. Seebeck measurements were taken using a custom-built instrument[40] in a low pressure (5 Torr) N_2 atmosphere from 300-775 K with multiple heating and cooling cycles. Graphite foil was placed between the sample and thermocouple to ensure proper electrical contact. A Netzsch Laser Flash Analysis (LFA) Microflash 457 instrument was used for thermal diffusivity measurements and thermal conductivity was calculated with the equation the equation $\kappa = \lambda \rho C_p$ where κ is the thermal conductivity, C_p is the Dulong-Petit heat capacity, λ is the thermal diffusivity, and ρ is the density of the sample. *zT* is estimated from the polynomial fits to the transport data. Data shown are third order polynomial fits and raw data are given in appendix 5.7.

5.4 Results and Discussion

Structure and composition

The structure of orthorhombic $Yb_5Sb_3H_x$ is shown in Figure 5-1. There are four Yb_4 polyhedra in each unit cell that can accommodate either an interstitial H^- ion or an anionic electron.[7,8] The polyhedra are separated by Sb^{3-} ions, as Sb—Sb distances are too long (~4.5) to be considered bonding interactions.[5] Previous work has shown that all Yb cations are Yb^{2+}, giving one excess electron per formula unit (5 x Yb^{2+} = 10 electrons donated, 3 x Sb^{3-} = 9 electrons accepted) and resulting in a formal valence state of $(Yb_5Sb_3)^+(e)^-$ unless H is incorporated, in which case the compound is charge-balanced as Yb_5Sb_3H.[5]

The orthorhombic phase is known to be stabilized by interstitial H. When synthesized with dehydrogenated metals, the hexagonal phase was produced, and when synthesized using YbH_2, the orthorhombic phase was produced, and heating under vacuum at 1100 °C for three weeks caused a transition from the orthorhombic to the hexagonal phase.[7,8] Because commercially available rare-earth metals are known to contain hydrogen impurities[38] and experimental methods of quantifying H content in solid state materials are limited, it is difficult to experimentally determine how much H is required to drive the structural transition from the hexagonal to the orthorhombic phase. Here, we employed total energy calculations to confirm that the orthorhombic phase is H-stabilized and to elucidate the minimum amount of H necessary to produce the orthorhombic structure.

To investigate the chemical stability of the thermoelectric materials, Yb_5Sb_3 and $Yb_5Sb_3H_x$, the formation energies were calculated by density functional theory (DFT) and shown in Figure 5-2. The formation energy is defined by equation 5-1.

Equation 5-1. Formation energy calculation

$$E_{form} = E_{Yb_5Sb_3H_x} - 5E_{Yb} - 3E_{Sb} - xE_H$$

All formation energies are negative, which indicates that the compounds are chemically stable. There is only a slight difference in the formation energy of Yb_5Sb_3 in either the orthorhombic Ca_5Sb_3F (*Pnma*) or hexagonal Mn_5Si_3 (*P6₃/mmc*) structure type by ~ 10 meV/atom, with the hexagonal structure being more stable. Filling the interstitial sites of both structure types with H, following the stoichiometry $Yb_5Sb_3H_x$, significantly stabilizes the compounds. The more stable structure type switches from hexagonal to orthorhombic when any amount of H is incorporated.

The presence of H likely stabilizes the orthorhombic structure type more so than the hexagonal structure, due to the tetrahedral nature of the interstitial site. The interstitial sites of the hexagonal structure type are octahedral, and thus the large volume is less favorable to H occupancy. This is consistent with other reports in which A_5Sb_3Z (A = Ca, Sr, Ba, Sm, Eu, Yb) compounds were found to crystallize in the orthorhombic *Pnma* space group for Z = H, F and the hexagonal $P6_3/mmc$ for Z = Cl, Br.[6] The orthorhombic and hexagonal structure types are competitive in their formation, which is due to the small difference in formation energies, however it is possible to selectively form the orthorhombic phase by introducing interstitial H into the structure.

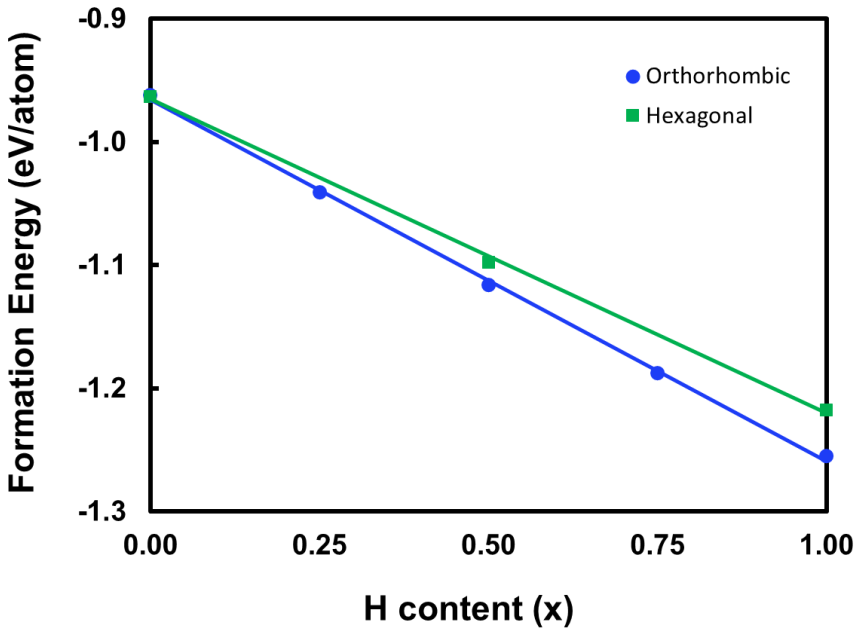


Figure 5-2. Calculated formation energy, in eV/atom, for $Yb_5Sb_3H_x$ in both the orthorhombic and hexagonal structure types as a function of H content (x).

Sample characterization

PXRD patterns for post-SPS'ed polycrystalline samples are shown in Figure 5-3, compared to the calculated pattern (bottom). The samples with higher H content (x = 0.5, 0.75, 1) can be refined as 100% orthorhombic structure type, and the lowest H-content sample (x = 0.25) contains ~15% of the hexagonal phase. While the calculations above show that any amount of H will stabilize the orthorhombic phase, samples were synthesized in sealed Ta tubes which are permeable to H_2 at high temperatures,[41,42] making it likely that not all H was incorporated into the compound, resulting in the hexagonal impurity. Previous experimental work on orthorhombic $Ca_5Sb_3H_x$ supports this hypothesis, as 0.5 equivalents of H were necessary in a welded Ta container to produce > 95% yield of the orthorhombic structure type.[28] This is consistent with other studies on A_5Pn_3 systems that have shown intermediate H content leads to the hexagonal and orthorhombic phases existing in equilibrium.[6,27–30] Samples with higher H content (x = 0.5, 0.75, 1) are 100% orthorhombic $Yb_5Sb_3H_x$.

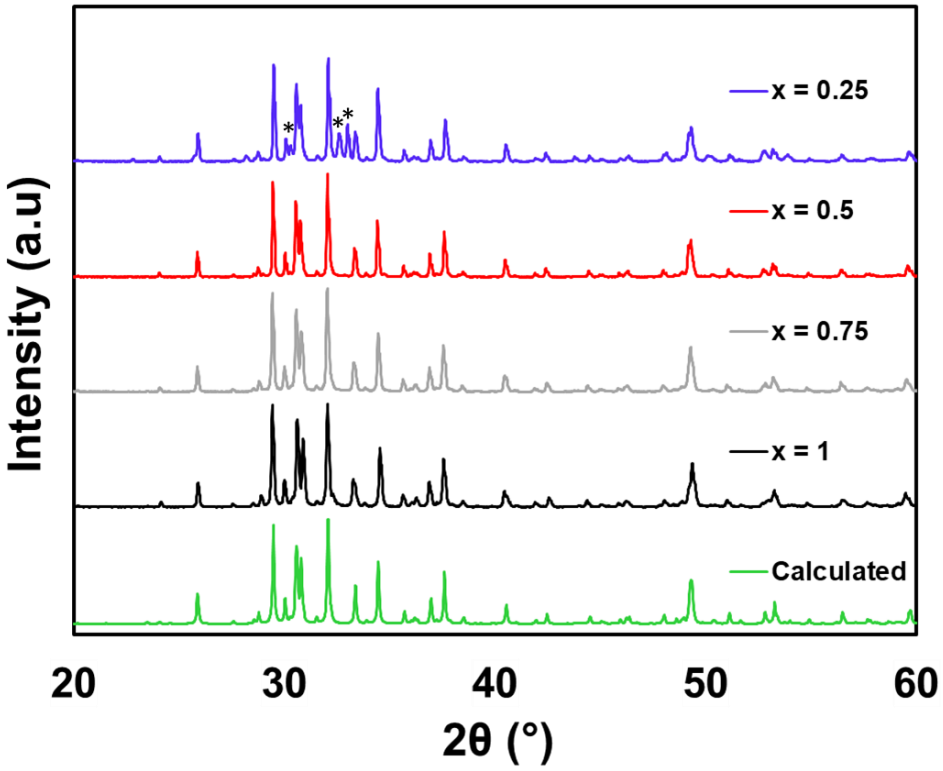


Figure 5-3. PXRD patterns of SPS'ed $Yb_5Sb_3H_x$ (x = 0.25, 0.5, 0.75, 1) samples compared to the calculated pattern (bottom). The asterisks in x = 0.25 indicate peaks corresponding to the hexagonal $Yb_5Sb_3H_x$ structure.

Lattice parameters determined via Rietveld refinement are given in Figure 5-4. The *a* lattice parameter decreases sharply with increasing H content, while the *b* and *c* parameters increase slightly. The systematic change in lattice parameters is an indication that H content varies between samples. Previously calculated electron densities showed oblong isosurfaces in the interstitial sites that extend in the crystallographic *a* direction.[5] The decreasing *a* parameter is consistent with decreased electronic repulsion that would accompany a shift from a confined electron in the interstitial site to a H atom. This result supports previous findings of decreasing cell volume with increasing H content in orthorhombic Ca_5Sb_3H[28] and the unexpectedly small lattice constants in other Mn_5Si_3-type phases due to interstitial H impurities.[6,7] Several other

studies on the A_5Pn_3 (A = Ca, Sr, Ba, Eu, Yb; Pn = Sb, Bi) compounds in the Ca_5Sb_3F structure type have used unit cell volume to estimate the amount of H in each sample.[6]

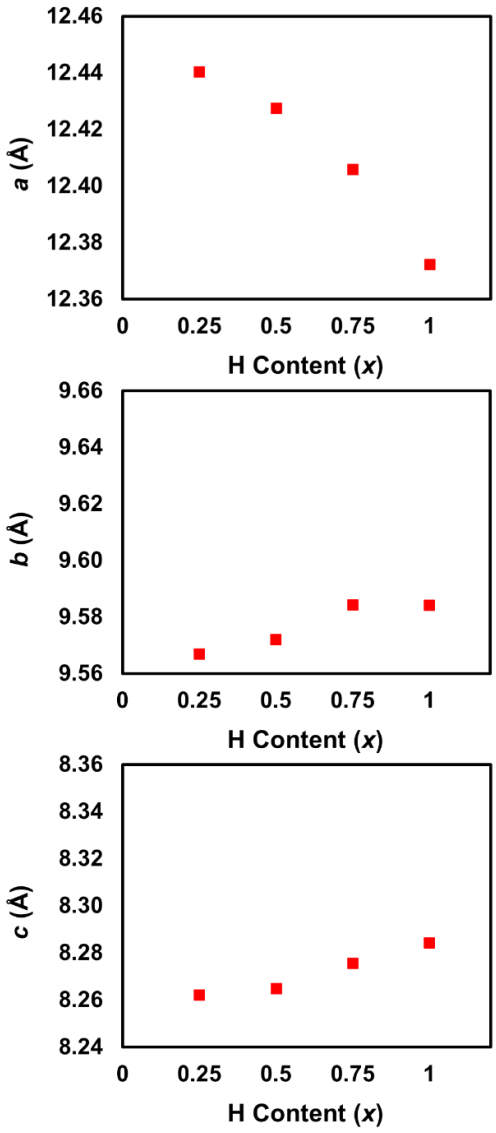


Figure 5-4.Lattice parameters of $Yb_5Sb_3H_x$ as a function of H content determined via Rietveld refinement of PXRD data.

Figure 5-5 depicts typical SEM micrographs and EDS elemental maps of Yb and Sb for the x = 0.5 sample. Backscattered electron images and elemental analysis confirm phase purity and uniform distribution of elements.

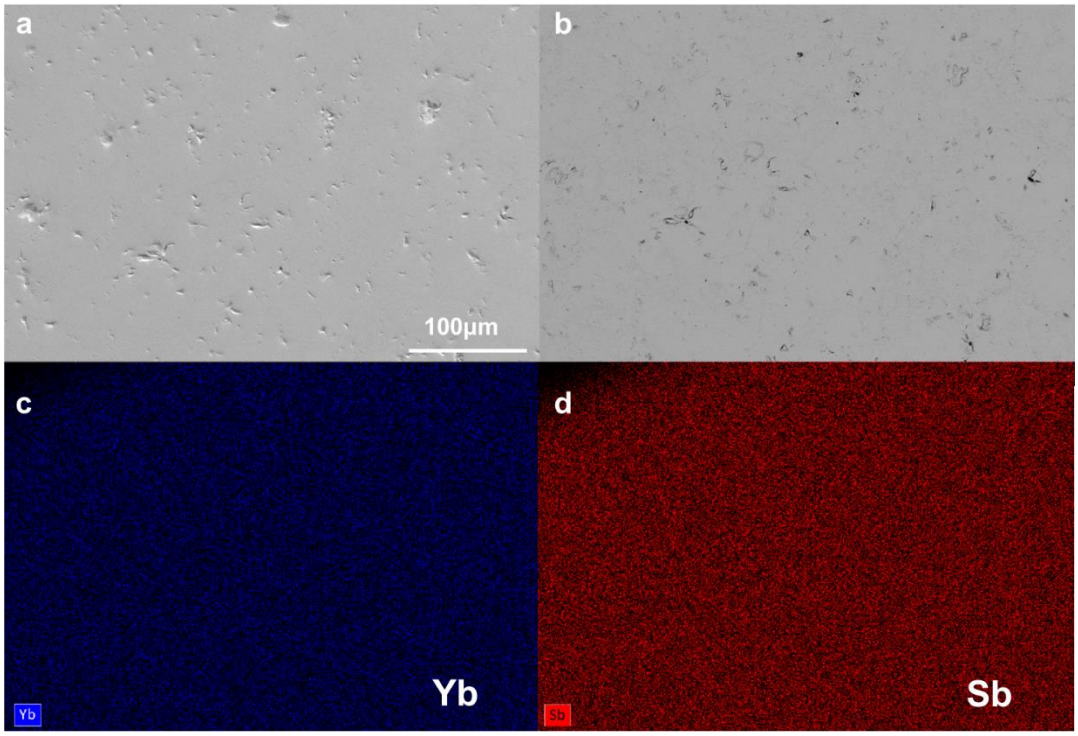


Figure 5-5. (a) Secondary electron SEM micrograph, (b) backscattered electron SEM micrograph, (c) Yb EDS elemental map, (d) Sb EDS elemental map for $Yb_5Sb_3H_x$, x = 0.75. The scale bar shown in panel (a) is the same for all panels.

After subtraction of the instrument background the ^{1}H MAS NMR spectra from the samples are displayed in Figure 5-6. ^{1}H NMR chemical shifts of metal hydrides are often in the range of 0 to 60 ppm,[43,44] and lead hydride is known to have a ^{1}H NMR shift of 31.3 ppm.[45] ^{1}H NMR signal intensities in these samples have been normalized by the sample weight. The isotropic chemical shift of the 1H NMR signals shifts to high field with increasing x values in the $Yb_5Sb_3H_x$ samples, from 17 ppm in $Yb_5Sb_3H_{0.25}$ to 9 ppm in $Yb_5Sb_3H_{0.75}$ and $Yb_5Sb_3H_{1.00}$. This

shift suggests shielding of the H that would be expected from a shorter metal hydride bond. This is consistent with the shorter Yb—H distances indicated by the *a* lattice parameter determined via PXRD that decreases as H content increases. As more of the interstitial sites take up H, the *a* lattice parameter gets smaller and the Yb—H bonds become shorter and stronger. Changing bond strengths may impact defect chemistry, as has been observed in other Zintl phases.[46] The peak width also increases with increasing *x* value. Broader lineshapes are caused by deviations in local magnetic fields that can be attributed to structural disorder and imperfect crystalline packing.[47] The ^{1}H MAS NMR signal integrations (after background subtraction and sample weight normalization) are listed in Table 5-1 and shown as a function of *x* in Figure 5-7.

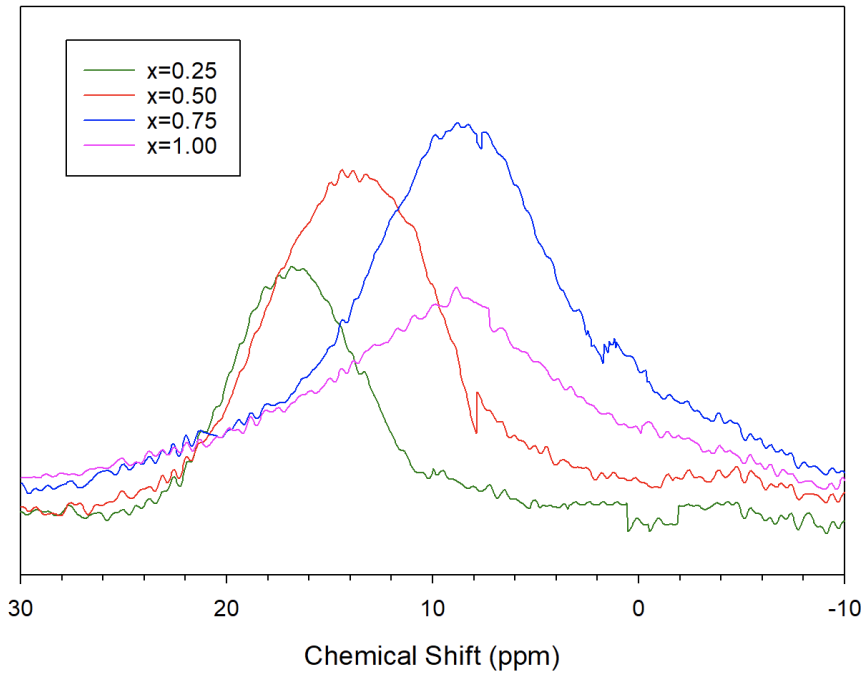
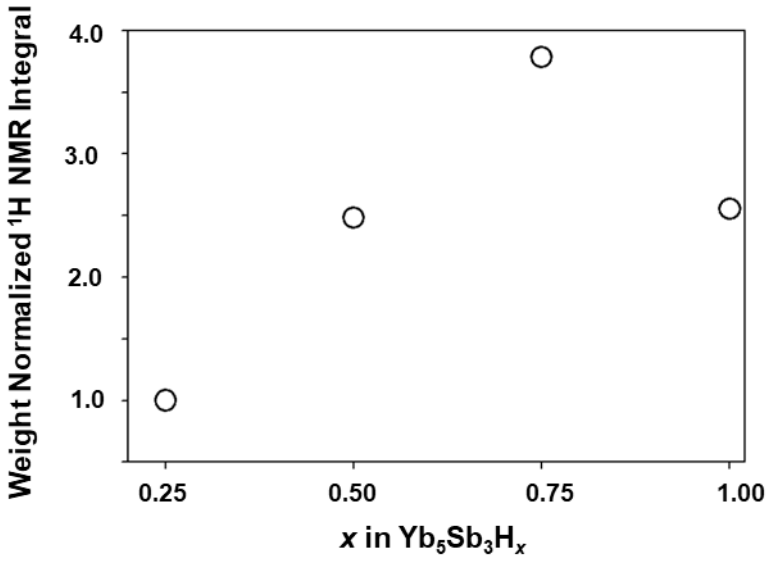


Figure 5-6.^{1}H NMR spectra in the isotropic chemical shift region, with instrument background deduction and sample weight normalization for $Yb_5Sb_3H_x$.

Table 5-5-1.[1]H MAS NMR Results for $Yb_5Sb_3H_x$

Sample	Integral (arb. unit)	Chemical Shit (ppm)	Full Width at Half Height (Hz)
$Yb_5Sb_3H_{0.25}$	1.0000	17	3190
$Yb_5Sb_3H_{0.50}$	2.4823	14.5	5383
$Yb_5Sb_3H_{0.75}$	3.7854	9	6200
$Yb_5Sb_3H_{1.00}$	2.5545	9	10500



.

Figure 5-7.[1]H MAS NMR signal intensity vs amount of hydrogen content in $Yb_5Sb_3H_x$.

Thermoelectric Property Measurements

Hall measurements show that all samples are *p*-type and carrier concentration decreases by several orders of magnitude as H content is increased (Figure 5-8), from ~8 x 10^{20} cm^{-3} for *x*

= 0.25 to ~2 x 10^{15} cm^{-3} for $x = 1$ at 300 K, indicating that H incorporation is an effective way to tune electronic properties. Band structure calculations[5] on $Yb_5Sb_3H_x$ show the presence of four localized electride bands at the Fermi level for $x = 0$, that are replaced by four localized H 1s states ~4 eV below the Fermi level for $Yb_5Sb_3H_x$ when $x = 1$ (the number of electride bands changes with x so that there are as many electride bands as unoccupied interstitial sites). The valence and conduction bands do not change significantly as x varies, and the appearance of additional bands as H is removed suggests that the extra electrons are retained at their original sites rather than being transferred into the conduction band. This may explain the experimentally observed *p*-type behavior of the system. Rather than conceptualizing the excess electrons as *n*-type dopants added to the conduction band, they are retained as anions in localized bands in 0D cavities with similar dispersion as the H 1*s* states. With this scenario, it is possible that the decrease in carrier concentration as H content increases is due to changing defect chemistry. If the dominant source of free holes in the system is Yb^{2+} vacancies, as is common in other ytterbium antimonides,[46,48,49] the presence of H inside the tetrahedral Yb_4 cages is likely to impact equilibrium defect concentration. Calculations show (Figure 5-2) that the orthorhombic structure becomes more stable as H content increases and the compound becomes charge-balanced at $x = 1$. In the absence of H, the structure is not charge balanced and Yb^{2+} vacancies could serve as a charge-compensating mechanism to reduce the number of anionic electrons and stabilize the structure. ^{1}H MAS NMR data shows H peaks shifting upfield as H content increases and the PXRD shows that the *a* lattice constant becomes smaller with increasing H. Both phenomena are consistent with shorter, stronger Yb—H bonding, which could lead to

greater defect formation energy for Yb vacancies and thereby lower carrier concentration as *x* increases.

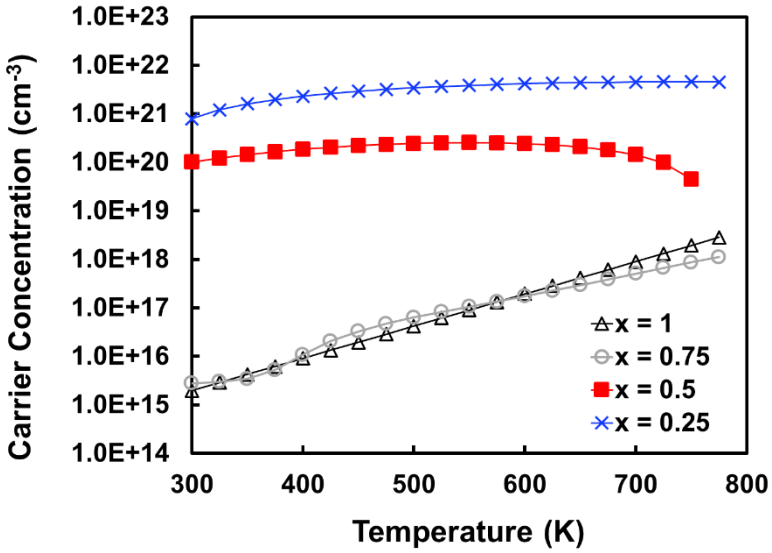


Figure 5-8. Charge carrier concentration determined via Hall effect measurements from 300 to 775 K for $Yb_5Sb_3H_x$.

The charge carrier mobility (Figure 5-9) increases dramatically as H is incorporated, that is, as the electride bands are removed, from ~0 cm^2/Vs to ~70 cm^2/Vs at 300 K. For $x = 1$, thermally activated mobility is observed below 400 K, which is often an indication of grain boundary scattering that reduces mobility at low temperatures. As discussed above, when electride bands are present, as expected for samples with $x < 1$, the trapped electrons are confined in 0D interstitial cavities that have similar symmetry to H 1*s* orbitals just below the Fermi level, resulting in low charge carrier mobility. High mobility has been reported in other, higher dimensional electrides, but the 0D nature of the tetrahedral holes in this system result in low mobility. The charge carrier mobility increases dramatically as the localized electride bands are removed (*i.e.* *x* approaches 1) and the Fermi level moves into the valence band, which is

primarily composed of Sb 5*p* states, with some contribution from Yb 5*d* orbitals, according to calculated DOS.

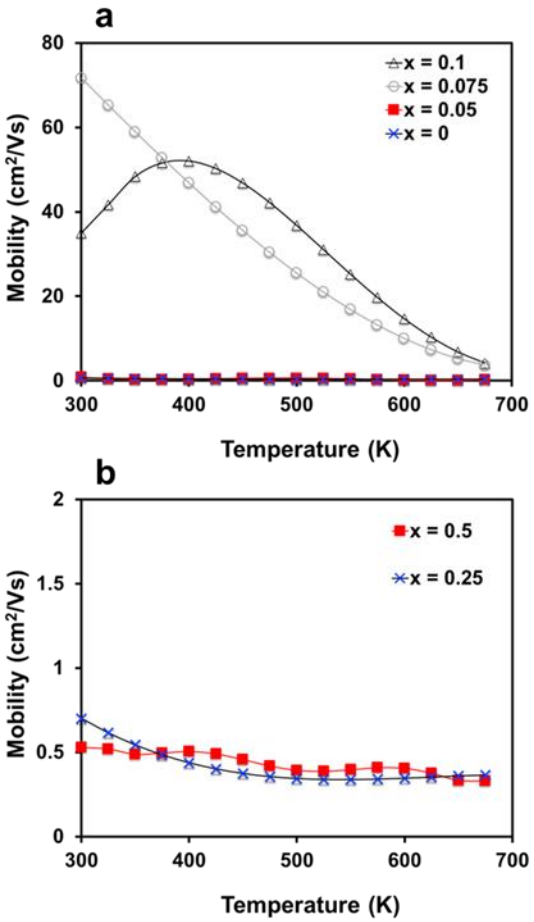


Figure 5-9.Charge carrier mobility from 300 to 775 K for $Yb_5Sb_3H_x$.

Electrical resistivity (Figure 5-10a and 5-10b) trends as expected, decreasing as carrier concentration increases. The room temperature resistivity for $x = 1$, ~74,000 mΩ-cm at 325 K, is insulating as expected from the low carrier concentration (~10^{15} cm^{-3}) and consistent with high values previously reported,[5] while a more moderate value of 23.4 mΩ-cm is observed for x =

0.25 due to the high carrier concentration and extremely low mobility. Seebeck coefficient (Figure 5-10c) also trends as expected based on carrier concentration data, with $x = 1$ exhibited the highest value of 330 μV/K at 650 K, then decreasing to 775 K, most likely due to the increasing carrier concentration with temperature. The lowest Seebeck coefficient is observed for $x = 0.25$, which reaches a maximum value of 48.2 μV/K at 450 K before decreasing due to increasing carrier concentration. The lower onset temperature of bipolar conduction for $x = 0.25$ compared to $x = 1$ could be explained by the smaller band gap in $x = 0.25$ due to the presence of electride bands ~0.5eV above the valence band maximum. In previous work, experimentally determined band gaps of Yb_5Sb_3F were smaller than calculated values, suggesting that a small amount of anionic electron states survived due to F deficiencies, which could explain the decreasing Seebeck coefficient for $x = 0.75$ and 1 at relatively low temperatures given that the gap calculated via DFT is 0.8 eV.[5]

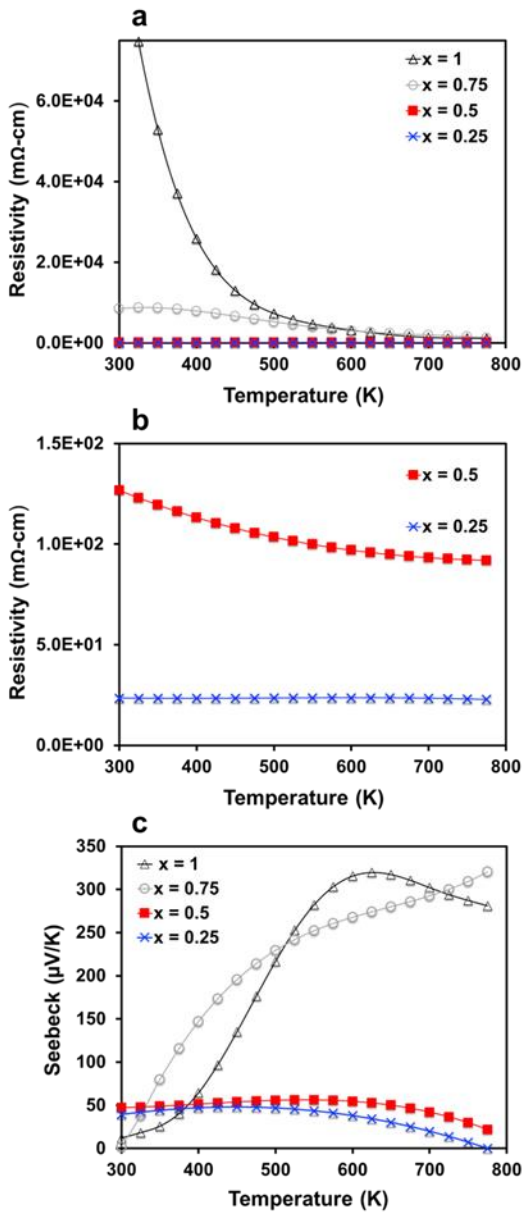


Figure 5-10.Temperature dependent (a) electrical resistivity and (b) Seebeck coefficient from 300 to 775 K for $Yb_5Sb_3H_x$.

The electronic properties fall into two distinct groups, with x = 0.25 and 0.5 giving high carrier concentration and low mobility, resistivity and Seebeck coefficient with similar

temperature dependence, behaving more like 0D electrides, while x = 0.75 and 1 exhibit low carrier concentration and high mobility, resistivity and Seebeck coefficient, behaving more like lightly doped charge-balanced semiconductors. This trend is supported by calculations that show the number of electride bands corresponds to the number of vacant interstitial sites.[5]

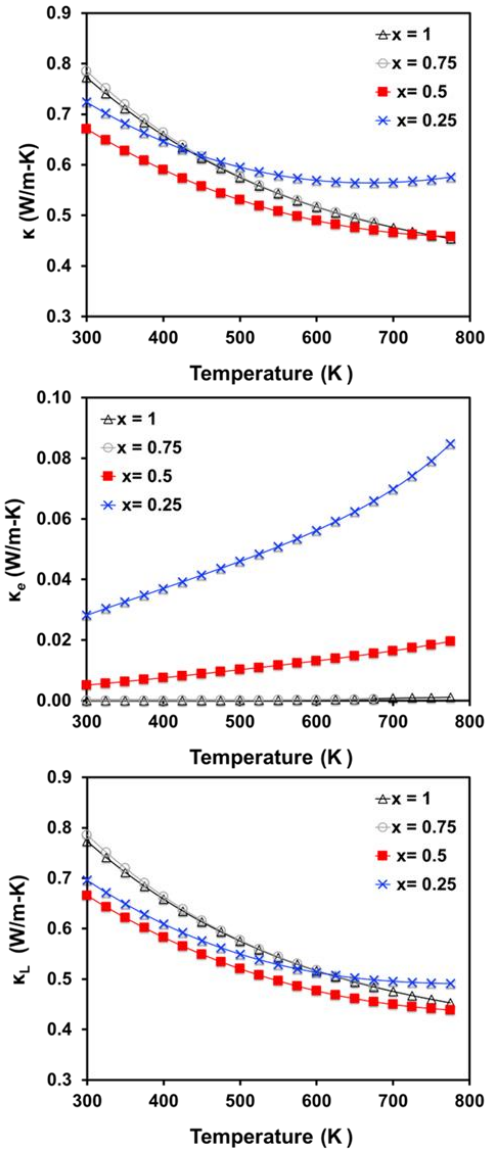


Figure 5-11. Total thermal conductivity (top); electronic component of thermal conductivity (middle) and lattice thermal conductivity (bottom) of $Yb_5Sb_3H_x$.

Thermal conductivity is shown in Figure 5-11 and was calculated from experimentally determined thermal diffusivity and heat capacity (Dulong-Petit law). Values are low for all samples, < 0.8 W/mK from 300 to 775 K, as expected for a compound containing heavy atoms and six unique crystallographic sites. The electronic contribution of the thermal conductivity was calculated using the Lorenz number derived from the Seebeck coefficient,[50] and was negligible for $x = 0.75$ and 1 due to the high electrical resistivity. Lattice thermal conductivity is lower for samples with lower H content, which could be due to phonon scattering at the electride site. The lowest lattice thermal conductivity is observed from $x = 0.5$, which has the greatest configurational entropy given its half-filled H site.

The thermoelectric figure of merit, zT, was low for all samples (Figure 5-12), reaching a maximum value of ~0.013 at 725 K for $x = 0.75$ and 1. Given the high charge carrier mobility and low lattice thermal conductivity of $x = 1$, higher zT may be achieved if carrier concentration is increased. Significant value peak zT is usually reached at carrier concentrations between 10^{19} cm^{-3} and 10^{21} cm^{-3}, several orders of magnitude higher than that of the samples we report here. Band structure calculations reveal three bands just below the Fermi level in $x = 1$, two heavy bands and one light. The combination of heavy and light bands and high valley degeneracy is favorable for thermoelectric performance and it is likely that better thermoelectric efficiency can be designed through chemical substitutions.[51–53]

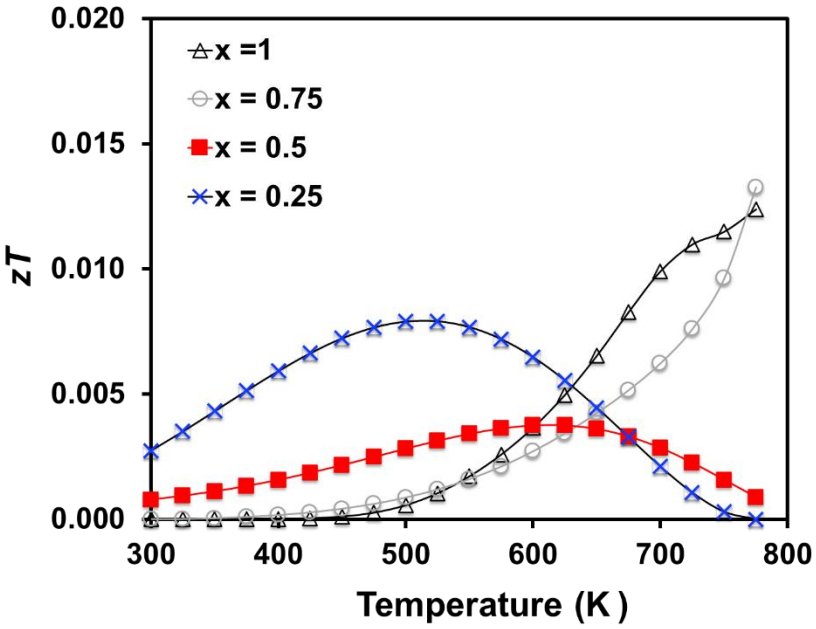


Figure 5-12. Thermoelectric figure of merit as a function of temperature for $Yb_5Sb_3H_x$.

5.5 Conclusions

We have reported the thermoelectric properties for $Yb_5Sb_3H_x$ (x = 0.25, 0.5, 0.75, 1) and characterized the structural and electronic changes as H content increases, causing a transition from an electride to a charge-balanced semiconductor. At low H content (x = 0.25, 0.5), the samples exhibit extremely low charge carrier mobility, consistent with anionic electrons localized in 0D cavities. However, given the low mobility, the electrical resistivity is moderate due to high carrier concentration that may be due to a large number of defects. The mobility increases dramatically with H content (x = 075, 1) as the localized electride bands near the Fermi level are replaced with lower lying bands with similar dispersion to H 1s orbitals, causing a transition to semiconducting behavior with charge transport dominated by delocalized states[5].

The highest *zT* was observed for $x = 1$ due to high charge carrier mobility, high Seebeck coefficient and low lattice thermal conductivity. Given the localized 0D nature of the electride cavities in orthorhombic Yb_5Sb_3H, the mobility is too low for applications in thermoelectrics, but higher *zT* is likely to be achievable for the semiconducting $x = 1$ material due to its excellent mobility if carrier concentration is able to be increased, for example, via *p*-type doping with an alkali metal. This work highlights the importance of understanding structure-property relationships and shows that minor changes in defects and composition can dramatically impact structure stability and electronic properties. It opens the door to the use of interstitial impurities, and especially H, to tune electronic properties in thermoelectrics, as well as other functional materials.

5.6 Acknowledgements

This work was supported by NSF DMR-2001156. SEM/EDS data were acquired from the Advanced Materials Characterization and Testing laboratory (AMCaT) supported by NSF DMR-1725618 at the University of California, Davis. Ashlee Hauble was supported by the University of California, Davis Dean's Distinguished Graduate Student Fellowship. E.S.T. and K.C. acknowledge DMR – 1555340 and DMR – 1729594.

5.7 Appendix

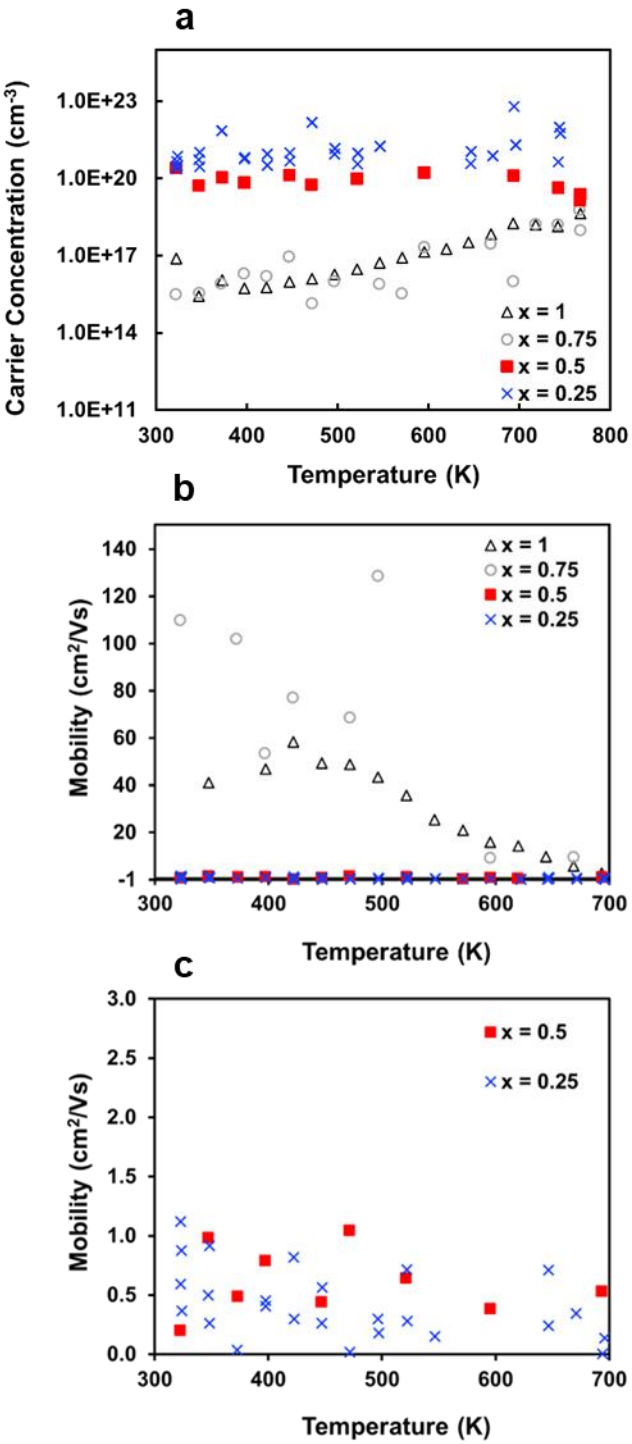


Figure 5-13. Experimental Hall effect measurement data. (a) carrier concentration; (b) mobility; (c) mobility scaled for x = 0.25 and 0.5

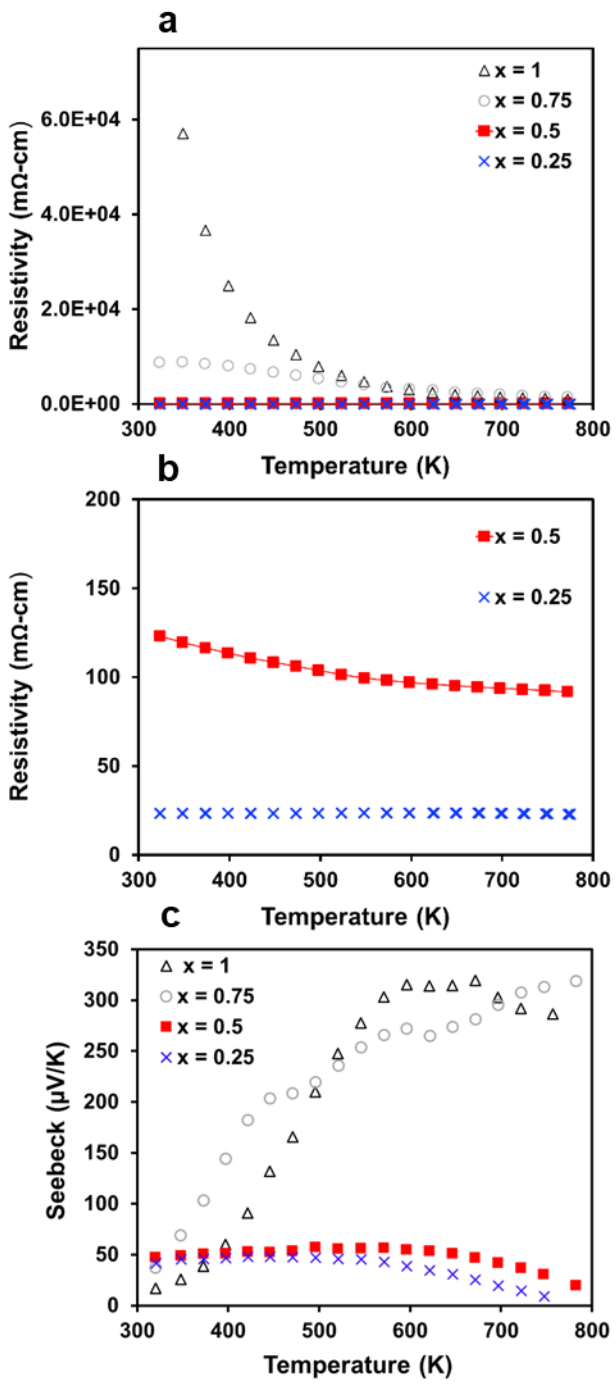


Figure 5-14. Experimental electronic transport data. (a) electrical resistivity; (b) electrical resistivity scaled for x = 0.25 and 0.5mobility; (c) Seebeck coefficients.

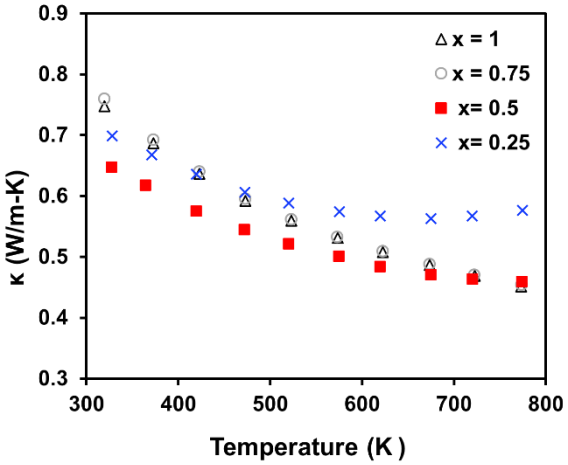
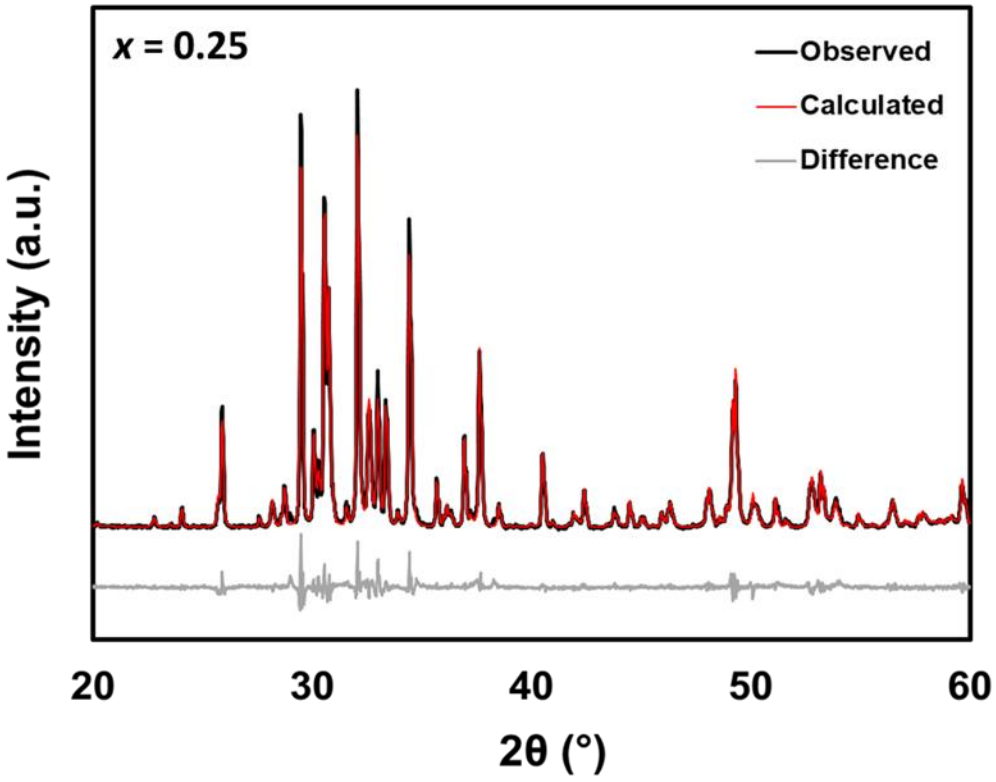
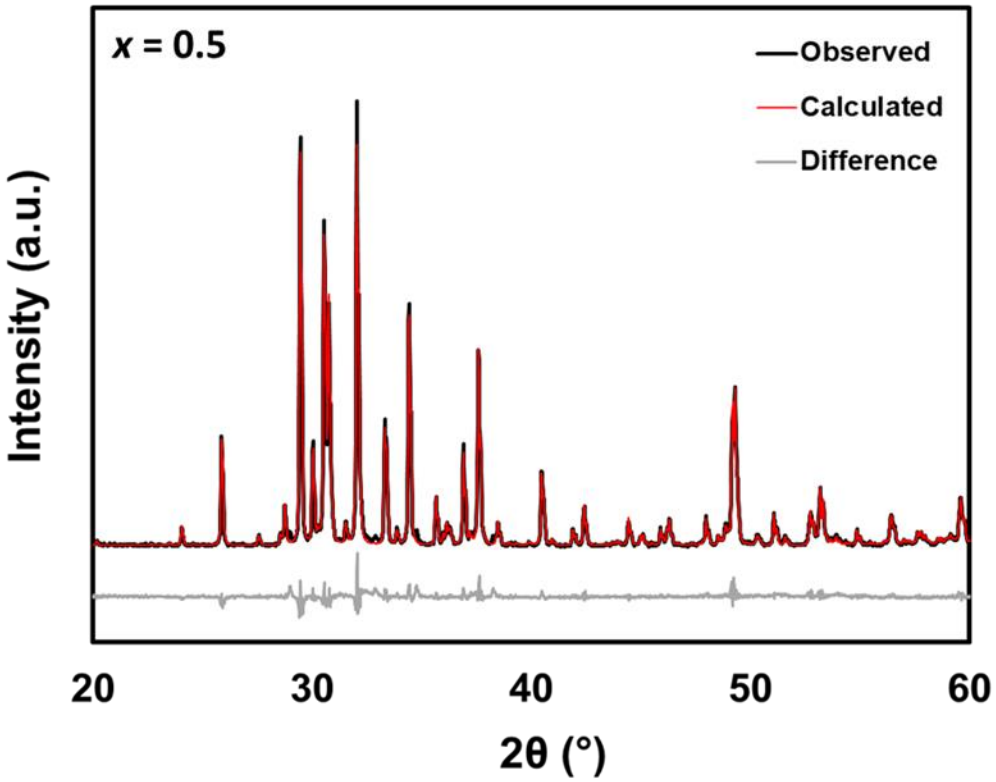


Figure 5-15. Experimental thermal conductivity data.


x = 0.25
Observed
Calculated
Difference
Intensity (a.u.)
20
30
40
50
60
2θ (°)


x = 0.5
Observed
Calculated
Difference
Intensity (a.u.)
20
30
40
50
60
2θ (°)

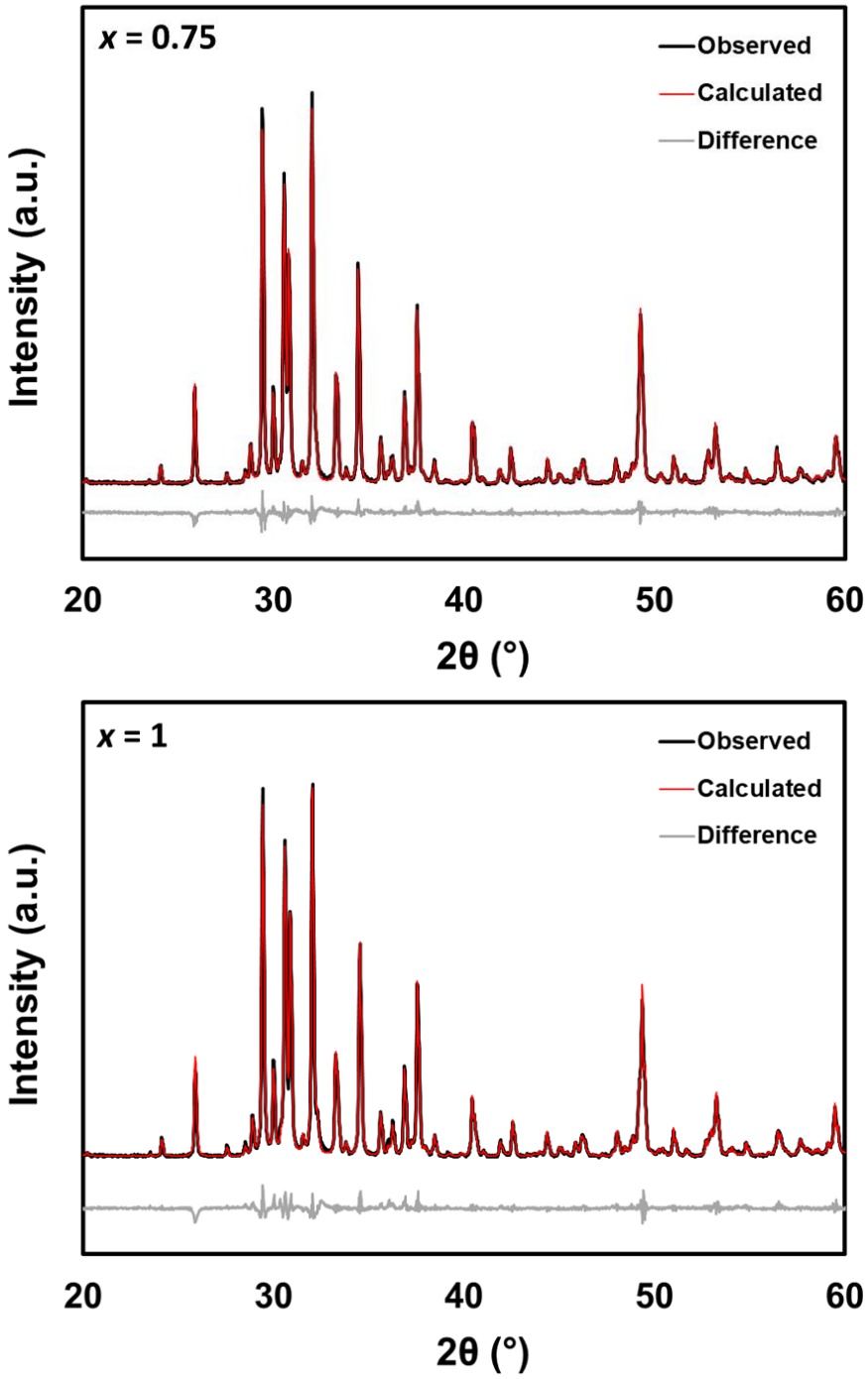


Figure 5-16. Portion of typical Rietveld refinements of $Yb_5Sb_3H_x$ (x = 0.25, 0.5, 0.75, 1). The observed data are shown in black, calculated pattern in red, and difference curve is in gray.

Table 5-2. Selected Rietveld Refinement Statistics from $Yb_5Sb_3H_x$.

x		**0.25**	**0.5**	**0.75**	**1**
Unit Cell Parameters	*a* (Å)	12.4405(2)	12.4276(2)	12.4060(2)	12.3723(2)
	b (Å)	9.5670(2)	9.5721(2)	9.5845(2)	9.5843(2)
	c (Å)	8.2622(2)	8.2650(2)	8.2757(1)	8.2843(2)
	V (Å^3)	983.34(3)	983.18(3)	984.02(3)	982.36(3)
Rp (%), Rwp (%)		7.87, 10.81	7.20, 10.12	5.65, 7.71	6.45, 8.61
Orthorhombic type (wt %)		83.17	100	100	100
Hexagonal type (wt %)		16.83	0	0	0

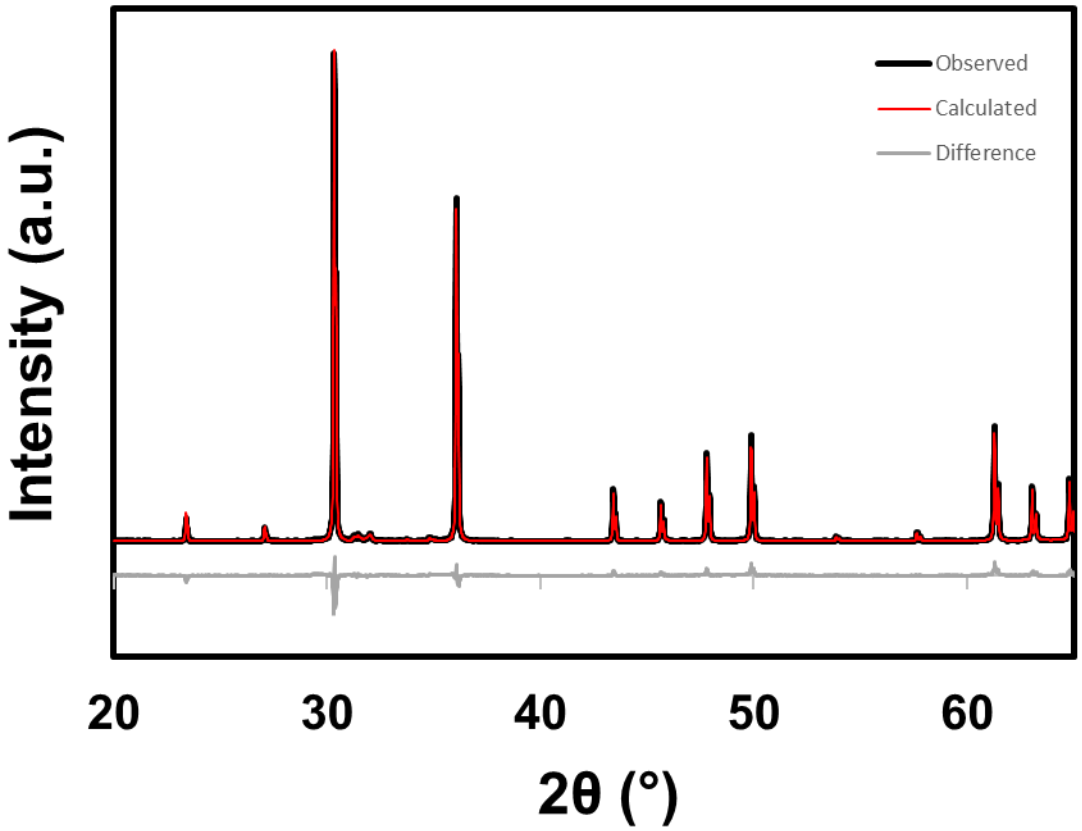


Figure 5-17. Portion of a typical Rietveld refinement of Yb_4Sb_3 precursor

Table 5-3. Selected Rietveld Refinement Statistics from Yb_4Sb_3 precursor

x		
Unit Cell Parameters	*a* (Å)	9.32397(1)
	V (Å^3)	810.59(2)
Rp (%), Rwp (%)	7.65	8.54
Yb_4Sb_3 (wt %)	93.90	
$Yb_{11}Sb_{10}$ (wt %)	6.10	

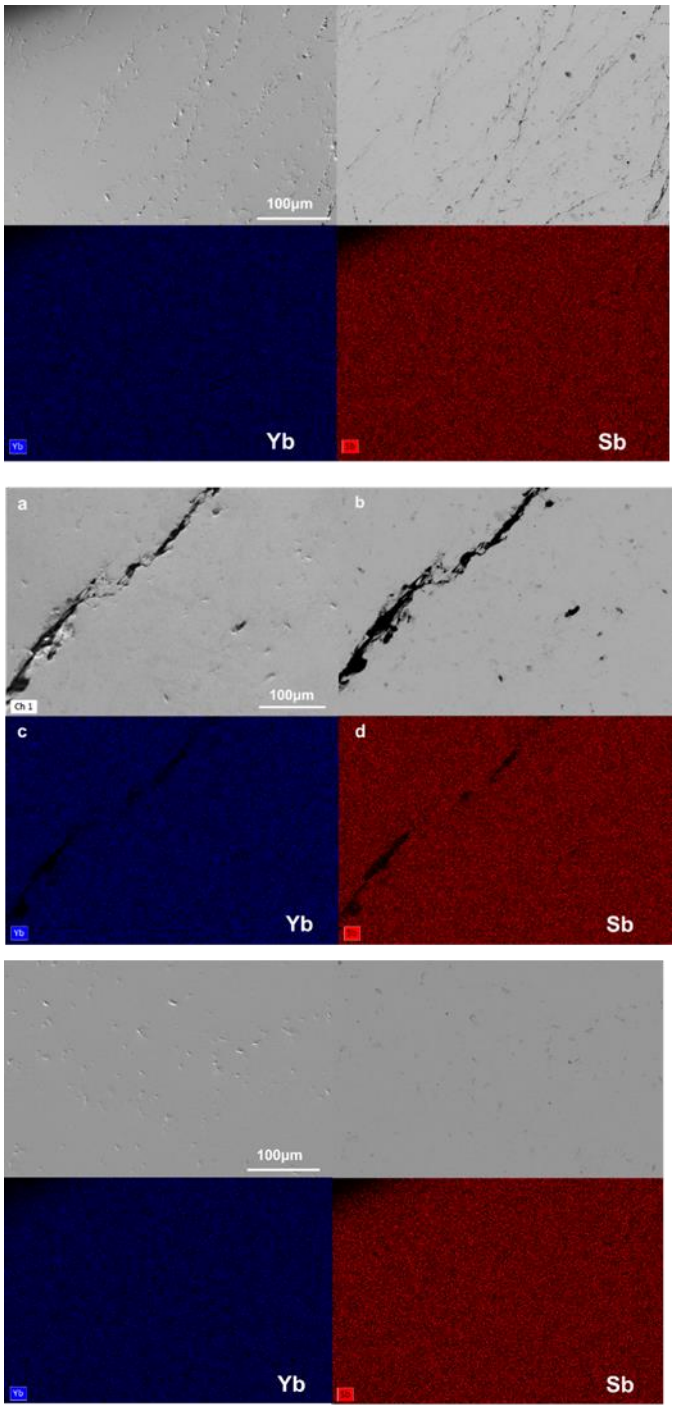


Figure 5-18. (a) Secondary electron SEM micrograph, (b) backscattered electron SEM micrograph, (c) Yb EDS elemental map, (d) Sb EDS elemental map for $x = 0.25$ (top), $x = 0.5$ (middle), and $x = 1$ (bottom). The scale bar shown in panel a is the same for all panels.

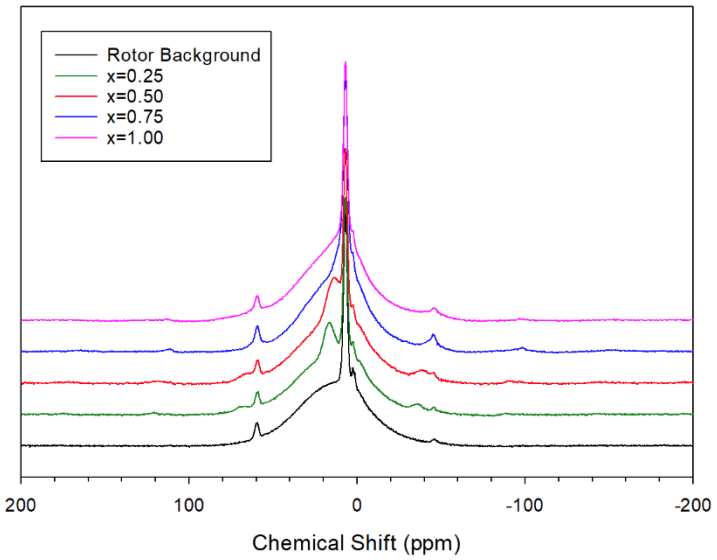


Figure 5-19. ^{1}H MAS NMR spectra of $Yb_5Sb_3H_x$ with x = 0.25, 0.50, 0.75 and 1.00. Instrument ^{1}H background is also displayed for comparison.

5.8 References

(1) Zhang, X.; Yang, G. Recent Advances and Applications of Inorganic Electrides. *J. Phys. Chem. Lett.* **2020**, *11* (10), 3841–3852. https://doi.org/10.1021/acs.jpclett.0c00671.

(2) Le, L. D.; Issa, D.; Van Eck, B.; Dye, J. L. Preparation of Alkalide and Electride Films by Direct Vapor Deposition. *J. Phys. Chem.* **1982**, *86* (1), 7–9. https://doi.org/10.1021/j100390a004.

(3) Hosono, H.; Kitano, M. Advances in Materials and Applications of Inorganic Electrides. *Chem. Rev.* **2021**, *121* (5), 3121–3185. https://doi.org/10.1021/acs.chemrev.0c01071.

(4) Novoselov, D. Y.; Anisimov, V. I.; Oganov, A. R. Strong Electronic Correlations in

Interstitial Magnetic Centers of Zero-Dimensional Electride β-Yb_5Sb_3. *Phys. Rev. B* **2021**, *103* (23), 1–6. https://doi.org/10.1103/PhysRevB.103.235126.

(5) Lu, Y.; Wang, J.; Li, J.; Wu, J.; Kanno, S.; Tada, T.; Hosono, H. Realization of Mott-Insulating Electrides in Dimorphic Yb_5Sb_3. *Phys. Rev. B* **2018**, *98* (12), 1–12. https://doi.org/10.1103/PhysRevB.98.125128.

(6) Corbett, J. D.; Garcia, E.; Guloy, A. M.; Hurng, W. M.; Kwon, Y. U.; Leon-Escamilla, E. A. Widespread Interstitial Chemistry of Mn_5Si_3-Type and Related Phases. Hidden Impurities and Opportunities. *Chem. Mater.* **1998**, *10* (10), 2824–2836. https://doi.org/10.1021/cm980223c.

(7) León-escamilla, E. A. Polar Intermetallic Compounds of the Silicon and Arsenic Family Elements and Their Ternary Hydrides and Fluorides, Iowa State University, Ames Iowa, 1996.

(8) Alejandro Leon-Escamilla, E.; Corbett, J. D. Hydrogen in Polar Intermetallics. Binary Pnictides of Divalent Metals with Mn_5Si_3-Type Structures and Their Isotypic Ternary Hydride Solutions. *Chem. Mater.* **2006**, *18* (20), 4782–4792. https://doi.org/10.1021/cm0612191.

(9) Zeng, X.; Zhao, S.; Li, Z.; Yang, J. Electron-Phonon Interaction in a Ca2 N Monolayer: Intrinsic Mobility of Electrene. *Phys. Rev. B* **2018**, *98* (15), 155443. https://doi.org/10.1103/PhysRevB.98.155443.

(10) Kim, S. W.; Matsuishi, S.; Nomura, T.; Kubota, Y.; Takata, M.; Hayashi, K.; Kamiya, T.; Hirano, M.; Hosono, H. Metallic State in a Lime-Alumina Compound with Nanoporous Structure. *Nano Lett.* **2007**, *7* (5), 1138–1143. https://doi.org/10.1021/nl062717b.

(11) Lee, K.; Kim, S. W.; Toda, Y.; Matsuishi, S.; Hosono, H. Dicalcium Nitride as a Two-Dimensional Electride with an Anionic Electron Layer. *Nature* **2013**, *494* (7437), 336–340. https://doi.org/10.1038/nature11812.

(12) Snyder, G. J.; Toberer, E. S. Complex Thermoelectric Materials. *Nat. Mater.* **2010**, *7* (February), 101–110. https://doi.org/10.1142/9789814317665_0016.

(13) Dresselhaus, M. S.; Chen, G.; Tang, M. Y.; Yang, R.; Lee, H.; Wang, D.; Ren, Z.; Fleurial, J.-P.; Gogna, P. New Directions for Low-Dimensional Thermoelectric Materials. *Adv. Mater.* **2007**, *19*, 1043–1053. https://doi.org/10.1002/adma.200600527.

(14) Parker, D.; Chen, X.; Singh, D. J. High Three-Dimensional Thermoelectric Performance from Low-Dimensional Bands. *Phys. Rev. Lett.* **2013**, *110* (14), 1–5. https://doi.org/10.1103/PhysRevLett.110.146601.

(15) Bilc, D. I.; Hautier, G.; Waroquiers, D.; Rignanese, G. M.; Ghosez, P. Low-Dimensional Transport and Large Thermoelectric Power Factors in Bulk Semiconductors by Band Engineering of Highly Directional Electronic States. *Phys. Rev. Lett.* **2015**, *114* (13), 1–5. https://doi.org/10.1103/PhysRevLett.114.136601.

(16) Kauzlarich, S. M.; Brown, S. R.; Snyder, G. J. Zintl Phases for Thermoelectric Devices.

2007. https://doi.org/10.1039/b702266b.

(17) Kawamura, A.; Hu, Y.; Kauzlarich, S. M. Synthesis and Thermoelectric Properties of the YbTe-YbSb System. *J. Electron. Mater.* **2016**, *45* (1), 779–785. https://doi.org/10.1007/s11664-015-4202-x.

(18) Grebenkemper, J. H.; Hu, Y.; Barrett, D.; Gogna, P.; Huang, C.-K.; Bux, S. K.; Kauzlarich, S. M. High Temperature Thermoelectric Properties of $Yb_{14}MnSb_{11}$ Prepared from Reaction of MnSb with the Elements. *Chem. Mater.* **2015**, *27* (16), 5791–5798. https://doi.org/10.1021/acs.chemmater.5b02446.

(19) Chamoire, A.; Gascoin, F.; Estournès, C.; Caillat, T.; Tédenac, J. C. High-Temperature Transport Properties of $Yb_{4-x}Sm_xSb_3$. *J. Electron. Mater.* **2010**, *39* (9), 1579–1582. https://doi.org/10.1007/s11664-010-1274-5.

(20) Rauscher, J. F.; Kauzlarich, S. M.; Ikeda, T.; Snyder, G. J. Synthesis, Structure, and High Temperature Thermoelectric Properties of $Yb_{11}Sb_{9.3}Ge_{0.5}$. *Zeitschrift fur Anorg. und Allg. Chemie* **2007**, *633* (10), 1587–1594. https://doi.org/10.1002/zaac.200700267.

(21) Brunton, G. D.; Steinfink, H. The Crystal Structure of β-Ytterbium Triantimonide, a Low-Temperature Phase. *Solid State Commun.* **2010**, *150* (9–10), 383–385. https://doi.org/10.1016/j.ssc.2010.01.002.

(22) Steinfink, H; Bodnar, R. E. . The Phase Equilibria and Crystal Chemistry of the Intermediate Phases in the Ytterbium-Antimony System. **1968**, *1111* (12), 1154–1157.

(23) Bodnar, R. E.; Steinfink, H.; Narasimhan, K. S. V. L. Magnetic and Electrical Properties of Some Yb--Sb Phases. *J. Appl. Phys.* **1968**, *39* (3), 1485–1489. https://doi.org/10.1063/1.1656385.

(24) Werwein, A.; Benndorf, C.; Bertmer, M.; Franz, A.; Oeckler, O.; Kohlmann, H. Hydrogenation Properties of $LnAl_2$ (Ln = La, Eu, Yb), $LaGa_2$, $LaSi_2$ and the Crystal Structure of $LaGa_2H_{0.71}$. *Crystals* **2019**, *9* (4), 193. https://doi.org/10.3390/cryst9040193.

(25) Häussermann, U.; Kranak, V. F.; Puhakainen, K. Hydrogenous Zintl Phases: Interstitial versus Polyanionic Hydrides. *Struct. Bond.* **2011**, *139* (July 2010), 143–161. https://doi.org/10.1007/430_2010_20.

(26) Kranak, V. Investigating Hydrogenous Behavior of Zintl Phases: Interstitial Hydrides, Polyanionic Hydrides, Complex Hydrides, Oxidative Decomposition. Department of Materials and Environmental Chemistry (MMK), Stockholm University 2017.

(27) Leon-Escamilla, E. A.; Corbett, J. D. Compounds of Alkaline-Earth and Divalent Rare-Earth Metals Stabilized by Hydrogen Impurities. The Yb_5Sb_3 and Mn_5Si_3 Structure Types for Pnictides. *J. Alloys Compd.* **1994**, *206* (2), 15–17. https://doi.org/10.1016/0925-8388(94)90025-6.

(28) Leon-Escamilla, E. A.; Corbett, J. D. Hydrogen Stabilization: Nine Isotypic Orthorhombic A_5Pn_3H Phases (among A=Ca, Sr, Ba, Sm, Eu, Yb; Pn=Sb, Bi) Formerly Described as Binary β-Yb_5Sb_3-Type Compounds. *J. Alloys Compd.* **1998**, *265* (1–2), 104–114. https://doi.org/10.1016/S0925-8388(97)00320-4.

(29) Mudring, A.-V.; Corbett, J. D. Unusual Electronic and Bonding Properties of the Zintl Phase Ca_5Ge_3 and Related Compounds: A Theoretical Analysis. *J. Am. Chem. Soc.* **2004**, *126* (16), 5277–5281. https://doi.org/10.1021/ja030216b.

(30) Hurng, W. M.; Corbett, J. D. Alkaline-Earth-Metal Antimonides and Bismuthides with the A_5Pn_3 Stoichiometry. Interstitial and Other Zintl Phases Formed on Their Reactions with Halogen or Sulfur. *Chem. Mater.* **1989**, *1* (3), 311–319. https://doi.org/10.1021/cm00003a008.

(31) Giannozzi, P.; Baroni, S.; Bonini, N.; Calandra, M.; Car, R.; Cavazzoni, C.; Ceresoli, D.; Chiarotti, G. L.; Cococcioni, M.; Dabo, I.; Corso, A. D.; Gironcoli, S. De; Fabris, S.; Fratesi, G.; Gebauer, R.; Gerstmann, U.; Gougoussis, C.; Kokalj, A.; Lazzeri, M.; Martin-samos, L.; Marzari, N.; Mauri, F.; Mazzarello, R.; Paolini, S.; Pasquarello, A.; Paulatto, L.; Sbraccia, C.; Smogunov, A.; Umari, P. QUANTUM ESPRESSO : A Modular and Open-Source Software Project for Quantum Simulations of Materials. *J. Phys. Condens. Matter* **2009**, *21* (395502). https://doi.org/10.1088/0953-8984/21/39/395502.

(32) Giannozzi, P.; Andreussi, O.; Brumme, T.; Bunau, O.; Buongiorno, M. Advanced Capabilities for Materials Modelling with Quantum ESPRESSO. *J. Phys. Condens. Matter* **2017**, *29* (465901).

(33) Perdew, J. P.; Ernzerhof, M.; Burke, K. Rationale for Mixing Exact Exchange with Density Functional Approximations Rationale for Mixing Exact Exchange with Density Functional Approximations. *J. Chem. Phys* **1996**, *105* (22).

(34) Perdew, J. P.; Burke, K.; Ernzerhof, M. Generalized Gradient Approximation Made Simple. *Phys. Rev. Lett.* **1996**, *77* (18), 3865–3868. https://doi.org/10.1103/PhysRevLett.77.3865.

(35) Kresse, G.; Joubert, D. From Ultrasoft Pseudopotentials to the Projector Augmented-Wave Method. *Phys. Rev. B - Condens. Matter Mater. Phys.* **1999**, *59* (3), 1758–1775. https://doi.org/10.1103/PhysRevB.59.1758.

(36) Barrett, B. Y. C. S.; Cucka, P.; Haeynet, K. The Crystal Structure of Antimony at 4.2, 78 and 298 K. *Acta Crystallogr. Sect. A* **1963**, *16* (451), 451–453. https://doi.org/10.1107/S0365110X63001262.

(37) Spedding, F. H.; Hanak, J. J.; Daane, A. H. HIGH TEMPERATURE ALLOTROPY AND THERMAL EXPANSION OF THE RARE-EARTH METALS. *J. Less-Common Met.* **1961**, *3* (940), 110–124.

(38) Peterson, D. T. Purification of Alkaline Earth Metals. *Jom* **1987**, *39* (5), 20–23. https://doi.org/10.1007/BF03258986.

(39) Borup, K. A.; Toberer, E. S.; Zoltan, L. D.; Nakatsukasa, G.; Errico, M.; Fleurial, J.-P.; Iversen, B. B. Measurement of the Electrical Resistivity and Hall Coefficient at High Temperatures. *Rev. Sci. Instrum* **2012**, *83* (123902), 123902. https://doi.org/10.1063/1.4770124.

(40) Iwanaga, S.; Toberer, E. S.; Lalonde, A.; Snyder, G. J. A High Temperature Apparatus for Measurement of the Seebeck Coefficient. *Rev. Sci. Instrum.* **2011**, *82* (6), 0639051–

0639056. https://doi.org/10.1063/1.3601358.

(41) E. Buxbaum, R.; B. Kinney, A. Hydrogen Transport through Tubular Membranes of Palladium-Coated Tantalum and Niobium. *Ind. Eng. Chem. Res.* **1996**, *35* (2), 530–537. https://doi.org/10.1021/ie950105o.

(42) Taxak, M.; Kumar, S.; Krishnamurthy, N.; Suri, A.; Tiwari, G. Change in Lattice Parameter of Tantalum Due to Dissolved Hydrogen. *Process. Appl. Ceram.* **2012**, *6* (2), 73–76. https://doi.org/10.2298/pac1202073t.

(43) Gao, P.; Hou, G. Recent Advances on Surface Metal Hydrides Studied by Solid-State Nuclear Magnetic Resonance Spectroscopy. *Magn. Reson. Lett.* **2022**, *2* (4), 1–12. https://doi.org/10.1016/j.mrl.2022.09.001.

(44) Xue, Z. L.; Cook, T. M.; Lamb, A. C. Trends in NMR Chemical Shifts of D0 Transition Metal Compounds. *J. Organomet. Chem.* **2017**, *852* (1), 74–93. https://doi.org/10.1016/j.jorganchem.2017.03.044.

(45) Schneider, J.; P. Sindlinger, C.; Eichele, K.; Schubert, H.; Wesemann, L. Low-Valent Lead Hydride and Its Extreme Low-Field 1H NMR Chemical Shift. *J. Am. Chem. Soc.* **2017**, *139* (19), 6542–6545. https://doi.org/10.1021/jacs.7b01856.

(46) Pomrehn, G. S.; Zevalkink, A.; Zeier, W. G.; Van De Walle, A.; Snyder, G. J. Defect-Controlled Electronic Properties in AZn_2Sb_2 Zintl Phases. *Angew. Chemie - Int. Ed.* **2014**, *53* (13), 3422–3426. https://doi.org/10.1002/anie.201311125.

(47) Chen, K. A Practical Review of NMR Lineshapes for Spin-1/2 and Quadrupolar Nuclei in Disordered Materials. *Int. J. Mol. Sci.* **2020**, *21* (16), 1–22. https://doi.org/10.3390/ijms21165666.

(48) Zevalkink, A.; Zeier, W. G.; Cheng, E.; Snyder, J.; Fleurial, J. P.; Bux, S. Nonstoichiometry in the Zintl Phase $Yb_{1-\delta}Zn_2Sb_2$ as a Route to Thermoelectric Optimization. *Chem. Mater.* **2014**, *26* (19), 5710–5717. https://doi.org/10.1021/cm502588r.

(49) Cooley, J. A.; Promkhan, P.; Gangopadhyay, S.; Donadio, D.; Pickett, W. E.; Ortiz, B. R.; Toberer, E. S.; Kauzlarich, S. M. High Seebeck Coefficient and Unusually Low Thermal Conductivity Near Ambient Temperatures in Layered Compound $Yb_{2-x}Eu_xCdSb_2$. *Chem. Mater.* **2018**, *30* (2), 484–493. https://doi.org/10.1021/acs.chemmater.7b04517.

(50) Kim, H. S.; Gibbs, Z. M.; Tang, Y.; Wang, H.; Snyder, G. J. Characterization of Lorenz Number with Seebeck Coefficient Measurement. *APL Mater.* **2015**, *3* (4), 1–6. https://doi.org/10.1063/1.4908244.

(51) Zhang, X.; Wang, C.; Wang, Y. X. Influence of the Elements (Pn = As, Sb, Bi) on the Transport Properties of p-Type Zintl Compounds Ba_2ZnPn_2. *Comput. Mater. Sci.* **2017**, *127*, 8–14. https://doi.org/10.1016/j.commatsci.2016.10.022.

(52) Pei, Y.; Shi, X.; Lalonde, A.; Wang, H.; Chen, L.; Snyder, G. J.; Snyder, & G. J. Convergence of Electronic Bands for High Performance Bulk Thermoelectrics. *Nature* **2011**, *473* (7345), 66–69. https://doi.org/10.1038/nature09996.

(53) Perez, C. J.; Wood, M.; Ricci, F.; Yu, G.; Vo, T.; Bux, S. K.; Hautier, G.; Rignanese, G.-M.; Snyder, G. J.; Kauzlarich, S. M. Discovery of Multivalley Fermi Surface Responsible for the High Thermoelectric Performance in $Yb_{14}MnSb_{11}$ and $Yb_{14}MgSb_{11}$. *Sci. Adv.* **2021**, *7* (4). https://doi.org/10.1126/sciadv.abe9439.